ISBN 978-82-326-5852-7 (printed ver.)
ISBN 978-82-326-6312-5 (electronic ver.)
ISSN 1503-8181 (printed ver.)
ISSN 2703-8084 (electronic ver.)

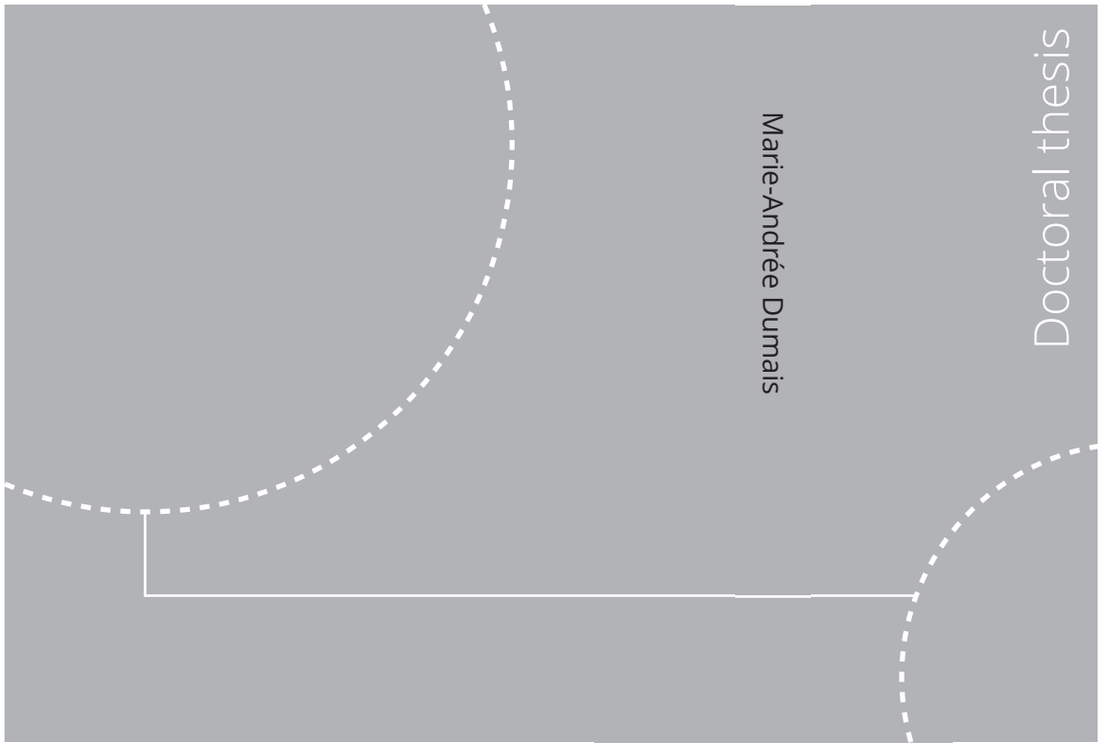

Doctoral theses at NTNU, 2021:421

Marie-Andrée Dumais

Regional tectonic and environmental assessments of the Norwegian Polar Regions using potential field methods

NTNU
Norwegian University of Science and Technology

Doctoral theses at NTNU, 2021:421

NTNU

NTNU
Norwegian University of Science and Technology
Thesis for the degree of Philosophiae Doctor
Faculty of Engineering
Department of Geoscience and Petroleum

NTNU
Norwegian University of Science and Technology

Marie-Andrée Dumais

Regional tectonic and environmental assessments of the Norwegian Polar Regions using potential field methods

Thesis for the degree of Philosophiae Doctor

Trondheim, December 2021

Norwegian University of Science and Technology
Faculty of Engineering
Department of Geoscience and Petroleum

NTNU
Norwegian University of
Science and Technology

NTNU
Norwegian University of Science and Technology

Thesis for the degree of Philosophiae Doctor

Faculty of Engineering
Department of Geoscience and Petroleum

ISBN 978-82-326-5852-7 (printed ver.)
ISBN 978-82-326-6312-5 (electronic ver.)
ISSN 1503-8181 (printed ver.)
ISSN 2703-8084 (electronic ver.)

Doctoral theses at NTNU, 2021:421

PRINTED IN NORWAY
NO - 1598

NORDIC SWAN ECOLABEL
Printed matter
2041 0731

Printed by Skipnes Kommunikasjon AS

This work is dedicated to my daughter
Léa and my husband Frode.

"Smooth seas to do not make good sailors." – common proverb

Preface

The polar regions are magnificent, yet terrifying and unforgivable. They are remote, difficult to access with turbulent weather systems, and yet unveil spectacular light phenomena. There are no smooth edges to the polar regions. We sail in their rough seas in the pursuit of knowledge, hopeful to uncover its mysteries.

The aim of this thesis is to shed light on the magmatic processes, tectonic history, and environmental settings of the Norwegian polar region and to discuss its implications on the current regional settings. Through my academic training at NTNU, I passed the following courses:

- TGB4280 – Geophysical Exploration for Natural Resources (7.5 ECTS)
- PG8212 - Interpretation of Combined Geophysics. Applications of Gravimetry and Magnetometry in Geological Models (7.5 ECTS)
- AG834 – Basins and Petroleum Provinces (10 ECTS, UNIS)
- AG845 – Polar Magnetospheric Substorms (10 ECTS, UNIS)
- IFEL8000 – Introduction to Research Methodology, Theory of Science and Ethics (3 ECTS)

Although not in my academic curriculum, I also attended the following course to improve my geophysical interpretation skills.

- TGB4265 – Structural Geology, Advanced Course (no credits)

For the acquisition, processing, and interpretation of the Fram Strait study (KRAS-16), the research funds were granted by the European Plate Observation System – Norway, the Geological Survey of Norway, and the Norwegian Petroleum Directorate. The gravity data used for the ice thickness model of Austfonna were provided by the Mapping Authority of Norway. The magnetic data were provided by the Geological Survey of Norway.

My research projects were mainly carried out at NGU. I took part in flight lines and survey designing and carried out data quality control, data processing, interpretation, and scientific writing. I took actively part in research groups at NTNU:

- Data Interpretation Group, IGP

- NTNU Oceans pilot program on deep-sea mining

I provided teaching assistance in magnetic processing and introduction to gravity and magnetic modelling with GMSYS-2D in the course TPG4195 (Fall 2016).

My work was presented at several international conferences:

- Arctic Days 2017 - Solvær
- Svalbard Science Conference 2017 - Oslo
- Radioactivity in the Arctic 2018 - Oslo
- 15th International Circumpolar Remote Sensing Symposium 2018 – Potsdam, Germany
- AGU Chapman – Large-Scale Volcanism in the Arctic: The Role of the Mantle and Tectonics 2019 – Selfoss, Iceland
- 34th Nordic Geological Winter Meeting 2020, Oslo

My work was also presented in Trondheim:

- PhD seminar (October 2016)
- IGP day (April 2018, April 2019)
- Trondhjemites (2018, 2019)

Acknowledgements

This work would not have been achieved without the help and support of many people. I am very grateful to my main supervisor Marco Brönner for taking the journey with me and allowing me to study what I like most in life: magnetic, gravity, glaciers and even the northern lights. Not everything went as planned, or perhaps nothing at all, but only rough seas make great sailors.

I thank my co-supervisors Ståle Johansen and Morten Smelror for their discussions and advices on topics closely related, or not, to my research. I am also greatly thankful to Laurent Gernigon and Odleiv Olesen for providing their support and for sharing their knowledge and wisdom during the last few years. I appreciated your mentorship in so many levels.

I also must thank my biggest fans, my parents Gervais and Nicole who always believed in me. At a very young age, my dad has put a hammer in my hands and showed me how to handle manual work. Even while studying the abstract concepts of engineering physics, astronomy, and geophysics, I keep a practical sight on the problems to solve. My mom taught me the value of work and to fight for what is right. I am grateful to my brother Jean-Sébastien for his support through all the journeys I take. As a kid, I dragged him into my expeditions to explore the neighbourhoods and we built so many Lego houses, spacecraft, and ship together. I also thank my god-parents Ginette and Ghislain who were always so supportive of me. They gave me my very first Atlas and it made me wonder if I would grow up to become a daring traveller or an intellectual studying of what the world consists. I thank the Dumais, Sénéchal, Ofstad and Johnsen families. I am lucky to have an astronomical number of relatives following up my endeavours and catching up with me from time to time. And to my nieces and nephews, I have only one advice: never stop asking questions; keep exploring and looking for answers!

I am grateful to my friends and colleagues that I met here in Trondheim. They came to visit me at the hospital when I could not walk, organized a last-minute bachelorette, and took time for a coffee or a meal occasionally. I must also thank a great PhD-buddy Anna for the many discussions about geophysics, the Mid-Atlantic Ridge and other life matters. I am also grateful to my friends across Canada, from Québec city to Victoria. No matter how far I go, I always find a home with you.

Last but not least, I am grateful to my husband Frode Ofstad for being courageous enough to walk the Mid-Atlantic Ridge, climb glaciers and walk this journey by my side. This thesis would not be without his endless support.

Abstract

Interest for the polar regions has increased during the last few decades. New technologies now allow to conduct research in this hostile environment. Tectonic history and timing of the opening of the Arctic is the key to understand the geological framework of this area. Climate and environmental research necessitate a deeper understanding of the polar regions to model the global ecosystem and create robust global weather and climate change prediction scenarios. In this work, we addressed the Norwegian Polar Regions by studying the spreading of the Knipovich Ridge, the regional tectonic of the Fram Strait and the Svalbard Margin, the thermal activity and fluid circulation of Loki's Castle and its surroundings, and the bed topography and geology under Austfonna icecap.

All these facets of the Norwegian Polar Regions have been investigated with a common methodology: potential fields theory. We developed tools to recognize the underground settings of various types of environments at different scale within the Norwegian Arctic. The data interpretation and analysis are mainly based on 2-D forward modelling, 3-D inversion modelling, Werner deconvolution and plate tectonic reconstruction.

Newly acquired aeromagnetic data revealed several fracture zones and lineaments in the Fram Strait. The high-resolution data identified the magnetic isochrons of the Knipovich Ridge. The ridge spreading initiated at C6 (20 Ma) and a ridge jump occurred at C5E. The 2-D magnetic and gravity forward modelling interpreted the crustal and thermal heterogeneities of the Fram Strait and Svalbard Margin. The crustal domains were consequently delineated and confirmed with the Werner deconvolution and Curie point depth estimation. The 3-D magnetic inversion modelling identified zone with weak magnetization along the rift valley correlated with the absence of volcanic and bathymetric rise evidence. The continent-ocean boundary on the east margin is relocated up to 160 km west of the location set by previous studies.

With an autonomous underwater vehicle, magnetic data were collected and analysed to identify hydrothermal mineral deposits. Loki's Castle, Mohn's Treasure and an area called AVR_2 were investigated to correlate the magnetic response to the hydrothermal venting activity at each location. Evidence of two new deposits was suggested through the study. Using the aeromagnetic data, a small-scale analysis, using 2-D forward model, linked to the geological structure, geometry, and fluid circulation beneath Loki's Castle, located in the rift valley of Mohn's Ridge. A thin crust is expected under the ridge and weak magnetization of the basalt layer is correlated to the fluid circulation.

2-D magnetic and gravity forward modelling improved the morphology and glacial bed topography derived from ground penetrating radar technique on Austfonna icecap. Enhanced with magnetic interpretation, the geology is also derived under the icecap revealing

a heterogeneous bedrock with variable erodibility and the presence of intrusions potentially important for the basal thermal regime of the icecap.

Table of Contents

1. Introduction

In 1970, the Knipovich Ridge was discovered by the Russian research vessel "Akademik Knipovich" and its name was later proposed by V.D. Dibner and Vladimir M. Litvin from the Polar Research Institute of Marine Fisheries and Oceanography (PINRO), Russia in 1975. The Knipovich Ridge was named in honour of Nikolai Mikhailovich Knipovich (1862 - 1939), Russian marine zoologist and oceanographer. He led several research expeditions in the Barents, Baltic, Black and Caspian seas and found a correlation between the distribution and migration of fish in the Barents Sea and warm currents.

The evolution of the Knipovich Ridge is the core of this work, complemented with studies of the western Barents Sea and Svalbard margins and other surrounding areas. An ice thickness study of the Austfonna glacier in Nordaustlandet, Svalbard underlines the universal potential of magnetic and gravity data. Through this work, potential field methods are used to characterize the lithological composition of the crust and to highlight the complex basement heterogeneity in the Arctic as well as the enormous impact of the volcanism and magmatic intrusion in the oceanic domain but also along the margin. This knowledge provides better understanding of the processes and development of this area, crucial for outstanding research in the Arctic.

1.1. Thesis objectives

Magnetic and gravity methods allow for the study of areas that are difficultly accessed such as crustal studies under a sediment cover, geological bodies buried by vegetation or ice. It has long been used to characterize crustal basement and understand underground regional tectonic and geological structures for mineral and petroleum exploration. This thesis presents the capability of airborne gravity and magnetic data to study the complex settings of the Arctic targeting different research questions in different scales, proposing to develop geophysical methodology to systematically study the remote and challenging Arctic environment, notably the Knipovich Ridge, Svalbard and their surrounding environment.

The first goal is to understand the spreading of the Knipovich Ridge and the development of the Fram Strait. The KRAS survey (Knipovich Ridge Aeromagnetic Survey) provides the missing piece in the Norwegian-Greenland Sea puzzle and enables the mapping of the complex system of abandoned spreading ridges and fracture zones in this area, providing new insights in the tectonic settings of the seafloor spreading system and the overall geological framework of the Arctic Ocean. The second goal is to focus on specific areas where these crustal heterogeneities are important to the hydrothermal activity at the bend of Mohns Ridge and Knipovich Ridge and the thermal regime of Austfonna ice cap link to its characteristic bed lithology and subglacial topography.

The Arctic is a changing environment, fragile and sensitive to anthropogenic sources. Developing knowledge from remote technology and techniques permits to study important processes involved in the Arctic environment in a non-invasive matter. High resolution data and data enhancement techniques lead to new observations with higher level of constraints in so far poorly investigated areas. The main objective of the research project is to maximize the use of less invasive potential field data to improve the tectonic, crustal, and environmental knowledge of the Norwegian Polar Regions. The study aims also to answer key questions that are still debated today in this under-explored area. The specific objectives are:

- *Resolving the seafloor spreading history of the Knipovich Ridge and refining the location of the continent-ocean boundary with aeromagnetic data (KRAS-16)*
- *Describing and explaining the crustal structure and the tectonic setting of the Fram Strait with the revised location of the continent-ocean boundary.*
- *Recognizing the geophysical signature of hydrothermal activity at Loki's Castle, Mohns Treasure and AVR$_2$ to develop a methodology enabling the identification of associated mineral deposits.*
- *Identifying the subglacial topography, ice thickness and regional geology of Austfonna on Nordaustlandet to evaluate a potential interaction of the overlying ice shield with the underlying geology and bedrock lithology.*

1.2. Underlying tectonic and geology of the Norwegian Polar Regions: a brief review

Despite the advancing climate change and continuous reduction of the Earth's ice masses large areas in the Arctic are still covered by ice with no means to access their bedrock. Then, the Arctic's remoteness and inhospitality significantly limits accessibility and consequently is the geological setting of the Norwegian Polar Regions poorly constrained. The geotectonic and environmental assessment for this thesis was focused on three main sub-areas: Knipovich Ridge, Loki's Castle and Austfonna (Figure 1.1). Although investigated at different scales depending on the nature of the environment studied, all these sub-areas have common challenges of remoteness combined with little prior geological knowledge.

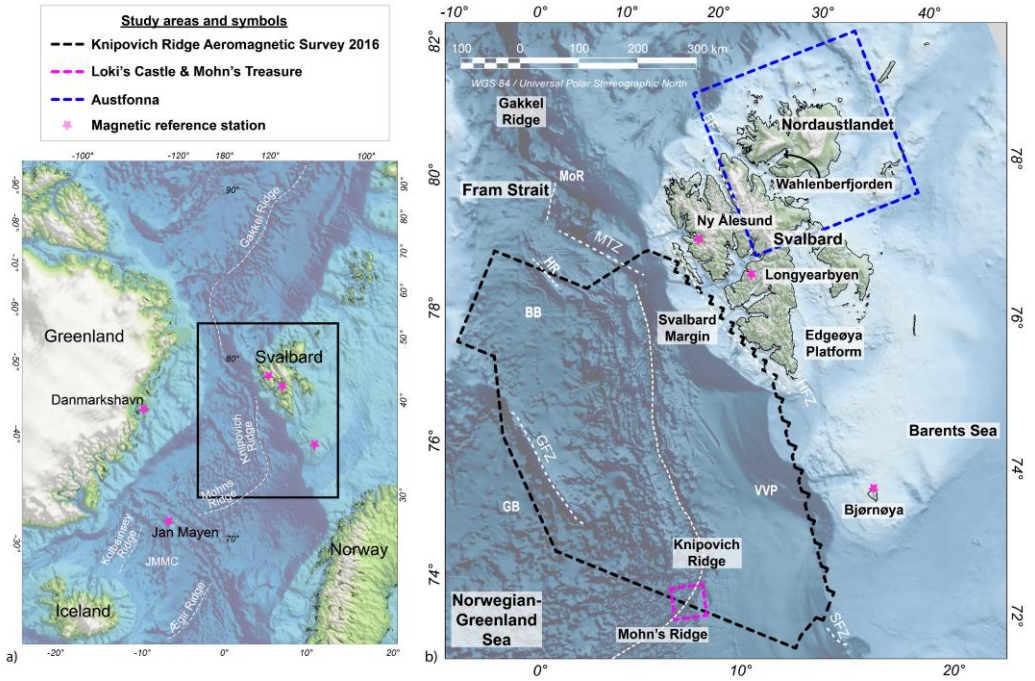

Figure 1.1 a) Overview of the Knipovich Ridge and the study areas. b) Norwegian Polar Regions with the main study areas highlighted. Flown with aircraft, KRAS-16 represents 254,000 km² (black), while Austfonna 70,000 km² (blue). Acquired with UAV, including Loki's Castle, Mohns Treasure and AVR₂ (purple). The tectonic processes of the Fram Strait are controlled by the Knipovich Ridge and the surrounding geological features. The new aeromagnetic data revealed the time of the seafloor spreading initiation and magmatic events on the eastern side of the ridge. The magnetic reference stations from the Tromsø Geophysical Observatory and the Technical University of Denmark (pink stars) have been used for the diurnal correction of the magnetic data. MoR: Molloy Ridge, VVP: Vestbakken Volcanic Province, BFZ: Billefjorden Fault Zone, SFZ: Senja Fracture Zone, HFZ: Hornsund Fault Complex Zone, GFZ: Greenland Fracture Zone, MTZ: Molloy Transform Zone, GB: Greenland Basin, BB: Boreas Basin, HR: Hovgaard Ridge.

1.2.1. Knipovich Ridge and Fram Strait

The Knipovich Ridge is the northernmost segment of the mid-Atlantic spreading axis and impetus for the opening of the Fram Strait between Greenland and Svalbard (Figure 1.1). Its seafloor spreading history has remained unclear primarily due to its challenging location. During this study, state-of-the-art aeromagnetic data were acquired. Classified as an ultraslow-oblique spreading system (with seafloor spreading rates of less than 20 mm/year), the Knipovich Ridge comprises the Arctic Mid-Ocean Ridge system and is delimited by the Mohns Ridge (~73°50' N) and the Molloy Fracture Zone (~78°30' N) between Greenland and NE Atlantic oceanic realms. Ultraslow spreading ridges account for ~20,000 km of the ~55,000 km global ridge systems [1989] but have been less studied than fast spreading ridges [*Dick et al.*, 2003]. Unlike slow- and fast-spreading ridges, ultraslow spreading ridges show a correlation between the seafloor spreading rate and the total crustal thickness [*Reid and Jackson*, 1981]. Thin crust associated to ultraslow spreading ridges is linked to low basaltic

productivity at the ridge crest caused by an increased cooling [*Jackson et al.*, 1982]. While negligible at fast spreading ridges, heat loss by conduction is significant at ultraslow ridges, causing a sharp reduction of the melt volume generated and changing its composition [*White et al.*, 2001; *Bown and White*, 1994]. A better understanding of these processes at ultraslow ridges may result in a better targeted mineral exploration.

The Knipovich Ridge trends from NW in the south to N in the north with a 130 km-wide escarpment and is largely covered with thick piles of sedimentary rocks along the Svalbard margin [*Engen et al.*, 2006]. Its tectonic structure differs from other oceanic ridges as it presents ultra-slow spreading features in an oblique system [*Vogt et al.*, 1982; *Talwani and Eldholm*, 1977]. The southern end of Knipovich Ridge intersects the Mohns Ridge with a 90° bend, a rare occurrence in plate tectonics. This affects the evolution of the Fram Strait and motivates the study of crustal deformation with this distinctive configuration.

Crustal thickness along the Mohns and Knivpovich ridges are estimated to 2–5 km from geophysical studies [*Hopper et al.*, 2014; *Hermann and Jokat*, 2013; *Conley and Dunn*, 2011; *Ritzmann et al.*, 2002] which is below the global average of 7±1 km [*Jokat et al.*, 2003; *Bown and White*, 1994]. These estimates remain uncertain because the correlation between seismic and igneous crust is not fully established for ultraslow spreading ridges [*Zhou and Dick*, 2013; *Jokat et al.*, 2003]. Other geophysical methods using magnetic, gravity and CSEM measurements can further improve the crustal thickness knowledge for this class of spreading ridges.

The Fram Strait developed after a Late Cretaceous-Eocene rifting event between the Barents Sea and the Northeast Greenland. It forms a complex system of conjugate shear margins characterized by distinct crustal, structural and magmatic properties [*Faleide et al.*, 2008; *Ritzmann and Jokat*, 2003; *Srivastava and Roest*, 1999]. During the Palaeocene-Eocene, the oblique system underwent a brief period of compression leading to the Eurekan-Spitsbergen fold and thrust belts [*Piepjohn et al.*, 2016].

1.2.2. Loki's Castle, Mohns Treasure, and their surroundings

Located on the southernmost edge of the study area, at the bend between the Knipovich and the Mohns ridges, three sites including Loki's Castle and Mohns Treasure have been investigated with magnetic data acquired from an autonomous underwater vehicle for their hydrothermal activity and mineral potential (Figure 1.2). The Mohns Ridge spreading was initiated around chron 24 (53 Ma; [*Vogt*, 1986; *Talwani and Eldholm*, 1977]) when the Greenland Sea opened [*Dauteuil and Brun*, 1993]. The Mohns Ridge spreading direction was perpendicular to its axis, with a full spreading rate of 25 mm yr^{-1} [*Vogt et al.*, 1982; *Talwani and Eldholm*, 1977]. A reorganization of the North Atlantic plate boundaries at 27 Ma led to an oblique spreading as seen today [*Dauteuil and Brun*, 1993].

At present day, the Mohns Ridge is an ultraslow-oblique spreading ridge with a full rate estimated at 15.6 mm yr^{-1} during the last 10 Ma [*Mosar et al.*, 2002; *Vogt*, 1986]. Both flanks of the rift valley and the valley floor are covered by sediments from the Bear Island Fan with thickness up to 800 m and a larger sediment deposit on the eastern flank [*Bruvoll et al.*, 2009].

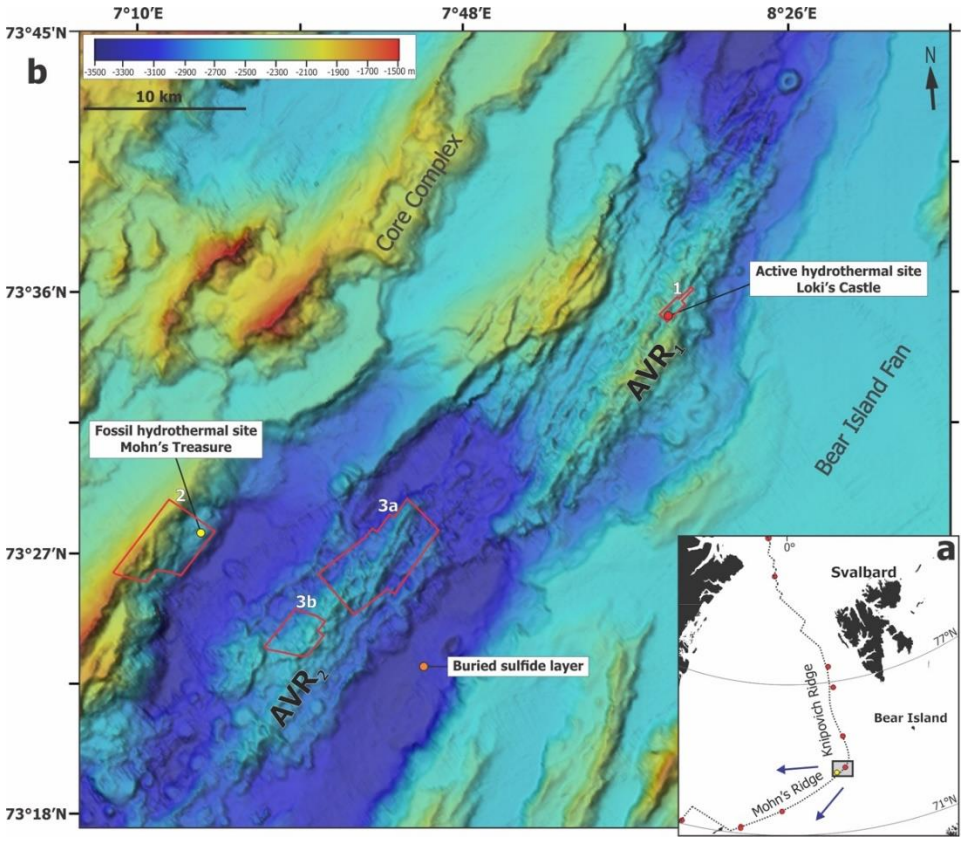

Figure 1.2 Survey areas 1,2,3a and 3b, in the Mohns Ridge south of the junction with Knipovich Ridge, have been investigated. (a) Regional overview map of the Mohns and Knipovich ridges. The grey rectangle identifies panel b. Red circles denote active hydrothermal venting sites, yellow circle—extinct hydrothermal sites [Beaulieu and Szafranski, 2018]. The black dotted line marks the spreading axis. Blue arrows denote the North American and Eurasian plate-movement directions relative to a fixed hotspot reference frame[Gripp and Gordon, 2002]. (b) Regional bathymetric map of the Mohns Ridge northernmost segment resolved at 100 m [Norwegian Mapping Authority, 2015]. Red lines mark survey outlines. Active hydrothermal venting site, Loki's Castle, is denoted by red filled circle, extinct venting site, Mohn's Treasure, by yellow filled circle, an orange circle denotes the location of sediment core sample where sulphide layer was found around 1.5-m subsurface [Pedersen et al., 2010]. Both flanks of the rift and the valley itself are covered by distal parts of Bear Island Fan sediments [Bruvoll et al., 2009]. AVR stands for axial volcanic ridge. Illustration from Lim at al. (2019).

Loki's Castle is an active hydrothermal venting field located in the Mohns Ridge northernmost axial volcanic ridge (AVR_1) of 30-km length and perpendicular to the seafloor

spreading direction. Loki's Castle rises ~1,300 m above the rift valley floor at 2,000-m depth. This geological feature is a basalt-hosted site as the geochemical analysis of the hydrothermal fluid collected from the black smokers supports magmatic influence. Mohn's Treasure is situated at the flank of the rift valley in an area composed of lithified and partly lithified sediments subsequently uplifted by the margin faults [*Pedersen et al.*, 2010].

The southernmost site called AVR_2, located in a neo-volcanic ridge exhibiting a terrain dominated by young pillow lava flows, extends over 25 km. The acquisition line orientation was SW-NE, orthogonal to the seafloor spreading direction. With an average rise of 500 m above the valley floor, the AVR_2 summit is located at the centre of the edifice at 2,500-m water depth, 800 m above the valley floor.

1.2.3. Austfonna, Svalbard

Northeast in the study area, the Austfonna icecap is located on Nordaustlandet, second largest island of the Svalbard archipelago. This area was revisited with pre-existing airborne magnetic and gravity data. It is covered by almost 700 m thick ice at its summit. Its basement topography has been studied with the help of few radio-echo sounding (RES) and ground-penetrating radar (GPR) campaigns (Figure 1.3). However, basement lithology and basal thermal regime are mostly unknown due to the difficulty to access it.

Covering 8,357 km², Austfonna is the largest icecap on Svalbard archipelago [*Dallmann*, 2015]. Its central dome with an ice thickness of up to 700 m [*Dowdeswell et al.*, 1986] feeds several drainage basins. Considered polythermal, consisting of a mixture of temperate and cold ice, it is relatively flat at its highest elevation and includes both land-terminating and tidewater glaciers. Studies suggest its basal temperature is near the pressure melting point [*Dunse et al.*, 2011]; thus, Austfonna experiences basal sliding and subglacial water might be present. Surging, or surge-type, glaciers have also been observed in the area [*Schytt*, 1969].

With few outcrop availabilities, the bed lithology has been difficult to assess. Basement outcrops from both side of the Wahlenbergfjorden are used to determine the existence of two basement types [*Dallmann*, 2015; *Johansson et al.*, 2002]. The basement in the northern shore is of pre-Caledonian origins with Mesoproterozoic and Neoproterozoic rock exposures [*Lauritzen and Ohta*, 1984]. With a characteristic magnetic signature, Caledonian granites, Grenvillian Rijpfjorden granites and migmatites are found on the northern tip of Prins Oscars Land [*Johansson et al.*, 2005; *Johansson et al.*, 2002], as well as Silurian diorites and gabbros located on Storøya [*Johansson et al.*, 2005]. The southern shore comprises a Tonian basement, composed of dolomite, sandstone, quartizite and limestone, intruded by Jurassic-Cretaceous doleritic dikes. Cretaceous sills have also been emplaced offshore Nordaustlandet [*Polteau et al.*, 2016; *Minakov et al.*, 2012; *Grogan et al.*, 2000].

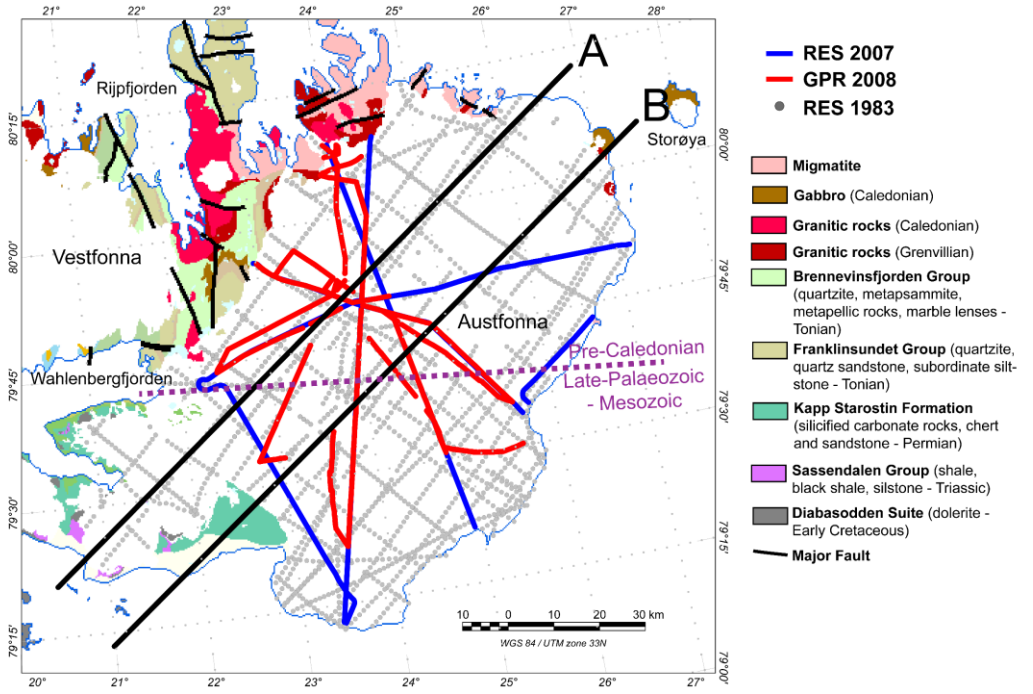

Figure 1.3 Geological map of Austfonna with ground-penetrating and radio-echo sounding campaign lines with the gravity–magnetic interpreted profiles A and B (modified from Dallmann [2015], and Dunse et al. [2011]). The interpreted profiles, labelled A and B, have been chosen to cover a large area of Austfonna and to capture important geological trends. The boundary between the Pre-Caledonian and the Late-Palaeozoic–Mesozoic basements, estimated from the observations on both shores of Wahlenbergfjorden, is identified in purple.

1.3. Contribution and organization of the thesis

The methodology is introduced in the second chapter of the thesis. The scientific findings are reported in the third chapter as manuscripts and research articles. The thesis is concluded with a work synthesis and a conclusion in the last two chapters.

The first manuscript, published in the Geophysical Journal International, discusses the complex opening of the Fram Strait and the spreading of the Knipovich Ridge. The magnetic interpretation sets the initiation of the seafloor spreading at C6 (20 Ma) and delineates the continent-ocean boundary. Several oceanic fracture zones and lineaments are also revealed. An abandoned ridge followed by a ridge jump are also disclosed in this study. This project was developed by Odleiv Olesen. Marie-Andrée Dumais conducted the magnetic data processing, the seafloor spreading rates model, the interpretation, and the writing of the

manuscript with the support from Laurent Gernigon, Odleiv Olesen, Ståle E. Johansen and Marco Brönner.

The second manuscript proposes a regional model of the Fram Strait and Svalbard areas revealing the crustal heterogeneities of the Norwegian Polar Regions. The combined gravity and magnetic interpretation underline the new location of the continent-ocean boundary using constrains from a refined crustal seismic interpretation, controlled source electromagnetic and magneto-telluric data. The oceanic, continental and transition domains are identified and characterized in terms of mantle and crustal properties. This work was performed by Marie-Andrée Dumais as lead author and researcher. Anna Lim contributed to the 2-D forward magnetic model of the CSEM/MT profile. Marco Brönner and Ståle E. Johansen participated as advisers. Laurent Gernigon and Odleiv Olesen contributed to the scientific discussions.

The third manuscript, published in "Geochemistry, Geophysics, Geosystems (G-cubed)", focuses on the hydrothermal activity on Mohns Ridge at the bend junction with Knipovich Ridge. Noteworthy, a magnetization high is associated with the extinct hydrothermal site Mohn's Treasure. The interpretation also suggests two new fossil hydrothermal site in the area. This work was led and mainly performed by Anna Lim. Marie-Andrée Dumais actively contributed to the magnetic data processing, magnetic modelling and writing of the manuscript.

The fourth manuscript, published in "The Cryosphere", discusses the gain from using potential field methods over glaciated areas to retrieve a more accurate bed topography and lithology. The regional study of the Fram Strait has mapped several magmatic intrusions in the transition and continental crustal domains, in the vicinity of Nordaustlandet. Under Austfonna ice cap, dyke and sill intrusions are also mapped through 2-D forward models and Werner and Euler deconvolution methods, questioning the bedrock thermal regime's potential impact on glacial dynamics as an underestimated factor in ice flux and global warming modelling. For this work, the ground-penetrating radar and radio-echo sounding data were provided by Thorben Dunse and the airborne gravity data by Rene Forsberg and Ove Omang. The work, including re-processing of the magnetic data, modelling, interpretation, analyses and writing the manuscript, was developed, and conducted by Marie-Andrée Dumais with Marco Brönner's supervision.

The appendices comprise the final report of the Knipovich Ridge Aeromagnetic Survey (KRAS-16) project presented to the financing partners and the re-processing of the aeromagnetic data acquired in Nordaustlandet.

2. Potential Field Methods in the Context of Polar Research

Potential field methods, notably gravity and magnetic interpretation, are the preferred research tools during this thesis. These methods are sensitive to lateral variations in the physical properties, at a range of scales, of the geologic materials in the study area. The magnetic and gravity signals are sensitive to lateral contrasts in magnetization (susceptibility and remanence) and density, respectively. Given their nature and a reasonable ambiguity in vertical resolution, these methods are most effective in combination with other types of data, e.g. seismic and ground penetrating radar measurements, where additional structural information can be derived, as well as rock samples analysis as petrophysical constrains.

Located at high arctic latitudes, the survey areas in this thesis are remote and challenging to access even by aircraft. Navigation and positioning are challenging due to the geometry configuration of the limited number of positioning satellites available. The Global Navigation Satellite System (GNSS) has dramatically improved during the last two decades. The Geometric Dilution of Precision (GDOP), which specified the error propagation in positioning, increase at higher latitude because the satellites are generally restricted just above the horizon. [*Swaszek et al.*, 2018; *Reid et al.*, 2016; *de Jong et al.*, 2014]. The effect of this poor geometry is important when measuring speed and acceleration for a gravity system. The Earth's magnetic field is sensitive to solar wind perturbations expressed through the polar magnetospheric substorms. These required appropriate processing before the geophysical properties can be assessed.

The results of this thesis are built from the new aeromagnetic dataset Knipovich Ridge Aeromagnetic Survey – 2016 (KRAS-16) acquired offshore Svalbard in the Fram Strait, funded by the Earth Plate Organization System – Norway (EPOS-N), the Geological Survey of Norway (NGU) and the Norwegian Petroleum Directorate (NPD). For the study area of Austfonna, previously flown datasets have been used for the study, but required adjustments using modern processing tools. The acquisition, processing and modelling techniques used in this thesis are detailed here. These techniques are also put into the context of polar regions and their inherent challenges.

2.1. Survey Planning

The survey line planning is critical to the survey accuracy and resolution. Preliminary knowledge of the area and the geology serve as guidelines to the planning. The size, the depth and the orientation of the sub-surface bodies contribute to the amplitude and frequency content of the magnetic and gravity signatures measured. Shallow sources generally have shorter wave-length responses than deep-seated sources [*Dentith and Mudge*, 2014]. One must ensure the data sampling is optimized for the frequency content expected.

The minimum survey height or the terrain clearance is often limited by the aviation regulations of the specific area surveyed e.g., built-up areas minimum clearance is 1,000 ft. For airborne surveys offshore, the depth of the seafloor limits the frequency response expected from the measurements. Longer wave-length responses are expected with higher altitude flown data and a larger area is necessary to cover the entire response of the source [*Dentith and Mudge*, 2014].

Surveys are usually acquired along parallel lines (often called "traverses"), generally designed equally spaced. The line spacing influences the resolution of the gridded data. A shorter line spacing is sensitive to shorter wavelengths. However, the chosen spacing depends on the depth of the source which is linked to the survey height. With longer wavelength expected, a wider line spacing is appropriate and cost-effective. The heading of the survey lines is mainly designed to be perpendicular to the strike of expected geological units. A set of lines called "tie lines" (or "control lines") are flown, with a spacing that is 5 to 10 times the survey line spacing and, perpendicular to the survey lines. These lines ensure data repeatability and are used to correct artefacts in the data. They are used to level the traverses to remove the diurnal signal external to the geological signature.

In the KRAS-16 study area the seafloor bed descends as deep as 2,500 to 3,000 m below sea-level [*Olesen et al.*, 2010]. The top of the magnetized sources is estimated to be near the surface at the ridge. The sediment cover in the sea-bed valleys adjacent to the ridge is estimated to be thin near the ridge and slowly increasing towards the continental crust by more than 3,000 m [*Klitzke et al.*, 2015; *Engen et al.*, 2006]. Therefore, a traverse line spacing of 4 to 5 km would have been appropriate. However due to budget restriction, the KRAS-16 survey was carried with a traverse line spacing of 5.5 km. Tie- (or control-) lines were spaced by 20 km (Figure 2.1). The traverse lines were oriented at 300° to optimize the coverage of the survey boundary and to cross the ridge perpendicularly. Narrow and shallow source anomalies might have been missed between the traverse lines, but the survey is sufficient for regional studies and seafloor spreading investigations.

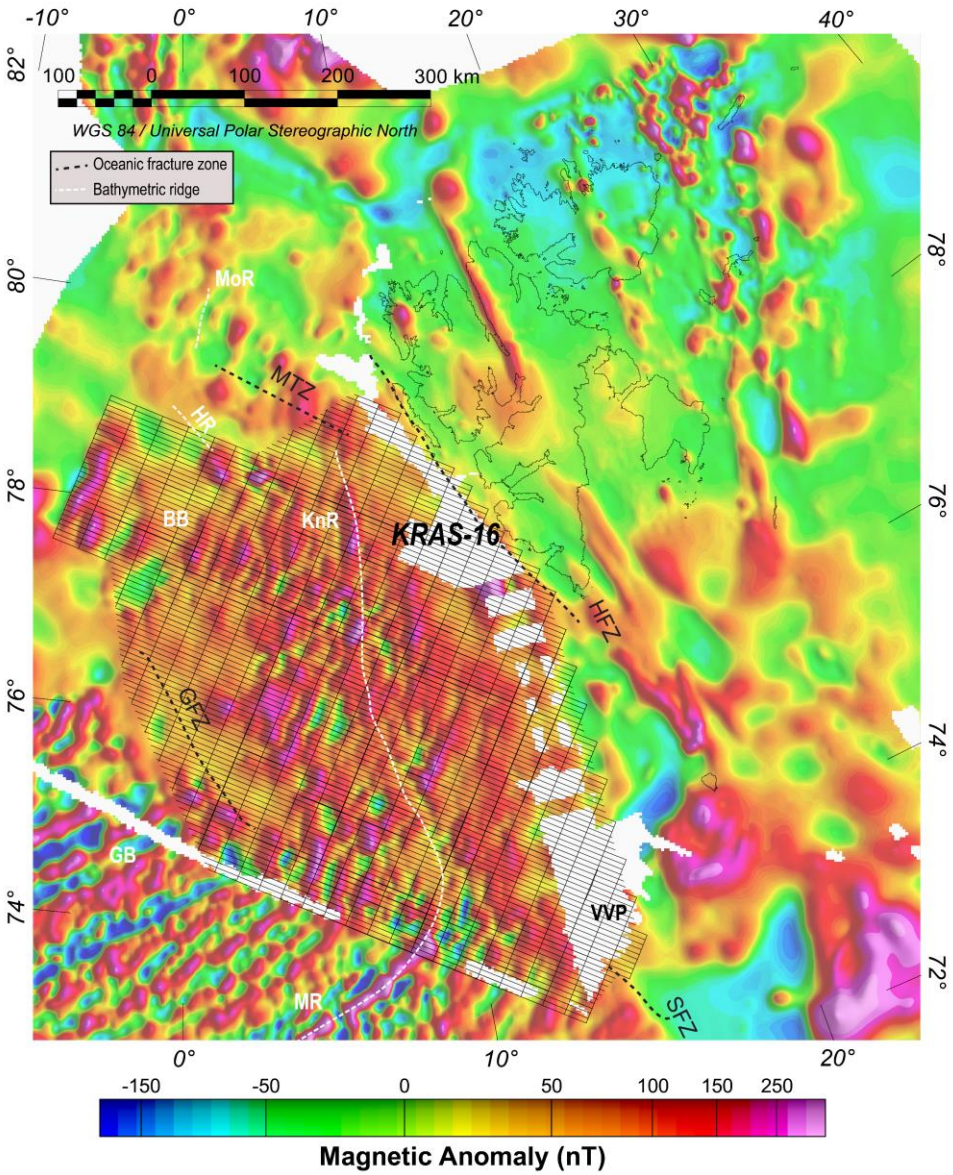

Figure 2.1 KRAS-16 planned flight lines superimposed on the pre-existing aeromagnetic data from Olesen et al. [2010]. The flight lines are spaced by 5.5 km and oriented at 300° to optimize the magnetic acquisition perpendicular to the seafloor spreading expected from the pre-existing aeromagnetic data [Olesen et al., 2010] showing large gaps (light grey) on the Svalbard Margin. Control lines are flown with a 20 km line spacing to correct the data for diurnal noise. MoR: Molloy Ridge, VVP: Vestbakken Volcanic Province, BFZ: Billefjorden Fault Zone, SFZ: Senja Fracture Zone, HFZ: Hornsund Fault Complex Zone, GFZ: Greenland Fracture Zone, MTZ: Molloy Transform Zone, GB: Greenland Basin, BB: Boreas Basin, HR: Hovgaard Ridge, KnR: Knipovich Ridge, MR: Mohns Ridge.

2.2. Gravity: acquisition and processing

The first part of the thesis uses satellite altimetry gravity data to study the regional geology of the Knipovich Ridge and the Svalbard Margin. The free-air gravity *Sandwell v23-1* grid [*Sandwell et al.*, 2014] has been chosen for its availability and reliability. However, the coverage is limited to latitudes below 80°N. Therefore, the glacial bed investigation of Austfonna uses airborne gravity data acquired by the Mapping Authority of Denmark and the Mapping Authority of Norway in 1999 [*Forsberg and Olesen*, 2010; *Forsberg et al.*, 2002]. The airborne gravity data contain higher frequencies then the Sandwell v23-1 gravity free-air data. They have also been acquired over a known period of time and can be compared to an ice coverage measured at a specific time. The following description is related to the gravimeter and gravity compilation used for the interpretation.

2.2.1. Gravimetry principles

Built in 1939, the first LaCoste gravimeter used the zero-length spring principle [*LaCoste*, 1934]. Over the decades, the gravimeter has been adapted to moving platform [*LaFehr*, 1980] – underwater, ship, aircraft – insuring data acquisition efficiency. More recently, the development of space communication and satellite positioning permitted to extend our understanding of gravity from observations of satellite paths, e.g. [*Sandwell et al.*, 2014; *Andersen et al.*, 2009]. It has significantly improved our knowledge of the shape of the Earth. When combined with shipborne gravity, it offers accurate data in offshore areas [*Dumais et al.*, 2020].

For this thesis, the airborne gravity data were inspected for quality prior to the modelling and interpretation. For the ice thickness and glacial bed studies, the free-air gravity data were necessary. For the Fram Strait regional model, Bouguer and isostasy corrections were tested on the free-air gravity available. However, the much higher resolution of the bathymetry and the non-isostatic state of the crust at the ridge and below glaciated areas introduced uncertainties in the interpretation. The methods presented below provide an overview of the data reduction and the type of uncertainties inherent to gravity measurements.

2.2.2. Gravity data reduction

Typically, relative gravimeters which do not directly measure the absolute gravity field are installed on a moving platform such as ship and aircraft. A "gravity tie" is necessary to adjust the relative measurement to a known absolute gravity value. The Norwegian Mapping Authority maintains a network of absolute gravity points in Norway. Inherent instrumental noise and other gravitational effects must be removed from the measurement to recover the gravity anomaly.

Instrumental drift and tidal effects

Instrument readings change, or drift, over time due to elastic creep in the spring or temperature variation in the instrument. This drift is estimated from repeat measurements during one acquisition day. Earth tides resulting from a gravity pull of the Moon affect the gravity measurements. Repeat measurements and tie lines intersections allow to estimate the necessary corrections for both the instrumental drifts and tidal effects.

Eötvös correction

On a moving platform, the velocity of the platform affects to the vertical component of the Coriolis acceleration. The outward-acting centrifugal acceleration with the speed and direction of the platform travelling over the curved surface of the Earth and the variation in the centrifugal acceleration from the movement of the vehicle relative to the Earth's rotational axis contribute to this correction [*Reynolds*, 2011]. The Eötvös correction g_E is given by [*Glicken*, 1962]:

$$g_E = 4.040V \cos\omega \sin\alpha + 0.001211V^2 \tag{2.1}$$

Where V is the speed of the vehicle in km/hr, ω the geographical latitude and α the azimuth. Noteworthy, this correction has a greater error sensitivity in east-west acquisition direction. For shipborne measurements acquired at a speed of 10 km hr^{-1} in east-west direction at a latitude of 75°N, this correction is 33.4 mGal. For airborne measurements acquired at the same location and in the same direction, the Eötvös correction is810 mGal.

Latitude correction

This correction is performed by subtracting the theoretical gravity based on a mathematical model of the Earth's gravity field, modelling the Earth as an ellipsoid instead of a sphere. The gravitation intensity varies with the latitude. Several models exist, corresponding to a gravity datum. The latest model of the latitude correction g_ω [*Dentith and Mudge*, 2014; *Moritz*, 1980] is expressed:

$$g_\omega = 9.7803267714 \frac{(1 + 0.00193185138639 \sin^2\omega)}{\sqrt{1 - 0.00669437999103 \sin^2\omega}} \tag{2.2}$$

This correction accounts for the variation with latitudes, where the intensity is greater at the poles than at the equator.

Free-air correction

In geophysics, the gravity anomaly is defined as "the difference between the observed gravity and the theoretical gravity predicted from the ellipsoid" [*Li and Götze*, 2001]. This correction compensates for the reduction of the gravity intensity with height above the ellipsoid.

For this correction, the Earth is approximated as a rotating sphere and regarded as an equipotential ellipsoid of revolution. An ellipsoid of revolution can be generated by rotating an ellipse about one of its axes and used to approximate the geoid (Sheriff). Commonly used in geophysics, the Geodetic Reference System 1967 (GRS 67), Geodetic Reference System 1980 (GRS80) and World Geodetic System 1984 (WGS 84) are "normal Earth" ellipsoid of revolution. It is defined as having the same angular velocity and same mass as the actual Earth with the potential on the ellipsoid surface equal to the potential on the geoid and a centre coincident with the centre of mass of the Earth.

The geoid is a reference surface defined as the gravitational equipotential surface that coincides with the mean sea level. It is used in geodesy as a reference to tie position measurements over long distances. The geoid is shaped with large undulations caused by mass differences in the mantle related to wide convection in the mantle and sensitive to mantle viscosity [*Hager*, 1984]. Short wavelengths of the geoid are due to topography and local mass imbalances within the lithosphere, e.g. ridges and mountains [*Marsh et al.*, 1992; *Milbert and Dewhurst*, 1992]. The difference between the geoid and the reference ellipsoid is generally below 50 m [*Lerch et al.*, 1979] with large scale variation. This inconsistency between the geoid and ellipsoid is often ignored but may be considered to regional survey of the scale of the geoid undulations [*Li and Götze*, 2001].

Thus, the free-air correction g_{FA} considers that only air is between the observation and the ellipsoid [*Sheriff*, 2002; *Li and Götze*, 2001]:

$$g_{FA} = \frac{2\gamma M_{\oplus}}{R_{\oplus}^3} h$$
$$g_{FA} = 0.3086h \qquad (2.3)$$

with h is the elevation in m, γ the gravitational constant (6.672 x 10-11 N m^2 kg^{-2}), $M_{\oplus}$ the Earth's mass and $R_{\oplus}$ the Earth's radius. The correction is positive above ellipsoid and negative below.

Bouguer correction

The Bouguer anomaly represents the lateral variation in density. While the free-air correction disregards any mass between the observation and the datum plane (geoid or ellipsoid), the role of the Bouguer correction is to remove the effect of this mass [*Blakely*, 1995; *Telford et al.*, 1990]. The simple Bouguer correction g_{SB} assumes a homogeneous infinite horizontal slab between the observation and the datum plane:

$$g_{SB} = 2\pi\gamma\rho h \qquad (2.4)$$

Where γ is the universal gravitational constant (6.672 x 10-11 N m^2 kg^{-2}), ρ the density of the slab and h the thickness of the slab. Onshore, a typical crustal density of 2,670 kg m^{-3} with h representing the height above the sea level. Offshore, the Bouguer correction is calculated to replace the water (1,000 kg m^{-3}) with a homogeneous infinite horizontal slab. The thickness of the slab is equal to the bathymetric depth. Some textbooks e.g. [*Blakely*, 1995], recommend using a crustal density of 2,670 kg m^{-3}, while others, e.g. [*Marello et al.*, 2013; *Murray and Tracey*, 2001], recommend the density of the uppermost rocks, commonly sediments (2,200 kg m^{-3}). The simple Bouguer correction offshore becomes:

$$g_{SB} = 2\pi\gamma\Delta\rho h$$
$$\Delta\rho = \rho_{rock} - \rho_{water} \quad (2.5)$$

In its approximation, the simple Bouguer correction ignores the topography in the vicinity of the observation point which causes lateral gravity attraction. Supplementary correction might be needed near topographic features or in regions with moderate to extreme topography. The terrain correction g_T requires high-resolution topography and computer resources. The complete Bouguer correction g_{CB} is computed as:

$$g_{CB} = g_{SB} + g_T \quad (2.6)$$

Isostasy correction

Isostasy is the gravitational balance between the Earth's lithosphere and the asthenosphere. The tectonic plates float in equilibrium on the mantle based on Archimedes' buoyancy principle: "any object, totally or partially immersed in a fluid or liquid, is buoyed up by a force equal to the weight of the fluid displaced by the object." According to Airy's hypothesis, isostatic compensation allows extra mass of large topographic features such as mountains to be compensated by deep crustal roots and large topographic depressions such as deep ocean basins by shallow roots (anti-roots) [*Airy*, 1855]. Pratt's hypothesis suggested the density varies laterally in the crust and a constant depth of the root allowing every crustal section to have an identical mass [*Pratt and Stokes*, 1859; *Pratt and Challis*, 1855]. The crustal flexure hypothesis, or Vening Meinesz hypothesis, suggests the plate has elastic properties and local topographic loads are compensated regionally and accommodated laterally over a broad region [*Meinesz*, 1931].

For large-scale modelling, it is preferable to remove the long-wavelength gravitational effects attributed to the isostatic compensation. A simple approach is to use Airy's model where the total mass is equal for all columns extending from the Earth's surface to the depth of compensation. As illustrated (Figure 2.2), the total mass of column A must equal the total mass of column B. Thus, the compensation depth (d_r) is calculated:

$$d_c\rho_c + (d_r - d_c)\rho_m = (h + d_r)\rho_c$$
$$d_r = h\frac{\rho_c}{(\rho_m - \rho_c)} + d_c \quad (2.7)$$

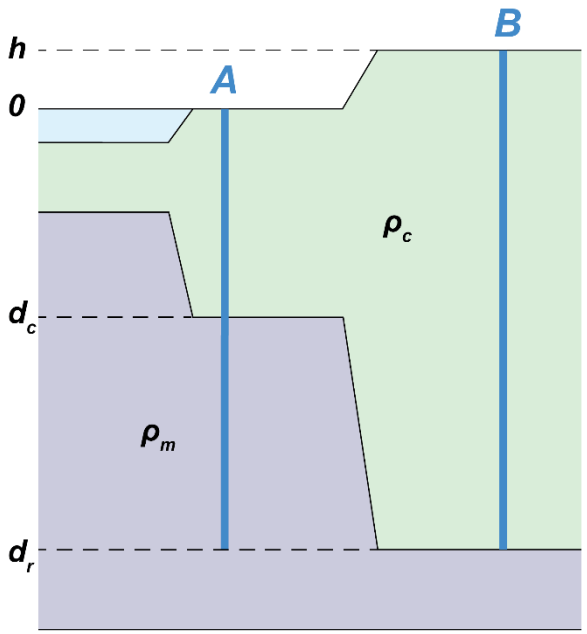

Figure 2.2 Example of a calculation of the depth of compensation.

From the depth of the compensating root, several algorithms, e.g. [*Simpson et al.*, 1986; *Simpson et al.*, 1983], propose to calculate the isostatic gravitational effect g_I.

The final isostatic gravity anomaly G is:

$$G = G_{observed} - g_\omega - g_{FA} - g_E - g_{SB} - g_T - g_I \quad (2.8)$$

Where $G_{observed}$ is the observed or measured gravity data from the gravimeter.

2.3. Magnetic: acquisition and processing

The first part of the thesis consists of the seafloor spreading analysis and geophysical mapping of the Knipovich Ridge. The Knipovich Ridge Aeromagnetic Survey 2016 (KRAS-16) has been acquired during late summer 2016 and summer 2018 (Figure 2.4). The second part of the thesis studies the bed topography and lithology of Austfonna in Svalbard, using reprocessed data acquired in 1989 and 1991.

Figure 2.3 Piper Navajo used for KRAS-16 acquisition, courtesy of Novatem, Inc. The aeromagnetic survey is located west of Svalbard entirely over the sea.

For this study, a fluxgate magnetometer, and an optical absorption magnetometer with a Caesium vapor chamber were used for the acquisition. The aeromagnetic data were compensated for aircraft noise and corrected for diurnal noise with a magnetic base station, levelling, and micro-levelling techniques (Figure 2.4). Figure 2.5 shows two profiles with the effects of the various processing steps. Magnetic profile L1015 is compared to the pre-existing magnetic compilation [*Olesen et al.*, 2010] with data acquired between 1972 and 1983. The large misfit is largely caused by the navigational errors, wider line spacing and lower data resolution. For this thesis, the magnetic compilation was completed with existing data from the surrounding areas: Gakkel Ridge, Boreas Basin, Barents Sea and Svalbard [*Jokat et al.*, 2016; *Trulsvik et al.*, 2011; *Olesen et al.*, 2010; *Jokat et al.*, 2008]. Levelling discrepancies between the various dataset were minimized by using the long wavelength (>300 km) from the Magnetic Field Model v.7 (MF7 - http://www.geomag.us/models/MF7.html, last accessed 24/04/2019), an update of the sixth generation [*Maus et al.*, 2008]. A brief description of the magnetic acquisition and processing performed for this thesis follows.

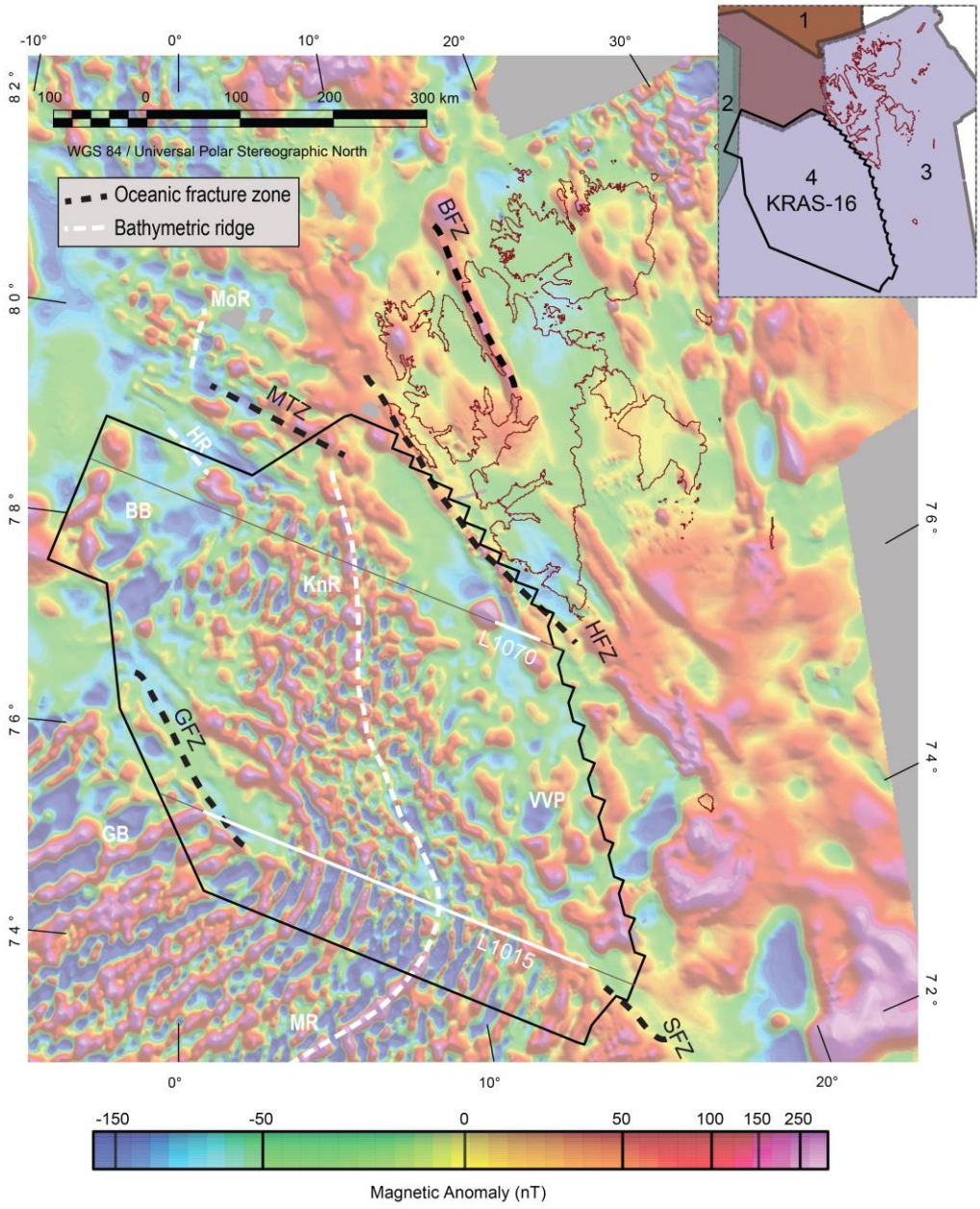

Figure 2.4 Magnetic compilation using the new aeromagnetic KRAS-16 data (black polygon). The aeromagnetic data were compensated for aircraft noise, and corrected for diurnal noise with magnetic base station, levelling, and micro-levelling techniques. The compilation includes surveys of various resolutions acquired over the last four decades and their location is presented in the inset map (1- Jokat et al. [2008, 2016] which overlap with survey 3; 2- Turlsvik et al. [2011]; 3- Olesen et al. [2010] which overlap with survey 1 and 4; 4- Dumais et al. [2020a, b]). Details of the processing are presented in appendix A. Magnetic profiles L1015 and L1070 shown on the map are presented in Figure 2.5. MoR: Molloy Ridge, VVP: Vestbakken

Volcanic Province, BFZ: Billefjorden Fault Zone, SFZ: Senja Fracture Zone, HFZ: Hornsund Fault Complex Zone, GFZ: Greenland Fracture Zone, MTZ: Molloy Transform Zone, GB: Greenland Basin, BB: Boreas Basin, HR: Hovgaard Ridge, KnR: Knipovich Ridge, MR: Mohns Ridge.

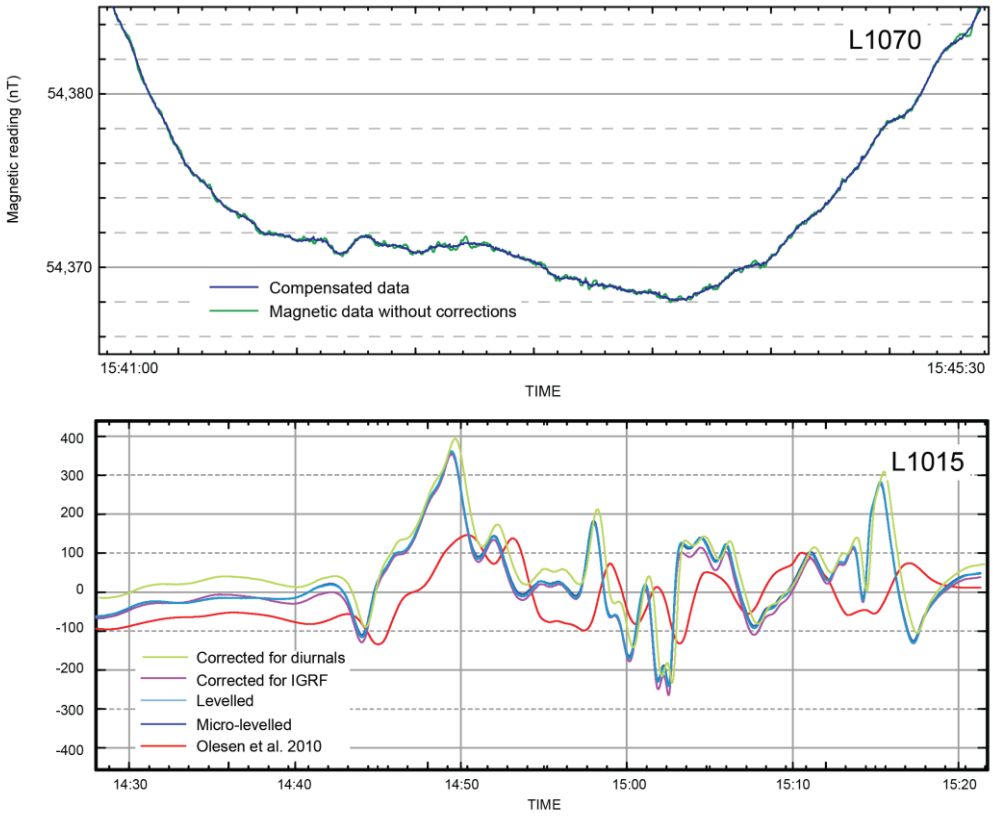

Figure 2.5 Magnetic profiles L1015 and L1070 representing the various corrections applied to the data. L1070 shows the magnetic data before and after the compensation filtered is applied to correct for the aircraft noise. L1015 shows the magnetic profiles after the correction for diurnal, IGRF, levelling and micro-levelling have been applied. L1015 is compared to the pre-existing compilation of Olesen et al. [2010].

2.3.1. Magnetometer Principles

During an airborne magnetic campaign, one or more magnetometers are installed on board the aircraft. Historically, the choice of instruments was based on economic means and accuracy. Over the last decades, magnetometers have developed to serve specific needs.

Fluxgate magnetometer (vector magnetometer)

The fluxgate magnetometer was originally designed to detect submarines during World War II and has been in use since then. Using the magnetic data continuously recorded as ships crossed the Atlantic and Pacific oceans, the scientists of the U.S. Naval Oceanographic Office

reported the presence of bands of alternating strong and weak magnetism in the rocks of the ocean floor. This was the first evidence of the magnetic reversal phenomenon. Vine and Matthews [1963] combined topographic maps to the magnetic recordings of the Mid-Atlantic Ridge to map a pattern of strong and weak magnetism arranged parallel and symmetrically centred to the ridge. This confirmed seafloor spreading [*Hess*, 1962] and theory of plate tectonics [*Wegener*, 1915].

The fluxgate magnetometer consists of a set of soft-iron cores, made of a highly magnetically permeable alloy, wrapped by two coils: the drive coil and the sense coil (Figure 2.6) [*Reynolds*, 2011; *Reeves*, 2005]. An alternating voltage drives the core continuously through a complete hysteresis loop. As the cores are oriented in opposite direction with regards to the drive coil, one core will generate a field in the same direction as the external field while the other will generate a field in the opposite direction of this same external field. In presence of an external magnetic field, the core's hysteresis loop will be altered. The core generating a field opposite to the external field reaches saturation sooner than the core generating a field aligned the external field. This change is recorded through measurements of current and voltage in the sense coil (Figure 2.7).

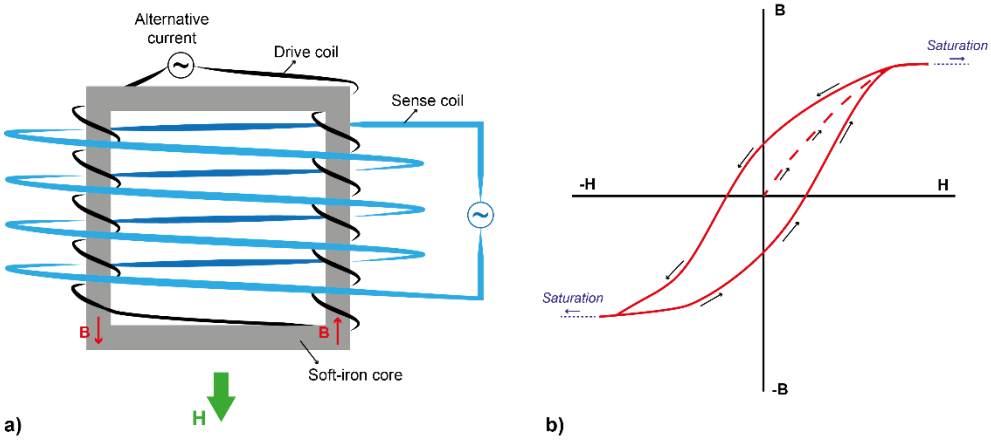

*Figure 2.6 a) Fluxgate magnetometer principle in an ambient magnetic field **H**. An induced magnetic field **B** is generated in the soft-iron core when an alternating-voltage is applied to the loop. b) The hysteresis magnetization curve illustrating the induced magnetic field **B** and the saturation point under an ambient field **H**.*

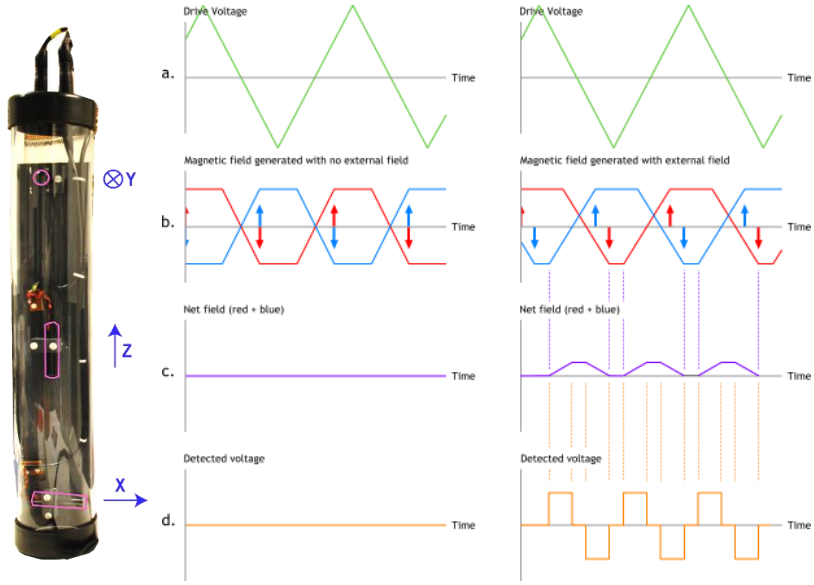

Figure 2.7 Left: Example of a 3-axial fluxgate magnetometer in the direction X, Y and Z. Right: response from the sensor without and with an external magnetic field (www.carisma.ca).

As a vector magnetometer, the fluxgate magnetometer has the advantage to measure the magnetic field precisely in a specific direction. In airborne geophysics, it uses the three axes and can extract the scalar value of the field. It is useful to measure small directional variation of the magnetic field and used to measure the noise from the aircraft. It serves for the compensation [*Bickel*, 1979], a technique to reduce noise correlated to the aircraft manoeuvres.

Optical absorption magnetometer (scalar magnetometer)

The optical absorption magnetometer uses the Zeeman effect principle. Commonly, this magnetometer is constituted of a Caesium (Cs) vapor chamber. Other gases can substitute the Caesium, such as Helium (He), Potassium (K), Rubidium (Rb) and are commercially available. Any alkali metals, with a single electron on their highest order s-orbital, are suitable for this principle. The magnetometer started to be in use during the early 1960 decade but is commonly used in airborne acquisition nowadays.

According to the Zeeman effect principle, when an atom is placed in a uniform external magnetic field, its energy levels are shifted. In the presence of an external magnetic field, a single energy level splits in two levels depending on the electron magnetic moment which is parallel or anti-parallel to the former. Using this principle, a polarized light at a specific frequency is applied to the Cs vapor in the chamber of the magnetometer causing the absorption and the shift of electrons from level 2 to level 3 (Figure 2.8). Spontaneous decay causes the electrons to populate level 1 and 2. Levels 1 and 2 are closed energy levels

separated by E_Z, linearly dependent of the ambient magnetic field (Figure 2.9). The process continues until level 1 is fully populated, causing the chamber to become transparent, which is detected by the photodetector. Once, this is reached, a depolarization is achieved with a RF (radiofrequency) power, causing the chamber to become opaque again and the lower energy (level 1) electrons to shift back to their original position (level 2). The frequency, called Larmor frequency, required to repopulate this energy level is linear to the ambient magnetic field. This Larmor frequency ω_0 is defined:

$$\omega_0 = \gamma_{Cs} B \tag{2.9}$$

where B is the ambient magnetic flux density and γ_{Cs} is the gyromagnetic constant of Caesium, which is 3.49872 Hz nT^{-1} [*Hrvoic et al.*, 2005; *Geometrics*, 2004].

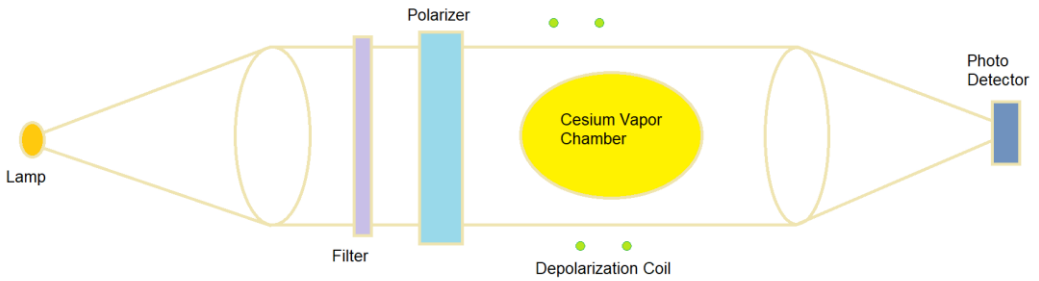

Figure 2.8 Schematic of Caesium vapor chamber (after www.gemsys.ca). A polarized light at a specific frequency is applied to the Cs vapor in the chamber of the magnetometer causing the absorption and the shift of electrons from level 2 to level 3. Spontaneous decay causes the electrons to populate level 1 and 2. Once, level 1 is fully populated, a RF depolarization is achieved, causing the chamber to become opaque again and the level 1 electrons to shift back to level 2.

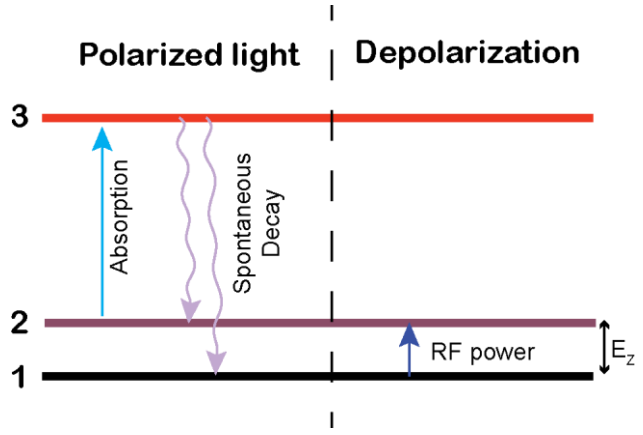

Figure 2.9 Schematic of electron energy absorption-emission lines. The energy separation E_Z between levels 1 and 2 is linearly dependent to the ambient magnetic field. In a first step, a polarized light is applied to the

chamber where the electrons from level 2 are absorbed. Spontaneous decay populates level 1 and 2. The process continues until no electrons are left at level 2. In a second step, the RF power repopulates level 2. The frequency required for the repopulation of level 2 is the Larmor frequency which is linear to the ambient magnetic field.

Figure 2.10 Example of Caesium vapor magnetometer used for NGU helicopter survey. The black cylinder contains the sensor, the red cylinder is the amplifier and the black box labelled KMAG 4 is the magnetometer counter.

Because of the constitution of the optical absorption, the magnetometer presents a polar and an equatorial "dead zone" that cannot measure the penetrating magnetic field (Figure 2.11). The intensity of the Zeeman effect depends on the direction of the ambient magnetic field with respect to the direction of the polarized light and RF power. The alignment of the sensor to the magnetic field is important to optimize the acquisition [*Hrvoic et al.*, 2005; *Geometrics*, 2004]. The active zone, sensitive to the penetrating magnetic field, is usually defined between 15° and 75° from the sensor axis.

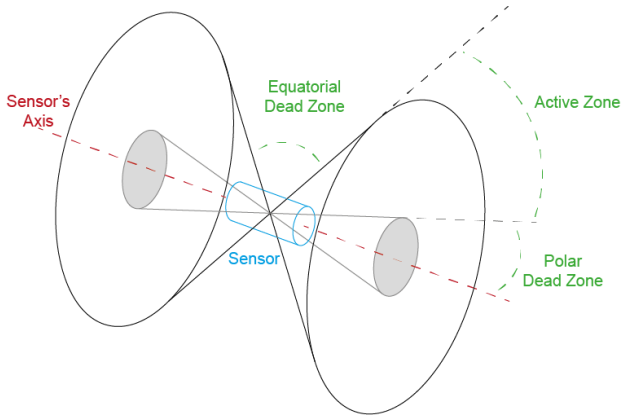

Figure 2.11 Schematic of the dead and active zones for an optical absorption magnetometer. The sensor orientation is important with respect to the aircraft flight line direction and the magnetic field orientation.

2.3.2. Magnetic noise reduction

The magnetic data used within this study were processed (KRAS-16) and re-processed (Austfonna) following the steps described below. The detailed processing of KRAS-16 and re-processing of Austfonna are found in appendices A and B, respectively. Noise reduction is critical to augment the accuracy of the interpretation.

Compensation

Magnetometers are commonly mounted on a stinger, a rigid extension of the aircraft, located at the front or back (Figure 2.3). It has the advantage that the exact location of the sensor can be derived from GNSS positioning with a simple lever-arm calculation. It is also safer to operate than the towed bird mounting system. However, its closeness to the aircraft generates unwanted noise. This noise is produced from the permanent magnetization of aircraft, the induced magnetization from the engine and the magnetic fields resulting from the electrical circuits within the aircraft [*Reeves*, 2005]. The last decades have seen the development of several techniques to compensate for this noise. A rather obsolete method is the passive compensation: positioning permanent magnets at various location on the aircraft to cancel magnetic noise form the aircraft itself. This method depended heavily on trial-and-errors and could only be truly tested during the flight [*Reeves*, 2005].

Nowadays, active compensation is the preferred method [*Bickel*, 1979; *Leliak*, 1961]. This analytical method describes with a mathematical approximation the disturbance of the magnetic field generated by the aircraft. The magnetic field $B(x, y, z, t)$ measured can be defined as:

$$B(x, y, z, t) = B_i(x, y, z, t) + B_e(x, y, z, t) + B_{dist}(X, Y, Z) \qquad (2.10)$$

Where B_i and B_e are the internal and external magnetic field from the natural environment, and B_{dist} is the magnetic field generated by the aircraft. The active compensation method proposes to measure B_{dist} at high altitude where B_i and B_e are considered uniform. The disturbance field is expressed:

$$\boldsymbol{B_{dist}} = B_{perm} + B_{ind} + B_{eddy}$$

$$\boldsymbol{B_{perm}} = a_1 \cos X + a_2 \cos Y + a_3 \cos Z$$

$$\begin{aligned}\boldsymbol{B_{ind}} = {} & a_4 B_t \cos^2 Z + a_5 B_t \cos X \cos Y + a_6 B_t \cos X \cos Z \\ & + a_7 B_t \cos^2 Y + a_8 B_t \cos Y \cos Z + a_9 B_t \cos^2 X\end{aligned} \tag{2.11}$$

$$\begin{aligned}\boldsymbol{B_{eddy}} = {} & a_{10} B_t \cos X \dot{\cos} X + a_{11} B_t \cos X \dot{\cos} Y \\ & + a_{12} B_t \cos X \dot{\cos} Z + a_{13} B_t \cos Y \cos X + a_{14} \dot{B}_t \cos Y \dot{\cos} Y \\ & + a_{15} B_t \cos Y \dot{\cos} Z + a_{16} B_t \cos Z \dot{\cos} X \\ & + a_{17} B_t \cos Z \dot{\cos} Y + a_{18} B_t \cos Z \dot{\cos} Z\end{aligned}$$

Where B_{perm} is the permanent magnetization and B_{ind} is the induced magnetization. B_{eddy} is the eddy magnetization generated by the magnetic fields from the aircraft. X, Y and Z are the angles between the principal directions of the aircraft and the B_t, the Earth magnetic field (Figure 2.12). The expression $\dot{\cos} X$ represents the derivative of $\cos X$.

At high altitude, B_t is approximate to the International Geomagnetic Reference Field (IGRF) field which is the estimate magnetic field removed from ground magnetic sources contamination. With a fluxgate magnetometer, the vector magnetic field B is measured for B_x, B_y and B_z. The cosines can be derived as:

$$\cos X = \frac{B_x}{B_t} \quad \cos Y = \frac{B_y}{B_t} \quad \cos Z = \frac{B_z}{B_t} \tag{2.12}$$

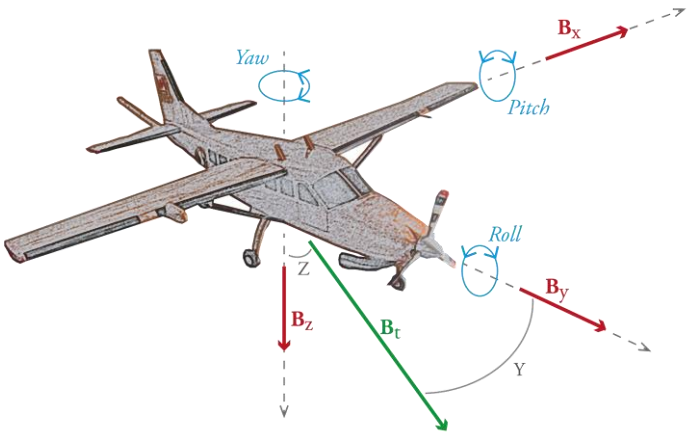

Figure 2.12 Aircraft manoeuvres and its directional angles. Directional angle X, between $\mathbf{B}_x$ and $\mathbf{B}_t$, is not shown. The compensation filter is based on a series of aircraft manoeuvres in a stable magnetic field.

According to Leliak [1961], the total intensity seen by the magnetometer is the projection of this field in the direction of the Earth's magnetic vector. Thus, the coefficients a_7 and a_{14} are not necessary due to the orthogonality of eigenvectors as:

$$\begin{aligned} \cos^2 Y &= 1 - \cos^2 X - \cos^2 Z \\ \cos Y \dot{\cos} Y &= -\cos X \dot{\cos} X - \cos Z \dot{\cos} Z \end{aligned} \tag{2.13}$$

Assuming the disturbance of the magnetic field is the only cause of variation at high altitude, equation (2.11) can be solved for 16 independent terms. To test the quality of the compensation, a criterion called Figure-of-Merit (FOM) has been developed. The test consists of flying a box in the same direction as the survey lines at high altitude. On each segment, a sequence of pitch, roll and yaw manoeuvres are achieved. The peak-to-peak difference of the magnetometer reading for each manoeuvre is defined as the remaining noise from the compensation. The industry standard for this value is to be lower than 1.5 nT.

Lag and heading errors

The lag error is defined as the time delay between the magnetometer response and the position of the causal magnetic source [*Reeves*, 2005]. It has two components: the physical delay and instrumental delay [*Coyle et al.*, 2014]. The physical delay is due to the spatial difference between the GNSS positioning antenna and the position of the magnetometer. Instruments are time synchronized, but depending on the configuration of the aircraft, the GNSS antenna or the magnetometer at the end of the stinger will overpass the magnetic source first. The instrumental delay is to process the signal between the acquisition and the recording. Nowadays, with the advancement of technology, the lag error is less than a second and is often negligible when flying with coarse line spacing.

The heading error is the discrepancy caused by the flight direction [*Reeves*, 2005]. This error is measured by comparing measurements at one point with the different flight directions of the lines and tie-lines.

Diurnal, secular variations and other temporal variations

The Earth's magnetic field experiences temporal variations over timescales ranging from seconds to millions year [*Sheriff*, 2002]. These variations affect the measurements and must be carefully reduced to leave only the anomaly caused by the source [*Reeves*, 2005].

The diurnal variations, per definition, refers to the variations arising from the rotation of the Earth with respect to the Sun [*Reeves*, 2005]. One of the most colourful, spectacular, and yet irritating noise sources are the magnetic disturbances generated by the solar wind – magnetosphere interaction. After their journey through the magnetosphere, following the field lines to the magnetic poles, the energetic charged particles interact with the ionosphere by ionisation and excitation causing the so-called northern lights [*Russell et al.*, 2016]. Unfortunately, these frequent polar magnetospheric substorms cause large disturbances of the Earth's magnetic field and propagate diurnal noise over a large area with significant temporal and spatial variations. In auroral physics, two types of auroras are considered: night-side and dayside. The night-side aurora is best-known as it is mostly occurring during evenings and nights and its visible ring extends from latitudes 65° to 75°. These aurorae are caused by the solar wind interacting with the tail of the magnetosphere. High energy substorms generates a larger extent of the aurora ring and may drag it further south. Similarly, low energy substorms will mainly affect the highest latitudes. Dayside aurorae are caused by solar wind interactions with the cusp of the magnetosphere located on the dayside at high latitude. These lower energy substorms are observed at high latitudes from 75° to 80° during midday. Substorms are transient processes causing disturbances of 300-800 nT of the horizontal field component over 0.5-3 hr.

Geomagnetic storms are global events, observed worldwide and more prominent at low- to mid-latitudes[*Russell et al.*, 2016; *Rastogi and Patel*, 1975]. They are caused by an intensification of the ring current (Figure 2.13) due to injection of energetic particles into the inner magnetosphere, generating disturbances of 30-150 nT over a period of 2-3 days. Under normal or "quiet" Sun conditions, the solar wind may distort the magnetosphere. Coupled with the daily rotation of the Earth, the distortion generates ionospheric currents on the dayside, causing magnetic disturbance of amplitude of less than 50 nT. These disturbances are focused between mid-latitudes and the equator [*Reeves*, 2005].

The intensity of the solar wind in terms of charged particles density, magnetic field and velocity is linked to the presence of sunspots and coronal holes, responsible for streaming energetic solar wind (also called fast-solar wind). The Sun undergoes a 11-year cycle. When

in "quiet" phase, the fast-solar wind is mainly streamed towards the poles – perpendicular to the Earth-Sun axis – with the presence of few or no sunspots, e.g. [*Phillips et al.*, 1995]. In period of high solar activity, numerous sunspots are seen at the surface of the Sun and coronal holes migrates more often towards the Sun equator causing an increase of energetic solar wind towards the Earth. The surveys presented in this thesis were acquired at high northern latitudes, subjected to both dayside and night-side diurnal variation and requiring a constant monitoring of base stations available in the Arctic. The aeromagnetic data acquired for KRAS-16 were acquired during low- to moderate- solar activity optimizing the data quality.

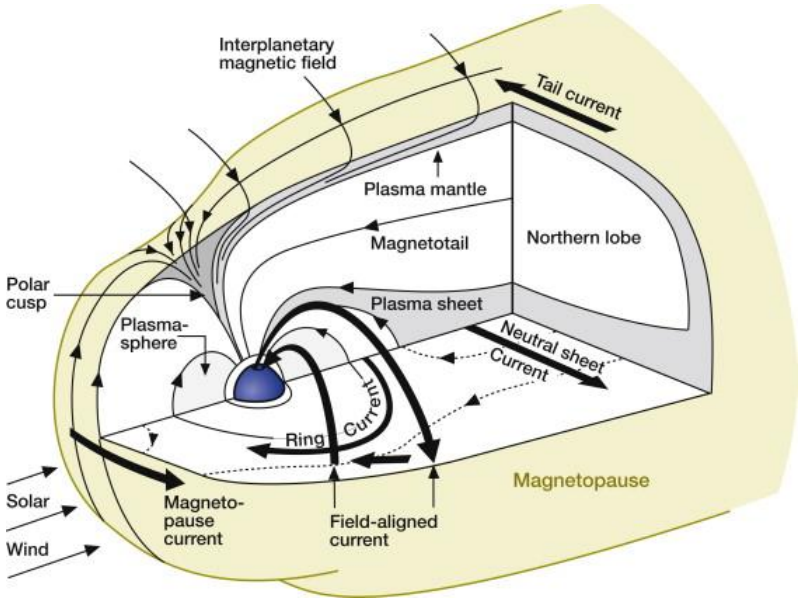

Figure 2.13 Schematic figure of the magnetosphere showing currents, field and plasma regions [Luhmann and Solomon, 2014]. The interaction between the solar wind particles and the magnetosphere is the principal source of diurnal noise seen in the aeromagnetic data.

Secular variations are global changes over hundreds of years. They are manifested by the changes in inclination, declination and field intensity due to the variation in the non-dipole field which drifts westward 20° per century; the decay and growth of the non-dipole field (~1000 yr); the dipole wobble (~10,000 yr), dipole strength variation which as decreased by half its intensity since the Roman time [*Hulot et al.*, 2010; *Genevey et al.*, 2009; *Nagata et al.*, 1963]. The secular variations are documented from historical data and recent accurate measurements [*Reeves*, 2005]. Models, such as the International Geomagnetic Reference Field (IGRF) with an root-mean-square vector error of about 10 nT [*Lowes*, 2000], have been reliable at predicting the secular variations[*Alken et al.*, 2021; *Thébault et al.*, 2015]. IGRF is commonly used to standardize and reference adjacent magnetic surveys.

Geomagnetic reversals, when the magnetic field reverses its polarity, occur at irregular intervals of 10,000 yr to more than 1,000,000 yr [*Ogg*, 2012; *Sheriff*, 2002]. These intervals can be measured from dating rock samples collected from seafloor spreading. These rocks show remanent magnetization properties correlated to the field polarity at the time of their formation. This order of temporal variation in the magnetic field are not directly relevant to magnetic surveys. However, the distribution of remanent magnetization affects the reliability of a reduction to the pole often used in mid- to equatorial latitudes to remove anomaly asymmetry caused by the inclination of the magnetic field. The correlation between the remanent magnetization and the period of the rock formation is useful for plate reconstruction as discussed in chapter 2.5.3.

Levelling and micro-levelling

To account for the temporal variation of the magnetic field, the intersections between traverse lines and control lines are used to correct the data. This technique is particularly useful when a magnetic base station is not available or too far from the survey area. Levelling algorithms calculate the difference between the crossing intersections and estimate the diurnal variations [*Nabighian et al.*, 2005; *Reford and Sumner*, 1964; *Whitham and Niblett*, 1961]. In areas with high diurnal activities, smoothing algorithms are performed on the intersection differences to ensure a smooth correction.

If necessary, the micro-levelling correction reduce the low-amplitude flight line noise remaining after the levelling [*Ferraccioli et al.*, 1998; *Minty*, 1991]. The levelling artefacts visible in the gridded data, or corrugations, are caused by the discrepancies between adjacent survey lines. The method removes anomalies of wavelength approximately equivalent of four times the line spacing, aligned with the flight line direction. The method can be applied for both traverse and control lines. Visual inspection may help to define the cut-off wavelength and the amplitude limit to applied to the correction.

2.4. Interpretation techniques

Qualitative potential field data interpretation is assessed by gridding data, superimposing them to topography or geological maps. Filtered data may be gridded to delineate body edges and establish the frequency content of the dataset. Quantitative interpretation provides depth estimates and creates models representing possible solutions. Gravity and magnetic models are non-unique as several geophysical configurations may yield to the same response. The ambiguity may be reduced with petrophysical data and additional structural information from other geophysical sources such as seismic data or geological concepts. The following techniques were used to assess the geophysical nature of the areas studied.

2.4.1. A review of potential field theory

A general definition of a field is a description of a physical effect as a function of space and time. Fields can be scalar (potentials) or vector (forces). A vector field has a magnitude and a direction, and is characterized by its field lines, which are tangent at every point to the vector field. By definition, a potential is a scalar field representing the potential energy per unit of some quantity due to a vector field. The field potential at a point can only be defined with respect to a reference point and differences in field potential are independent of the choice of reference. The force $\boldsymbol{F}$ giving rise to a conservative field can be derived from a scalar potential function *U*:

$$\boldsymbol{\nabla} U(x,y,z) = \frac{-\boldsymbol{F}(x,y,z)}{f} \tag{2.14}$$

Where f is a quantity specific to the type of field – mass for gravity field, electric charge for electric field, etc.

In general, the work W done by $\boldsymbol{F}$ is the change in kinetic energy required to move a particle from P_0 to P. It is expressed as the product of the force and the displacement $\boldsymbol{s}$ in the direction of the force:

$$W(P,P_0) = \int_{P_0}^{P} \boldsymbol{F} \cdot \boldsymbol{ds} \tag{2.15}$$

The work of forces generated by a potential function is known as potential energy. If the work for an applied force is independent of the path, the vector field is said conservative. Gravity and magnetic fields are conservative fields. The derivative of the work in any direction is equal to the component of the force in that direction [*Kellogg*, 1953]:

$$\boldsymbol{F}(x,y,z) = \left(\frac{\partial W}{\partial x}, \frac{\partial W}{\partial y}, \frac{\partial W}{\partial z}\right) = \boldsymbol{\nabla} W \tag{2.16}$$

In this case, the work depends only on the values of W at start-point P_0 and end-point P, and is independent of the path, as defined by conservative field. Therefore, the work function can be described as the potential φ of a vector field $\boldsymbol{F}$:

$$\boldsymbol{F} = \boldsymbol{\nabla}\varphi \tag{2.17}$$

Kellogg [1953] noted that if particles of the same charge attract each other (gravity field), then $\boldsymbol{F} = \boldsymbol{\nabla}\varphi$. While, if particles of the same charge repel each other (electric field), then $\boldsymbol{F} = -\boldsymbol{\nabla}\varphi$. Therefore, the value of the potential at a specific point is not as important as the

difference in potential between two separate points. A field that satisfies this relation is conservative and called potential field.

An important concept is the equipotential surface defined as a surface on which the potential remains constant:

$$\varphi(x, y, z) = constant \tag{2.18}$$

If a unit vector ($\boldsymbol{s}$) is tangent to an equipotential surface of $\boldsymbol{F}$, then $\boldsymbol{s} \cdot \boldsymbol{F} = \frac{\partial \varphi}{\partial s}$ at any point and must vanish according to the definition of an equipotential surface. Field lines at any points are always perpendicular to their equipotential surfaces. Hence, no work is done in moving a particle along an equipotential surface.

Gravitational potential

In the specific case of gravity, Newton's law of universal gravitation states that every particle attracts every other particle in the universe with a force which is directly proportional to the product of their masses and inversely proportional to the square of the distance between their centres. The mutual force between a particle of mass m_1 centred at $P_1(x_1, y_1, z_1)$ and a particle of mass m_0 centred at $P_0(x_0, y_0, z_0)$:

$$\boldsymbol{F} = \gamma \frac{m_1 m_0}{r^2} \boldsymbol{r} \tag{2.19}$$

where,

$$r = \sqrt{(x_1 - x_0)^2 + (y_1 - y_0)^2 + (z_1 - z_0)^2}$$

$\boldsymbol{r}$ is the unit vector directed from m_0 toward m_1 and γ is the universal gravitational constant (6.672×10^{-11} N m^2 kg^{-2}, in SI unit).

In the specific case of Earth, this can be re-written as:

$$\boldsymbol{F} = \gamma \frac{M_\oplus m_0}{R_\oplus^2} \boldsymbol{r} = m_0 \boldsymbol{g} \tag{2.20}$$

With $\boldsymbol{g}$ the acceleration of gravity, $M_\oplus$ and $R_\oplus$, the mass and radius of Earth respectively, and $\boldsymbol{r}$ directed downward toward the centre of the Earth. The gravitational field is conservative which means that the work done in moving a mass in a gravitational field is independent of the path traversed and depends only on the end points. If the mass returns to its original position, the net energy spent is zero, independent of the path taken. The sum of kinetic energy and the potential energy is constant within a closed system.

In spherical coordinates (r, θ, ϕ), the gravitational potential $\nabla U(r, \theta, \phi)$ can be written from equations (2.14) and (2.20):

$$\nabla U(r, \theta, \phi) = \frac{-\boldsymbol{F}(r, \theta, \phi)}{m_0} = -\boldsymbol{g}(r, \theta, \phi) \tag{2.21}$$

Solving for the gravitational potential, we obtain:

$$U(r, \theta, \phi) = -\int_{\infty}^{r} (\nabla U) \cdot d\boldsymbol{r} = -\int_{\infty}^{r} \boldsymbol{g}(r, \theta, \phi) \cdot d\boldsymbol{r} \tag{2.22}$$

Then, the gravitational potential $U(r, \theta, \phi)$ is equal to the work done by the gravitational field moving a unit mass from infinity to point r. Using equation (2.20):

$$U(r) = -\gamma \int_{\infty}^{r} \frac{m}{r^2} dr = \frac{\gamma m}{r} \tag{2.23}$$

Assuming an arbitrary shape of a mass of density ρ, the potential is expressed:

$$U = \int \frac{\gamma dm}{r} = \gamma \rho \int_{V} \frac{dv}{r} \tag{2.24}$$

Where dv is the infinitesimal volume ($dv = dx\, dy\, dz$).

Magnetic potential

The magnetic force can be conceptualized like the gravity field:

$$\boldsymbol{B} = \frac{\mu_0}{4\pi} \frac{p_1 p_2}{r^2} \boldsymbol{r} \tag{2.25}$$

With p representing a fictitious isolated magnetic monopole. A magnetic dipole is then two poles with strength $+p$ and $-p$ separated by a certain distance as seen in Figure 2.14. For a separation of $2l$, the magnetic dipole moment $\boldsymbol{m}$ is defined as:

$$\boldsymbol{m} = 2lp\boldsymbol{r} \tag{2.26}$$

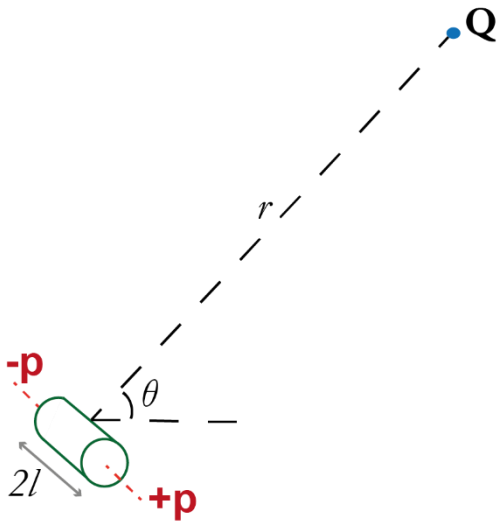

Figure 2.14 Representation of a magnetic dipole separated by a distance 2l measured at point Q at a distance r from the dipole.

Using the general definition of a potential field, equation (2.15) for the magnetic potential $\mathrm{A}(r)$ is described:

$$\mathrm{A}(r) = -\int_{-\infty}^{r} \boldsymbol{B}(r) \cdot d\boldsymbol{r} = \frac{p}{r} \tag{2.27}$$

$$\mathrm{A}(r) = \frac{\mu_0}{4\pi}\left[\frac{p}{r_1} - \frac{p}{r_2}\right] \tag{2.28}$$

$$\mathrm{A}(r) = \frac{\mu_0 p}{4\pi}\left[\frac{1}{\sqrt{r^2 + l^2 - 2lr\cos\theta}} - \frac{1}{\sqrt{r^2 + l^2 + 2lr\cos\theta}}\right] \tag{2.29}$$

And the vector F is derived:

$$\mathbf{B}(r) = -\boldsymbol{\nabla} A(r) = -\frac{\partial A}{\partial r}\boldsymbol{r} - \frac{1}{r}\frac{\partial A}{\partial \theta}\boldsymbol{\theta} \tag{2.30}$$

Where

$$-\frac{\partial A}{\partial r}\boldsymbol{r} = -\frac{\mu_0 p}{4\pi}\left[\frac{r + l\cos\theta}{(r^2 + l^2 + 2lr\cos\theta)^{3/2}} - \frac{r - l\cos\theta}{(r^2 + l^2 - 2lr\cos\theta)^{3/2}}\right]\boldsymbol{r}$$
$$-\frac{1}{r}\frac{\partial A}{\partial \theta}\boldsymbol{\theta} = \frac{\mu_0 p}{4\pi}\left[\frac{l\sin\theta}{(r^2 + l^2 + 2lr\cos\theta)^{3/2}} + \frac{l\sin\theta}{(r^2 + l^2 - 2lr\cos\theta)^{3/2}}\right]\boldsymbol{\theta} \quad (2.31)$$

In the case where $r \gg l$, the description of the force and potential can be simplified to:

$$A(r) \approx \frac{\mu_0}{4\pi}\frac{|\boldsymbol{m}|\cos\theta}{r^2}$$
$$\boldsymbol{B} \approx \frac{\mu_0}{4\pi}\left[\frac{2M\cos\theta}{r^3}\mathbf{r} + \frac{M\sin\theta}{r^3}\boldsymbol{\theta}\right] \quad (2.32)$$
$$|\boldsymbol{B}| \approx \frac{\mu_0}{4\pi}\frac{m}{r^3}\sqrt{1 + 3\cos^2\theta}$$

Considering the magnetic body with a distribution of individual magnetic dipoles, the vector sum of individual dipole moments:

$$\boldsymbol{M} = \frac{1}{V}\sum_i \boldsymbol{m}_i \quad (2.33)$$

And the potential field is expressed:

$$A(r) = -\boldsymbol{M}(r)\cdot\boldsymbol{\nabla}\left(\frac{1}{r}\right) = -\int_V \boldsymbol{M}\cdot\boldsymbol{\nabla}\frac{1}{|\boldsymbol{r_1} - \boldsymbol{r_2}|}dv \quad (2.34)$$

The fourth Maxwell's equation, modified from Ampère's law, states that the curl of $\boldsymbol{B}$ is equivalent to the sum of all the currents in the region:

$$\boldsymbol{\nabla}\times\boldsymbol{B} = \mu_0\left(\boldsymbol{J} + \varepsilon_0\frac{\partial \boldsymbol{E}}{\partial t}\right) \quad (2.35)$$

Where $\partial\boldsymbol{E}/\partial t$ represents the changing electric field or "displacement current" and is assumed negligible at survey scale. **J** is the current density expressed by the magnetization **M** and the macroscopic currents $\mathbf{I}_m$:

$$\mathbf{J} = \boldsymbol{I_m} + \boldsymbol{\nabla}\times\boldsymbol{M} \quad (2.36)$$

Equation (2.35) can be expressed with a quantity **H** is called the magnetic field intensity:

$$\nabla \times \left(\frac{\boldsymbol{B}}{\mu_0} - \boldsymbol{M}\right) = \nabla \times \boldsymbol{H} = \boldsymbol{I}_m$$
$$\boldsymbol{H} = \frac{\boldsymbol{B}}{\mu_0} - \boldsymbol{M} \tag{2.37}$$

In the presence of an external magnetic field, materials can acquire a component of magnetization called induced magnetization $\mathbf{M_i}$, proportional and parallel to the Earth's magnetic field:

$$\mathbf{M_i} = \chi \mathbf{H} \tag{2.38}$$

With χ the magnetic susceptibility. Some materials, such as ferromagnetic, have the property to retain a magnetization even in absence of an external magnetic field. This is remanent magnetization $\mathbf{M_r}$. The total magnetization $\mathbf{M}$ of a rock is expressed:

$$\mathbf{M} = \mathbf{M_i} + \mathbf{M_r} = \chi \mathbf{H} + \mathbf{M_r} \tag{2.39}$$

Often, the relative importance of the magnetization types is measured to provide the rock characteristics in terms of the *Koenigsberger ratio* Q:

$$Q = \frac{|\mathbf{M}_r|}{|\mathbf{M}_i|} = \frac{\mathbf{M}_r}{\chi \mathbf{H}} \tag{2.40}$$

Ambiguity of potential fields anomalies

The Gauss theorem, or the divergence theorem, stipulates that the divergence of a vector field $\boldsymbol{A}$ over a region of space V is equal to the integral of the outward normal component of the field over the surface S enclosing the region:

$$\int_V (\nabla \cdot \boldsymbol{A}) dv = \oint_S \boldsymbol{A} \cdot d\boldsymbol{S} \tag{2.41}$$

Using the divergence theorem, equation (2.41) and considering the normal component of the gravity field,

$$\int_V (\nabla \cdot \boldsymbol{g}) dv = \oint_S \boldsymbol{g} \cdot d\boldsymbol{S} = \int_S g_n ds \tag{2.42}$$

Considering a vacuum or a source free environment within the volume, then $\nabla \cdot \boldsymbol{g} = 0$ and the field satisfies Laplace's equation:

$$-\boldsymbol{\nabla}\cdot\boldsymbol{g}=\boldsymbol{\nabla}\cdot\boldsymbol{\nabla}U=\nabla^2U=0 \tag{2.43}$$

Considering a particle of a mass at the centre of a sphere of radius r, from equations (2.23) and (2.42), then:

$$\int_S g_n ds=-\frac{\gamma m}{r^2}(4\pi r^2)=-4\pi\gamma m \tag{2.44}$$

For an arbitrary shape mass enclosed within a surface S:

$$\int_V(\boldsymbol{\nabla}\cdot\boldsymbol{g})dv=\int_S g_n ds=-4\pi\gamma\int_V\rho dv \tag{2.45}$$

Equation (2.45) merely describes that the component normal to the surface equals the equivalent surface density. Poisson's equation is derived from this mass distribution:

$$\boldsymbol{\nabla}\cdot\boldsymbol{g}=\nabla^2U=-4\pi\gamma\rho \tag{2.46}$$

This implies that in free space the gravitational potential satisfies Laplace's equation while in region containing mass, it satisfies Poisson's equation. Similarly, the magnetic potential satisfies Laplace's and Poisson's equations:

$$\boldsymbol{\nabla}\cdot\boldsymbol{F}=-\nabla^2A=4\pi\mu p=4\pi\mu\boldsymbol{\nabla}\cdot\boldsymbol{M}(r) \tag{2.47}$$

And in a non-magnetic medium, $\nabla^2A=0$. Thus, various mass or magnetization distributions may produce the same potential field over a surface [*Skeels*, 1947], highlighting the "ambiguity" issue with gravity and magnetic interpretations.

2.4.2. Enhanced filters

Applied on grids, enhanced filters allow for the study of the frequency content of the data and to separate the regional (long wavelengths) and residual (short wavelengths) information which is assumed to correlate with the source depth [*Dentith and Mudge*, 2014]. It also removes noise or anomalies that may not be relevant to the geology interpreted. The high-pass filter aims to create a visualization of the short wavelengths that may be associated with the shallow geological sources. The upward continuation filter mimics a measurement of the anomaly at a higher altitude. It serves as a low-pass filter and is sensitive to regional geology, e.g., in the case of gravity, basin shape, top basement topography or Mohorovičićs discontinuity (crust-mantle interface).

Derivative filters (or gradients) are commonly used in potential fields interpretation to emphasize on the high frequencies in presence of low frequencies that may be correlated to

deeper-seated geophysical features. The horizontal gradients $\left\{\frac{\partial f}{\partial x}, \frac{\partial f}{\partial y}\right\}$ can be directly calculated on the gridded data, while the vertical gradient is derived from the Laplace equation $\nabla^2 f = 0$, valid for a conservative field. The vertical gradient can also be calculated as the difference between the upward- and downward-continued data.

Because high frequencies from shallow sources may create large amplitudes in the vertical and horizontal gradient, the tilt derivative, or θ, balances these amplitudes with a ratio of the vertical and total horizontal gradients [*Miller and Singh*, 1994].

$$\theta(x,y) = \tan^{-1}\left[\frac{\frac{\partial f}{\partial z}}{\sqrt{\left(\frac{\partial f}{\partial x}\right)^2 + \left(\frac{\partial f}{\partial y}\right)^2}}\right] \tag{2.48}$$

It is positive over the source of gravity and vertical magnetized bodies signatures, and negative outside. Therefore, the mapped zero-value contour line delineates the upper boundaries of the causative source.

2.4.3. Depth and edge detection of a magnetic source

Blakely et al. [2016] have developed a method to estimate the edge of a body and its depth by using the reciprocal of the horizontal gradient at the zero contour of the tilt derivative grid [*Fairhead et al.*, 2008]. The method maximizes the advantages of the tilt derivative which allows to treat weakly and strongly magnetic bodies with the same weight. As described by Salem et al. [2007], it can be expressed simply over a vertical contact as:

$$\theta = \tan^{-1}({}^{x}/_{z}) \tag{2.49}$$

where x is the horizontal distance from the contact and z, the depth. Noteworthy, when $x = z$, $\theta = \pi/4$. Thus, Salem et al. [2010] proposed to estimate z by measuring the horizontal distance between the zero and $\pi/4$ contours of the tilt derivative map. This distance provides an estimate of the depth z along the contour. Therefore, along the zero contour of the tilt derivative map, which is indicative of the shape of the magnetic source, the horizontal distance, calculated between the zero and $\pi/4$ contours, provides an estimate of the depth of this source.

Blakely et al. [2016] proposed to derive a depth estimate of a magnetic source from the horizontal gradient of θ at $x = 0$, such as:

$$\frac{d\theta}{dh} = \frac{z}{(x^2 + z^2)} \tag{2.50}$$

is reduced to:

$$z = \left[\frac{d\theta}{dh}\right]^{-1} \tag{2.51}$$

Therefore, the edges of a causative source are estimated from the tilt derivative, and its depth from the horizontal gradient of the tilt derivative. This method should be applied to reduced-to-pole magnetic anomalies or magnetic anomalies acquired near the poles.

2.4.4. Depth-to-source estimation

The potential field responses contain a wide range of frequencies which are related, in part, to the specific depth of the top of the geological sources. The depth-to-source estimation technique is an inverse modelling technique that provides a relatively quick depth analysis of the data. A popular depth-to-source interpretation is the depth-to-basement estimation which relies on sources near the top of the basement generating the dominant observed magnetic anomalies [*Nabighian et al.*, 2005]. In geophysical exploration, several basement interpretations exist: geologic, magnetic and acoustic, e.g. [*Goussev and Peirce*, 2010]. These different "flavours" serve different purposes. The geologic basement is defined as "the crust of the Earth below sedimentary deposits, extending downward to the Mohorovičićs discontinuity" ([*Neuendorf*, 2005], p. 57). It is also composed of igneous and metamorphic rocks [*Neuendorf*, 2005]. The magnetic basement refers to "the upper surface of extensive heterogeneous rocks having relatively large magnetic susceptibilities compared with those of the sediments; often but not necessarily coincident with the geologic basement" ([*Neuendorf*, 2005], p. 389). The acoustic, or seismic basement refers to "the deepest more-or-less continuous seismic reflector; often an unconformity below which seismic energy returns are poor or absent" [*Sheriff*, 2002]. The acoustic basement can be close or coincident with the magnetic basement, or it also can be much shallower than the magnetic basement [*Goussev and Peirce*, 2010]. Furthermore, if the velocity contrast is too little between the lowermost sediments and the crustal basement, the acoustic basement might not be resolved [*Marello et al.*, 2013]. The gravity or density basement is "where a very large density contrast exists so that anomalies resulting from deeper contrasts are lost in the noise" [*Sheriff*, 2002]. The derivative of the gravity signal, mathematically equivalent to the magnetic signal, can be used to estimate the depth of the gravity basement [*Kilty*, 1983]. The Euler deconvolution and the Werner deconvolution have been widely used, developed, and automated to estimate the depth-to-source from gravity and magnetic data.

Euler deconvolution

Euler deconvolution is a semi-automated method that requires an assumption of the type of source geometry [*Reid et al.*, 1990; *Thompson*, 1982]. It assumes a homogeneous field $f(\boldsymbol{v})$ following Euler's homogeneity relation:

$$f(t\boldsymbol{v}) = t^n f(\boldsymbol{v}) \tag{2.52}$$

And Euler's differential equation becomes:

$$\boldsymbol{v}\nabla f(\boldsymbol{v}) = nf(\boldsymbol{v}) \tag{2.53}$$

Where $\boldsymbol{v} = (v_1, v_2, \dots, v_k)$ is a set of components, t is real, and n is an integer representing the degree of homogeneity of $f(\boldsymbol{v})$. Assuming source bodies described in at location (x, y, z) of infinite length-dimensioned size parameters, potential fields are expressed:

$$f(x, y, z) = \frac{1}{r^N} \tag{2.54}$$

Where $r = \left(\boldsymbol{x^2} + \boldsymbol{y^2} + \boldsymbol{z^2}\right)^{1/2}$ and, N is a non-negative integer, identified as $-n$ and commonly called the Structural Index (Table 2.1). The Euler equation to solve is expressed:

$$(x - x_0)\frac{\partial T}{\partial x} + (y - y_0)\frac{\partial T}{\partial y} + (z - z_0)\frac{\partial T}{\partial z} = N(B - T) \tag{2.55}$$

Where (x_0, y_0, z_0) is the position of the causal source generating the total field $\boldsymbol{T}$ at location (x, y, z) and B is the regional value or the background of the anomalous field. Within a small window of a larger dataset, the method consists in resolving this equation for a set of several measurements to locate the source (x_0, y_0, z_0) and sometimes, its structural index $\boldsymbol{N}$. $\boldsymbol{B}$, $\boldsymbol{T}$ and its derivatives can be measured or calculated, while the structural index may be input by the interpreter. The method is usually automated to consistently repeat the procedure over several windows until the dataset is entirely covered. The method assumes the presence of a single source within one window. Thus, the size of the window must be chosen carefully with regards to the resolution of the dataset and the expected size and depth of the causal sources. The measured data and calculated gradient must have relatively low noise. Shallow sources might not be resolved if there is significant interference between the smaller wavelength caused by shallow sources and the noise frequencies [*Reid et al.*, 2014].

The difference between magnetic and gravity structural index is attributed to the relation of the anomaly size decay with source-to-depth. For a point source, magnetic anomaly size decays with d^{-3} while the gravity anomaly size decays with d^{-2}, where d is the depth of the causal source.

Model	Structural Index N	
	Magnetic	Gravity
Point, Sphere	3	2
Line, cylinder, thin bed fault	2	1
Thin sheet edge, thin sill, thin dyke	1	0
Thick sheet edge	0	-1
Contact of infinite depth extent	0	-

Table 2.1 Euler structural index N definition for magnetic and gravity models.

Werner deconvolution

The Werner deconvolution is an automated depth-to-source estimation algorithm originally developed by Werner [1953] and later automated [*Phillips*, 1997; *Kilty*, 1983; *Ku and Sharp*, 1983; *Jain*, 1976; *Hartman et al.*, 1971]. It assumes that all magnetic anomalies are generated by a series of dykes and edge interfaces (contacts). From the total magnetic field and its derivatives, the method estimates the depth, dip, horizontal location and susceptibility contrast for a presumed dyke or contact. The depth and edges of a source are estimated from these empirical basement indicators sensitive to susceptibility variations and representing an assemblage of simplified geometries of dykes and contacts [*Goussev and Peirce*, 2010].

The fundamental principle lies in the description of the magnetic anomaly $F(x)$ for a dipping dyke as:

$$F(x) = \frac{\{M(x - x_0) + Nz\}}{\{(x - x_0)^2 + z^2\}} \tag{2.56}$$

where $x_0$is the surface point directly above the centre of the top of the dyke, z is the depth to the top and x is the point of observation, with the x-axis is normal to the strike. While M and N are unknown functions of the dyke geometry and mineralization. Equation (2.56) is rearranged in the polynomial form:

$$x^2F(x) = a_0 + a_1x + b_0F(x) + b_1xF(x) \tag{2.57}$$

where,

$$a_0 = -Mx_0 + Nz \qquad b_1 = 2x_0$$
$$a_1 = M \qquad x_0 = \frac{b_1}{2}$$
$$b_0 = -x_0^2 - z^2 \qquad z = \frac{\sqrt{-4b_0 - b_1^2}}{2}$$

With this in hand, the location of the source x_0 and its depth z is calculated by measuring $F(x)$ at four points and solving equation (2.57). Considering noise and interference caused by neighbouring anomalies, the polynomial of the field observed $\mathcal{F}$ can be expressed as:

$$\mathcal{F} = F(x) + c_0 + c_1 x + \cdots + c_n x^n \tag{2.58}$$

Where $F(x)$ has been described in equation (2.56). This expression requires solving equation (2.58) for $n + 5$ unknown quantities. Usually, the polynomial is first or second order and only six or seven measurements are necessary for a solution. To solve contacts, basement topography, faults and magnetic interfaces, the horizontal derivative is used instead of $F(x)$.

The algorithm is designed to find solutions along one direction only and optimal orthogonal to the strike of the anomalies. Goussev & Peirce [2010] has developed an empirical set of basement indicators for identification and correlation of the magnetic basement (Figure 2.15 & Figure 2.16). These set of distribution of Werner solutions along the magnetic basement can also be observed in their mirror configuration, i.e., above and below the magnetic basement. It is designed to resolve only dikes and contacts, assuming every geological body can be modelled as a combination of these two shapes. Other major limitations of Werner remain in the resolution between neighbouring geological sources and the lack of discrimination among parameters causing an inherent correlation between the mineralization and geometry of the sources.

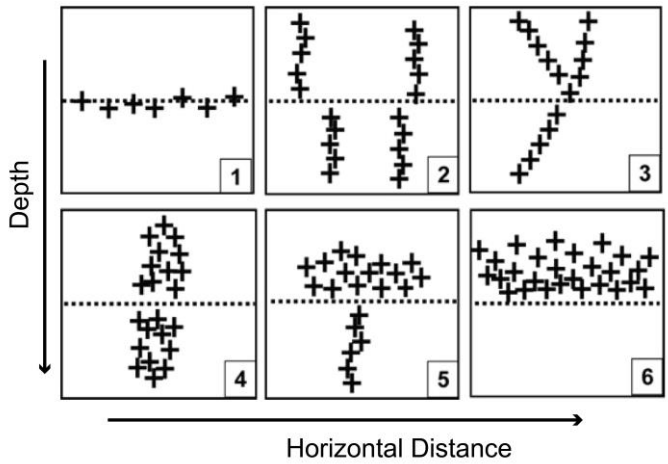

Figure 2.15 Empirical magnetic basement indicators from the Werner deconvolution solutions defined by Goussev & Peirce [2010]. Black crosses represent the solutions and black dotted line is the magnetic basement. 1) lateral alignment, 2) truncation, 3) change of dip, 4) gap, 5) alignment into cloud, 6) bunded noise. Their mirror character can also be observed. Illustration from [Goussev and Peirce, 2010].

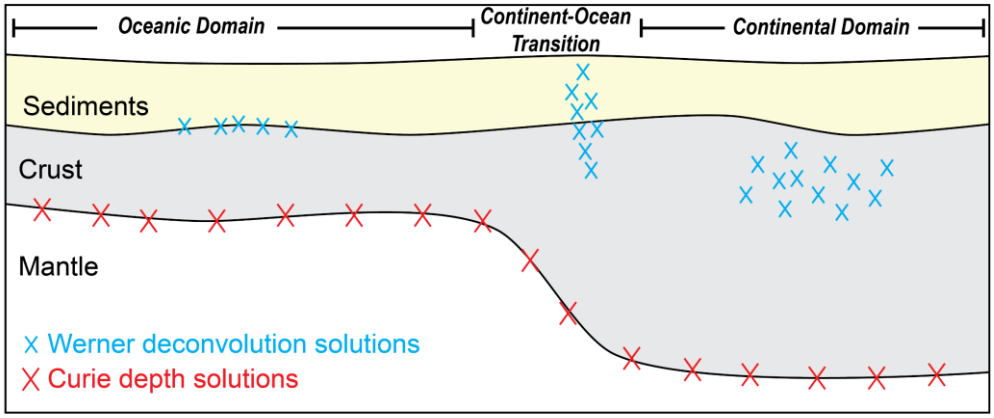

Figure 2.16 Werner deconvolution solutions indicators (blue crosses) of the top of the magnetic basement and Curie depth solutions (red crosses) delimiting the bottom of the crustal basement. Werner deconvolution solutions are shown with the possible configuration 1, 4 and 6. The crustal basement is expected thinner in the oceanic domain compared to the continental domain.

Curie depth

The Curie depth represents the isotherm of the Curie temperature of magnetite (580 °C), the main mineral producing magnetic anomalies. Above this temperature, magnetite loses its spontaneous magnetization. The Curie depth is expected to be shallow under the mid-oceanic ridges and in the oceanic domains, where higher temperatures (>580 °C) in the lithosphere are expected from the magma supply feeding the spreading ridges. Conversely, the Curie depth is expected to be deeper in the continental domains, expressing a colder mantle.

Derived from the magnetic data, several methods can be used to estimate the Curie depth. These methods assume that the depth of Curie temperature correlates with the depth extent of the crustal magnetic sources (Figure 2.16). Analysis of the power spectrum of the magnetic anomalies in the Fourier domain allows the estimation of depth distribution of magnetic sources [*Spector and Grant*, 1970]. One requirement is that the magnetic dataset is large enough to contain the long wavelengths necessary to resolve the Curie depth.

For this thesis, Curie depths were estimated with the Pycurious [*Mather and Delhaye*, 2019] python code using the Bouligand et al. [2009] algorithm. It uses a model of fractal random magnetization suggested as a realistic representation for crustal magnetization and assumes the power spectrum of the magnetization (Φ) proportional to the wave number ($\mathbf{k}$) raised to the power -β [*Maus et al.*, 1997].

$$\Phi(k_x, k_y, k_z) \propto k^{-\beta} \tag{2.59}$$

Bouligand et al. [2009] demonstrated the expression on the right hand side of equation (2.59) can be determined for three independent parameters: the depths to the top and bottom of the magnetic source layer and the fractal exponent -β. The method repeats the calculation over several windows until the dataset is entirely analysed and resolves one Curie depth within one window. The size of the window is selected with careful consideration to the resolution of the dataset and the expected Curie depth of the area. The results in deep oceanic areas might yield to incorrect depth estimates since the algorithm assumes random magnetization in all direction, unlike the remanent magnetization found in a typical oceanic crust.

2.4.5. Modelling

A potential field model describes the Earth and its targets by a spatial distribution of gravity and magnetic sources. The modelling approach provides a quantitative estimation of the geometry of physical properties that relate to the underlying geology and its petrophysical properties in terms of density and susceptibility. Models provide a better understanding of the observations by calculating the geophysical effects of a certain geologic concept and comparing to the observed magnetic and gravity anomalies.

The model response is the sum of the responses of all its constituents. A model called shape-based consists of simple geometrical bodies each with a specific assigned physical property value. Shape-based models are useful for simple homogeneous subsurface bodies or to simplify a complex model when little physical properties and geometries are known about the subsurface [*Dentith and Mudge*, 2014]. A cell-based model can create complex physical properties and geometries by representing the entire subsurface as a distribution of discrete elements or cells. Each cell is assigned a homogeneous physical property. The cell geometry and positions remain constant, but the physical properties are adjusted to represent the desired subsurface. A few algorithms allow the user to modify the cell geometry in only one direction, generally the vertical. The cell-based model has the advantage to create complex subsurface but requires greater computer resources. Both shape-based and cell-based models demand a model extending beyond the area of interest to prevent unwanted effect caused by the abrupt change in physical properties at the edge of the model [*Dentith and Mudge*, 2014].

Models can be defined in several dimensions, commonly 2-D, 2.5-D, and 3-D. 2-D models consider a physical property distribution in the depth and the distance along a profile. The third dimension, horizontally perpendicular to the profile, is considered infinite. This assumption is reasonable for profiles perpendicular to the regional strike or to geological features having a long strike length relative to the profile. 2.5-D models are a variation of the 2-D models and consider a finite strike length perpendicular to the profile. The strike of each geological can be defined as needed. It allows to analyse the 3-D effect without the complexity of the 3-D model. 3-D models consider subsurface physical property distribution in all three directions. It is useful to model map data. However, 3-D models require greater

computer resources to view, manipulate and calculate the geometry of the subsurface. The observed and modelled responses are often displayed as several parallel equally spaced profiles across the area of interest.

Two different potential field modelling methods are commonly used: the forward method and the inverse method. The forward method involves creation of an initial model that is built based on known physical properties and geometries or on geologic and geophysical intuition [*Blakely*, 1995]. The response of the model is calculated and compared with the observed anomaly data. The model parameters are then adjusted interactively and repeatedly until satisfactory resemblance between the calculated response and the observed anomaly is obtained. The inverse method is an iterative process automatically calculating the physical parameters and geometries directly from the observed anomaly based on various assumptions. In theory, the inverse method requires less interaction from the interpreter but might yield numerous geologically improbable solutions due to the inherent ambiguity of potential field methods. The interpreter often needs to provide an initial model allowing the algorithm to converge towards a realistic solution. For this thesis, two types of modelling were used: 2-D forward modelling and 3-D inversion modelling.

2-D forward modelling

2-D forward models are generally built from "pre-known" constraints from e.g. borehole, seismic, ground penetrating radar or a combination of measurements. The commercial package *GM-SYS* [*Geosoft*, 2006] was preferred to carry the interpretation for its robustness and availability at the Geological Survey of Norway offices. The software sums the effects of irregular polygons, a method modified after Talwani et al. [1959] and uses the divergence theorem for the magnetic modelling [*Blakely*, 1995]. The petrophysical properties and geometry of the models are adjusted iteratively to obtain the best fit to the observed magnetic and gravity data.

3-D inversion modelling

The commercial package GM-Sys 3D Modelling [*Geosoft*, 2014] was used to create surface-oriented 3-D inversion models. With this package, a model is defined by stacked surface layers, each with a specified density and magnetization surface distribution. The crustal magnetization was derived for the KRAS-16 area using a known bathymetry, an estimated sediment thickness [*Engen et al.*, 2006] and an estimated Moho [*Funck et al.*, 2017], where both mantle and sediment have a negligible magnetization. The model was inverted to obtain the magnetization of the crust from the aeromagnetic data. The inversion calculation is based on Parker and Huestis [1974] and Oldenburg [1974] methodologies.

2.5. Geological and environmental assessments of the Norwegian Polar Regions

Both magnetic and gravity signatures are sensitive to a lateral contrast, in susceptibility and remanence, and density respectively, between the body of interest and country rock. It is important to assess the geological body of interest but also understand the properties of the surrounding geology. When interpreting geophysical data, petrophysics and other available data provide a link between the geological environment and the geophysical response. Not all combined datasets were acquired simultaneously, and their resolution and sensitivity vary greatly. Near-surface cover, e.g. soil, and glaciers, may distort or attenuate the bedrock response. Therefore, the geophysical interpretation must recognize and consider the limits of each dataset. However, these variations in the magnetic and gravity responses provide valuable guidelines when the interpretation is applied to a specific environment in the Polar Regions.

2.5.1. Crustal domains

Continental crust has a typical thickness of 30 - 35 km, with bulk densities of 2,800 - 2,900 kg m^{-1}. Oceanic crust is younger, thinner - with an average thickness of ~7 km [*LaFemina*, 2015; *Jokat et al.*, 2003; *Bown and White*, 1994], densities of 2,900 - 3,000 kg m^{-1}, mainly composed of extruded basalts dominated by remanent magnetization. The oceanic lithosphere is characterized by four layers, where the upper three layers comprise the crust and layer 4, at the bottom, comprises the upper mantle [*LaFemina*, 2015; *Perfit*, 1999] (Figure 2.17). Layer 1 is a sediment cover of hundreds of meters thickening with age as the lithosphere moves away from the ridge axis. Layer 2A has a thickness of 0.5-1 km consisting of basaltic lava flows erupted as pillow or sheet lava flows within the neo-volcanic zone along the mid-ocean ridge axis [*LaFemina*, 2015; *Perfit*, 1999] . Layer 2b consists of vertically oriented, sheeted diabase dikes with a thickness of approximately 1.5 km [*LaFemina*, 2015; *Perfit*, 1999]. These dykes formed by the injection of mid-ocean ridge basaltic magmas from central volcanic crustal or subcrustal magma chambers along the ridge, accommodate the 1-12 cm yr^{-1} of relative plate motion at mid-ocean ridges as they are intruded into the crust. The number of magma chambers is correlated to the seafloor spreading rate, length of the ridge segment, and magma supply to the ridge [*LaFemina*, 2015; *Dick et al.*, 2003]. Layer 3 is the gabbroic lower crust formed by lateral flow and cooling at the edge of the magmatic bodies [*Coogan and O'Hara*, 2015; *LaFemina*, 2015]. The oceanic crust cools and becomes denser as the plate moves away from the mid-ocean ridge.

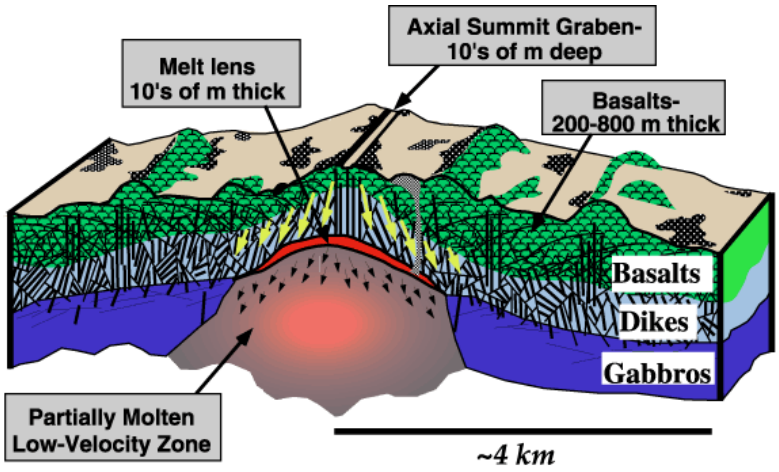

Figure 2.17 Oceanic crust illustration at a mid-ocean ridge with the typical crustal layers 2A (Basalts), 2B (dikes) and 3 (gabbros). Layer 2A is 0.5-1km thick, layer 2B is approximately 1.5 km thick, while the total crustal thickness is approximately 7 km [Jokat et al., 2003; Bown and White, 1994]. Illustration from Karsen et al. [2002].

The seafloor spreading rate affects the morphology, the composition, and the thickness of the oceanic crust (Figure 2.18). Slow and ultraslow spreading ridges have distinctive bathymetric profiles characterized with a rough and faulted topography, and 1.5-3.0 km deep rift valleys [*Macdonald*, 1982; *van Andel and Bowin*, 1968]. Comparatively, intermediate spreading ridges have a shallow rift valley and fast spreading ridges present an axial rise and an axial summit trough [*Macdonald*, 1982]. Ultraslow spreading ridges show a correlation between the seafloor spreading rate and the total crustal thickness [*Reid and Jackson*, 1981].

The magnetic response of oceanic crust is characterized by a striped pattern parallel to its spreading ridge. These magnetic stripes are caused by the magnetic field poles alternation (normal and reverse) responsible for the variation in remanent magnetization of the layer 2A. No continental crust processes would yield to a striped pattern response similar to a stable seafloor spreading. When interpreting magnetic data, the crustal oceanic domain may be delineated by the presence of the striped magnetic pattern. This demarcation as the first order is referred to as the magnetic continent-ocean boundary (COB) [*Vine and Matthews*, 1963].

The concept of COB demarks the geophysical contrast observed from a continental to an oceanic crust across a given margin and is often mapped as a line but in reality, is a zone. The uncertainty of the COB is related to the resolution and accuracy of the geophysical data. The uncertainty is also related to the data interpretation when the physical characteristics of the underlying crust can be attributed to both continental and oceanic crustal types. Instead of delineating a COB, a continent-ocean transition zone (COTZ) can be mapped. Three possible scenarios have been suggested for COTZ [*Whitmarsh and Miles*, 1995]. The first

scenario is a heavily intruded continental crust, possibly buried by extrusive material (e.g., [*Lundin and Doré*, 2011; *Blaich et al.*, 2010; *Boillot and Froitzheim*, 2001]. The second scenario is a crust surrounded by unroofed upper material. In the third scenario, the COTZ is a mixture of upper mantle and volcanic products from ultraslow seafloor spreading (e.g. [*Scott*, 2000; *Mjelde et al.*, 1997; *Roots et al.*, 1979].

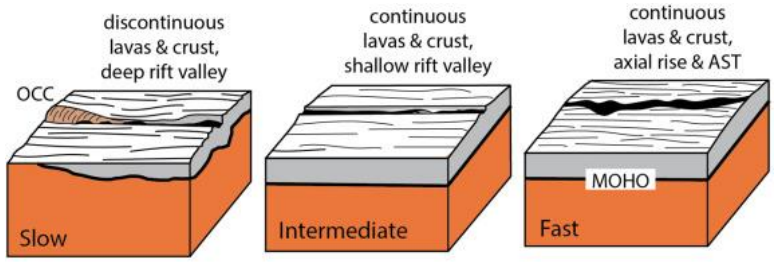

Figure 2.18 Illustration of the oceanic crust morphology, magma budget and crustal thickness. Slow and ultraslow spreading ridges have a rough and faulted topography and a deep rift valley [Macdonald, 1982; van Andel and Bowin, 1968]. Comparatively, intermediate spreading ridges have a shallow rift valley and fast spreading ridges present an axial rise and an axial summit trough (AST). Due to the magmatic and amagmatic accretion processes, oceanic core complex (OCC) and serpentinized crust might be present. Illustration from Karson [2017].

2.5.2. Dykes, sills, and other magmatic intrusions

Magnetic and gravity map superimposed on a geological map allow the association of known outcrops to a gravity or magnetic response. From the size and shape of the associated anomaly, the depth and extent of the geological body can be estimated. With additional petrophysical data from rock samples, the volume of the body can be estimated. Moreover, the symmetry or the asymmetry of an anomaly is indicative of the dip or plunge of the causative geological body [*Dentith and Mudge*, 2014]. This is particularly useful for magmatic intrusions. Igneous rocks have a strong magnetization and density contrast compared with the background lithology. Due to their magnetite content, related to the abundance of iron and oxygen, they can express either remanence or induced magnetism or both. Moreover, when modelling the magnetization in term of remanence, one can infer the age of the formation from the inclination vector of the remanence magnetization, e.g. [*Mendel et al.*, 2005]. The rock retains all the vector parameters of the ambient geomagnetic field when it cools below the Curie temperature. The direction of the magnetization provides an insight into the polarity of the external field and the geolocation of the rock compared to the magnetic poles at the time of the cooling. Metamorphism and rock alteration can significantly change the magnetic properties of the rock by creating or destroying magnetic minerals.

Magmatic and amagmatic accretion processes occur at ultraslow mid-ocean ridges as seen on the Gakkel Ridge (e.g. [*Morozov et al.*, 2016; *Schmidt-Aursch and Jokat*, 2016; *Zhang et al.*, 2015;

Urlaub et al., 2009; *Jokat and Schmidt-Aursch*, 2007; *Schlindwein et al.*, 2005; *Cochran et al.*, 2003; *Jokat et al.*, 2003; *Michael et al.*, 2003]) and South West Indian Ridge [*Momoh et al.*, 2017; *Gao et al.*, 2016; *Schmid and Schlindwein*, 2016; *Sauter et al.*, 2013; *Cannat et al.*, 2008; *Cannat et al.*, 2006; *Minshull et al.*, 2006; *Sauter et al.*, 2004; *Seyler et al.*, 2003; *Cannat et al.*, 1999; *Muller et al.*, 1999]. Magmatic accretion takes place along the spreading axis but might be interrupted by segments of amagmatic accretion that emplace mantle peridotites to the ridge axis through low-angle normal faulting and exhumation [*Cann et al.*, 1997; *Tucholke and Lin*, 1994]. Amagmatic accretion processes are common along oblique ultraslow spreading ridges [*LaFemina*, 2015; *Dick et al.*, 2003]. Steeply dipping normal faults, low-angle normal faults and oceanic core complexes are observed along slow and ultraslow spreading ridges (Figure 2.18) [*LaFemina*, 2015; *Cannat et al.*, 2006; *Smith et al.*, 2006; *Tucholke et al.*, 1998]. Ocean water penetrates the crust in the pathways created by normal faulting. This hydrothermal circulation causes alteration such as serpentinization and cooling of the crust. Oceanic core complexes formed by low-angle detachment faulting expose peridotite upper mantle and serpentinized crust. These processes will change the magnetization of the oceanic crust. Other examples of magmatic intrusions are the doleritic dikes found on Nordaustlandet [*Dallmann*, 2015] and the Cretaceous sills emplaced offshore Nordaustlandet [*Polteau et al.*, 2016; *Minakov et al.*, 2012; *Grogan et al.*, 2000]. These magmatic intrusions can be assessed, in terms of size, volume, dip and plunge, with a qualitative analysis of the magnetic and gravity maps coupled with other sources of geological knowledge [*Dentith and Mudge*, 2014].

2.5.3. Remanent magnetization and seafloor spreading process

Isolating high frequencies of the magnetic data allows the recognition of the oceanic domain with its typical shallow and linear magnetized features. These latter are identified as the remanence magnetized basalt layer 2A formed through the seafloor spreading process of the mid-oceanic ridges. During their formation, through the cooling phase, those basalts record the ambient geomagnetic field at the time when they cooled below their Curie temperature. As the ambient geomagnetic field undergoes magnetic pole reversals, layers of basalts are formed providing a linear magnetic striped signature along spreading ridges [*Ogg*, 2012]. With the spatial variation of the magnetic anomaly, the seafloor spreading history of mid-oceanic ridge and the plate tectonic can be deduced.

A magnetic chron refers to the time interval between two polarity reversals of the geomagnetic field. Depending on the resolution of the magnetic data or the length of a magnetic chron, magnetic isochrons are assigned by picking the young (y) or old (o) end of the magnetic anomaly correlated to a magnetic chron [*Seton et al.*, 2014]. In some case, where the magnetic anomaly boundaries are unclear, the centre (c) or middle point (m) is picked (Figure 2.19). The young and old end of the magnetic isochrons were picked for the interpretation of the KRAS-16 aeromagnetic data.

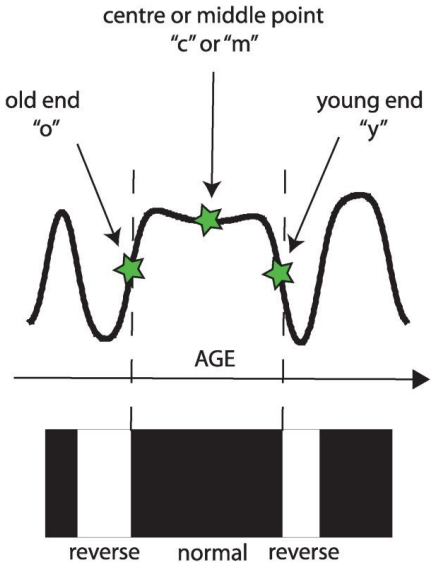

Figure 2.19 Picking technique for a magnetic chron, between two geomagnetic field reversals. The young and old isochrons are picked where the resolution and accuracy of magnetic anomalies allow it [Seton et al., 2014].

The Knipovich Ridge is an oblique seafloor spreading ridge [*Vogt et al.*, 1982; *Talwani and Eldholm*, 1977] intersecting Mohns Ridge with a sharp bend where magmatic and amagmatic accretion processes might occur along the ridge. Under this configuration, the striped magnetic anomaly pattern expected along mid-ocean ridge might be disrupted by amagmatic accretion processes or serpentinization.

Seafloor spreading rates calculation

Magnetic isochrons are commonly identified by the comparison between the observations and a synthetic 2-D forward model of a seafloor spreading sequence comprised of alternating bodies with an assigned magnetization. The seafloor spreading rates are adjusted iteratively until the calculated response correlate with the observed data. An automated identification method has been proposed by Zhizhin et al. [1997] with moderate success and required manual correction to align the seafloor spreading model to the observed data. Several parameters are defined by the synthetic crustal model such as the remanent magnetization parameters, ambient geomagnetic field directions, spreading rates, spreading asymmetry, the spreading ridge orientation, and the vertical orientation of the magnetized body. These are uncertainties to the interpretation along with the uncertainty related to the magnetic data accuracy.

For this study, *MODMAG*, a *MATLAB*-based software designed to replicate a seafloor spreading model along a selected line [*Mendel et al.*, 2005], was used for the seafloor spreading

interpretation. It has the advantage to consider asymmetric seafloor spreading and axial ridge jumps. The interface allows the user to perform forward modelling of a specific seafloor spreading pattern, giving rate and asymmetry values, and then compare the model with the observed data. The topography along the profile and the magnetic signature are input in the software. The seafloor spreading rates and their respective asymmetries are also provided to build the forward model. Parameters are modified by iteration to fit the observed data. The software considers either a constant thickness upper crust draped along the bathymetry or an upper crust at constant depth. This approximation might not be truly representative of the upper crust, but it is expected that the shallowest basalts are the most prominent sources of the magnetic anomaly. With the given seafloor spreading rates, it creates a series of normal and reverse magnetized units according to the international geological time scale [*Ogg*, 2012].

For this study, the magnetic isochron interpretation is calibrated with the latest interpretation of the Mohns Ridge [*Gernigon et al.*, 2019; *Matthews et al.*, 2016; *Engen et al.*, 2008] at the bend with the Knipovich Ridge. This is only possible as the magnetic signature is continuous along the bend between the two ridges. The sediment cover is transparent to the magnetization but hinders the signal by causing the magnetized source to be buried and at greater distance relative to the acquisition platform. To account for the presence of sediment on the near-surface of the seafloor, sediment thickness is estimated [*Engen et al.*, 2006] for the specific seafloor spreading model of the Knipovich Ridge.

Plate tectonic reconstruction

Plate tectonic reconstruction is the quantitative description of the relative motion of tectonic plates in the geological past. Plate tectonics theory assumes the plates are internally rigid and move without much deformation. Their motion is described by Euler's Theorem as a rotation about a virtual axis that passes through the centre of the sphere called a rotation pole or Euler pole (Figure 2.20). Thus, the theory considers the Euler pole which is defined as the latitude and longitude of the angular velocity vector that describes the plate motion or rotation [*Wessel and Müller*, 2007]. The interplay of the plates is observed through the occurrence of earthquakes, transform faults and the formation of mountains, sedimentary basins, seamounts, volcanoes, island arcs and deep ocean trenches [*Wang and Liu*, 2019; *Wessel and Müller*, 2007]. Plate tectonic reconstruction often uses these observables along with other knowledge such as the location of the plate boundaries at a specific time in the past, rock dating, paleomagnetic measurements geochemistry data, geophysical data, or any combination. Considering the seafloor spreading rate varies as the angular distance from the rotation pole, the seafloor spreading rates calculated from magnetic anomalies are commonly used to determine a rotation pole [*Wessel and Müller*, 2007]. An important uncertainty of the plate tectonics theory is the assumption of the rigidity of the plates and their deformation associated with zones of lithospheric weakness. This assumption is valid if the zone of deformation is much narrower than the rigid zone [*Wessel and Müller*, 2007; *Dickinson*, 2003].

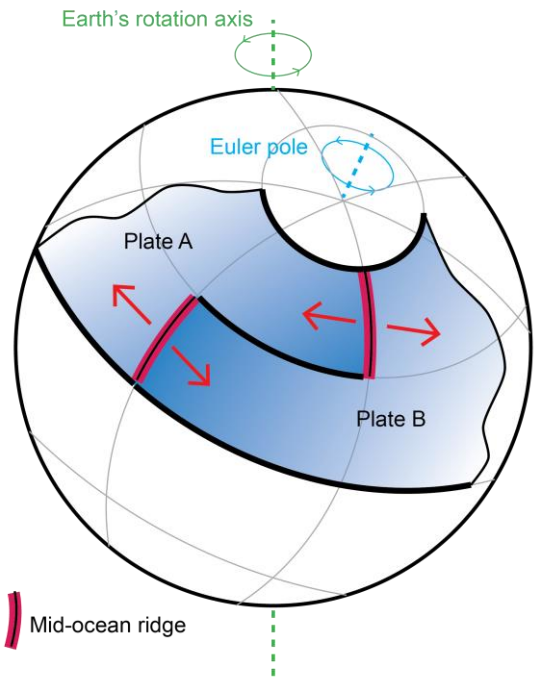

Figure 2.20 Principle of the plate tectonic where the plate motion rotates about a Euler pole. The plate tectonic theory assumes the plates are rigid and do not deform much through the process.

For this study, the magnetic map of the Knipovich Ridge and the interpretation of its seafloor spreading history were used to reconstruct the plate kinematics of the area. The plate reconstruction was carried out using the geographic information system (GIS) open-source *GPlates 2.2 software* [*Müller et al.*, 2018]. The interface allows the visualization and the manipulation of the plate tectonic reconstruction. Features are input in the software such as coastlines, plate boundaries and isochron files [*Gernigon et al.*, 2019; *Matthews et al.*, 2016]. The plate boundary and the magnetic anomaly picks defined for the Knipovich Ridge are input in the feature collection. An age is assigned to the magnetic anomaly picks estimated from the modelling performed with *MODMAG* [*Mendel et al.*, 2005]. Geometries are edited to allow the formation and cessation of the abandoned spreading ridge, west of the current Knipovich Ridge. A qualitative fitting was used to calculate the rotation pole of the magnetic isochrons.

2.5.4. Subglacial bed topography

When gravity data are acquired above a glaciated bed, the density contrast and the topography of the bedrock-ice interface contributes to the sharpest and most prominent gravity variations. A valid approach to resolve the bedrock topography is to assume a simple basement geometry, with a homogeneous density. Analogous to sedimentary basins

interpretation [*Bott*, 1960] and treating the glacier as an infinite slab, the free-air anomaly (F.A.$_c$) along a profile is reconstructed:

$$F.A._c = 2\pi G\rho_{ice}t_{ice} + 2\pi G(\rho_{bed} - \rho_{ice})T_{ice} + 2\pi G\rho_{bed}t_{bed} \tag{2.60}$$

where G is the gravitational constant (6.67 x 10^{-11} N m^2 kg^{-2}), ρ the density, t_{bed} the topography of the bed above sea-level and t_{ice} and T_{ice} the thickness of ice above sea-level and below sea-level, respectively. (t_{ice}+T_{ice}) represents the full extent of the ice thickness. The free-air anomaly is referenced to the geoid. Thus, the ice above sea-level is regarded as excess of mass while a deficiency of mass below sea-level. The influence of the ice (910 kg m^{-3}) depends on the surrounded medium, which is air (around 1 kg m^{-3}, negligible) and the bed (2670 kg m^{-3}) in this case. This reduction technique is valid under the condition that the thickness of the ice is smaller than the horizontal dimensions of the ice cap by several magnitudes.

Assuming the difference between the free-air anomaly observed (F.A.$_o$) and the free-air anomaly calculated is caused by erroneous bed topography measurements, the correction of the bed topography is:

$$\partial t_{bed} = \begin{cases} \dfrac{(F.A._o - F.A._c)}{2\pi G(\rho_{bed} - \rho_{ice})}, & \text{if the bed topography is below sea-level} \\ \dfrac{(F.A._o - F.A._c)}{2\pi G(\rho_{bed})}, & \text{if the bed topography is above sea-level} \end{cases} \tag{2.61}$$

2.5.5. Subglacial bed lithology and basal thermal regime

Gravity is sensitive to the lateral density contrast between the various geological bodies, and ice in this case. Low gravity measurements reflect low densities which is often linked to sediment accumulation or sedimentary basins. The magnetic intensity is correlated with the type and level of magnetization which in turn is mainly related to the iron content, time of formation or metamorphic processes of the minerals found in the basement. Thus, the magnetization is a strong indicator of the mineralogy of the basement and its lithology.

The physical properties of the basement rocks under the ice provide indications of the basement types for softness and erodibility and provide information about potential intrusions found under the icefield with their characteristics. Sills, granitic intrusions, and carbonate rocks can be inferred from the modelling, and their evolution set in a geo-tectonic time frame with potential field methods. Each geological body has a different impact on the thermal basal regime and the erodibility of the basement consequently can reveal accurate basal ice sliding rates.

The temperature of the ice at the base, which controls the basal thermal regime, is usually determined by ice thickness, accumulation rate (by advection), ice surface temperature, geothermal heat, and frictional heat (related to softness and topography). Irregular basal topography that can be retrieved from a combination of GPR and gravity measurement would lead to complex localized pattern of the thermal regime. The lithology identified with potentially higher radiogenic heat production can be correlated with areas of faster ice surface velocities or ice thickness variations [*Paterson and Clarke*, 1978]. Combining all these factors with the appropriate ice thickness and bed physical properties leads to more accurate basal thermal regime model and improves the understanding of melting processes. This provides important boundary conditions for e.g., ice loss modelling and climate change prediction.

2.5.6. Hydrothermal vents and resource potential assessment

Hydrothermal processes are frequent along mid-ocean ridges. The interaction of heat supplied by upwelling of magma from the mantle, and the seawater penetrating through faults and fissures in the fresh ridge-crest basalt cause hydrothermal activity. As the seawater migrates through the hot rocks, it becomes heated and produces highly chemically reactive fluids exchanging elements with the host rocks. These heated fluids are buoyant and emerge on the seafloor as hydrothermal vents. These vents discharge fluids of a wide range of properties, with temperatures up to >400°C. Acid or alkali, with higher or lower salinities than seawater, these fluids transport dissolved minerals that may precipitate on the seafloor [*Searle*, 2013]. The dissolved elements – Ca, Fe, Mn, Zn, Ni, Cu and Au – and the gases – H_2, He, CO_2 and CH_4 – have a significant impact on the chemistry balance of the ocean [*Trocine and Trefry*, 1988; *Edmond et al.*, 1979]. In large quantities, they may form mineral deposits of high economical potential.

Studies on the East Pacific Rise [*Haymon*, 1996; *Francheteau and Ballard*, 1983] suggested the magmatic budget controls the hydrothermal activity. Since then, more studies have shown a positive correlation between magma supply and the frequency of groups of vents [*Baker and German*, 2004; *German and Parson*, 1998]. The distribution of hydrothermal sites is likely primary controlled by the variability in magma supply [*Searle*, 2013].

Along mid-ocean ridges, particularly in the Arctic, the exploration of hydrothermal vents requires access to deep and remote environments. The diversity of the geological settings of the various hosting hydrothermal fields calls for a cost-effective approach to identify mineral deposit and assess their volume. The combination of magnetic and bathymetric maps establishes a correlation between bathymetric rises on the ridge crest with the magnetization of the host rock and potential ore deposit. Further magnetic mapping of the tilt derivative and vertical derivative provides an assessment of the extent and depth of the causal magnetic body. Along with petrophysical data of rock samples, 2-D forward modelling provides a visualisation of the depth extent of the causal magnetic body. Studying and categorizing the

magnetic signature of hydrothermal vents improves the overall understanding of geophysical and geochemical properties, settings, and formation of the hydrothermal vents. This leads to the development of localization and resources assessment methodologies. Evaluating the volume, the population size and the composition will also contribute to measure the impact of hydrothermal activity on the ocean chemistry balance

3. Manuscripts

New interpretation of the spreading evolution of the Knipovich Ridge derived from aeromagnetic data

M.-A. Dumais, L. Gernigon, O. Olesen, S.E. Johansen & M. Brönner

Research article published in Geophysical Journal International, 2020

My contribution to this article consisted in processing the KRAS-16 data and compiling with the adjacent data available, producing the spreading rates model, producing the plate tectonic reconstruction, and writing the manuscript. Laurent Gernigon, Odleiv Olesen, Ståle Johansen and Marco Brönner, contributed to the scientific discussions and improvement of the manuscript.

Geophysical Journal International

Geophys. J. Int. (2021) **224,** 1422–1428
Advance Access publication 2020 November 05
GJI Geodynamics and Tectonics

doi: 10.1093/gji/ggaa527

New interpretation of the spreading evolution of the Knipovich Ridge derived from aeromagnetic data

M.-A. Dumais[1,2] L. Gernigon,[1] O. Olesen,[1] S.E. Johansen[2] and M. Brönner[1]

[1]*Geological Survey of Norway,* 7040 *Trondheim, Norway. E-mail: marie-andree.dumais@ngu.no*
[2]*Department of Geoscience and Petroleum, Norwegian University of Science and Technology,* 7031 *Trondheim, Norway*

Accepted 2020 November 3. Received 2020 October 30; in original form 2020 June 9

SUMMARY

Insights into the spreading evolution of the Knipovich Ridge and development of the Fram Strait are revealed from a recent aeromagnetic survey. As an ultraslow spreading ridge in an oblique system located between the Svalbard–Barents Sea and the Northeast Greenland rifted margins, the dynamics of the Knipovich Ridge opening has long been debated. Its 90° bend with the Mohns Ridge, rare in plate tectonics, affects the evolution of the Fram Strait and motivates the study of crustal deformation with this distinctive configuration. We identified magnetic isochrons on either side of the present-day Knipovich Ridge. These magnetic observations considerably reduce the mapped extent of the oceanic domain and question the present understanding of the conjugate rifted margins. Our analysis reveals a failed spreading system before a major spreading reorganization of the Fram Strait gateway around magnetic chron C6 (circa 20 Ma).

Key words: Arctic region; Magnetic anomalies: modelling and interpretation; Mid-ocean ridge processes.

INTRODUCTION

The Fram Strait is a key region for the understanding of the rift-to-drift evolution between the Northeast Greenland and Svalbard–Barents Sea rifted margins. Linking the Atlantic and Arctic spreading systems, the Knipovich Ridge (KnR) initiated following the complete cessation of the Mid-Labrador Ridge spreading in the Early Oligocene (33.7 Ma, C13; Engen *et al.* 2008; Oakey & Chalmers 2012; Hosseinpour *et al.* 2013; Suckro *et al.* 2013) and the diachronous initiation of the Reykjanes, Ægir and Mohns ridges in the Early Eocene (54 Ma, C24r; Talwani & Eldholm 1977; Gaina *et al.* 2009; Gernigon *et al.* 2019). For decades, the structure and evolution of the Fram Strait have been debated due to the scarce data availability in this remote area. In this study, the Fram Strait evolution is interpreted from new state-of-the-art aeromagnetic data, acquired by the Geological Survey of Norway. We revise models for the spreading evolution of the KnR, clearly identify a ridge jump explaining the asymmetric magnetic signature of the ridge and question the present understanding of the Boreas Basin.

Classified as an ultraslow oblique spreading system (with spreading rates of less than 20 mm yr^{-1}), KnR comprises the Arctic Mid-Ocean Ridge system delimited by the Mohns Ridge (MR; ∼73°50′N) and the Molloy Transform Zone (MTZ; ∼78°30′N) between the Greenland Sea and the Barents Sea realms (Fig. 1). It is surrounded by the Vestbakken Volcanic Province (VVP) and the Hornsund Fault Complex Zone (HFZ) to the east, and by the Boreas and East Greenland basins to the west. At present day, the KnR trend changes from NNW–SSE in the south to N–S in the north, with a 130 km wide escarpment and thick piles of sedimentary rocks along the Svalbard margin (Engen *et al.* 2008). The Fram Strait development initiated after a Late Cretaceous-Eocene rifting event between the Barents Sea and Northeast Greenland. It forms a complex system of conjugate shear margins characterized by distinct crustal, structural and magmatic properties (Faleide *et al.* 2008). During the Palaeocene–Eocene, the oblique rifted margins underwent a brief period of compression leading to the Eurekan–Spitsbergen fold and thrust belts (Piepjohn *et al.* 2016). Northwards, KnR is linked through the MTZ to the Gakkel Ridge (GaR; Glebovsky *et al.* 2006). The Hovgaard Ridge and the East Greenland Ridge, along the Greenland Fracture Zone (GFZ), may include continental fragments preserved within the oceanic domain (Nemčok *et al.* 2016).

In the Norwegian–Greenland Sea, the breakup occurred around 53.9–57.1 Ma (C24r) and propagated progressively to the south towards the juvenile volcanic margins during the Early Eocene (Gernigon *et al.* 2019). After the extinction of the Mid-Labrador Ridge (Labrador Sea) around 33 Ma (C13), the azimuth of the relative motion between Norway and Greenland underwent a counterclockwise rotation from NNW–SSE to WNW–ESE (31–28 Ma, C12-10; Gaina *et al.* 2009). From this reorganization, the ultraslow spreading Ægir Ridge became extinct around C10, subsequently causing the development of the Kolbeinsey Ridge (KoR) and

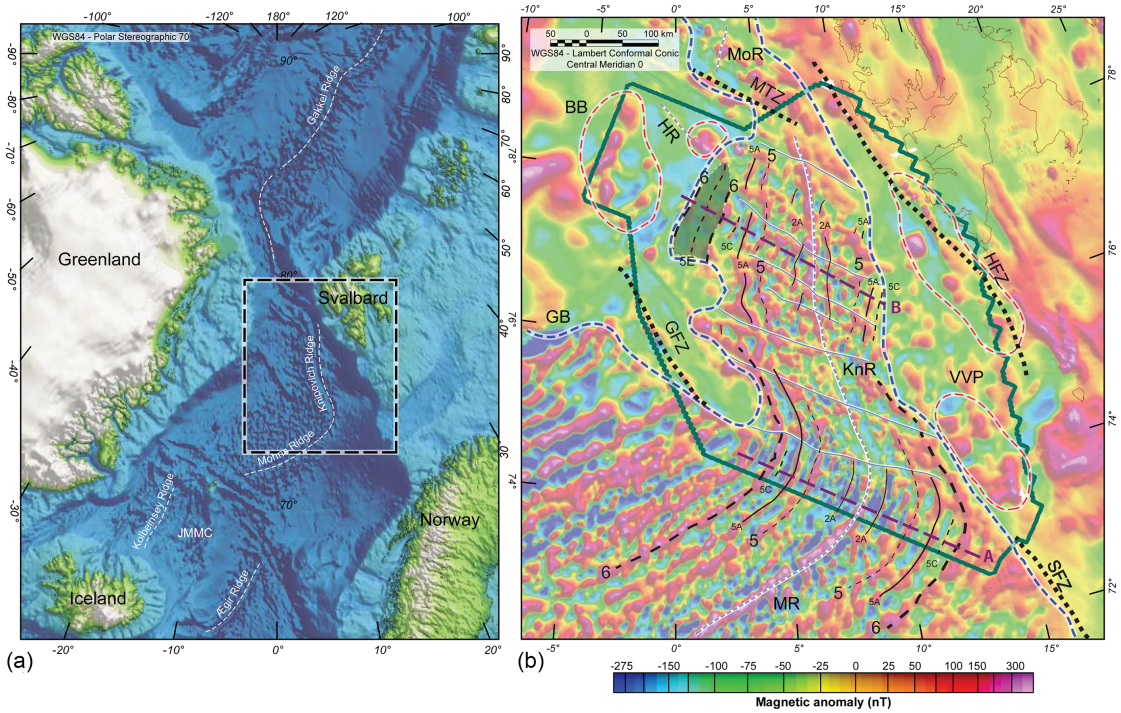

Figure 1. Survey area and aeromagnetic data. (a) Location of the Knipovich Ridge with respect to the North Atlantic realms with SRTM topographic data (Becker *et al.* 2009). (b) The new aeromagnetic data revealed the timing of the breakup (C6) and magmatic events on the eastern side of the ridge. Profiles A and B are in purple. MoR: Molloy Ridge; MTZ: Molloy Transform Zone; HR: Hovgaard Ridge; BB: Boreas Basin; HFZ: Hornsund Fracture Zone; KnR: Knipovich Ridge; GFZ: Greenland Fracture Zone; GB: Greenland Basin; JMMC: Jan Mayen Microplate Complex; VVP: Vestbakken Volcanic Province; MR: Mohns Ridge; SFZ: Senja Fracture Zone. New oceanic fracture zones are displayed with grey lines, new COB demarcation is in dashed blue line and volcanic areas are delimited by the dashed red lines. The abandoned ridge is highlighted in grey shading.

leading to the formation of the Jan Mayen Microplate Complex at ~24 Ma (C7-6; Blischke *et al.* 2017). To the north, the GaR was initiated at 58–59 Ma (C26n-25r) followed by a spreading rate decrease from C13 (Schreider *et al.* 2019). A 250-km long section of the GaR, north of Svalbard, ending in the Fram Strait, opened much later between C8 and C5 (Glebovsky *et al.* 2006). Similarly, the Molloy Ridge spreading was initiated in the Early Miocene (20 Ma; Srivastava & Tapscott 1986). Earlier studies set the KnR opening at C13 (~33 Ma; Talwani & Eldholm 1977), between C23 and C13 (Faleide *et al.* 2008) or between C24 and C13 (Nemčok *et al.* 2016). Our new interpretation of the magnetic isochrons significantly changes the time of the KnR spreading initiation and consequently the location of the continent–ocean boundary (COB) compared to previous studies.

DATA

Aeromagnetic survey

The aeromagnetic data were acquired in the summers of 2016 and 2018 during a period of moderate to low diurnal magnetic activity (Novatem 2018; Dumais *et al.* 2020). Located at high latitude, the survey area is particularly sensitive to diurnal noise. Magnetic base station recordings from five locations provided by the Tromsø Geophysical Observatory and the Technical University of Denmark were used, ensuring high confidence of the data set. Flown at the low altitude of 120 m, with flight lines oriented at 121–301° from N and with a 5500 m line spacing, the data were corrected for the 12th IGRF Field (Thébault *et al.* 2015) and standard levelling using the adjustment of the line intersections (Whitham & Niblett 1961; Reford & Sumner 1964; Nabighian *et al.* 2005) was applied. The lines were designed perpendicular to the ridge axis and the expected spreading anomalies, optimizing the identification of magnetic isochrons. The compilation was completed with existing data from the surrounding areas: GaR, Boreas Basin, Barents Sea and Svalbard (Jokat *et al.* 2008; Olesen *et al.* 2010; Jokat *et al.* 2016).

METHODS

Spreading rate model

ModMag (Mendel *et al.* 2005) was used to map the spreading on profiles A and B (Fig. 2), chosen for their complete signature of the spreading. Profile A was tested for an upper crust of a constant 1 km thickness (Johansen *et al.* 2019), representative of the basalt layer 2A (Fig. 2a), allowing a good agreement between the modelled and observed anomalies. Since the magnetic signature is continuous from MR to KnR at the bend, initial identification of the

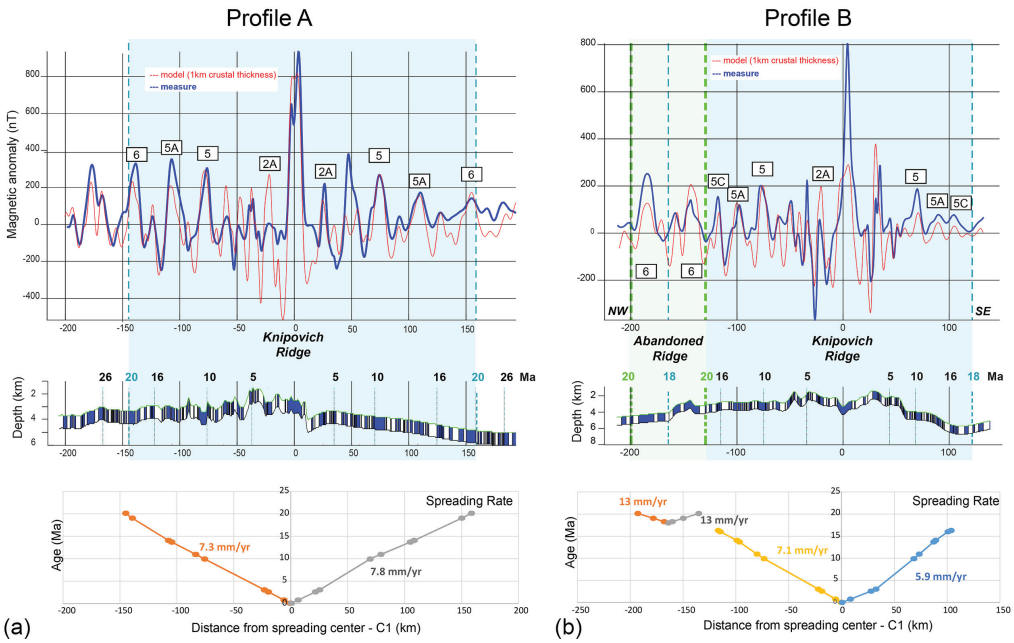

Figure 2. Spreading models (profiles A and B, as identified in Fig. 1) for an upper crust of 1 km. The spreading is faster towards west on profile B while slightly faster towards east on profile A. The presence of an abandoned ridge at C5E-C5C (18 Ma) explains the strong asymmetry of profile B.

magnetic isochrons were derived from the MR interpretation (Vogt *et al.* 1986; Engen *et al.* 2008) to model Profile A consistently. All parameters were adjusted by iteration to fit the observed data. To ensure a data fit with the model and account for the burial of the source layer, a sediment thickness was estimated from Engen *et al.* (2006).

Plate reconstruction

The plate reconstruction was carried out with *GPlates 2.2* (Müller *et al.* 2018), allowing the visualization and the manipulation of the plate-tectonic reconstruction using available refined plate boundaries and isochron layers (Matthews *et al.* 2016; Gernigon *et al.* 2019). The new magnetic isochrons were defined with the magnetic gridded data and their respective age were identified from the spreading rate model results along profiles A and B. Geometries were edited in accordance with the magnetic interpretation.

RESULTS

Oceanic domain of the Fram Strait

The new aeromagnetic data reflect the complexity of the Fram Strait development and the oblique character of the KnR. Spatial analysis of patterns in the frequency content of the data reveals the crustal affinities and demarks various crustal domains (Fig. 1). Areas displaying high-frequency striped magnetic anomalies delineate the oceanic domain, characterized by magnetized basalt and magnetic isochrons correlated to the chronostratigraphic chart of Ogg (2012). Magnetic isochron C6 is assigned to the first unambiguous striped anomaly. C5A, C5 and C1 are also assigned as they extend continuously from the MR to the KnR. Modelling of the high-frequency magnetic isochrons with 1 km upper crustal thickness replicates the magnetic signature with high confidence and gives new insights in the spreading history. The data set captures previously unresolved magnetic isochrons, for example, C2A, facilitating a more detailed and better constrained plate reconstruction. These also characterize the oceanic domain, where C6 demarks the first unambiguous magnetic isochron and revises the location of the expected COB landwards of C6. Unlike its adjacent ridges, MR and GaR, the KnR magnetic signature suggests the presence of several asymmetrical discontinuous spreading segments (Fig. 1). Not previously observed on bathymetric data, new oceanic transfer faults between these segments are delineated, running parallel to the GFZ and the MTZ but perpendicular to the spreading anomalies.

Rifted margin, transitional domain and continental fragments

Outside the oceanic domain, the magnetic signature mainly contains intermediate-to-long wavelength anomalies without evidence of any magnetic isochrons, which is characteristic of continental or transitional crustal domains. Intermediate-size round anomalies (20–50 km diameter) found in the VVP and along the HFZ most likely express the volcanism of the Svalbard margin. On the Greenland margins, intermediate-frequency magnetic anomalies are observed along the GFZ, MTZ and the Hovgaard Ridge (Fig. 1). The new location of the COB extends the continental domain towards the

Hovgaard and East Greenland Ridges. It also envelopes the Boreas Basin which mainly shows characteristics of a continental domain. These continental fragments appear strongly linked to the continent without indications of strong discontinuities.

Spreading rates and instability: evidence of a failed spreading system

With the magnetic data, the oceanic fracture zones are clearly delineated, highlighting the segmented nature of the spreading system. Furthermore, some of these segments exhibit evidence for strong asymmetrical spreading, while others show small amplitudes and poor magnetization (Fig. 1b), which underlines the complexity and heterogeneity of this ultraslow spreading system in a sheared setting. The bathymetric data indicate that the strike of the KnR varies from 347°, at the junction with MR, to 002°, at the MTZ junction (Curewitz *et al.* 2010). On the magnetic data, the direction of the visible spreading anomalies is 300° (Fig. 1). Given the orientation of plate motion and the large rotation in the ridge-crest strike through the study area, the obliquity varies from ∼45°, at MR, to ∼30°, at MTZ. The thick sedimentary cover of the Barents Sea fan (Engen *et al.* 2006) on the eastern flank of KnR means that the magnetic sources in the crust are further away from the magnetic measurements. This causes the presence of wider anomalies compared to their conjugate. According to the model, the extent of the spreading anomalies remains slightly asymmetric, implying the spreading evolution with moderately faster rates towards east at the bend connecting MR and KnR (Fig. 2). Between profile A and B, the spreading rates decrease east of KnR, while they appear to keep similar rates on the west side (Fig. 2b). Thus, around N76°, the asymmetry reverses, and the western oceanic domain becomes apparently larger.

Consequently, the segment between N76° and N78° reveals a pronounced asymmetry with a broader extent of the oceanic domain west of the present-day KnR (Fig. 2). The new magnetic data indicate the presence of an atypical and failed spreading system, immediately west of the current ridge and east of the continental Boreas Basin, explaining the evident asymmetry of the spreading. The abandoned ridge model is favoured over a model with one single highly asymmetric system. The latter model would require much faster spreading towards the west, an unequal number of magnetic isochrons on either side of the ridge and very different spreading rates from north to south. While sedimentary cover prevails the direct observation of a ridge-typical bathymetric depression, both, top basement interpretation from seismic data (Hermann & Jokat 2013) and the new magnetic data underline the high potential for the existence of an abandoned rift valley. Thus, the failed spreading system with a ridge jump hypothesis was tested along profile B located in the most asymmetric segment of the KnR. The final model presents slower spreading rates particularly towards the east and confirms the presence of an atypical oceanic domain initiated at C6. In addition, it suggests a ridge jump between C5E and C5C, required to explain this asymmetry (Figs 1 and 2).

Reconstruction of the Fram Strait

In our reconstruction of the Fram Strait (Figs 1–3), the spreading initiated at C6 (20 Ma). Around 18 Ma (C5E-C5C), the section between N77° and N78° was abandoned and migrated to the east where the spreading continued, forming today's KnR (Fig. 4). Within this new section, the spreading becomes faster towards the Boreas Basin. Between N75° and N76°, the striped anomalies disappear ridgewards of C5 (10 Ma), implying relatively weak magnetization of the crust, which needs further investigation. The segment linking the MTZ shows a magnetic isochron corresponding to C1, with no further striped anomalies parallel to it, suggesting an opening more recent than C2A. Seafloor spreading anomalies allow us to delineate discrete corridors with contrasting histories of spreading rate variation and asymmetry, caused by ridge abandonment and migration episodes. The edges of these corridors appear to be marked by oceanic fracture zones.

DISCUSSION

Our results demark the much-debated COB in the North Atlantic and Arctic Oceans and in the Fram Strait in particular (Breivik *et al.* 1999; Voss & Jokat 2007; Faleide *et al.* 2008; Gernigon *et al.* 2019), and confirm the opening of the KnR initiated at 20 Ma (C6) where the first unambiguous magnetic anomaly appears. The KnR lies oblique to the MR and developed after the opening of the Norwegian–Greenland Sea and the Eurasian Basin which had already initiated in the Early Eocene (Brozena *et al.* 2003) and after the complete extinction of the Mid-Labrador Ridge at C13 (Gaina *et al.* 2009; Oakey & Chalmers 2012; Hosseinpour *et al.* 2013; Suckro *et al.* 2013). This coincides with the opening of the Molloy Ridge (20 Ma; Trulsvik *et al.* 2011) and KoR (C7-6; Blischke *et al.* 2017), and the GaR penetrating in the Fram Strait (C8-5; Glebovsky *et al.* 2006).

East of KnR, the new COB is closer to the ridge by up to 150 km compared to the previous interpretations (Breivik *et al.* 1999). The oceanic crust, enclosed by magnetic isochrons C6, is relatively thin, up to 5 km (Johansen *et al.* 2019), and characterized by remanently magnetized basalts. The crustal sections between magnetic isochrons C6 and the rifted margins, on either side of the KnR, are representative of a stretched continental crust due to the apparent absence of striped magnetic anomalies associated with an authentic oceanic crust. The presence of rounded, intermediate-size magnetic anomalies suggests the occurrence of intrusive magmatic bodies in this area. Therefore, we postulate the presence of an exhumed and intruded lower continental crust before the development of an oceanic accretion in the Fram Strait (Fig. 4). Along the West Barents Sea margin, magmatic intrusions were likely emplaced in two phases in the VVP, estimated at 35 Ma from seismic observations (Faleide *et al.* 2008) and 5 Ma from borehole age dating (Mørk & Duncan 1993). On either side of the ridge, the basement shares affinities despite magmatism being mostly constrained to the West Barents shear margin. Magmatism may have occurred before and after the KnR initiation (Fig. 1). Recent studies have shown the possibility for intruded lower continental crust to flow laterally before the establishment of steady-state oceanic crust (Foulger *et al.* 2019; Guan *et al.* 2019; Bécel *et al.* 2020; Yuan *et al.* 2020). The intermediate-to-long wavelength magnetic anomalies observed continent-ward of C6 may represent a similar intruded lower crust instead of an oceanic crust. This interpretation challenges previous interpretations of the nature and lateral extent of the conjugate margins. Further investigation is required to fully understand the tectonic processes by acquiring additional seismic data covering the different crustal domains, revisiting the existing seismic interpretation of the area, and developing a thermal model of the mantle.

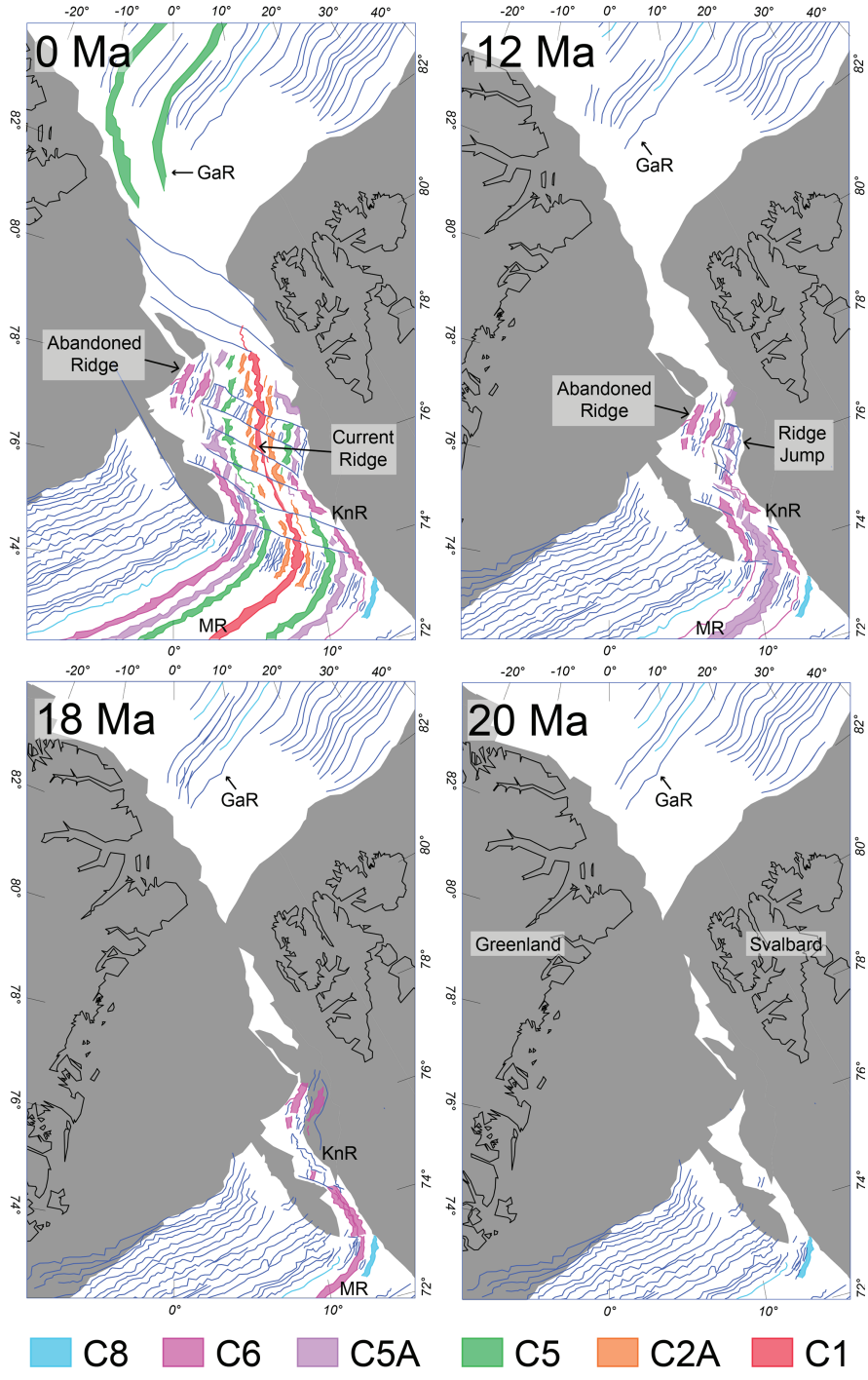

Figure 3. Reconstruction of the opening of the KnR. The ridge in the Boreas Basin is abandoned at 18 Ma and jumped eastwards towards Svalbard (GaR: Gakkel Ridge; KnR: Knipovich Ridge; MR: Mohns Ridge). Oceanic fracture zones, lineaments and magnetic isochrons are shown in blue. The plate boundary and magnetic isochron layers displayed along the KnR have been extracted from the new data set. The topography, plate boundary and magnetic isochron layers outside the KnR uses previous studies (Amante & Eakins 2009; Matthews *et al.* 2016; Gernigon *et al.* 2019).

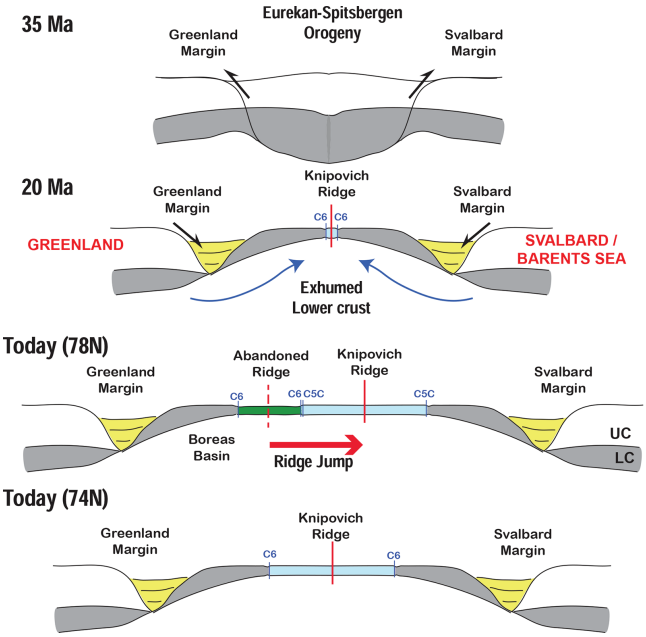

Chron	Age (Ma)	Event	References
	55-35	Eurekan-Spitsbergen orogeny	
13	36	Labrador ridge cessation	Engen et al., 2008 Oakey & Chalmers, 2012 Suckro et al., 2013
	35	VVP magnetic intrusion	Faleide at al., 2008
8-5		GaR opening in the Fram Strait	Glebovsky et al. 2006
7-6	24	KoR opening	Blischke et al., 2017
6	20	KnR opening	This study
5C-5E	18	Ridge migration to the east	This study
	10-15	Svalbard margin formation	
	5	VVP magnetic intrusion	Mørk & Duncan, 1993
	0-20	Svalbard undergoes erosion	

Figure 4. Schematic of the opening of the KnR. At 78°N, the ridge in the Boreas Basin is abandoned and jumped eastwards to become present-day Knipovich Ridge. At 74°N, the ridge has continuously opened since breakup around 20 Ma. UC: Upper crust; LC: Lower crust.

CONCLUSION

Our aeromagnetic data shed light on the development and crustal deformation to the rare configuration of two ultraslow spreading segments of the NE Atlantic spreading system intersecting at a 90° angle:

(1) Despite this 90° bend between the MR and the KnR, the opening at the southern section of the KnR is continuous from the Monhs Ridge, underlining the eminent transtensional plate motion in the high Arctic.

(2) Our study sets the KnR opening at 20 Ma and suggests the presence of numerous oceanic fracture zones and a broad continent–ocean transition interpreted as exhumed lower continental material.

(3) The presence of a failed oceanic basin east of the Boreas Basin with a thin crust explains the peculiar strong asymmetry of the spreading system. Consequently, a ridge jump is inferred in the Fram Strait around 18 Ma.

(4) The KnR opening occurred shortly after of the Kolbeinsey Ridge opening and Gakkel Ridge prolongation. It may indicate a common link of mid-Atlantic ridge segments allowing a synchronous initiation of breakup at several locations of the North Atlantic–Arctic realm.

ACKNOWLEDGEMENTS

We are thankful to the EPOS-Norway (EPOS-N) Project funded by the Research Council of Norway (Project no. 245763), the Norwegian Petroleum Directorate and the Geological Survey of Norway to help funding the project. We thank Novatem, Inc. for the data acquisition, and our colleagues from AWI (Wilfried Jokat) and TGS (Reidun Myklebust) for providing aeromagnetic data from adjacent areas. The new aeromagnetic data are available on NGU Geoscience Data Service repository (https://geo.ngu.no/geoscienceportalopen) and on EPOS-N Portal (https://epos-no.uib.no:444/#/view/project). We thank Richard Saltus, Graeme Eagles and editor Joerg Renner for their insightful comments on the manuscript.

REFERENCES

Amante, C. & Eakins, B.W., 2009. ETOPO1 arc-minute global relief model: procedures, data sources and analysis. NOAA Technical Memorandum NESDIS NGDC-24, *National Geophysical Data Center, NOAA,* **10,** V5C8276M.

Bécel, A., Davis, J.K., Shuck, B.D., Van Avendonk, H.J.A. & Gibson, J.C., 2020. Evidence for a prolonged continental breakup resulting from slow extension rates at the Eastern North American Volcanic Rifted Margin, *J. geophys. Res.,* **125,** e2020JB020093, doi:10.1029/2020jb020093.

Becker, J.J. *et al.*, 2009. Global bathymetry and elevation data at 30 Arc seconds resolution: SRTM30_PLUS, *Mar. Geod.,* **32,** 355–371.

Blischke, A., Gaina, C., Hopper, J.R., Péron-Pinvidic, G., Brandsdóttir, B., Guarnieri, P., Erlendsson, Ö. & Gunnarsson, K., 2017. The Jan Mayen microcontinent: an update of its architecture, structural development and role during the transition from the Ægir Ridge to the mid-oceanic Kolbeinsey Ridge, *Geol. Soc., London, Spec. Publ.,* **447,** 299–337.

Breivik, A.J., Verhoef, J. & Faleide, J.I., 1999. Effect of thermal contrasts on gravity modeling at passive margins: results from the western Barents Sea, *J. geophys. Res.,* **104,** 15 293–15 311.

Brozena, J.M., Childers, V.A., Lawver, L.A., Gahagan, L.M., Forsberg, R., Faleide, J.I. & Eldholm, O., 2003. New aerogeophysical study of the Eurasia Basin and Lomonosov Ridge: implications for basin development, *Geology,* **31,** 825.

Curewitz, D., Okino, K., Asada, M., Baranov, B., Gusev, E. & Tamaki, K., 2010. Structural analysis of fault populations along the oblique, ultra-slow spreading Knipovich Ridge, North Atlantic Ocean, 74°30′N-77°50′N, *J. Struct. Geol.,* **32,** 727–740.

Dumais, M.A., Olesen, O., Gernigon, L., Brönner, M., Lim, A. & Johansen, S.E., 2020. Knipovich Ridge Aeromagnetic Survey 2016: processing and interpretation, NGU-rapport 2020.030.

Engen, Ø., Faleide, J.I. & Dyreng, T.K., 2008. Opening of the Fram Strait gateway: a review of plate tectonic constraints, *Tectonophysics,* **450,** 51–69.

Engen, Ø., Frazer, L.N., Wessel, P. & Faleide, J.I., 2006. Prediction of sediment thickness in the Norwegian-Greenland Sea from gravity inversion, *J. geophys. Res.,* **111,** B11403, doi:10.1029/2005JB003924.

Faleide, J.I., Tsikalas, F., Breivik, A., Mjelde, R., Ritzmann, O., Engen, Ø., Wilson, J. & Eldholm, O., 2008. Structure and evolution of the continental margin off Norway and Barents Sea, *Episodes,* **31,** 82–91.

Foulger, G.R. *et al.*, 2019. The Iceland Microcontinent and a continental Greenland-Iceland-Faroe Ridge, *Earth Sci. Rev.,* 102926, doi:10.1016/j.earscirev.2019.102926.

Gaina, C., Gernigon, L. & Ball, P., 2009. Palaeocene—recent plate boundaries in the NE Atlantic and the formation of the Jan Mayen microcontinent, *J. Geol. Soc.,* **166,** 601–616.

Gernigon, L., Franke, D., Geoffroy, L., Schiffer, C., Foulger, G.R. & Stoker, M., 2019. Crustal fragmentation, magmatism, and the diachronous opening of the Norwegian-Greenland Sea, *Earth Sci. Rev.,* doi:10.1016/j.earscirev.2019.04.011.

Glebovsky, V.Y., Kaminsky, V.D., Minakov, A.N., Merkur'ev, S.A., Childers, V.A. & Brozena, J.M., 2006. Formation of the Eurasia Basin in the Arctic Ocean as inferred from geohistorical analysis of the anomalous magnetic field, *Geotectonics,* **40,** 263–281.

Guan, H., Geoffroy, L., Gernigon, L., Chauvet, F., Grigné, C. & Werner, P., 2019. Magmatic ocean–continent transitions, *Mar. Pet. Geol.,* **104,** 438–450.

Hermann, T. & Jokat, W., 2013. Crustal structures of the Boreas Basin and the Knipovich Ridge, North Atlantic, *Geophys. J. Int.,* **193,** 1399–1414.

Hosseinpour, M., R.D., M., Williams, S.E. & Whittaker, J.M., 2013. Full-fit reconstruction of the Labrador Sea and Baffin Bay, *Solid Earth,* **4,** 461–479.

Johansen, S.E., Panzner, M., Mittet, R., Amundsen, H.E.F., Lim, A., Vik, E., Landrø, M. & Arntsen, B., 2019. Deep electrical imaging of the ultraslow-spreading Mohns Ridge, *Nature,* **567,** 379–383.

Jokat, W., Geissler, W. & Voss, M., 2008. Basement structure of the north-western Yermak Plateau, *Geophys. Res. Lett.,* **35,** doi:10.1029/2007gl032892.

Jokat, W., Lehmann, P., Damaske, D. & Bradley Nelson, J., 2016. Magnetic signature of North-East Greenland, the Morris Jesup Rise, the Yermak Plateau, the central Fram Strait: constraints for the rift/drift history between Greenland and Svalbard since the Eocene, *Tectonophysics,* **691,** 98–109.

Matthews, K.J., Maloney, K.T., Zahirovic, S., Williams, S.E., Seton, M. & Müller, R.D., 2016. Global plate boundary evolution and kinematics since the late Paleozoic, *Glob. Planet. Change,* **146,** 226–250.

Mendel, V., Munschy, M. & Sauter, D., 2005. MODMAG, a MATLAB program to model marine magnetic anomalies, *Comput. Geosci.,* **31,** 589–597.

Mørk, M.B.E. & Duncan, R.A., 1993. Late Pliocene basaltic volcanism on the Western Barents Shelf margin: implications from petrology and ^{40}Ar-^{39}Ar dating of volcaniclastic debris from a shallow drill core, *Nor. Geol. Tidsskr.,* **73,** I993.

Müller, R.D. *et al.*, 2018. GPlates: building a virtual earth through deep time, *Geochem. Geophys. Geosyst.,* **19,** 2243–2261.

Nabighian, M.N., Grauch, V.J.S., Hansen, R.O., LaFehr, T.R., Li, Y., Peirce, J.W., Phillips, J.D. & Ruder, M.E., 2005. The historical development of the magnetic method in exploration, *Geophysics,* **70,** 33ND–61ND.

Nemčok, M., Sinha, S.T., Doré, A.G., Lundin, E.R., Mascle, J. & Rybár, S., 2016. Mechanisms of microcontinent release associated with wrenching-involved continental break-up; a review, *Geol. Soc., London, Spec. Publ.,* **431,** 323, doi:10.1144/sp431.14.

Novatem, 2018, Knipovich Ridge airborne survey 2016 (KRAS-16)—Technical Report, 32pp.

Oakey, G.N. & Chalmers, J.A., 2012. A new model for the Paleogene motion of Greenland relative to North America: plate reconstructions of the Davis Strait and Nares Strait regions between Canada and Greenland, *J. geophys. Res.,* **117,** doi:10.1029/2011jb008942.

Ogg, J.G., 2012. Geomagnetic polarity time scale, in *The Geologic Time Scale,* pp. 85–113, eds Gradstein, F.M., Ogg, J.G., Schmitz, M.D. & Ogg, G.M., Elsevier, doi:10.1016/b978-0-444-59425-9.00005-6.

Olesen, O. *et al.*, 2010. New aeromagnetic and gravity compilations from Norway and adjacent areas: methods and applications, *Geol. Soc., London, Pet. Geol. Conf. Ser.,* **7,** 559–586.

Piepjohn, K., von Gosen, W. & Tessensohn, F., 2016. The Eurekan deformation in the Arctic: an outline, *J. Geol. Soc.,* **173,** 1007–1024.

Reford, M.S. & Sumner, J.S., 1964. Aeromagnetics, *Geophysics,* **29,** 482–516.

Schreider, A.A., Schreider, A., Sazhneva, A., Kluev, M. & Brehovskih, A., 2019. Kinematic model of development of eastern areas of the Gakkel Mid-Ocean Ridge in the Eurasian Basin of the Arctic Ocean, *Oceanology,* **59,** 133–142.

Srivastava, S.P. & Tapscott, C.R., 1986. Plate kinematics of the North Atlantic, in *The Western North Atlantic Region,* eds Vogt, P.R. & Tucholke, B.E., Geological Society of America.

Suckro, S.K., Gohl, K., Funck, T., Heyde, I., Schreckenberger, B., Gerlings, J. & Damm, V., 2013. The Davis Strait crust—a transform margin between two oceanic basins, *Geophys. J. Int.,* **193,** 78–97.

Talwani, M. & Eldholm, O., 1977. Evolution of the Norwegian–Greenland Sea, *Bull. geol. Soc. Am.,* **88,** 969–999.

Thébault, E. *et al.*, 2015. International geomagnetic reference field: the 12th generation, *Earth Planets Space,* **67,** doi:10.1186/s40623-015-0228-9.

Trulsvik, M., Myklebust, R., Polteau, S. & Planke, S., 2011. *Geophysical Atlas of the East Greenland Basin: Integrated Seismic, Gravity and Magnetic Interpretation,* Volcanic Basin Petroleum Research AS, TGS-NOPEC Geophysical Company.

Vogt, P.R., Fruik, C., Jewett, I., Klitgord, K., Vink, G. & Duncan, R., 1986. *Magnetic anomalies of the North Atlantic Ocean,* Geological Society of America.

Voss, M. & Jokat, W., 2007. Continent–ocean transition and voluminous magmatic underplating derived from *P*-wave velocity modelling of the East Greenland continental margin, *Geophys. J. Int.,* **170,** 580–604.

Whitham, K. & Niblett, E.R., 1961. The diurnal problem in aeromagnetic surveying in Canada, *Geophysics,* **26,** 211–228.

Yuan, X., Korenaga, J., Holbrook, W.S. & Kelemen, P.B., 2020. Crustal structure of the Greenland–Iceland ridge from joint refraction and reflection seismic tomography, *J. geophys. Res.,* **125,** e2020JB019847, doi:10.1029/2020jb019847.

Crustal and thermal heterogeneities across the Fram Strait and the Svalbard Margin

M.-A. Dumais, L. Gernigon, O. Olesen, A. Lim, S.E. Johansen & M. Brönner

Research article to be submitted

My contribution to this article consisted in producing the 2-D forward models, calculating the Bouguer gravity anomaly, producing the Curie Depth grid, producing the 3-D magnetization inversion model, and writing the manuscript. Anna Lim contributed to the 2-D forward magnetic model of the EM profile. Laurent Gernigon, Odleiv Olesen, Ståle Johansen and Marco Brönner, contributed to the scientific discussions and improvement of the manuscript

Crustal and Thermal Heterogeneities across the Fram Strait and the Svalbard Margin

M.-A. Dumais[1,2], L. Gernigon[2], O. Olesen[2], A. Lim[1], S.E. Johansen[1], and M. Brönner[2]

[1]Department of Geoscience and Petroleum, Norwegian University of Science and Technology

[2]Geological Survey of Norway

Corresponding author: Marie-Andrée Dumais (marie-andree.dumais@ngu.no)

Key Points:

- Potential field 2-D forward models delineate thecrustal domains and unify the seismic interpretations
- Magnetization in the oceanic domain is linked to the presence of volcanoes and bathymetric highs in the rift valley of the Knipovich Ridge
- A wide transition lithospheric domain is delineated likely comprising an exhumed lower crust or mantle

Abstract

The crustal and lithospheric structure of the Fram Strait and the transition from the Knipovich Ridge to the Barents Sea shelf and Svalbard is still poorly understood. Several multi-geophysical investigations from various campaigns since the 90s along the western Barents Sea margin and the Northeast Greenland margin resulted in insuffient and contradicting interpretations of the crustal and upper mantle settings in the oceanic and continental domains. New airborne magnetic data across the Knipovich Ridge and west of Svalbard provide new insights, reveal the complexity of the seafloor spreading history of the Arctic Atlantic Ocean and indicate a European-Eurasian continent-ocean boundary located c. 150 km farther west than previously suggested. This new location of the continent-ocean boundary derived from the aeromagnetic data prompted to revise the existing 2-D seismic interpretations in terms of crustal domains and tectono-stratigraphic setting. This is tested using joint 2-D gravity and magnetic field modelling to derive an improved crust-mantle model of the study area to better understand the development of this key area in the High Arctic. One recently acquired combined 2-D controlled Source Electromagnetic / magneto-telluric profile across the Mohn's Ridge was also modeled with potential field data and provided new insights in the tectonic settings of the crust and the mantle thermal anomalies. This study proposes to unify the various seismic and Controlled Source Electromagnetic / magneto-telluric interpretations using the new aeromagnetic compilation.

Plain Language Summary

The opening of the Fram Strait between Svalbard and Greenland is still poorly understood. Studying the seafloor spreading of the Knipovich Ridge is central to understand the development history of this key area located between the Northeast Atlantic and Arctic oceans. New high-resolution magnetic data flown above the sea reveal the complexity of the seafloor spreading history of the area. The extent of the seafloor spreading is smaller than previously suggested. The new airborne magnetic data are modeled and tested to derive an improved crust-mantle model to better understand the development of this key area in the High Arctic.

1 Introduction

The Fram Strait and Svalbard are important regions to understand the geological development of the entire High Arctic. Tectonic issues such as the extent and timing of the Eurekan orogeny (Piepjohn et al., 2016) and the spreading development of the Knipovich Ridge remain problematic and questionable. The timing of the Knipovich Ridge initiation and the location of the continent-ocean boundary (COB) have been debated for decades leading to various interpretations (Breivik et al., 1999; Dumais et al., 2020a; Engen et al., 2008; Engen et al., 2006; Faleide et al., 1991; Franke et al., 2019; Gernigon et al., 2019; Libak et al., 2012; Lundin & Doré, 2011; Mosar et al., 2002; Scott, 2000; Seton et al., 2012; Vorren et al., 1991; Voss & Jokat, 2007), see review by Eagles (2015). Little geological, geochemical, and geophysical data have been available, compared to other areas in the North Atlantic, due to the remoteness of the area to constrain those models. Aeromagnetic data were acquired four decades ago above the Knipovich Ridge, with a large gap remaining at the Svalbard margin and the western Barents Sea margin (Olesen et al., 2010) (Fig.1b, Table 1), hampering an adequate crustal characterization of the area to further constrain the interpretation along existing regional 2-D seismic profiles. However, various crustal domains have been previously derived from regional gravity data and a few 2-D seismic data, e.g. Breivik (Breivik et al., 2003, 2005; 1999), Czuba (2005), Libak (2012). Ocean bottom seismic (OBS) data have been acquired in the Fram Strait across the Knipovich Ridge and through the continental domain of the Barents Sea and the Svalbard Platform (Table 2). These data offer a constraint on the crustal

geometry and expected lithology as seismic data are sensitive to the acoustic impedance contrast between the various lithologies and the associated densities. Controlled Source Electromagnetic / magneto-telluric (CSEM/MT) data have also assessed the crustal thickness, crustal resistivity and estimated the temperature of the mantle across the Knipovich Ridge (Johansen et al., 2019).

Recently acquired by the Geological Survey of Norway (NGU), aeromagnetic data in the Fram Strait area analysed together with available regional gravity data, seismic and CSEM/MT allow us to initiate an integrated interpretation of the study area (Fig. 1). The magnetic field variations derived from the aeromagnetic data provide indications about the crustal and thermal properties of the area (e.g. Curie point depth estimation (Ebbing et al., 2009). In this study, new geophysical data are interpreted to obtain an improved crust-mantle model to better understand the development of this key area in the Arctic. The new interpretation of the COB changes the estimate of the timing of the continental break-up and the current understanding of the tectonic development of the area (Dumais et al., 2020a). This study investigates the structural settings of the crust in the Fram Strait and its lithological heterogeneities from the oceanic domain at the Knipovich Ridge to the continental domain on the Svalbard Margin and Barents Sea margins.

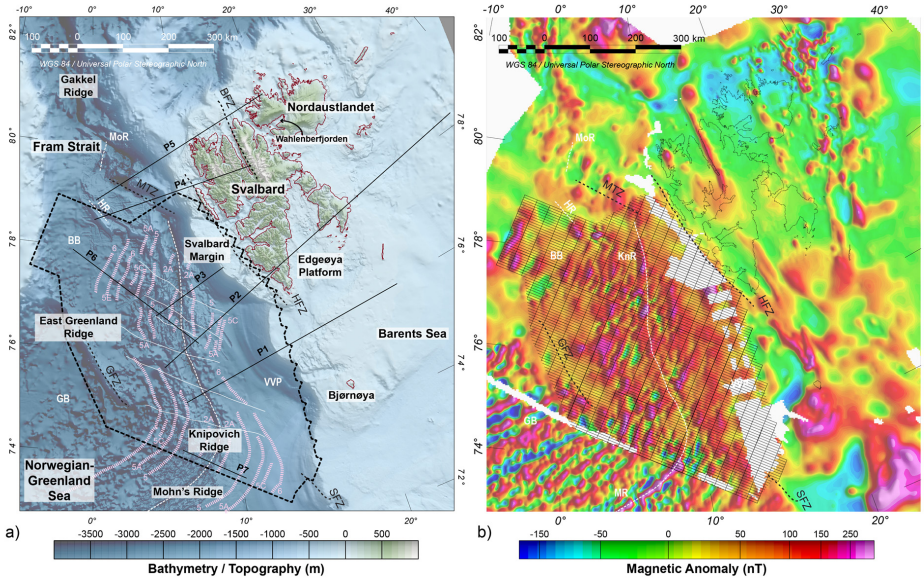

Figure 1. a. Aeromagnetic survey area (black dotted polygon) with the modelled 2-D profiles (P, black lines) interpreted as described in Table 2. The magnetic isochrons (dotted pink line) and magnetic lineaments (white line) (Dumais et al., 2020a) are superimposed on the bathymetric data (Olesen et al., 2010). **b.** Aeromagnetic flight path superimposed on the pre-existing aeromagnetic data (Olesen et al., 2010). MoR: Molloy Ridge, VVP: Vestbakken Volcanic Province, BFZ: Billefjorden Fault Zone, SFZ: Senja Fracture Zone, HFZ: Hornsund Fault Complex Zone, GFZ: Greenland Fracture Zone, MTZ: Molloy Transform Zone, GB: Greenland Basin, BB: Boreas Basin, HR: Hovgaard Ridge, KnR: Knipovich Ridge, MR: Mohns Ridge.

2 Geological Background

The study area encompasses the Fram Strait, Svalbard, Edgeøya Platform and Nordaustlandet (Fig. 1). The Fram Strait is characterized by the Knipovich Ridge as the physiographic expression of the seafloor spreading. Earlier studies set the seafloor spreading of Knipovich between ~55 and 33 Ma (Faleide et al., 2008; Nemčok et al., 2016; Talwani & Eldholm, 1977), while the new aeromagnetic data (Dumais et al., 2020a; Dumais et al., 2020b) confirm the initiation at c. 20 Ma, after the Eurekan orogeny (Dumais et al., 2020a). Classified as an ultraslow-oblique spreading system (with seafloor spreading rates of less than 20 mm/yr), the Knipovich Ridge is a segment of the NE Atlantic-Arctic Mid-Ocean Ridge system along with the Mohn's Ridge, the Molloy Transform Zone and the Gakkel Ridge (Fig. 1). The Knipovich Ridge is surrounded by the Vestbakken Volcanic Province, and the Hornsund Fault Zone on the eastern side, and by the Boreas and East Greenland Basins on the western side (Fig. 1). At the present day, the Knipovich Ridge trends from NW-SE in the south to N-S in the north with a 130 km-wide escarpment. On the west side, the Svalbard margin is largely covered with thick piles of sedimentary rocks along the Svalbard margin (Engen et al., 2006; Klitzke et al., 2015). The Fram Strait oceanic domain developed after a Late Cretaceous-Eocene rifting event between the Barents Sea and the Northeast Greenland and forms a complex system of conjugate shear margins characterized by distinct crustal, structural and magmatic properties (Faleide et al., 2008; Hamann et al., 2005; Ritzmann & Jokat, 2003; Srivastava & Roest, 1999). During the Paleocene-Eocene, the continental rifted system underwent a brief episode of compression in the Eurekan-Spitsbergen fold and thrust belts (Piepjohn et al., 2016). Northwards, the Knipovich Ridge is linked through the Molloy Transform Zone to the Gakkel Ridge located in the High Arctic region, north of Svalbard (Brozena et al., 2003; Glebovsky et al., 2006). The Hovgaard Ridge and the East Greenland Ridge, along the Greenland Fracture Zone, represent characteristic bathymetric features (Fig. 1a) and may include several continental fragments preserved within the oceanic domain (Døssing et al., 2008; Døssing & Funck, 2012; Engen et al., 2008; Faleide et al., 2008; Knies & Gaina, 2008; Nemčok et al., 2016).

In the Norwegian-Greenland Sea, the Mohn's and Ægir ridges spreading initiated at 52.8 Ma (C24r) (Gaina et al., 2009; Talwani & Eldholm, 1977) and propagated progressively to the south towards the juvenile volcanic margins during the Early Eocene (Franke et al., 2019; Gernigon et al., 2019). After the extinction of the Mid-Labrador Ridge (Labrador Basin Bay) in the Early Oligocene (33.7 Ma, C13) (Oakey & Chalmers, 2012; Roest & Srivastava, 1989; Srivastava & Roest, 1999; Suckro et al., 2013), the relative motion between Norway and Greenland changed from NNW-SSE to WNW-ESE (31-28 Ma, C12-10) (Gaina et al., 2017). From this reorganization, the ultra-slow spreading Ægir Ridge became extinct after C10, causing the development of the Kolbeinsey Ridge and the detachment of Jan Mayen Microplate Complex from Greenland at ~24 Ma (C7-6) (Blischke et al., 2017; Gernigon et al., 2015; Schiffer et al., 2019). To the north, the Knipovich Ridge initiated at c. 20 Ma (C6) (Dumais et al., 2020a). While earlier a failed rifting in the Boreas Basin was disputed (Hermann & Jokat, 2013; Skogseid et al., 2000), Dumais et al. (2020a) also observed an extinct rift in the Boreas Basin with a thin crust explaining the peculiar strong asymmetry of the spreading system and consequently, infer a ridge jump in the Fram Strait at around 18 Ma. The Gakkel Ridge was initiated at ~58-59 Ma (C26n-25r) followed by a seafloor spreading rate decrease from C13 (Brozena et al., 2003; Glebovsky et al., 2006; Schreider et al., 2019). A 250-km section of the Gakkel Ridge, north of Svalbard, ending in the Fram Strait, opened much later between C8 and C5 (Brozena et al., 2003; Glebovsky et al., 2006). Similarly, the Molloy Ridge spreading segment initiated in the Early Miocene (10-20 Ma, C5-C6) (Engen et al., 2008; Srivastava & Tapscott, 1986).

On the continental domain, with bedrock fragments of Precambrian to Cenozoic age (Dallmann, 2015) and basement deformations from the Caledonian orogeny (Holtedahl, 1926; Ohta, 1994), the Svalbard Archipelago have been influenced by the rifting and seafloor spreading in the Fram Strait (Skilbrei, 1992). During the Cenozoic, the Eurekan Orogeny might have merged with the West Spitsbergen Thrust and Fold Belt that developed along the west coast of Spitsbergen (Harland, 1969; Piepjohn et al., 2016; Vamvaka et al., 2019).

The Edgeøya Platform to the east (Fig. 1) is mainly characterized by sub-horizontal layers of Triassic sediment successions (Dallmann, 2015). Farther east, Nordaustlandet, an island of the Svalbard archipelago, is mostly covered by glaciers. With few outcrop availabilities, the regions lithology is difficult to assess. Two basement types determined by basement outcrops from both sides of Wahlenbergfjorden, partly dividing Nordaustlandet (Dallmann, 2015; Johansson et al., 2002), and confirmed and refined from aeromagnetic data (Dumais & Brönner, 2020). The basement on the north shore is of pre-Caledonian origin with Mesoproterozoic and Neoproterozoic rock exposures (Lauritzen & Ohta, 1984). Caledonian granites, Grenvillian Rijpfjorden granites and migmatites are found on the northern tip of Nordaustlandet (Johansson et al., 2005; Johansson et al., 2002), as well as Silurian diorites and gabbro located on the northeast of Nordaustlandet (Johansson et al., 2005). The south shore comprises a Tonian basement, composed of dolomite, sandstone, quartzite, and limestone, intruded by Jurassic-Cretaceous doleritic dikes. Cretaceous sills have also been emplaced on- and offshore Nordaustlandet (Dumais & Brönner, 2020; Grogan et al., 2000; Minakov et al., 2012; Polteau et al., 2016).

3 Methods and Data

To further resolve the complexity of the crustal setting and achieve a consistent interpretation with various observations, we integrated existing results from various geophysical and petrophysical data and geological concepts into the modelling. Magnetic and gravity 2-D forward models are used to investigate and improve the understanding of the crustal architecture of the study area. The gravity field is sensitive to crustal and mantle composition, isostacy, crustal flexure and thermal variation in the lithosphere. All those mechanisms and properties are peculiar in the oceanic domain, not in isostatic equilibrium, where the mantle and crustal densities are controlled by the magma influx associated with the seafloor spreading and mantle decompression at the ridge. The magnetic field is sensitive to iron content and distribution in the crust down to the Curie temperature isotherm when the magnetization of the minerals is annihilated.

3.1 Aeromagnetic Data

With the acquisition of the KRAS-16 aeromagentic data, a comprehensive magnetic dataset from different campaigns, covering the entire Fram Strait was compiled to a continuous magnetic grid (Fig. 2, (Dumais et al., 2020a; Dumais et al., 2020b)). The acquisition and processing of KRAS-16 is described in the report from Dumais et al. (2020b). A compilation of surveys with various resolutions and acquired over the last four decades (Jokat et al., 2008; Jokat et al., 2016; Olesen et al., 2010; Trulsvik et al., 2011) was carefully merged to minimized the discrepancies due to different resolution caused by the line spacing (Table 1), as well as navigation, positionning and sensor technologies. Geosoft Gridknit (Geosoft, 2013) calculated a minimal shift with the overlaps between the survey and applied it to the grids to merge the data. However, minimal noise in the data remains in the surveys adjacent to KRAS-16, e.g., the linear trends observed parallel to the Molloy Transform Zone are artefacts

from the flight navigation.

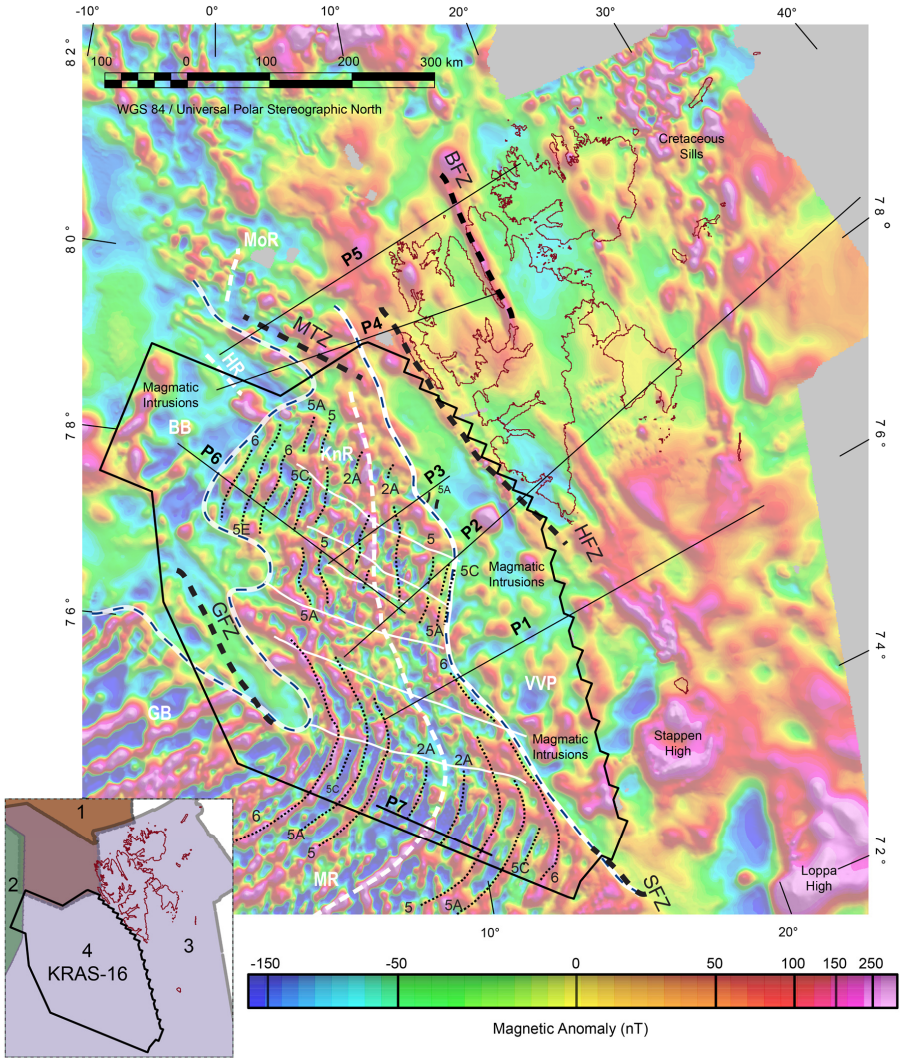

Figure 2. Aeromagnetic anomaly of the area. Magnetic striped patterns represent the oceanic domain. Round intermediate-size anomalies are observed in the Vestbakken Volcanic Province. The linear trends observed parallel to the Molloy Transform Zone are artefacts from the flying configuration. Small round high amplitude anomalies oberserved east of Nordaustlandet are Cretaceous sills. (COB: blue and white dashed line, KRAS-16 boundary: red, isochron anomalies: dotted black, 2-D profiles P: black, lineaments maped from the magnetic data: white, ridge axis: dotted white, MoR: Molloy Ridge, VVP: Vestbakken Volcanic Province, BFZ: Billefjorden Fault Zone, SFZ: Senja Fracture Zone, HFZ: Hornsund Fault Complex Zone, GFZ: Greenland Fracture Zone, MTZ: Molloy Transform Zone, GB: Greenland Basin, BB: Boreas Basin, HR: Hovgaard Ridge, KnR: Knipovich Ridge, MR:

Mohn's Ridge). The aeromagnetic survey boundaries used for the compilation in the figure inset are described in Table 1 (1- Jokat et al. (2008, 2016) which overlap with survey 3; 2- Turlsvik et al. (2011); 3- Olesen et al. (2010) which overlap with survey 1 and 4; 4- Dumais et al. (2020a, b))

Survey	Line Spacing	Year	Acquired / compiled by	References
1	3000-7500 m	1993-2011	Alfred Wegener Institute	Jokat et al., 2008(Jokat et al., 2008; Jokat et al., 2016) Jokat et al, 2016
2	4000 m	2008-2009	TGS-NOPEC Geophysical Company	Trulsvik et al. (2011)
3	4000-10 000 m	1969-1991	Geological Survey of Norway	Olesen et al. (2010)
4	5500 m	2016-2018	Geological Survey of Norway	Dumais et al. (2020a, b)

Table 1. Description and reference of the aeromagnetic datasets merged. The acquisition parameters are valid for the section of the dataset used, e.g. Olesen et al. (2010) is partially used. The location of the datasets is displayed in Fig. 2.

3.2 Gravity Data

The gravity data (Fig. 3) used for latitudes below 80°N is the global gravity model which has a grid cell size of 1 arcminute and an accuracy of 2 mGal with a high correlation between seafloor topography and gravity anoamlies in the 12-km-to-160-km wavelength band where the sediment cover is thin (Sandwell et al., 2014). Above 80°N, the gravity data relies on the Arctic Gravity Project (ArcGP) data compilation which has 5 arcminute resolution (Kenyon et al., 2008). The free-air anomaly data have been used for the 2-D forward models. The Bouguer correction could not be reliably calculated given the difference in accuracy among the coarse free-air gravity data, the high resolution bathymetry and the small extent of the ridge crest.

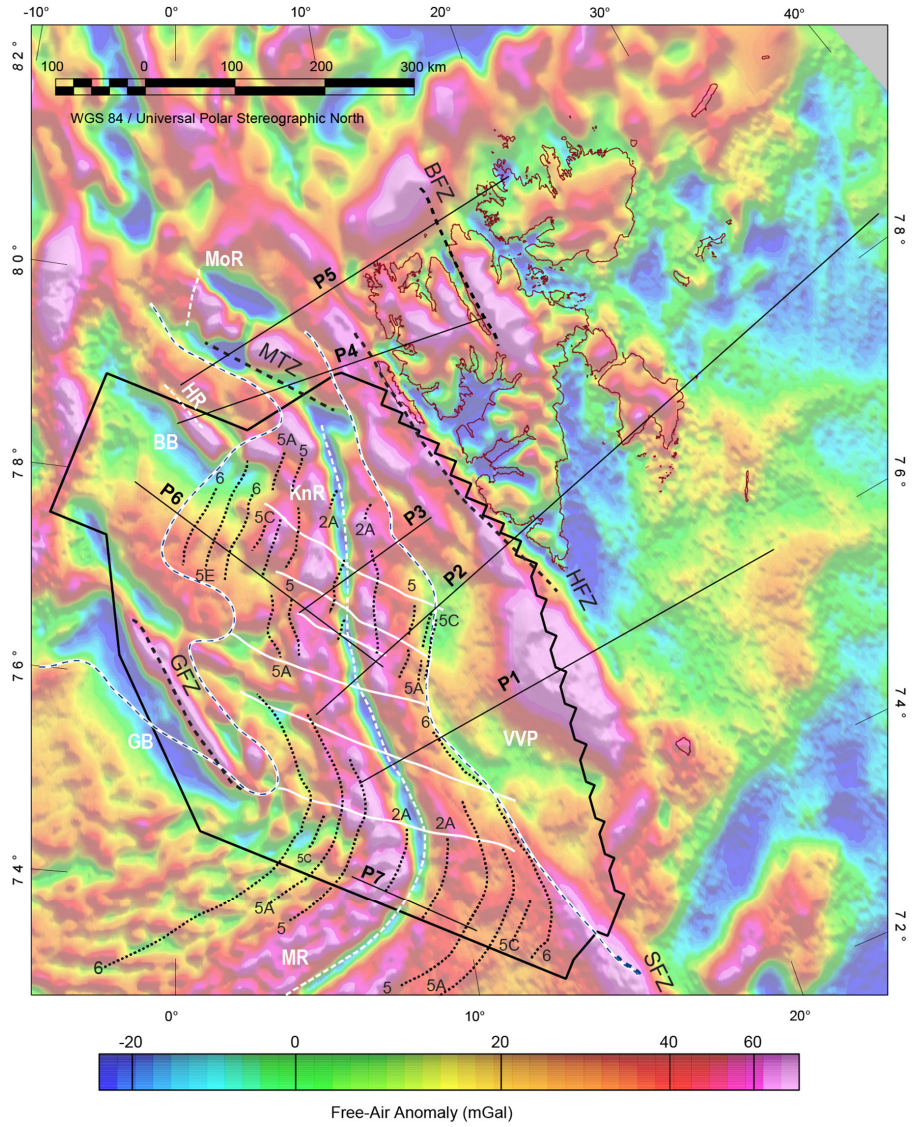

Figure 3. Free-air gravity anomaly maps of the area. The magnetic isochrons coincide with the high free-air anomalies along the Knipovich Ridge. (COB: blue and white dashed line, KRAS-16 boundary: black, magnetic isochron anomalies: dotted black, 2-D profiles P: black, magnetic lineaments maped from the magnetic data: white, ridge axis: dotted white, MoR: Molloy Ridge, BFZ: Billefjorden Fault Zone, HFZ: Hornsund Fault Zone, GFZ: Greenland Fracture Zone, MTZ: Molloy Transform Zone, GB: Greenland Basin, BB: Boreas Basin, HR: Hovgaard Ridge, KnR: Knipovich Ridge, MR: Mohn's Ridge).

226 3.3 Bathymetric Data

227 The bathymetric data in the rift valley of the Knipovich Ridge were acquired by the
228 Geological Institute of the Russian Academy of Sciences and the Norwegian Petroleum
229 Directorate with a multibeam acoustic sonar between 2006 and 2010, resulting in a digital
230 topography model with 100 m cell size (Zarayskaya, 2017). This dataset is used to correlate
231 the bathymetric highs with the magnetic anomalies (Fig. 5). The regional bathymetric data
232 outside the rift valley is a compilation with 250 m cell size a from various surveys ((Olesen et
233 al., 2010), Fig. 1). This regional dataset is mainly used to constrain the 2D-forward models.

234 3.4 Seismic Data

235 Published seismic profiles from different deep seismic experiments were applied as
236 structural constrains and horizon interpretation (Table 2). Profile locations are shown on Fig. 1.
237 All profiles have been interpreted for the Moho, top crustal basement, and sedimentary layers
238 in accordance with the seismic velocities.

Profile	Lines	Characteristics	Crustal type	Velocity-Density relationship methodology	References
1	Barents 98 Line 3W & E	OBS Seismic	Oceanic / Continental	(Barton, 1986; Ludwig et al., 1970)	(Breivik et al., 2003) (Breivik et al., 2005) (Breivik & Mjelde, 2001a, 2001b)
2	Barents 98 Line 8 & 10, Hoersted'05	OBS Seismic	Oceanic / Continental	Nafe-Drake density-curve (Ludwig et al., 1970)	(Ljones et al., 2004) (Breivik et al., 2005) (Czuba et al., 2008) (Grad & Majorowicz, 2020) (Breivik & Mjelde, 2001a, 2001b)
3	Barents 98 Line 9	OBS Seismic	Oceanic	(Christensen & Mooney, 1995)	(Ritzmann et al., 2002) (Breivik & Mjelde, 2001a, 2001b)
4	AWI 99400	OBS Seismic	Oceanic / Continental	(Christensen & Mooney, 1995)	(Ritzmann et al., 2004)
5	AWI 99200	OBS Seismic	Oceanic / Continental	No gravity modelling	(Czuba et al., 2005)
6	AWI 20090200	OBS Seismic	Oceanic	Nafe-Drake density-curve	(Hermann & Jokat, 2013)

				(Ludwig et al., 1970)	
7	-	CSEM / MT	Oceanic	No gravity modelling	(Johansen et al., 2019) (Lim, 2020)

Table 2. Description and reference of the 2-D modelling constrains. The location of the profiles is displayed in Figs. 1, 2 and 3.

3.5 2-D CSEM and MT Profile

Applied CSEM and MT profiles are based on Johansen at al. (2019) and Lim (2020). A detailed description of the data acquisition and processing can be found in Johansen et al. (2019). From these interpretations, the Moho and the top crustal basement have been derived from the variation in the resistivity.

3.6 Curie Point Depth Estimation

Derived from the magnetic data, the Curie point depth (Fig. 4a) was estimated with the Pycurious Python code (Mather & Delhaye, 2019) using the Bouligand et al. (2009) algorithm. The Curie point depth represents the isotherm of the Curie temperature of magnetite (580˚C). Above this temperature, the magnetite loses its magnetization. Therefore, the Curie point depth estimation should coincide with the bottom of the deepest causal magnetic source, which is often expected close to the crust-mantle boundary. As the oceanic crust is thinner and the mantle closer to the surface, the Curie point depth is expected to be shallow. On the opposite, the thick continental crust expect deeper estimates for the Curie point depth. The Curie point depth estimation is based on the aeromagnetic compilation of the high-resolution KRAS-16 dataset with the adjacent aeromagnetic datasets. The accuracy of the Curie point depth estimation from the magnetic data in the oceanic domain could be biased since the magnetization acquired during the seafloor spreading is not entirely random in all directions as expected by the methodology. However, given the observations from the magnetic data and the profile modelling, the results appear reasonable and at least reliable to separate oceanic and continental domains. The inversion also reveals a linear trend in the Mohn's Ridge area, few kilometers south of KRAS-16 survey. This coincides with coarse resolution in the magnetic data compilation probably caused by insufficient overlap with the adjacent survey to the south or a profile filtered for noise reduction (Figs. 1 and 2). Since the Curie point depth calculation is sensitive to the frequency content of the magnetic data to derive the depth, shallow depths as expected in the oceanic domain cannot be resolved for this linear section (Fig. 4a). The adjacent survey flown in the Greenland and Boreas basins, west of the KRAS-16 survey, also caused small discrepancies in the Curie point depth with deeper values (Fig. 4a) likely due to levelling issues of this adjacent survey.

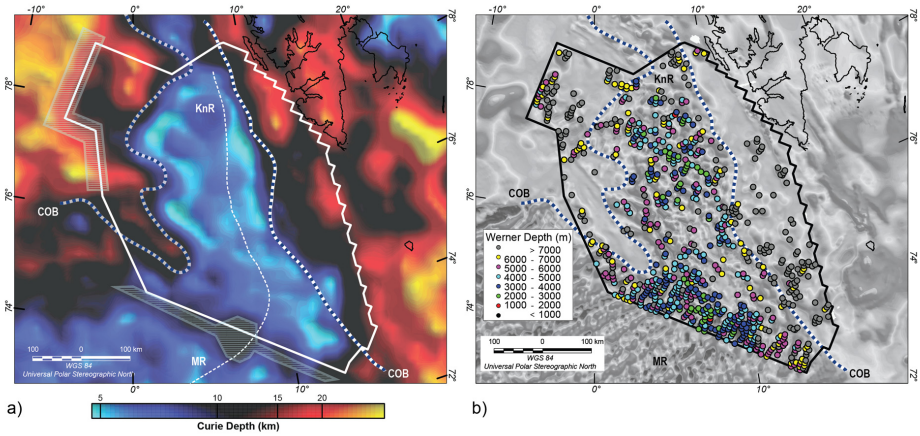

Figure 4. a. Curie point depth representing the bottom of the causal magnetic source calculated from the aeromagnetic compilation. The shallowest depth area agrees with the COB depicted from the magnetic data and constrains the oceanic domain. The grey hatched zone is the location where the Curie point depth is assumed erroneous due to poorer data quality. **b.** Werner deconvolution solutions derived from the aeromagnetic data representing the top of the causal magnetic source. Shallower depth solutions are observed in the oceanic domain. (KnR: Knipovich Ridge, MR: Mohn's Ridge, COB: Continent-ocean boundary).

3.7 Werner Deconvolution

The Werner deconvolution (Ku & Sharp, 1983; Phillips, 1997; Werner, 1955), an automated depth-to-source estimation method, was derived from the magnetic data. Using these empirical basement indicators, sensitive to susceptibility variations, and approximating the geological source to a simplified geometry of features such as contacts and dikes (Goussev & Peirce, 2010), the depth and morphology of the magnetic top basement and intrusions are estimated (Fig. 4b). The Werner deconvolution solutions represent the depth to the top of the causal sources where specific clusters are observed. The resolution of the depth solutions depends on the resolution and accuracy of the magnetic data, but also on the profile direction. 2-D Werner deconvolution provides most accurate results when calculated perpendicular to the trend of a magnetic anomaly. Given the magnetic anomalies from the seafloor spreading are generally oriented perpendicular to the flight lines, the high-resolution KRAS-16 survey allowed reliable depth solutions, in contrary to the aeromagnetic data in the adjacent areas, covered with larger line-spacing and often filtered for noise reduction. Therefore, our depth estimation along the seismic profiles provided poor results due to the lower resolution of the areas adjacent to KRAS-16.

3.8 Modelling

A 3-D magnetization model of the recent aeromagnetic dataset was calculated using an inversion method implemented in GM-SYS-3D (Geosoft, 2014; Parker & Huestis, 1974). The model was constrained by a Moho depth derived from seismic data (Funck et al., 2017), a sedimentary thickness (Engen et al., 2006) and bathymetric data (Olesen et al., 2010). These datasets are chosen for their availability and coverage of the full area studied. The sediment thickness (Engen et al., 2006) is mainly derived from gravity and bathymetry data. It is also calibrated for the age of the crust with magnetic isochron and for the base of the sediment layer

and the Moho depth with seismic data. It provides a sufficient approximation of the location of the top of the basalt layer to provide reasonable magnetization amplitudes in the 3-D model. The magnetization derived from the data represents the overall magnetization of the crust without differentiation of the lithology of the upper crust, lower crust, and numerous intrusions. It provides preliminary insights of the type of magnetization, induced or remanent, expected for the 2-D forward models.

GM-SYS-2D has been used to produce the forward models of the studied profiles (Geosoft, 2006). The sediment and crustal layers in the models were constrained by the available seismic and EM data (Table 2). The initial densities were extracted from the published seismic and gravity modelling (Breivik et al., 2003, 2005; Breivik & Mjelde, 2001a, 2001b; Czuba et al., 2008; Grad & Majorowicz, 2020; Hermann & Jokat, 2013; Ljones et al., 2004; Ritzmann et al., 2004; Ritzmann et al., 2002), whilst magnetization was taken from general publications for the oceanic domain (e.g. Dentith & Mudge (2014), Tivey & Johnson (1993)) and regional models of the Barents Sea (Barrère et al., 2009, 2011; Marello et al., 2013). They were subsequently are modified to a certain degree to fit the magnetic and gravity modelling and to be comparable from profile to profile. The geometries from the seismic profiles are also modified when necessary to obtain realistic density and susceptibility. A mismatch between seismic profiles is found at their intersection. The best fit with magnetic and gravity modelling is used to solve the mismatch. The Werner deconvolution provided a certain degree of constraints to map the top of the crustal basement and magmatic intrusions. For the modelling, earthquakes events were not used since their location is believed erroneous and required re-processing (Loviknes et al., 2020).

4 Interpretation and Results

4.1 Magnetic Map Interpretation

Striped linear magnetic anomalies located in the Fram Strait delineate the oceanic domain composed of basalts. Intermediate-size rounded anomalies with high amplitude are found in the Boreas Basin and the Vestbakken Province extending to Bjørnøya and Stappen High. These are associated with volcanic and magmatic activities, correlated to the presence of sills and volcanic mounds (Faleide et al., 1988; Mork & Duncan, 1993; Omosanya et al., 2016). Similar anomalies are also found east of Nordaustlandet and Edgeøya (Dumais & Brönner, 2020; Grogan et al., 2000; Minakov et al., 2012; Polteau et al., 2016). High-amplitude isolated linear anomalies are also observed along known fracture zones such as Billefjorden and Hornsund fault zones. Prominent regional high-amplitude anomalies are found on the northeast coast of Greenland, on the Edgeøya Platform, on the Stappen High and on the Loppa High. These anomalies are associated with thicker crust for the northeast coast of Greenland and Edgeøya Platform. The Stappen and Loppa highs have a Precambrian magnetized basement causing strong anomalies (Gernigon et al., 2014; Marello et al., 2013). Lineaments and oceanic fracture zones perpendicular to the seafloor spreading, previously interpreted by Dossing (2016) in the Boreas Basin, are also apparent in the new aeromagnetic data (Fig. 2) and are reinterpreted on both side of the Knipovich Ridge (Dumais et al., 2020a)).

The Werner deconvolution solutions correlate with the oceanic domain interpreted form the magnetic data. Shallow sources of less than 5 km depth are observed in the oceanic domain (Fig. 4b). Also, in the oceanic domain, the Curie point depth estimation indicates shallow depths varying between 5 and 7 km, where higher temperatures in the lithosphere are expected from the magma supply feeding the spreading ridge (Fig. 4a). The oceanic crust thickness is estimated to extend from less than 5 km (top) to 7 km (bottom) depth. The Curie point depth transitions to greater depths of 25 km in the continental domain, expressing a colder crust-

mantle system. A large transition zone between the shallow oceanic basement (4-6 km) and the deep continental basement (25-30 km) is observed along the west boundary of the KRAS-16 survey. This section correlates with deeper Werner deconvolution solutions resolving deeper intrusions or a deeper top basement suggesting a thick sedimentary cover (Fig. 4b). Thus, the top of the magnetic sources is expected at larger depth than 7 km and the bottom layer at 12 km+/-2 km depth.

4.2 Gravity Map Interpretation

Free-air gravity anomaly lows are correlated to smaller densities in sedimentary basins such as the Boreas Basin and the Greenland Basin (Fig. 3). The Knipovich Ridge, the Mohn's Ridge and the Molloy Transform Zone are expressed as a narrow band associated with low gravity data while the ridge flanks display free-air gravity anomaly highs with some degree of correlation with the seafloor topography. The magnetic isochron anomalies location correlate with the free-air gravity high found on the Knipovich Ridge flanks. (Fig. 3) The Hovgaard and East Greenland ridges appear as high free-air gravity anomalies. An important free-air gravity high is also present north-west of Bjørnøya, delimiting the Hornsund Fault Zone and investigated in the 2-D model analysis (Ch. 4.4).

4.3 3-D Magnetization Inversion Results

At the southern tip of the Knipovich Ridge, high-amplitude stripes of magnetization demark the transition from the Mohn's Ridge, alternating from -4 to +8 Am^{-1} associated with normal and reverse remanent magnetization (Fig. 5a). Following the Knipovich Ridge northward, at latitudes 74˚N-76˚N, the magnetization degrades to 0 to 4 A m^{-1} with rare occurrences of strong magnetization. A close analysis of the bathymetry within the rift valley draws a correlation between the presence of volcanoes and crater-shaped features, and bathymetric highs with high magnetization values (Fig. 5b). However, the physical extent and the intensity of the high magnetization may vary. Bathymetric highs and volcanoes generally occur in a rich magma supply setting. On the contrary, a low magma supply or an iron- and oxide-poor magma chamber, producing new oceanic crust poor in magnetite, would result in low magnetization (Dentith & Mudge, 2014).Crater-shaped features are rare to non-existent where the magnetization amplitude is very small, near a zero value (Fig. 5c). Magmatic accretion along the spreading axis discontinued by segments of amagmatic accretion is common at oblique ultraslow spreading ridges (Dick et al., 2003). Seawater can percolate through fractures and change the thermal and chemical properties of the crust (Searle, 2013). Numerous lineaments and fracture zones are identified from the aeromagnetic dataset, which are partly linked with linear features from the bathymetric data. Fluid circulation leads to oxidation and degradation of the well-oriented magnetic grains, possibly changing the strong remanent magnetization into induced magnetization (Kent & Gee, 1996). At latitudes of 76˚N-78˚N, the central magnetic anomaly amplitude increases to reach values expected from a normal oriented remanence. Outside the oceanic domain delimited by C6 (Fig. 5), few strongly magnetized bodies are identified, but no notable linear hihgly magnetized body are observed supporting the presence of a continental crust and the absence of basalt layer. The intermetiate rounded anomalies found east of C6 on the east flank could not be explained by neither magmatic nor amagmatic accretion. On the west flank, west of C6, no visible anomaly can support a conjugate domain from magmatic or amagmatic accretion.

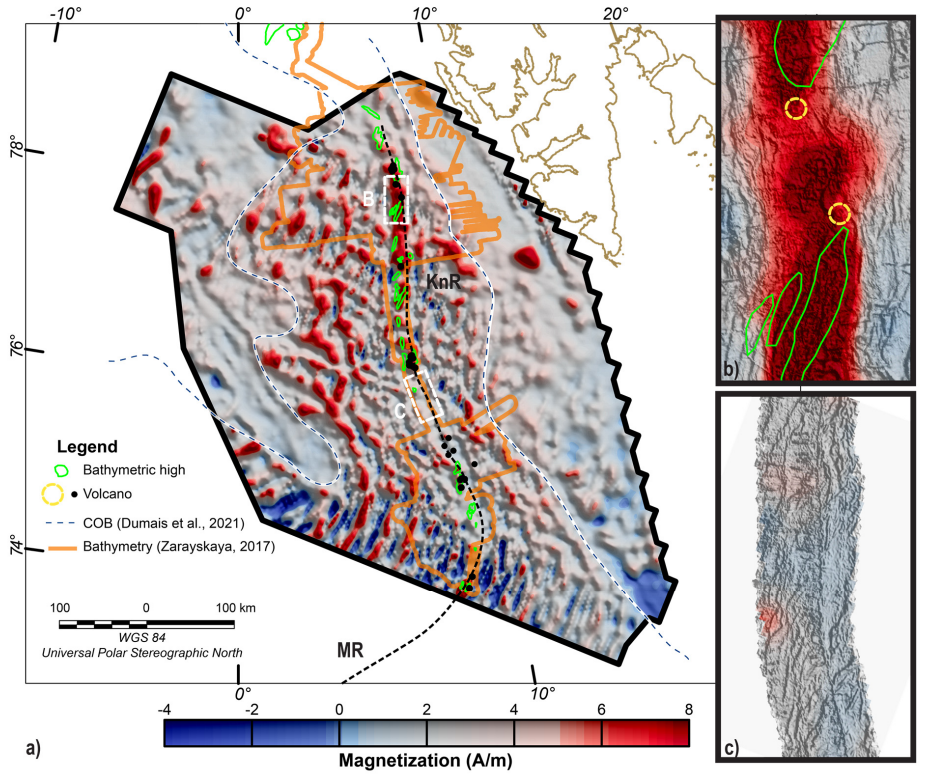

Figure 5. a. Magnetization with volcanoes (black dots) and bathymetric highs (green outline) within the rift valley, white frames show the location of b and c. The 100 m gridded bathymetric data (Zarayskaya, 2017) is shown in the window frames b and c. **b.** Example of high magnetization in the rift valley correlating with bathymetric highs and the presence of volcanoes **c.** Example of low magnetization in the rift valley correlating with the absence of volcanoes or bathymetric features.

4.4 2-D Forward Modelling

The 2-D forward models are constrained by the seismic interpreted horizons for each profile (white dotes lines in Figs. 6 and 7). The same constants are applied to the calculated gravity and magnetic response for each model to match the observed data, an option in GM-SYS (Geosoft, 2006) allowing a common adjustment between the synthetic geometry of the models and the datum used for the observed data (Geosoft, 2013). The different interpreted layers of the crust and mantle use similar values for density, susceptibility and remanence. This ensures a certain homogeneity between the models. No rock samples, representative of the crustal lithology, were available in the Fram Strait. Initial densities input in the models were defined by the gravity modelling after the seismic interpretation when available as described in Table 2. The densities were then modified to fit the gravity data and to be comparable amongst the interpreted profiles. Where the 2-D model could not reach a realistic geological

density, the horizons constrained by seismic or CSEM/MT were modified. Where profiles intersected, the horizons are also modified to reduce the mismatch between the different seismic interpretation. The seismic and CSEM/MT horizons are shown in Figs. 6 and 7. The susceptibility and remanence parameters were chosen to represent the lithology variation between the layers from gabbro to basalts from the literature (Tivey & Johnson (1993) for the oceanic crust; Barrère et al. (Barrère et al., 2009, 2011) and Marello et al. (2013) for the continental crust). Magmatic intrusions were modelled to fit the magnetic signature.

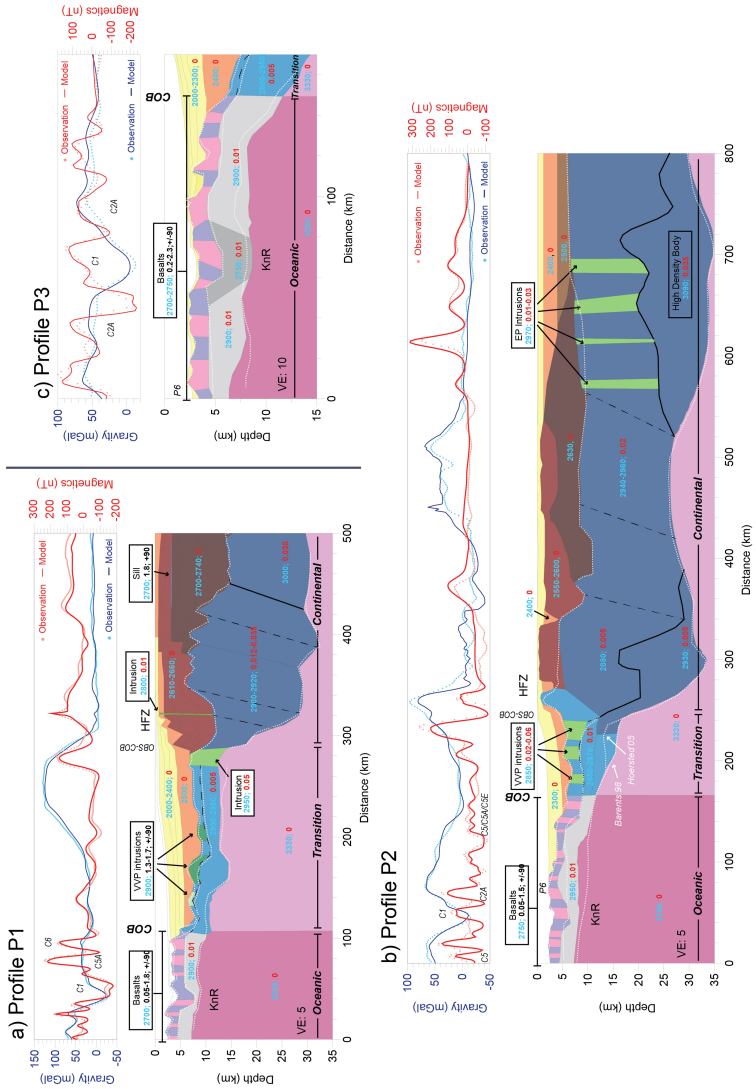

Figure 6. 2-D profiles with the modelled and observed data for gravity and densities (kg m^{-3}, blue), and for the magnetic, susceptibility (SI, red) and magnetization (A m^{-1}; inclination °) are

shown. The bathymetric horizon is derived from (Olesen et al., 2010) and shows good correlation with the seismic horizons displayed as white dashed lines (Breivik et al., 2003, 2005; Breivik & Mjelde, 2001a, 2001b; Czuba et al., 2008; Grad & Majorowicz, 2020; Ljones et al., 2004; Ritzmann et al., 2002). The magnetic isochrons resolved are identified on the profiles. (EP: Edgeøya Platform, KnR: Knipovich Ridge, HFZ: Hornsund Fault Zone, P6: Profile P6, VE: Vertical Exaggeration, OBS-COB: COB from seismic interpretation (Breivik et al., 2003; Ljones et al., 2004; Ritzmann et al., 2002)) **a.** Profile P1. **b.** Profile P2. **c.** Profile P3.

4.4.1 Profile P1 (Fig. 6a)

This profile crosses the ridge and ends in the Barents Sea, south of Svalbard. It presents a large free-air gravity anomaly which was used to estimate the COB location in earlier studies, e.g. Breivik et al. (1999). The magnetic anomaly striped pattern shows that the COB (Dumais et al., 2020a) is located about 160 km farther west on P1. This magnetic description of the COB is used for all models and data analysis of this current study. On P1, high frequencies on the magnetic signal are observed from 0 to ~110 km which is defined as the oceanic domain. Between ~110 and ~270 km, the magnetic signal amplitude is generally low with two wide with low amplitude anomalies. From 300 km to the end of the profile, the magnetic signal amplitude is generally higher than the rest of the profile with one very high anomaly at ~320 km. The central magnetic isochron C1 is amagmatic, with no clear magnetic signal, and modelled with low remanent magnetization. Intrusions or volcanic mounds in the Vestbakken Volcanic Province could explain the magnetic signature between the COB and the Hornsund Fault Zone. This 200-km section between the COB and the Hornsund Fault Zone showing no clear striped magnetic pattern is defined as a transition domain between the continental and the steady state oceanic crust domains. A low susceptibility (0.005 SI), lower than the one assigned to the continental crust (0.012-0.038 SI) is needed to fit the magnetic data observed. This corresponds to the transition domain in the 2-D model interpretation. One large intrusion is modelled at the boundary between the transition and continental domain. The Hornsund Fault Zone is also denoted with a shallow narrow elongated intrusion due to the high frequency of the related magnetic anomaly. The depth of the bottom of this causal body cannot be reliably estimated from the modelling, but the small response on the gravity signal suggests a small body in volume. East of the Hornsund Fault Zone, corresponding to a magnetic high, several intermediate magnetic anomalies are found on the Svalbard margin. These anomalies are modelled with several continental crustal layers superposed at an angle and with varying susceptibilities that are possibly related to old Caledonian nappes. There is no indication on the seismic data of a basement change in the lithology which is consistent with the small density variation between the crustal layers.

A good correlation between the observed and calculated gravity anomalies requires a variation in the crustal and mantle densities. The upper crust in the oceanic domain consists of basalt with densities of 2,700-2,750 kg m^{-3} while the gabbro of the lower crust has a density of 2,900 kg m^{-3}. Densities in the transition domain defined in this study are 2900 kg m^{-3} and do not support a clear delimitation between the upper and lower crust which is consistent with the velocity observed along the seismic transect (Breivik et al., 2003; Breivik & Mjelde, 2001a, 2001b). A wide high gravity anomaly is identified west of the Hornsund Fault Zone covering half of the transition domain. No single lithological body causes this large anomaly, but is caused by the configuration of the lithology. On the west side, the anomaly increases as the sediment thickness increases and the seafloor rises. The anomaly decreases abruptly with the sharp increase of the crustal thickness. The continental crust has densities of 2,900-2,990 kg m^{-}

^{3} overlain by felsic-granite rocks with density of 2,600-2,750 kg m^{-3} embedded by two sills imaged from the seismic data (Breivik & Mjelde, 2001b). The density variation was suggested by Breivik at al. (2005), the 2-D forward model presented in this study attempt to link both variation in susceptibility and density. A gradual density variation from a thermal mantle was attempted as suggested by Breivik et al. (2003) for the continental section of the profile but could not explain the gravity for the full profile including both continental and oceanic section. The gravity did, however, require a density variation in the mantle. This was achieved with a lower density solely below the oceanic crust, suggesting that the variation of temperature in the mantle is local and does not require thermal variation over a long distance towards the transition or continental domain.

4.4.2 Profile P2 (Fig. 6b)

Profile P2 crosses the Knipovich Ridge axis, the Svalbard Margin, Svalbard mainland, and terminates on the Edgeøya Platform. The seismic data were acquired over several campaigns between 1998 and 2005 with seismic stations onshore and offshore (Czuba et al., 2008). The COB depicted from the magnetic striped anomalies correlates with the gradual change in the velocity of the seismic interpretation in the upper crust from about 4.5-5.0 km s^{-1} to 5.5-6.0 km s^{-1} (Breivik & Mjelde, 2001a). The seismic interpretation of Profile 6 intersecting at point P6 on Fig. 6b observed a mantle-crust interface at 6 km depth (Hermann & Jokat, 2013) instead of 9 km (Grad & Majorowicz, 2020). Between 0 and ~120 km, the present gravity model requires a thinner crust with a Moho 2 km higher than the Moho derived from the seismic interpretation for the oceanic domain comparable to the seismic interpretation of Hermann & Jokat (2013). The transition domain defined between the COB and the Hornsund Fault Zone is demarked with a thickening of the lower crust between ~160 km and 250 km. Densities in the transition domain are 2800-2970 kg m^{-3} consistent with the seismic velocities for both the upper and lower crusts (Breivik & Mjelde, 2001a, 2001b; Grad & Majorowicz, 2020). However, west of Hornsund Fault Zone between 180 km and 240 km, the seismic interpretations differs (Breivik & Mjelde, 2001a, 2001b; Czuba et al., 2008; Grad & Majorowicz, 2020; Ljones et al., 2004) (Fig. 6b). The free-air gravity anomaly requires a lower crust modelled similar to Breivik & Mjelde (2001a) with more gradual thickening than the interpretation from Czuba et al. (2008) and Grad & Majorowicz (2020). Several magnetic anomalies are modelled with higher susceptibilities representative of dikes in the transition domain. The magnetic anomaly and free-air gravity anomaly highs located at the Hornsund Fault Zone are likely caused by the geometry of the crust. The mantle density also increases from the oceanic to the transition and continental domains. East of the Hornsund Fault Zone, the crustal properties change with higher densities and susceptibilities with a thicker crust (30 km), consistent to a continental crust. A density variation in the continental crust was also suggested by Breivik at al. (2005), the crustal 2-D forward model attempt to link both variation in susceptibility and density to the observed data. Intrusions are modelled on the Edgeøya Platform where sills and dikes are expected (Dumais & Brönner, 2020; Grogan et al., 2000; Minakov et al., 2012; Polteau et al., 2016). However, the current resolution of the magnetic data does not allow us to resolve the depth and volume of these magnetized bodies. Two high density bodies are modelled in the lower crust agreeing with the high velocity bodies interpreted with the seismic data which were correlated with the lithosphere-asthenosphere boundary (LAB) uplift (Grad & Majorowicz, 2020).

4.4.3 Profile P3 (Fig. 6c)

This profile crosses the Knipovich Ridge axis to the Svalbard Margin. The profile is located between two magmatic segments in the rift valley. Like Profile P2, the COB demarked by the striped magnetic anomaly correlates with the gradual change in the velocity of the

seismic interpretation in the upper crust (Breivik & Mjelde, 2001a). The lower crust below the Knipovich Ridge requires a lower density (2750 kg m^{-3}) than the surroundings. The gravity model also requires a lower mantle density in the oceanic domain (3280 kg m^{-3}). The profile was modelled to match Profile P6 at point "P6" as interpreted with a thinner crust by Hermann & Jokat (2013) and the observed free-air gravity anomaly (Fig. 6c). The Moho was raised up by 2 km west of the rift valley improving the agreement between the modelled and observed gravity profile. This also reduces the crustal thickness difference at the intersection between Profiles P3 and P6. On the western flank, where sediments are accumulated, the crust beneath is modelled 1-2 km thicker than the seismic interpretation to fit the free-air gravity anomaly. The transition domain is demarked at 150 km where a lower susceptibility and no remanence are required for the crust and higher density for the mantle.

4.4.4 Profile P4 (Fig. 7a)

This profile starts at the Hovgaard Ridge extending through the Molloy Transform Zone and terminates onshore Svalbard. The crust below the Molloy Transform Zone was modelled with a density of 2800 kg m^{-3} that is lower than the values beneath the Knipovich Ridge (2900 kg m^{-3}). Two magmatic bodies are modelled between the Molloy Transform Zone and Spitsbergen. In that area, east of the Molloy Transform Zone, the observed magnetic profile has higher values than the modelled magnetic profile. This section is challenging to interpret due to the poor data quality. It is near the junction of the Knipovich Ridge and the Molloy Transform Zone, where fluids penetration in the crust and interaction with the crustal composition might be expected. The profile could be modelled with remanent magnetization diagnostic of an oceanic crust; however, no clear magnetic striped pattern is observed in the gridded data (Fig. 2). A serpentinization process could explain both the reduced density of the mantle required below the Molloy Transform Zone and the magnetic high in the section between ~120 km and ~190 km. The oceanic and transition crust necessitate higher susceptibilities than those on the Knipovich Ridge.

Similar to Profiles P1 and P2, a thick continental crust with high density (2930-3000 kg m^{-3}) is modelled. The original seismic interpretation (Ritzmann et al., 2004) suggested a low velocity crust but the gravity modelling necessitates higher densities than expected. The mantle density under the Molloy Transform Zone is reduced to 3270 kg m^{-3}, a value slightly lower than the interpretation under the Knipovih Ridge. The continental section of the profile can be interpreted as compacted sediments of Devonian age (2730 kg m^{-3} and <0.0001 SI) on a basement of Precambrian age (2920-2950 kg m^{-3} and 0.03 SI).

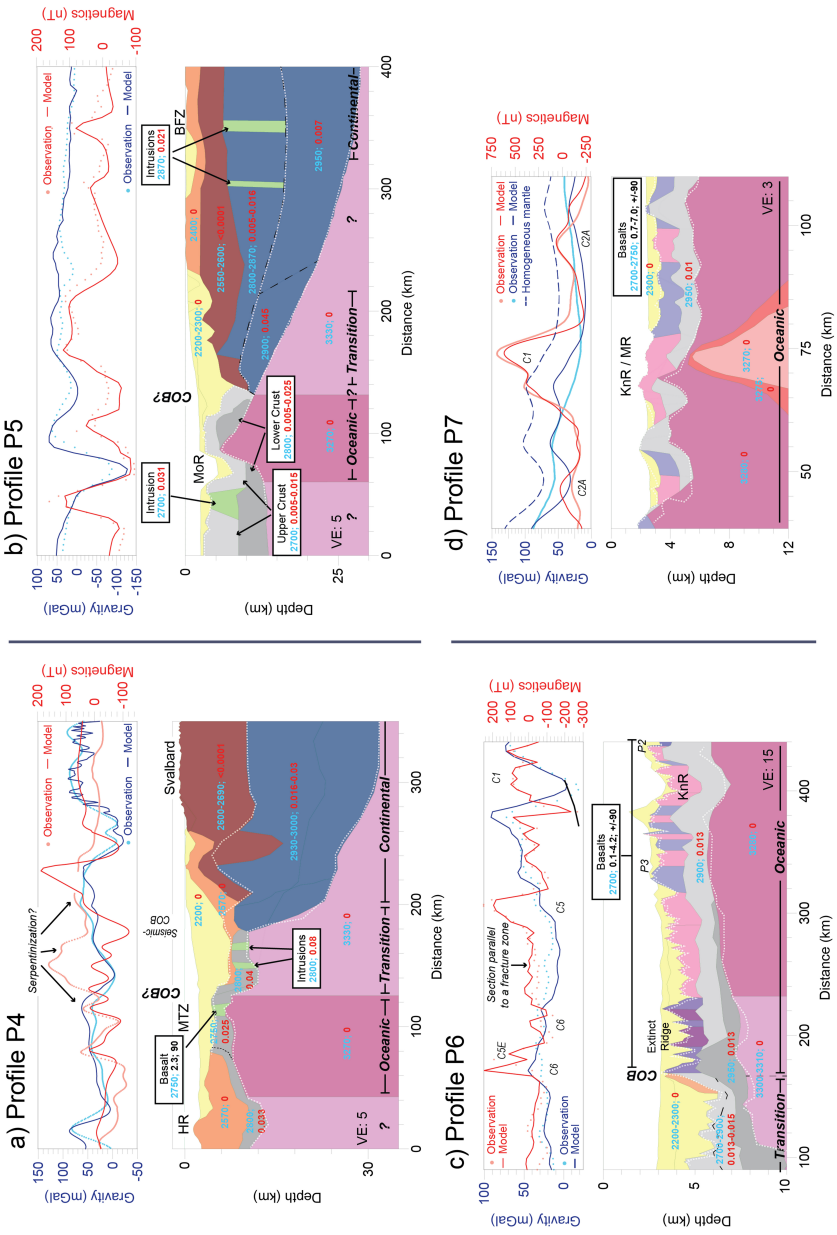

551

552 **Figure 7.** 2-D profiles with the modelled and observed data for gravity and densities (kg m^{-3},
553 blue), and for the magnetic, susceptibility (SI, red) and magnetization (A m^{-1}; inclination °) are
554 shown. The bathymetric horizon is derived from Olesen et al. (2010) and shows good

correlation with the seismic and CSEM/MT horizons displayed as white dashed lines (Czuba et al., 2005; Hermann & Jokat, 2013; Johansen et al., 2019; Lim, 2020; Ritzmann et al., 2004). The magnetic isochrons resolved are identified on the profiles. (HR: Hovgaard Ridge, KnR: Knipovich Ridge, MR: Mohn's Ridge, MoR: Molloy Ridge, BFZ: Billefjorden Fault Zone, MTZ: Molloy Transform Zone, P2: Profile P2, P3: Profile P3, VE: Vertical Exaggeration) **a.** Profile P4. **b.** Profile P5. **c.** Profile P6. **d.** Profile P7.

4.4.5 Profile P5 (Fig. 7b)

Profile P5 starts west of the Molloy Ridge, crosses north of Spitsbergen and ends offshore Nordaustlandet. The rift valley is not aligned with the highest section of the Moho. The magnetic striped pattern indicative of an oceanic crust is not observed on the gridded magnetic data (Fig. 2). The data accuracy and resolution could not allow us to resolve magnetic isochrons or to determine the spreading of the Molloy Ridge. Therefore, the COB is difficult to interpret from the magnetic data as the profile is located outside the high-resolution KRAS-16 survey. The Billefjorden Fault Zone is associated with a magnetic high as previously described by Skilbrei (1992) (Fig. 7b). A large magmatic intrusion is modelled west of the rift valley. The thin lower crust between the Molloy Ridge and Spitsbergen is strongly magnetized (0.025 SI) with lower density than the lower crust interpreted beneath the Knipovich Ridge.

Similar to Profile P4, low crustal velocities (6.0-6.5 km s^{-1}) were interpreted on Profile P5 (Czuba et al., 2005). However, the gravity model requires higher densities (2900-2950 kg m^{-3}) than expected by the seismic velocities. The densities for the crustal and sediment layers in the model are similar to those found in the continental domain of profiles P1, P2, P3 and P4. The horizons from the seismic interpretation were strongly used for the gravity and magnetic model. Given the density and susceptibility comparable to Profile P4 (Fig. 7a), the continental domain can be interpreted as Devonian compacted sediments on a Precambrian basement. The gravity interpretation of the mantle correlates with Profile P4 requiring low density (3270 kg m^{-3}) beneath the Molloy Ridge and higher densities (3330 kg m^{-3}) farther away. The gravity model slightly disagrees with the observed data at the Molloy Ridge and at the shallowest point of the Moho. The Molloy Ridge requires an increase of density or a thinner crust while the shallowest point of the mantle requires a decrease of density or a thicker crust. Modifying the geometry of the crust would move the shallowest point of the mantle towards the Molloy Ridge improving the alignment between the rift valley and the shallow Moho.

4.4.6 Profile P6 (Fig. 7c)

This profile starts from the Boreas Basin and crosses the Knipovich Ridge. It also intersects Profiles P2 and P3 at points "P2" and "P3", respectively. At these points, the seismic interpretation of Profile 6 is different. Its interpretation is used to test and compare the 2-D forward interpretation of profiles P1 and P2. It is mostly located in the oceanic domain where the striped magnetic signal is found. A small portion is located in the transition domain. In the Boreas Basin, an extinct oceanic ridge has been confirmed from the KRAS-16 dataset (Dumais et al., 2020a). The horizons from the seismic interpretation are used in the 2-D model. The densities are modified from the seismic interpretation to be comparable to the other profiles, but the density contrasts and their interpretation are respected amongst the geological bodies. The magnetization values are generally low, and the striped pattern is not clear between the current Knipovich Ridge and the extinct ridge (Fig. 7c). At this location, the gridded magnetic data show a fracture zone or lineament underlying the seismic profile consistent with the lack of a magnetic striped pattern. However, the magnetic striped pattern is clearly recognized a few kilometers away from the profile. The crustal thickness and densities below the extinct ridge and the current spreading ridge are similar. On the western half of the extinct ridge, the crustal density increases. The crustal thickness increases west of the extinct ridge. The mantle density

603 is lower below the present-day spreading ridge like profiles P1, P2 and P3. Along profiles P2
604 and P3, the crustal thickness has been adjusted to Profile P6 as the crustal thickness of P6 is
605 more representative of a slow-spreading system. For profiles P2, P3 and P6, the resulting
606 models with a thinner crust agree with the observed gravity data. The mantle density under the
607 extinct ridge is higher than the mantle density under the present-day ridge, perhaps indicative
608 of a colder mantle. The mantle density increases west of the abandoned ridge but remains lower
609 than the transition mantle densities modelled east of the Knipovich Ridge for profiles P1, P2
610 and P3.

611 4.4.7 Profile P7 - CSEM and MT (Fig. 7d)

612 Profile P7 is located on the oceanic domain located at the junction between the
613 Knipovich and Mohn's ridges. The magnetic interpretation was described by Lim (2020) .
614 Densities used in the 2-D forward model are comparable to the other profiles, particularly the
615 closest Profile P1. The central anomaly presents a small depression in the middle of the
616 anomaly caused by the presence of two mounts in the rift valley. The eastern lobe of the central
617 anomaly is slightly higher than the western lobe. The basalt layer is about 1 km in thickness
618 with a heterogeneous magnetization. The magnetization values have slightly changed from Lim
619 (2020) interpretation due to adjustment between the profiled data and the merged magnetic
620 compilation, but the geometry remains unchanged. The mantle density directly under the rift
621 valley is reduced as suggested by the mantle temperature gradient (Johansen et al., 2019). The
622 disagreement between the modelled and observed gravity profiles is explained by the coarse
623 resolution of the gravity data compared to the resolution and accuracy of the CSEM/MT
624 interpretation. The geometry of the CSEM/MT interpretation requires smaller wavelengths not
625 recorded in the gravity data. However, the gravity model requires a lateral density variation of
626 the mantle as suggested by the MT thermal interpretation (Fig. 7d). This local density variation
627 indicates the narrow nature of the thermal model. However, higher resolution gravity data is
628 necessary to reconstruct the density gradient below the Knipovich Ridge.

629 **5 Discussion**

630 The 3-D magnetization model and the 2-D forward gravity and magnetic models
631 illustrate the spatial variation of the crustal densities and magnetic properties along the
632 Knipovich Ridge and across the Svalbard Margin. All the 2-D forward interpretation are
633 homogenized for modelling parameters and physical parameters to offer a unified model of the
634 Fram Strait as shown in Table 3. Fig. 8a illustrates the 2-D forward models in a 3-D perspective
635 with the Knipovich Ridge and the COB.

Unit	Lithology	Density (kgm^{-3})	Susceptibility (S.I.)	Remanence Amplitude;Inclinaison (Am^{-1};°)
	Sediment	2000-2400	0	-
	Sediment	2400-2570	0	-
	Compacted sediment	2550-2690	0	-
	Continental Basement	2630-2740	Low	-
	Intrusion	2700-2970	0.01-0.08	-
	Intrusion	2900	Low	1.65;90
	Intrusion	2900	Low	1.30-1.45
	Basalt (normal field remare-manence)	2700-2750	Low	0.05-7.50;90
	Basalt (reversed field rema-nence)	2700-2750	Low	0.05-5.00;-90
	Basalt (normal field remare-manence) - Extinct Ridge	2700	Low	0.9-3.8;90
	Basalt (reversed field rema-nence) - Extinct Ridge	2700	Low	0.6;-90
	Continental crust	2880-3090	0.005-0.045	-
	Transitional crust	2800-2970	0.005-0.01	-
	Gabbroic oceanic crust	2900-2950	0.005-0.026	-
	Gabbroic oceanic crust	2750-2850	0.005-0.04	-
	Mantle oceanic domain	3270-3280	0	-
	Mantle continental domain	3310-3330	0	-

Table 3. Description and parameters for density, susceptibility and remanence of the main units interpretated in the 2-D forward models. The 2-D forward model were constructed with a common constant to render the models comparable. A small variation in density, susceptibility and remanence within a single geological unit is seen on individual and from profile to profile. However, there is a good correlation overall between the profile interpretations.

5.1 Oceanic Domain

The Oceanic domain, delimited by the COB ridge-ward, comprises striped magnetized anomalies. As observed in the 3-D magnetization model and the 2-D forward models, the rift valley of the ridge varies northward from almost none to high magnetization. The 3-D magnetization model assumes a homogeneous crust from the bottom of the sediment layer to the top of the mantle without differentiation for layers 2A, 2B and 3, the classical division of the oceanic crust (LaFemina, 2015; Perfit, 1999). Layer 2A composition and thickness has the most influence on the magnetic anomaly (Tivey & Johnson, 1993). Layer 2A is typically thin (less than 1 km) and its magnetization values are typically higher than the other layers. However, the 3-D magnetization model provides information on the type of magnetization found along the Knipovich Ridge. The magnetization pattern along the Knipovich suggests magmatic and amagmatic accretion processes are present. The high magnetization areas in the north correlate with the presence of volcanoes and the bathymetric highs in the rift valley of

the Knipovich Ridge, suggesting the oceanic crust has different physical properties here than at the southern latitudes of the Knipovich Ridge. Therefore, the mantle processes, the volume and composition of the magma chamber below the ridge and the cooling processes are expected to vary from south to north. An iron- or oxide-rich magma chamber at latitudes 76˚N-78˚N compared to the southern section of the Knipovich Ridge could explain the presence of volcanoes and higher magnetization (Fig. 5b). Multiple fracture zones and the bend with the Mohn's Ridge may cause a fluid interaction with the basalt layers of the oceanic crust, de-magnetizing the basalts. Given the low magnetization at the lower latitudes (74˚N-76˚N), an amagmatic segment is proposed to explain the low magnetization. This long amagmatic segment is comprised between two bent elongated C6 anomalies segmented by lineaments strongly visible on the magnetic data. Along this amagmatic segment very few Werner solutions are derived (Fig. 4b), however a shallow top of the mantle is infirmed by the Curie point depth estimation.

At the Molloy Transform Zone, profiles P4 and P5 demark a narrow oceanic domain with a thin crust identified by seismic interpretation with high susceptibility values derived from the 2-D forward models. East of the Molloy Transform Zone, Profile P4 presents a section of the crust with low density values and a very high magnetic anomaly observed. The aeromagnetic data quality is not optimal in this section, but such a wide high magnetic anomaly could be explained with deep serpentinized peridotite. The process of serpentinization affects the physical properties of the crust. The density is usually inversely proportional to the degree of serpentinization while the magnetism often increases as magnetite is produced (Dentith & Mudge, 2014). Profile 4 is near the junction of the Knipovich Ridge and the Molloy Transform Zone, where fluids penetration in the crust and upper mantle changing their composition and magnetization.

The shallowest values of the Curie point depth estimation correlate with the COB independently of the magnetization intensity (Fig. 4a). The Curie point depth estimation is around 6 km below the sea-level in the oceanic domain and slowly increases landwards. The Werner deconvolution resolves a shallow crustal basement in the oceanic domain with solution depths of 2-4 km below the sea-level, representing the basalt layer lying near the seafloor surface. At magnetic isochron C6, the solutions are at 5-6 km below the sea-level suggesting a thicker sediment layer. No Werner deconvolution solutions are found where the magnetization is likely induced with positive but low magnitude value (0-4 Am^{-1}).

A lateral density variation was modelled for the mantle for all the 2-D forward profiles. This lateral density variation is interpreted as thermal variation in the mantle from hotter mantle directly below the ridge to a colder mantle in the continental domain. Local decreased mantle densities are interpreted in the oceanic domain. Low mantle densities are also required under the extinct ridge identified on Profile P6 (Fig. 7c). The lowest mantle densities are found under the active rift valley in Profile P7 (Fig. 7d), the highest resolution profile which offers a unique view of the Knipovich Ridge thermal heat variation. However, the gravity data resolution does not allow to accurately model the density variation correlated to the thermal mantle variation. The 2-D forward model (Fig. 7d) does not support an isostatic equilibrium thermal distribution but agrees with a thermal variation between the oceanic and continental domains as suggested by Breivik et al. (1999). The lateral variation is more discrete and narrowly concentrated under the oceanic domain.

Unfortunately, Profile P6 aligns with a magnetic lineaments possibly associated to a fracture zone. A better image and description of the extent of the extinct ridge could

be achived by acquiring a seismic line perpendicular to the magnetic anomaly in the Boreas Basin combined with a 2-D forward model.5.2 Continental Domain

The continental domain lies roughly eastward from the Hornsund Fault Zone (Fig. 6). This demarcation is seen on the 2-D forward models where the crust is thick, with densities of 2850-2950 kg m^{-3} and Moho depth of 30 km below the sea-level. The densities used in the continental crust are similar to the ones applied for gravity modelling in the original seismic interpretation (Breivik et al., 2003, 2005; Breivik & Mjelde, 2001b; Czuba et al., 2008; Czuba et al., 2005; Grad & Majorowicz, 2020; Ritzmann et al., 2004). The Curie depth (Fig. 4a) also reaches a depth of 25-30 km depicting a colder crust compared to the oceanic domain. The free-air and magnetic maps contain low-frequency anomalies, associated with a deep basement (Figs. 2 and 3). Intermediate anomalies (Fig. 2) are likely associated with magmatic intrusions such as dikes or sills. Their emplacement and depth are estimated in the 2-D forward models (Fig. 6). A high magnetic anomaly is found along the Hornsund Fault Zone where the basement rises to the seafloor on profile P2 (Fig. 6). On Profile P1 (Fig. 6a), the magnetic anomaly is pronounced (Fig. 2) and requires a magmatic intrusion (0.01 SI) along the Hornsund Fault Zone. Dikes and sills are modelled on the Edgeøya platform expressing a largely intruded basement. On Profile P5 (Fig. 7b), the basement is more magnetized between the Molloy Ridge and Spitsbergen and an intrusion is associated with Billefjorden Fault Zone.

The susceptibilities used in the continental and continent-ocean transition crust and the magmatic intrusion are in accordance with the values found in the continental shelf of the Barents Sea. Marello et al. (2013) have compiled susceptibilities of 0.00004-0.029 SI for the upper crust, 0.00006-0.007 SI for the lower crust and 0.003 to 0.01 SI for the continent-ocean transition crust. Barrère et al. (Barrère et al., 2009, 2011) differentiates the Caledonian Nappes upper crust with susceptibilities of 0.0001-0.01 SI, the Archean-proterozoic upper crust with 0.01-0.20 SI, the lower crust with 0.0001 SI and mafic intrusion with 0.015-0.05 SI. On Nordaustlandet, Dumais & Brönner (2020) derived a Mesoproterozoic-Neoproterozoic basement more magnetic than the Caledonian Nappes basement. The continent-ocean transition crust interpreted with the 2-D forward models has susceptibilities of 0.005-0.01 SI similar to the study of Marello et al. (2013). The continental crust is interpreted with susceptibilities 0.005-0.045 SI. The highest crustal susceptibilies are modelled deep to fit the long wavelengths of the magnetic data. Generally, the continental crust along the southern section of the Knipovich Ridge (Profiles P1 and P2) is interpreted with Archean-Proterozoic and Caledonean Nappes basement in accordance to Barrère et al. (Barrère et al., 2009, 2011). The continental crust interpreted in profile P4 and P5 might be apparent to a Mesoproterozoic-Neoproterozoic basement with generally higher susceptibilities than those compiled for the Caledonian Nappes. Therefore, on Profiles P1 and P2, the basement susceptibility and density gradually vary across the continental domain. These variations can be associated with possible Caledonian nappes gradually extending on the margin. Profiles P4 and P5 present a different basement configuration with higher susceptibility and density in the lower crust modelled at the demarcation between the transition and the continental domains.

5.3 Transition Domain: Three Possible Scenarios

The oceanic and continental domains have a clear signature on the gravity and magnetic maps and are well tested and illustrated by the 2-D forward models. The oceanic and continental domains are separated by a distinct transition domain that extends for tens of kilometers (Figs. 2 and 8). The Curie depth allows to estimate the extent of the transition domain on both sides of the ridge (Fig. 4a) where the Curie point depth migrates from shallow (6 km below sea-level) to deep (25-20 km below sea-level). This transition is also marked by a gradual thickening of the crust and a lack of magnetic striped pattern (Figs. 6 and 7). The

transition domain shares higher mantle densities compared to the adjacent oceanic domain. Similar mantle densities are also expected in the continental domain (Figs. 6 and 7). The transition domain is wider at latitude 76°N and slowly narrows until latitude 80°N where it reaches its minimal extent on the eastern margin. However, such a wide transition zone is not unique, it is also observed along the northern Mozambican margin (Vormann & Jokat, 2021). Vormann and Jokat (2021) describe the Mozambican margin formed in an oblique phase with continental stretching and then oceanic crust accretion taking place between Africa and Davie Ridge. In the Fram Strait, the presence of Mohns Ridge and the East Greenland Ridge, on the west of southernmost section of Knipovich Ridge, could explain for the more prominent continental stretching on the eastern margin. Longer seismic profiles of P1 and P2, above the western margin and Greenland Fault Zone, would confirm the nature of the crust between the ocean spreading of Knipovich and Monhs ridges. On the western margin, the transition domain comprises the East-Greenland Ridge and a large portion of the Boreas Basin.

Sparse magnetized bodies in the transition domain have an estimated depth of 6-7 km below the sea-level or deeper which locate them in the upper crustal layer on the eastern margin while they can be shallower (5-7 km below sea-level) on the western margin according to the Werner deconvolution (Fig. 4b). Intrusions are more numerous in the south-east margin, near the Vestbakken Volcanic Province. At that latitude, the conjugate margin is demarked by the prominent East-Greenland Ridge and a long amagmatic segment of the Knipovich Ridge characterized with low magnetization. On the north-east margin of the Knipovich Ridge, few major intrusions are found, but more prominent intrusions are located at the same latitude on the western margin in the Boreas Basin.

The Knipovich Ridge initiated in a transtensional system, where the plate was sliding along the Hornsund Fault Zone causing pull-apart basin infilling with thick sediments. Three scenarios could provide explanation to the observations in the transition zone.

1. The transition domain could comprise an oceanic crust buried under a thick sediment layer. One may consider the numerous intrusions found on profiles P1 and P2 in the transition domain have similar magnetic response to the oceanic magnetic isochrons. However, those intrusions have a rounded shape in the magnetic map and are not linear as commonly expected for oceanic seafloor spreading anomalies. Moreover, no corresponding anomalies are found on the conjugate margin. The crustal properties of the transition domain are similar to the continental crust with higher densities in the transition domain on profiles P1, P2 and P3 (Fig. 6).

2. Alternatively, the transition domain could be formed by mantle exhumation and serpentinization. During the rifting before the spreading of the ridge, the continental crust was extended and thinned while the rift was filled with sediments. Significant hyperextension could have initiated the progressive exhumation and denudation as of the exhumed mantle as acknowledged on the Iberian margin (Pérez-Gussinyé et al., 2001; Sutra & Manatschal, 2012; Whitmarsh et al., 1993).This is consistent with the crustal structure interpreted by the seismic profiles and the crustal properties apparent in the continental domain. The crust could have been highly intruded during the mantle exhumation. The high-density lower crust could represent exhumed serpentinized mantle (Minshull, 2009). However, the Moho is well defined by the refraction waves whereas it is usually unclear in a heavily serpentinized mantle setting (Horen et al. 1996, Christensen, 1996, Christensen, 1966, Christensen 1978).

3. Finally, the transition domain could represent an exhumed lower continental crust as observed in many hyperextended rift systems (Clerc et al., 2015). During the rifting but before the seafloor spreading initiation at C6, the intruded continental lower crust could have gradually migrated and exhumed (Fig. 8b) towards the proto-oceanic domain. A pre-

existing thick and low-viscosity lower continental crust caused by the Eurekan orogeny could explain a lateral flow of the ductile lower crust. Given the seafloor spreading initiation at C6 (20 Ma), the Eurekan deformation occurred prior to the ridge spreading (Piepjohn et al., 2016). The Eurekan deformation could have thickened and softened the crust. A rapid collapse and rifting could have led to a lateral escape of the lower continental material. This scenario is consistent with the crustal and mantle properties interpreted in the 2-D forward models.

The third scenario is favored given the tectonic setting in the Fram Strait before the seafloor spreading initiation of the Knipovich Ridge. The 2-D forward models illustrate the evolution of the spreading ridge from the continental to the oceanic crust (Fig. 8a). On the 2-D forward model, a wide continent-ocean transition zone is interpreted on the east flank of the southern section of the Knipovich Ridge (74°N) characterized with an intruded crust and possibly exhumed mantle. However, the western flank of the southern section of the Knipovich Ridge, a much narrower continent-ocean transition zone, with less intrusion in the crust, is suggested by the aeromagnetic data (Fig. 2). On the northern section of the Knipovich Ridge (78°N), a narrowing of the continent-ocean transition zone on the eastern flank and a ridge jump are interpreted from both the 2-D forward models and the aeromagnetic data. The crust is also more intruded on the eastern flank as suggested by the aeromagnetic data (Fig. 2). This asymmetric opening of the Fram Strait is illustrated in Fig. 8b. Numerous lineaments and important variation of the magnetization along the Knipovich Ridge are interpreted from the aeromagnetic data suggesting magmatic and amagmatic accretion and possibly mantle exhumation and fluids penetration changing the crustal composition. The structure and composition of the crust, and the properties of the mantle were extracted from the profiles across the Knipovich Ridge. However, the modelling used seismic constraints from independent interpretations and not directly from digital seismic data. This remains an inherent uncertainty to the geometries and physical properties derived from the potential field modelling in this study. Nevertheless, the gravity and magnetic interpretation indicates that the Fram Strait has opened in a complex setting causing the asymmetric and heterogeneous oceanic and transition domains.

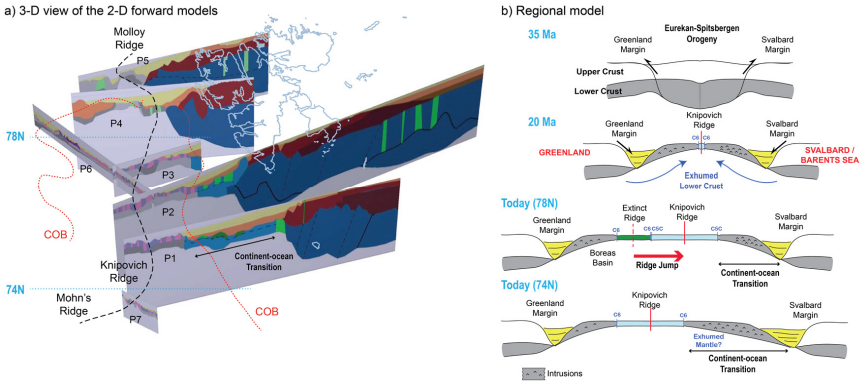

Figure 8. a. 3-D view of the 2-D forward models with location of Svalbard (not georeferenced), the Mid-Ocean Ridge and the COB seen from the surface. The gravity and magnetic forward models have been done with a common adjustement to the calculated response and homogeneized in terms of geometries and geophysical parameter. A wide continent-ocean transition along the Knipovich Ridge is interpreted on Profile P1 but is reduced in width in Profile P2. **b.** Stages of the seafloor spreading history of the Knipovich Ridge for the last

35 Ma. The Eurekan-Spitsbergen orogeny has likely thickened the crust, followed by the exhumation of the lower crust before the seafloor spreading initiation at isochron C6 (20 Ma). Present day's seafloor spreading involves a ridge jump at latitude 78N and a continuous seafloor spreading with a wider continent-ocean transition zone and possibly exhumed mantle on the east flank of the Knipovich Ridge at latitude 74N, (adapted after Dumais et al. (2020a), Fig. 4).

6 Conclusions

This study aimed to describe and model the crustal and mantle heterogeneities along the Knipovich Ridge and its surrounding margins. The new KRAS-16 aeromagnetic dataset enclosed the oceanic and transition domains. Aeromagnetic data from previous works were compiled to provide a global overview of the transition to the continental domain. The gravity compilation, the EM interpretation and the seismic interpretation provided indications and constraints to the gravity and magnetic interpretation.

1 The oceanic crust is clearly demarked by the striped magnetic pattern and its location confirmed by the 2-D forward models. The COB is derived from this interpretation and confirmed by the modelling.

2 The initiation of the seafloor spreading is delineated by magnetic isochron C6 (20 Ma) and an extinct ridge is modelled in the Boreas Basin. 2-D forward models are revised and unified accordingly suggesting the presence of a wide transition domain.

3 The magnetization in the oceanic domain is linked to the presence of volcanoes and bathymetric highs in the rift valley. Iron- and oxide-rich segments are identified along the rift valley.

4 The delineation of several lineaments and the bend configurationof the Knipovich Ridge is associated with a variation in the magnetization and settings along the Knipovich Ridge. Along with magmatic and amagmatic accretion, it possibly controls the seafloor spreading settings and fluid circulation influencing its composition and magnetization.

5 Mantle heterogeneities occur with an east-west lateral density variation east-west and indicate a transition from a hotter mantle in the oceanic domain to a colder mantle underneath the older continental crust.

6 We favor the presence of a wide transition lithospheric domain comprising an exhumed lower crust or mantle. The oblique spreading constrained by the Mohns Ridge and the East Greenland Ridge may have favored a continental stretching on the eastern margin. Compared to previous interpretation, we extend the Norwegian continental domain by up to 150 km farther west in the study area, a rare occurrence in plate tectonics.

Acknowledgments, Samples, and Data

We are thankful to the European Plate Observing System – Norway, the Norwegian Petroleum Directorate, and the Geological Survey of Norway to help funding the project. We thank Novatem, Inc. for the data acquisition, and our colleagues from AWI (Wilfried Jokat) and TGS (Reidun Myklebust) for providing aeromagnetic data from adjacent areas. The KRAS-16 aeromagnetic data are available in the Geological Survey of Norway public repository (https://geo.ngu.no/geoscienceportalopen) and on EPOS-N Portal (https://epos-no.uib.no:444/#/view/project). Due to data confidentiality, the regional magnetic compilation

cannot be disclosed. High-resolution bathymetric data are available upon request from the Norwegian Petroleum Directorate.

References

Barrère, C., Ebbing, J., & Gernigon, L. (2009). Offshore prolongation of Caledonian structures and basement characterisation in the western Barents Sea from geophysical modelling. *Tectonophysics*, *470*(1), 71-88. https://doi.org/https://doi.org/10.1016/j.tecto.2008.07.012

Barrère, C., Ebbing, J., & Gernigon, L. (2011). 3-D density and magnetic crustal characterization of the southwestern Barents Shelf: implications for the offshore prolongation of the Norwegian Caledonides. *Geophysical Journal International*, *184*(3), 1147-1166. https://doi.org/10.1111/j.1365-246X.2010.04888.x

Barton, P. J. (1986). The relationship between seismic velocity and density in the continental crust — a useful constraint? *Geophysical Journal International*, *87*(1), 195-208. https://doi.org/10.1111/j.1365-246X.1986.tb04553.x

Blischke, A., Gaina, C., Hopper, J. R., Péron-Pinvidic, G., Brandsdóttir, B., Guarnieri, P., et al. (2017). The Jan Mayen microcontinent: an update of its architecture, structural development and role during the transition from the Ægir Ridge to the mid-oceanic Kolbeinsey Ridge. *Geological Society, London, Special Publications*, *447*(1), 299-337. https://doi.org/10.1144/sp447.5

Bouligand, C., Glen, J. M. G., & Blakely, R. J. (2009). Mapping Curie temperature depth in the western United States with a fractal model for crustal magnetization. *Journal of Geophysical Research: Solid Earth*, *114*(B11). https://doi.org/10.1029/2009jb006494

Breivik, A., Mjelde, R., Grogan, P., Shimamura, H., Murai, Y., & Nishimura, Y. (2003). Crustal structure and transform margin development south of Svalbard based on ocean bottom seismometer data. *Tectonophysics*, *369*, 37-70.

Breivik, A., Mjelde, R., Grogan, P., Shimamura, H., Murai, Y., & Nishimura, Y. (2005). Caledonide development offshore–onshore Svalbard based on ocean bottom seismometer, conventional seismic, and potential field data. *Tectonophysics*, *401*, 79-117.

Breivik, A. J., & Mjelde, R. (2001a). Obs-98 survey: Final report oceanic profiles. *Report*, *Univ. of Bergen, Alleġt. 41, N-5007 Bergen*.

Breivik, A. J., & Mjelde, R. (2001b). Obs-98 survey: Final report western continental profiles. *Report*, *Univ. of Bergen, Alleġt. 41, N-5007 Bergen*.

Breivik, A. J., Verhoef, J., & Faleide, J. I. (1999). Effect of thermal contrasts on gravity modeling at passive margins: Results from the western Barents Sea. *Journal of Geophysical Research: Solid Earth*, *104*(B7), 15293-15311. https://doi.org/10.1029/1998jb900022

Brozena, J. M., Childers, V. A., Lawver, L. A., Gahagan, L. M., Forsberg, R., Faleide, J. I., & Eldholm, O. (2003). New aerogeophysical study of the Eurasia Basin and Lomonosov Ridge: implications for basin development.(Author Abstract). *Geology*, *31*(9), 825. https://doi.org/10.1130/g19528.1

Christensen, N. I., & Mooney, W. D. (1995). Seismic velocity structure and composition of the continental crust: A global view. *Journal of Geophysical Research: Solid Earth*, *100*(B6), 9761-9788. https://doi.org/https://doi.org/10.1029/95JB00259

Clerc, C., Jolivet, L., & Ringenbach, J.-C. (2015). Ductile extensional shear zones in the lower crust of a passive margin. *Earth and Planetary Science Letters*, *431*, 1-7. https://doi.org/10.1016/j.epsl.2015.08.038

Czuba, W., Grad, M., Guterch, A., Majdański, M., Malinowski, M., Mjelde, R., et al. (2008). Seismic crustal structure along the deep transect Horsted'05, Svalbard. *Polish Polar Research*, *29*(3), 279-290.

Czuba, W., Ritzmann, O., Nishimura, Y., Grad, M., Mjelde, R., Guterch, A., & Jokat, W. (2005). Crustal structure of northern Spitsbergen along the deep seismic transect between the Molloy Deep and Nordaustlandet. *Geophysical Journal International*, *161*(2), 347-364.

Dallmann, W. K. (2015). *Geoscience Atlas of Svalbard*.

Dentith, M., & Mudge, S. T. (2014). *Geophysics for the mineral exploration geoscientist*, Cambridge University Press.

Dick, H. J. B., Lin, J., & Schouten, H. (2003). An ultraslow-spreading class of ocean ridge. *Nature*, *426*(6965), 405-412. https://doi.org/10.1038/nature02128

Døssing, A., Dahl-Jensen, T., Thybo, H., Mjelde, R., & Nishimura, Y. (2008). East Greenland Ridge in the North Atlantic Ocean: An integrated geophysical study of a continental sliver in a boundary transform fault setting. *Journal of Geophysical Research: Solid Earth*, *113*(B10). https://doi.org/https://doi.org/10.1029/2007JB005536

Døssing, A., & Funck, T. (2012). Greenland Fracture Zone-East Greenland Ridge(s) revisited: Indications of a C22-change in plate motion? *Journal of Geophysical Research: Solid Earth*, *117*(B1), B01103. https://doi.org/10.1029/2011jb008393

Døssing, A., Jaspen, P., Watts, A. B., Nielsen, T., Jokat, W., Thybo, H., & Dahl-Jensen, T. (2016). Miocene uplift of the NE Greenland margin linked to plate tectonics: Seismic evidence from the Greenland Fracture Zone, NE Atlantic. *Tectonics*, *35*. https://doi.org/10.1002/2015tc004079

Dumais, M.-A., Gernigon, L., Olesen, O., Johansen, S. E., & Brönner, M. (2020a). New interpretation of the spreading evolution of the Knipovich Ridge derived from aeromagnetic data. *Geophysical Journal International*, *224*(2), 1422-1428. https://doi.org/10.1093/gji/ggaa527

Dumais, M. A., & Brönner, M. (2020). Revisiting Austfonna, Svalbard, with potential field methods – a new characterization of the bed topography and its physical properties. *The Cryosphere*, *14*(1), 183-197. https://doi.org/10.5194/tc-14-183-2020

Dumais, M. A., Olesen, O., Gernigon, L., Brönner, M., Lim, A., & Johansen, S. E. (2020b). KRAS-16: processing and interpretation. *NGU-rapport 2020.030*.

Eagles, G., Pérez-Díaz, L., & Scarselli, N. (2015). Getting over continent ocean boundaries. *Earth-Science Reviews*, *151*, 244-265.

Ebbing, J., Gernigon, L., Pascal, C., Olesen, O., & Osmundsen, P. T. (2009). A discussion of structural and thermal control of magnetic anomalies on the mid-Norwegian margin. *Geophysical Prospecting*, *57*(4), 665-681. https://doi.org/10.1111/j.1365-2478.2009.00800.x

Engen, Ø., Faleide, J. I., & Dyreng, T. K. (2008). Opening of the Fram Strait gateway: A review of plate tectonic constraints. *Tectonophysics*, *450*, 51-69.

Engen, Ø., Frazer, L. N., Wessel, P., & Faleide, J. I. (2006). Prediction of sediment thickness in the Norwegian-Greenland Sea from gravity inversion. *Journal of geophysical research*, *111*, B11403.

Faleide, J. I., Gudlaugsson, S. T., Eldholm, O., Myhre, A. M., & Jackson, H. R. (1991). Deep seismic transects across the sheared western Barents Sea-Svalbard continental margin. *Tectonophysics*, *189*(1), 73-89. https://doi.org/https://doi.org/10.1016/0040-1951(91)90488-E

Faleide, J. I., Myhre, A. M., & Eldholm, O. (1988). Early Tertiary volcanism at the western Barents Sea margin. *Geological Society, London, Special Publications*, *39*(1), 135. https://doi.org/10.1144/gsl.sp.1988.039.01.13

Faleide, J. I., Tsikalas, F., Breivik, A., Mjelde, R., Ritzmann, O., Engen, Ø., et al. (2008). Structure and evolution of the continental margin off Norway and Barents Sea. *Episodes*, *31*(1), 82-91.

Franke, D., Klitzke, P., Barckhausen, U., Berglar, K., Berndt, C., Damm, V., et al. (2019). Polyphase Magmatism During the Formation of the Northern East Greenland Continental Margin. *Tectonics*, *38*(8), 2961-2982. https://doi.org/10.1029/2019tc005552

Funck, T., Geissler, W. H., Kimbell, G. S., Gradmann, S., Erlendsson, Ö., McDermott, K., & Petersen, U. K. (2017). Moho and basement depth in the NE Atlantic Ocean based on seismic refraction data and receiver functions. *Geological Society, London, Special Publications*, *447*(1), 207-231. https://doi.org/10.1144/sp447.1

Gaina, C., Gernigon, L., & Ball, P. (2009). Palaeocene–Recent plate boundaries in the NE Atlantic and the formation of the Jan Mayen microcontinent. *Journal of the Geological Society*, *166*(4), 601-616. https://doi.org/10.1144/0016-76492008-112

Gaina, C., Nasuti, A., Kimbell, G. S., & Blischke, A. (2017). Break-up and seafloor spreading domains in the NE Atlantic. *Geological Society, London, Special Publications*, *447*(1), 393. https://doi.org/10.1144/sp447.12

Geosoft (2006). GM-SYS profile modeling. Gravity and Magnetic Modeling Software, v. 4.10. *Geosoft Incorporated*, p.116.

Geosoft (2013). How-to Guide. *Geosoft Incorporated*.

Geosoft (2014). Geosoft Oasis Montaj extension - GM-SYS 3D Modelling, Feature Sheet, *Geosoft Inc.*

Gernigon, L., Blischke, A., Nasuti, A., & Sand, M. (2015). Conjugate volcanic rifted margins, seafloor spreading, and microcontinent: Insights from new high-resolution aeromagnetic surveys in the Norway Basin. *Tectonics*, *34*(5), 907-933. https://doi.org/10.1002/2014tc003717

Gernigon, L., Brönner, M., Roberts, D., Olesen, O., Nasuti, A., & Yamasaki, T. (2014). Crustal and basin evolution of the southwestern Barents Sea: From Caledonian orogeny to continental breakup. *Tectonics*, *33*(4), 347-373. https://doi.org/10.1002/2013tc003439

Gernigon, L., Franke, D., Geoffroy, L., Schiffer, C., Foulger, G. R., & Stoker, M. (2019). Crustal fragmentation, magmatism, and the diachronous opening of the Norwegian-Greenland Sea. *Earth-Science Reviews*. https://doi.org/10.1016/j.earscirev.2019.04.011

Glebovsky, V. Y., Kaminsky, V. D., Minakov, A. N., Merkur'ev, S. A., Childers, V. A., & Brozena, J. M. (2006). Formation of the Eurasia Basin in the Arctic Ocean as inferred from geohistorical analysis of the anomalous magnetic field. *Geotectonics*, *40*(4), 263-281. https://doi.org/10.1134/s0016852106040029

Goussev, S. A., & Peirce, J. W. (2010). Magnetic basement: gravity-guided magnetic source depth analysis and interpretation. *Geophysical Prospecting*, *58*, 321-334. https://doi.org/10.1111/j.1365-2478.2009.00817.x

Grad, M., & Majorowicz, J. (2020). Geophysical properties of the crust and upper mantle of the ocean-continent transition in Svalbard area. *Polish Polar Research*, 1-22.

Grogan, P., Nyberg, K., Fotland, B., Myklebust, R., Dahlgren, S., & Riis, F. (2000). Cretaceous Magmatism South and East of Svalbard: Evidence from Seismic Reflection and Magnetic Data. *Polarforschung*, *68*, 25-34.

Hamann, N. E., Whittaker, R. C., & Stemmerik, L. (2005). Geological development of the Northeast Greenland Shelf. *Geological Society, London, Petroleum Geology Conference series*, *6*(1), 887. https://doi.org/10.1144/0060887

Harland, W. B. (1969). Contribution of Spitsbergen to Understanding of Tectonic Evolution of North Atlantic Region: Chapter 58: Arctic Regions.

Hermann, T., & Jokat, W. (2013). Crustal structures of the Boreas Basin and the Knipovich Ridge, North Atlantic. *Geophysical Journal International*, *193*, 1399-1414.

Holtedahl, O. (1926). Notes on the geology of northwestern Spitsbergen. *Det norske videnskaps-akademi i Oslo*.

Johansen, S. E., Panzner, M., Mittet, R., Amundsen, H. E. F., Lim, A., Vik, E., et al. (2019). Deep electrical imaging of the ultraslow-spreading Mohns Ridge. *Nature*, *567*(7748), 379-383. https://doi.org/10.1038/s41586-019-1010-0

Johansson, Å., Gee, D. G., Larionov, A. N., Ohta, Y., & Tebenkov, A. M. (2005). Grenvillian and Caledonian evolution of eastern Svalbard – a tale of two orogenies. *Terra Nova*, *17*, 317-325. https://doi.org/10.1111/j.1365-3121.2005.00616.x

Johansson, Å., Larionov, A. N., Tebenkov, A. M., Ohta, Y., & Gee, D. G. (2002). Caledonian granites of western and central Nordaustlandet, northeast Svalbard. *GFF*, *124*(3), 135-148. https://doi.org/10.1080/11035890201243135

Jokat, W., Geissler, W., & Voss, M. (2008). Basement structure of the north-western Yermak Plateau. *Geophysical Research Letters*, *35*(5). https://doi.org/10.1029/2007gl032892

Jokat, W., Lehmann, P., Damaske, D., & Bradley Nelson, J. (2016). Magnetic signature of North-East Greenland, the Morris Jesup Rise, the Yermak Plateau, the central Fram Strait: Constraints for the rift/drift history between Greenland and Svalbard since the Eocene. *Tectonophysics*, *691*, 98-109. https://doi.org/10.1016/j.tecto.2015.12.002

Kent, D. V., & Gee, J. (1996). Magnetic alteration of zero-age oceanic basalt. *Geology*, *24*(8), 703-706. https://doi.org/10.1130/0091-7613(1996)024<0703:maozao>2.3.co;2

Kenyon, S., Forsberg, R., & Coakley, B. (2008). New Gravity Field for the Arctic. *Eos, Transactions American Geophysical Union*, *89*(32), 289-290. https://doi.org/10.1029/2008eo320002

Klitzke, P., Faleide, J. I., Scheck-Wenderoth, M., & Sippel, J. (2015). A lithosphere-scale structural model of the Barents Sea and Kara Sea region. *Solid Earth*, *6*(1), 153-172. https://doi.org/10.5194/se-6-153-2015

Knies, J., & Gaina, C. (2008). Middle Miocene ice sheet expansion in the Arctic: Views from the Barents Sea. *Geochemistry, Geophysics, Geosystems*, *9*(2). https://doi.org/https://doi.org/10.1029/2007GC001824

Ku, C. C., & Sharp, J. A. (1983). Werner deconvolution for automated magnetic interpretation and its refinement using Marquart's inverse modeling. *Geophysics*, *48*(6), 754-774. https://doi.org/10.1190/1.1441505

LaFemina, P. C. (2015). Chapter 3 - Plate Tectonics and Volcanism. in *The Encyclopedia of Volcanoes (Second Edition)*. edited by H. Sigurdsson, pp. 65-92, Academic Press, Amsterdam.

Lauritzen, Ø., & Ohta, Y. (1984). Geological map of Svalbard 1:500,000. Sheet 4G, Nordaustlandet. *Nor. Polarinst. Skr. 154C*.

Libak, A., Mjelde, R., Keers, H., Faleide, J. I., & Murai, Y. (2012). An integrated geophysical study of Vestbakken Volcanic Province, western Barents Sea continental margin, and adjacent oceanic crust. *Marine Geophysical Researches*, *33*, 185-207.

Lim, A. (2020). Subsurface structure and hydrothermal fluid circulation at the Mohns mid-ocean ridge: a multi-geophysical investigation, Doctoral Thesis, 147 pp, Norwegian University of Science and Technology.

Ljones, F., Kuwano, A., Mjelde, R., Breivik, A., Shimamura, H., Murai, Y., & Nishimura, Y. (2004). Crustal transect from the North Atlantic Knipovich Ridge to the Svalbard Margin west of Hornsund. *Tectonophysics*, *378*, 17-41.

Loviknes, K., Jeddi, Z., Ottemöller, L., & Barreyre, T. (2020). When Clocks Are Not Working: OBS Time Correction. *Seismological Research Letters*.

Ludwig, W., Nafe, J., & Drake, C. (1970). Seismic refraction. *The sea*, *4*(1), 53-84.

Lundin, E. R., & Doré, A. G. (2011). Hyperextension, serpentinization, and weakening: A new paradigm for rifted margin compressional deformation. *Geology*, *39*(4), 347-350. https://doi.org/10.1130/g31499.1

Marello, L., Ebbing, J., & Gernigon, L. (2013). Basement inhomogeneities and crustal setting in the Barents Sea from a combined 3D gravity and magnetic model. *Geophysical Journal International*, *193*(2), 557-584. https://doi.org/10.1093/gji/ggt018

Mather, B., & Delhaye, R. (2019). PyCurious: A Python module for computing the Curie depth from the magnetic anomaly. *Journal of Open Source Software*, *4*(39), 1544.

Minakov, A., Mjelde, R., Faleide, J. I., Flueh, E. R., Dannowski, A., & Keers, H. (2012). Mafic intrusions east of Svalbard imaged by active-source seismic tomography. *Tectonophysics*, *518-521*, 106-118. https://doi.org/10.1016/j.tecto.2011.11.015

Minshull, T. A. (2009). Geophysical characterisation of the ocean–continent transition at magma-poor rifted margins. *Comptes Rendus Geoscience*, *341*(5), 382-393. https://doi.org/10.1016/j.crte.2008.09.003

Mork, M. E., & Duncan, R. (1993). Late Pliocene basaltic volcanism on the Western Barents Shelf margin: implications from petrology and 40Ar-39Ar dating of volcaniclastic debris from a shallow drill core. *Norsk Geologisk Tidsskrift*, *73*(4), 209-225.

Mosar, J., Lewis, G., & Torsvik, T. (2002). North Atlantic sea-floor spreading rates: implications for the Tertiary development of inversion structures of the Norwegian–Greenland Sea. *Journal of the Geological Society*, *159*(5), 503. https://doi.org/10.1144/0016-764901-135

Nemčok, M., Sinha, S. T., Doré, A. G., Lundin, E. R., Mascle, J., & Rybár, S. (2016). Mechanisms of microcontinent release associated with wrenching-involved continental break-up; a review. *Geological Society, London, Special Publications*, *431*(1), 323. https://doi.org/10.1144/sp431.14

Oakey, G. N., & Chalmers, J. A. (2012). A new model for the Paleogene motion of Greenland relative to North America: Plate reconstructions of the Davis Strait and Nares Strait regions between Canada and Greenland. *Journal of Geophysical Research: Solid Earth*, *117*(B10). https://doi.org/10.1029/2011jb008942

Ohta, Y. (1994). Caledonian and precambrian history in Svalbard: a review, and an implication of escape tectonics. *Tectonophysics*, *231*(1), 183-194. https://doi.org/10.1016/0040-1951(94)90129-5

Olesen, O., Brönner, M., Ebbing, J., Gellein, J., Gernigon, L., Koziel, J., et al. (2010). New aeromagnetic and gravity compilations from Norway and adjacent areas: methods and applications. *Geological Society, London, Petroleum Geology Conference series*, *7*(1), 559-586. https://doi.org/10.1144/0070559

Omosanya, K. O., Johansen, S. E., & Abrahamson, P. (2016). Magmatic activity during the breakup of Greenland-Eurasia and fluid-flow in Stappen High, SW Barents Sea. *Marine and Petroleum Geology*, *76*, 397-411. https://doi.org/10.1016/j.marpetgeo.2016.05.017

Parker, R. L., & Huestis, S. P. (1974). The inversion of magnetic anomalies in the presence of topography. *Journal of Geophysical Research (1896-1977)*, *79*(11), 1587-1593. https://doi.org/10.1029/JB079i011p01587

Pérez-Gussinyé, M., Reston, T. J., & Phipps Morgan, J. (2001). Serpentinization and magmatism during extension at non-volcanic margins: the effect of initial lithospheric structure. *Geological Society, London, Special Publications*, *187*(1), 551. https://doi.org/10.1144/gsl.sp.2001.187.01.27

Perfit, M. (1999). Earth's oceanic crust. *CP Marshall & RW Fairbridge (eds.): Encyclopedia of Geochemistry. Berlin–New York, Springer Verlag, 179*, *182*.

Phillips, J. D. (1997). Potential-Field Geophysical Software for the PC, version 2.2. *USGS open-File Report*, *97*. https://doi.org/10.3133/ofr97725

Piepjohn, K., von Gosen, W., & Tessensohn, F. (2016). The Eurekan deformation in the Arctic: an outline. *Journal of the Geological Society*, *173*(6), 1007-1024. https://doi.org/10.1144/jgs2016-081

Polteau, S., Hendriks, B. W. H., Planke, S., Ganerød, M., Corfu, F., Faleide, J. I., et al. (2016). The early cretaceous Barents Sea sill complex: distribution, 40Ar/39Ar geochronology, and implications for carbon gas formation. *Palaeogeography, Palaeoclimatology, Palaeoecology*, *441*, 83-95. https://doi.org/10.1016/j.palaeo.2015.07.007

Ritzmann, O., & Jokat, W. (2003). Crustal structure of northwestern Svalbard and the adjacent Yermak Plateau: evidence for Oligocene detachment tectonics and non-volcanic breakup. *Geophysical Journal International*, *152*(1), 139-159. https://doi.org/10.1046/j.1365-246X.2003.01836.x

Ritzmann, O., Jokat, W., Czuba, W., Guterch, A., Mjelde, R., & Nishimura, Y. (2004). A deep seismic transect from Hovgård Ridge to northwestern Svalbard across the continental-ocean transition: A sheared margin study. *Geophysical Journal International*, *157*, 683-702.

Ritzmann, O., Jokat, W., Mjelde, R., & Shimamura, H. (2002). Crustal structure between the Knipovich Ridge and the Van Mijenfjorden (Svalbard). *Marine Geophysical Researches*, *23*(5-6), 379-401.

Roest, W., & Srivastava, S. (1989). Sea-floor spreading in the Labrador Sea: A new reconstruction. *Geology*, *17*(11), 1000-1003.

Sandwell, D. T., Müller, R. D., Smith, W. H. F., Garcia, E., & Francis, R. (2014). New global marine gravity model from CryoSat-2 and Jason-1 reveals buried tectonic structure. *Science*, *346*(6205), 65. https://doi.org/10.1126/science.1258213

Schiffer, C., Peace, A., Phethean, J., Gernigon, L., McCaffrey, K., Petersen, K. D., & Foulger, G. (2019). The Jan Mayen microplate complex and the Wilson cycle. *Geological Society, London, Special Publications*, *470*(1), 393. https://doi.org/10.1144/sp470.2

Schreider, A. A., Schreider, A., Sazhneva, A., Kluev, M., & Brehovskih, A. (2019). Kinematic Model of Development of Eastern Areas of the Gakkel Mid-Ocean Ridge in the Eurasian Basin of the Arctic Ocean. *Oceanology*, *59*(1), 133-142.

Scott, R. A. (2000). Mesozoic-Cenozoic evolution of East Greenland: implications of a reinterpreted continent-ocean boundary location. *Polarforschung*, *68*, 83-91.

Searle, R. (2013). *Mid-ocean ridges*, Cambridge University Press.

Seton, M., Müller, R. D., Zahirovic, S., Gaina, C., Torsvik, T., Shephard, G., et al. (2012). Global continental and ocean basin reconstructions since 200Ma. *Earth-Science Reviews*, *113*(3), 212-270. https://doi.org/https://doi.org/10.1016/j.earscirev.2012.03.002

Skilbrei, J. R. (1992). Preliminary interpretation of aeromagnetic data from Spitsbergen, Svalbard Archipelago (76°–79°N): Implications for structure of the basement. *Marine Geology*, *106*(1), 53-68. https://doi.org/10.1016/0025-3227(92)90054-L

Skogseid, J., Planke, S., Faleide, J. I., Pedersen, T., Eldholm, O., & Neverdal, F. (2000). NE Atlantic continental rifting and volcanic margin formation. *Geological Society, London, Special Publications*, *167*(1), 295. https://doi.org/10.1144/gsl.sp.2000.167.01.12

Srivastava, S. P., & Roest, W. R. (1999). Extent of oceanic crust in the Labrador Sea. *Marine and Petroleum Geology*, *16*(1), 65-84. https://doi.org/10.1016/S0264-8172(98)00041-5

Srivastava, S. P., & Tapscott, C. R. (1986). Plate kinematics of the North Atlantic. in *The Western North Atlantic Region*. edited by P. R. Vogt and B. E. Tucholke, Geological Society of America.

Suckro, S. K., Gohl, K., Funck, T., Heyde, I., Schreckenberger, B., Gerlings, J., & Damm, V. (2013). The Davis Strait crust—a transform margin between two oceanic basins. *Geophysical Journal International*, *193*(1), 78-97. https://doi.org/10.1093/gji/ggs126

Sutra, E., & Manatschal, G. (2012). How does the continental crust thin in a hyperextended rifted margin? Insights from the Iberia margin. *Geology*, *40*(2), 139-142. https://doi.org/10.1130/g32786.1

Talwani, M., & Eldholm, O. (1977). Evolution of the Norwegian-Greenland Sea. *Geological Society of America Bulletin*, *88*, 969-999.

Tivey, M. A., & Johnson, H. P. (1993). Variations in oceanic crustal structure and implications for the fine-scale magnetic anomaly signal. *Geophysical Research Letters*, *20*(17), 1879-1882. https://doi.org/https://doi.org/10.1029/93GL01485

Trulsvik, M., Myklebust, R., Polteau, S., & Planke, S. (2011). Geophysical atlas of the East Greenland Basin: Integrated seismic, gravity and magnetic interpretation. *Volcanic Basin Petroleum Research AS, TGS-NOPEC Geophysical Company*

Vamvaka, A., Pross, J., Monien, P., Piepjohn, K., Estrada, S., Lisker, F., & Spiegel, C. (2019). Exhuming the Top End of North America: Episodic Evolution of the Eurekan Belt and Its Potential Relationships to North Atlantic Plate Tectonics and Arctic Climate Change. *Tectonics*. https://doi.org/10.1029/2019tc005621

Vormann, M., & Jokat, W. (2021). Crustal variability along the rifted/sheared East African margin: a review. *Geo-Marine Letters*, *41*(2), 19. https://doi.org/10.1007/s00367-021-00690-y

Vorren, T. O., Richardsen, G., Knutsen, S.-M., & Henriksen, E. (1991). Cenozoic erosion and sedimentation in the western Barents Sea. *Marine and Petroleum Geology*, *8*(3), 317-340.

Voss, M., & Jokat, W. (2007). Continent-ocean transition and voluminous magmatic underplating derived fromP-wave velocity modelling of the East Greenland continental margin. *Geophysical Journal International*, *170*(2), 580-604. https://doi.org/10.1111/j.1365-246X.2007.03438.x

Werner, S. (1955). Interpretation of magnetic anomalies as sheet-like bodies. *Sveriges Geologiska Undersökning, Series C, Årsbok*, *43*(6).

Whitmarsh, R. B., Pinheiro, L. M., Miles, P. R., Recq, M., & Sibuet, J.-C. (1993). Thin crust at the western Iberia Ocean-Continent transition and ophiolites. *Tectonics*, *12*(5), 1230-1239. https://doi.org/10.1029/93tc00059

Zarayskaya, Y. A. (2017). Segmentation and seismicity of the ultraslow Knipovich and Gakkel mid-ocean ridges. *Geotectonics*, *51*(2), 163-175. https://doi.org/10.1134/s0016852117010095

Hydrothermal Activity at the Ultraslow-Spreading Mohns Ridge: New Insights from Near-Seafloor Magnetics

A. Lim, M. Brönner, S. Johansen & **M.-A. Dumais**

Research article published in Geochemistry, Geophysics, Geosystems, 2019

My contribution to this article consisted in assisting in the data processing, 2-D forward model, data interpretation and improvement of the manuscript. Anna Lim acquired the data and samples on the MARMINE/NTNU research cruise, conducted data processing and interpretation, and primary wrote the manuscript. Ståle Johansen and Marco Brönner contributed to the scientific discussions

Geochemistry, Geophysics, Geosystems

RESEARCH ARTICLE
10.1029/2019GC008439

Hydrothermal Activity at the Ultraslow-Spreading Mohns Ridge: New Insights From Near-Seafloor Magnetics

Anna Lim[1], Marco Brönner[1,2], Ståle Emil Johansen[1], and Marie-Andrée Dumais[1,2]

[1]Department of Geoscience and Petroleum, Norwegian University of Science and Technology, Trondheim, Norway, [2]Geological Survey of Norway, Trondheim, Norway

Key Points:

- We present first geophysical observations from the basalt-hosted active hydrothermal site Loki's Castle, situated at the axial volcanic ridge
- Sediment-hosted extinct hydrothermal site Mohn's Treasure, located at the ridge flank, is associated with magnetization high
- Magnetic data analysis reveals two new fossil hydrothermal sites in the vicinity of the Mohn's Treasure

Correspondence to:
A. Lim,
anna.lim@ntnu.no

Citation:
Lim, A., Brönner, M., Johansen, S. E., & Dumais, M.-A. (2019). Hydrothermal activity at the ultraslow-spreading Mohns Ridge: New insights from near-seafloor magnetics. *Geochemistry, Geophysics, Geosystems*, *20*. https://doi.org/10.1029/2019GC008439

Received 15 MAY 2019
Accepted 24 OCT 2019
Accepted article online 19 NOV 2019

Abstract Hydrothermal circulation is a process fundamental to all types of mid-ocean ridges that largely impacts the chemical and physical balance of the World Ocean. However, diversity of geological settings hosting hydrothermal fields complicates the exploration and requires thorough investigation of each individual case study before effective criteria can be established. Analysis of high-resolution bathymetric and magnetic data, coupled with video and rock samples material, furthers our knowledge about mid-ocean-ridge-hosted venting sites and aid in the interpretation of the interplay between magmatic and tectonic processes along the axial volcanic ridges. The rock-magnetic data provide constraints on the interpretation of the observed contrasts in crustal magnetization. We map the areal extent of the previously discovered active basalt-hosted Loki's Castle and inactive sediment-hosted Mohn's Treasure massive sulfide deposits and infer their subsurface extent. Remarkably, extinct hydrothermal sites have enhanced magnetizations and display clear magnetic signatures allowing their confident identification and delineation. Identified magnetic signatures exert two new fossil hydrothermal deposits, MT-2 and MT-3. The Loki's Castle site coincides with negative magnetic anomaly observed in the 2-D magnetic profile data crossing the deposit. First geophysical investigations in this area reveal the complexity of the geological setting and the variation of the physical properties in the subsurface.

1. Introduction

Marine magnetic data provided one of the most powerful tools in the development of plate tectonic theory (Vine & Wilson, 1965) and have largely contributed to mid-ocean ridge (MOR) research ever since. Discoveries of hydrothermal activity along the MORs and the resource potential associated with these processes have brought more extensive and detailed exploration to these deep and remote environments. Early studies only attributed hydrothermal activities to fast spreading ridges. Reports of hydrothermal venting at the slow and ultra-slow spreading ridges (less than 20 mm/year; Baker et al., 2004; Dick et al., 2003; Edmonds et al., 2003; German et al., 1998; Pedersen et al., 2010) have opened new areas, like the Arctic Mid-Ocean Ridge (AMOR), to more rigorous research and exploration. At the ultra-slow MOR system north of Iceland, 37 hydrothermal vent sites have been reported since the first discovery in 1980 in the area (Varentsov et al., 1980), followed by more systematic exploration at the end of the 1990s (Beaulieu & Szafranski, 2018). The Mohns ultra-slow-spreading ridge hosts five vent sites (Figure 1a), two of these sites are discussed in this paper. Loki's Castle is an active basalt-hosted vent field investigated by several research cruises (Baumberger et al., 2016; Johansen et al., 2019; Ludvigsen et al., 2016; Pedersen, Thorseth, et al., 2010). High-resolution magnetic data, however, are presented in this paper for the first time. Mohn's Treasure is an extinct vent field approximately 30 km southwest of Loki's Castle (Figure 1b) that was discovered by dredging of sulfide material from the seafloor (Pedersen et al., 2010) but has not yet been studied in detail.

Earlier studies have employed video surveying and water column measurements (Beaulieu & Szafranski, 2018) that have very localized relevance and are only applicable to active venting sites. Thus, geophysical remote sensing becomes critical for locating extinct hydrothermal areas, especially when buried by sediments or lava flows. Several studies (Zierenberg et al., 1998, and references therein) have stated the higher economic potential of such sites that are usually mature and well-developed deposits (Houghton et al., 2004). In this study, we report two new potential fossil hydrothermal deposits in the vicinity of the previously discovered Mohn's Treasure. Even though active sites are easier to identify in this respect, the factual subsurface database from these areas is largely incomplete due to ethical concerns of direct drilling, and technical

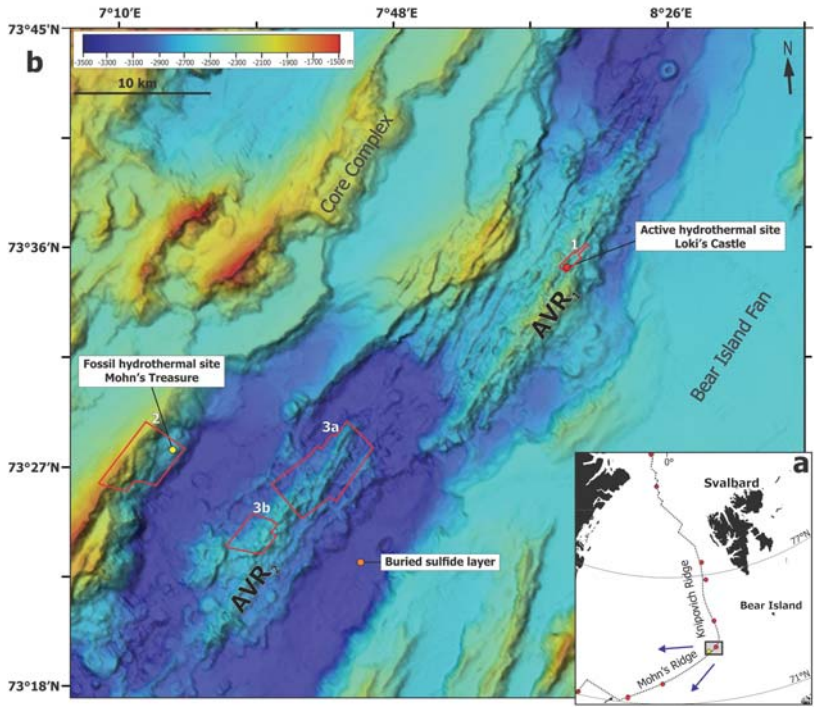

Figure 1. Location of the near-seafloor surveys. **(**a) Regional bathymetric map of the Mohns Ridge northernmost segment resolved at 100 m (Norwegian Mapping Authority, 2015). Red lines mark survey outlines. Active hydrothermal venting site, Loki's Castle, is denoted by red filled circle, extinct venting site, Mohn's Treasure, by yellow filled circle, an orange circle denotes the location of sediment core sample where sulfide layer was found around 1.5-m subsurface (Pedersen, Rapp, et al., 2010). Both flanks of the rift and the valley itself are covered by distal parts of Bear Island Fan sediments (Bruvoll et al., 2009). AVR stands for axial volcanic ridge. (b) Regional overview map of the Mohn's and Knipovich ridges. The black rectangle marks the location of panel a. Red circles denote active hydrothermal venting sites, yellow circle—extinct hydrothermalism sites (Beaulieu & Szafranski, 2018). The black dotted line marks the spreading axis. Blue arrows denote the North American and Eurasian plate-movement directions relative to a fixed hotspot reference frame (Gripp & Gordon, 2002).

challenges associated with it. Detailed magnetic data helps us in constraining both areal and depth extent of the identified deposits.

Regional, publicly available bathymetry (Norwegian Mapping Authority, 2015), electromagnetic and magnetotelluric data (Johansen et al., 2019), reflection seismic data (Bruvoll et al., 2009) proved to be highly instrumental in understanding and describing large-scale processes driving hydrothermal circulation. However, the localization of the associated deposits within the permissive tracts, favorable for exploration, is still not well understood and mainly based on probabilistic assessment rather than on geological and physical characteristics (Juliani & Ellefmo, 2018). Here, we use the interpretation of high-resolution bathymetry and near-seafloor magnetics from the confirmed active and inactive hydrothermal sites and adjacent axial volcanic ridges to further our understanding about the factors controlling the occurrence of such deposits. By doing so, we contribute to the current knowledge base in a local context of the Mohns Ridge geology, and the global context of mid-ocean-ridge venting. The data examination provides a few insights on subsurface processes of hydrothermal circulation and its interplay with tectonic and magmatic processes at the slow-spreading ridges.

2. Geological Setting

The study area is located at the northern part of the Mohns Ridge where the MOR transitions into the Knipovich Ridge after bending ~80° along axis strike (Figure 1a). The Mohn-Knipovich Bend was formed as a result of the major plate boundaries reorganization, involving a 30° shift in the plate motion, followed by the initiation of oblique spreading of the previously orthogonal spreading Mohns Ridge and the inception of the Knipovich Ridge at about chron 13 (38 Ma; Talwani & Eldholm, 1977; Vogt, 1986). The Mohns Ridge is an ultraslow and obliquely spreading ridge with a full rate estimated at ~15.6 mm/year for the last 10 Ma (Mosar et al., 2002; Vogt, 1986). Topography is rough and has a pronounced difference between the ridge flanks, reflecting the complexity of the spreading history of the Norwegian-Greenland basins. The asymmetry is expressed at multiple levels and is attributed to the oblique and asymmetric motion of the European and North American plates rather than asymmetric sediment loading, which barely follows the basement topography (Johansen et al., 2019; Talwani & Eldholm, 1977; *P* Vogt et al., 1982). Both flanks of the rift valley and the valley floor are covered by sediments from the Bear Island Fan with thickness reaching up to ~800 m with larger volumes deposited on the eastern side (Bruvoll et al., 2009).

Transform faults do not dissect the ridge, yet the MOR is characterized by linked magmatic (volcanic) and amagmatic (tectonic) segments (Dick et al., 2003). Topographic highs present in the axial valley of the study area are interpreted as being volcanic in origin (Crane et al., 1999; Géli et al., 1994). Abundant volcanic features such as prominent cones, flat-topped volcanoes, and volcanic ridges, are observed in the bathymetric data and have corresponding short-wavelength anomalies in regional magnetic data (Géli et al., 1994; Pedersen, Rapp, et al., 2010) that support the hypothesis that the two domed elongated edifices discussed in this paper are neovolcanic axial volcanic ridges (AVR_1 and AVR_2). The life cycle of an AVR alternates between magmatic and tectonic phases, following the intermittent magmatic and tectonic focusing and defocusing along the axis due to restricted magma supply (Parson et al., 1993). The area is seismically active—earthquake epicenters located within the ridge valley closely correlates with the major faults and volcanoes at the graben floor, suggesting a tight link between melt placement and faulting processes (Hopper et al., 2014; International Seismological Centre, 2018; Johansen et al., 2019). The interplay between these processes is of major importance for hydrothermal circulation along the ridges (McCaig et al., 2007).

Loki's Castle is an active high-temperature hydrothermal venting field discovered in 2008 (Pedersen, Thorseth, et al., 2010). It occurs at the northernmost AVR of the Mohns Ridge that rises approximately 1,300 m above the rift valley floor at 2,000-m depth. This AVR is locally perpendicular to the spreading direction and reaches around 30-km length. Topographically the ridge is composed of hummocky terrain with notable tectonic disruption. En echelon faults can be traced along the entire ridge, which is locally covered by fresh lava flows. Volcanic cones, smaller ridges, flat-topped volcanoes are common features. Sediment thickness varies across the area providing information on the relative age of the underlying volcanic features (Mitchell et al., 1998). Geochemical analysis of the hydrothermal fluid collected from the black smokers, that is, end-member volatile concentrations, supports magmatic influence in the area (Pedersen, Thorseth, et al., 2010), confirming that Loki's Castle is a basalt-hosted site. There are also indications of fluid interaction with ultramafic rocks and a significant footprint of sediment influence (Baumberger et al., 2016), which likely results from the deep fault and across-axis circulation as shown in a recent deep electromagnetic imaging study across the ridge by Johansen et al. (2019).

Unlike the AVR hosting Loki's Castle, the southern neo-volcanic ridge (AVR_2) is less pronounced and exhibits terrain strongly dominated by young pillow flows. The tectonic disruption here is less prominent than at the northern AVR and is primarily attributed to syn-magmatic tectonism. Vertical disruption is not significant, whereas crustal fissures are a common observation. The AVR extends for approximately 25 km in a northeasterly direction and is locally orthogonal to the spreading direction and rises on average 500 m above the valley floor. The summit is located at the center of the neo-volcanic zone, at 2,500-m water depth reaching around 800 m above the valley floor.

Mohn's Treasure area is the most geologically distinctive among three study areas as it is situated at the flank of a rift valley, west of the AVR_2. The general trend of the major extensional fault creating the inner wall of the axial rift is about 039°N. The area is predominantly composed of lithified and partly lithified sediments that represent distal parts of Bear Island fan deposited in the rift valley, subsequently uplifted by the marginal faults, and then mass wasted (Pedersen, Rapp, et al., 2010).

3. Data Collection and Processing

Near-bottom high-resolution magnetic data, bathymetry, and rock samples were collected during the MarMine cruise onboard *Polar King* multipurpose vessel in 2016 (Ludvigsen et al., 2016). Data acquisition was carried out using an autonomous underwater vehicle (AUV) *Hugin* by *Kongsberg Maritime*. Two heavy-duty remotely operated vehicles (ROVs), *Triton XLX* and *XLR*, were used for sampling and video surveying.

A total of five different AUV dives are presented in this paper and are grouped according to their location into three survey areas: Loki's Castle active venting site: Survey Area 1 (AVR_1); Mohn's Treasure extinct venting site: Survey Area 2; axial volcanic ridge (AVR_2) exploration areas: Survey Areas 3a and 3b (Figure 1). The AUV surveyed along parallel profiles spaced by 150 m apart (250 m for Surveys 3a and b) at the nominal altitude of 100 m above the valley floor, ranging from 40 to 270 m. The bathymetric data were provided by a combination of *EM 2040* multibeam echosounder and interferometric side-scan sonar *HiSAS 1030* (both provided by *Kongsberg Maritime*). Resulting bathymetric maps were gridded at 1 m each, except for the Mohn's Treasure site where the grid resolution is 4 m due to the difficulties experienced by the AUV while surveying a steep slope. The regional overview bathymetric map is a ship-based grid resolved at 100 m collected for the *Norwegian Petroleum Directorate* in 2000 (Norwegian Mapping Authority, 2015).

3.1. Magnetic Data

The high-resolution vector magnetic field data were collected using a self-compensating three-axis fluxgate magnetometer system developed by *Ocean Floor Geophysics* that was rigidly mounted inside the AUV. The dynamic range of the magnetometer covers ±65,000 nT with a resolution of 0.01 nT, and ± 0.5-nT peak-to-peak noise level. Raw data consisted of magnetic intensity for three components, and vehicle attitude data (heading, roll, and pitch) that were logged simultaneously and interpolated to the magnetic data sampling rate of 19 Hz. The topography of the seafloor acquired by the multibeam echosounder was sampled to 1-m cell size grid (and 4 m for Survey 2).

Even though the AUV body is made from nonmagnetic carbon fiber laminate and synthetic foam, the propulsion motor and other payload sensors still affect the magnetic measurements. At the beginning of each survey, calibration maneuvers were performed to estimate the best correction for the vehicle-induced field and its interaction with the Earth's magnetic field. It involved flying a square pattern with the change of both the heading and altitude, creating a set of reciprocal lines. Recorded data were then used to calculate correction terms to remove the influence of the vehicle movements and the heading effects on the measured magnetic data as described by Honsho et al. (2013) and Bloomer et al. (2014). The maneuver and correction were performed for each dive separately. The level of noise related to the platform in the recorded data was estimated to be ±10 nT. The correction removed most of the false maneuver-related short-wavelength apparent anomalies and improved the noise level marginally.

No crossing tie-lines were performed during the survey to correct for variations of the Earth's magnetic field due to ionospheric influences and/or ocean current induced magnetic fields; neither there was a base station on the seafloor. Geomagnetic observatory recordings of the magnetic field at Bjørnøya and Tromsø, and calibrated variometers at Longyearbyen and Jan Mayen showed moderate magnetic activity during the surveys with a peak magnitude of around 100–150 nT (Tromsø Geophysical Observatory, 2018). However, no correlation was found upon visual inspection when comparing the diurnal data with recorded magnetic field data, and consequently, no such correction was performed on the data. The compensated magnetic field data for all datasets were low-pass filtered to remove residual uncompensated vehicle motion noise at wavelengths shorter than 50 m using a Butterworth filter.

Due to autonomous character of the data acquisition in a relatively poorly known and very rugged topography—the NMA 2015 bathymetric map of 100-m grid resolution was used for survey planning and navigational purposes—recorded survey altitudes were not consistent with the nominal constant drape values. While direct effects of vehicle behavior like heading change, pitching, rolling, and vehicle-induced field noise was taken care of in the first steps of the processing sequence, nonconsistent terrain clearance caused a loss of signal resolution and distortion of some anomalies. To account for these issues, we used the *CompuDrape* extension integrated into *Oasis Montaj* software suite (Paterson et al., 1990). It computes the continued field at a set of different levels then interpolating the values on a specified draped surface. As

pointed out by several studies (Cordell, 1985; Pilkington & Roest, 1992; Pilkington & Thurston, 2001), even though this method is not very rigorous mathematically it proved to work well in practice. It maintains the data resolution compared to other upward continuation approaches. An example of the drape correction applicability test is illustrated in Figure 2. Having measurements at two different altitudes at the Loki's Castle survey allowed us to test this method. We compared the continued field intensity profiles using low- and high-flight modes data. Assuming the drape-fixed TMI profile from high-flight data is close to ideal, as the terrain clearance is highly consistent for the most part, and thus the corrections were minor (Figures 2b and 2c), the comparison of this profile and the TMI profile computed from the low-flight data, acquired 40 m lower on average, demonstrates satisfactory results and the utility of the approach. A standard deviation lies within 150 nT for all profiles with two flight-modes tested. However, the decline in the resolution for larger altitude difference is considerable. As this method involves both a downward field continuation and a more stable upward field continuation, careful attention was given to the choice of the new observation height. This choice was based on the dominant altitude value, and the magnetic frequency content to minimize downward continuation noise amplification and upward continuation signal loss. Thus, the drape recomputed nominal altitude was set to 100 m for surveys 1, 2, and 3a, 150 m for the Survey 3b, and 60 m for Loki's Castle low-altitude dataset. Given the average variation in the flight altitude for all surveys and the frequency content of the signal of interest, the results of this method are satisfactory. We also tested both line- and grid-based approaches on the data, displaying better results in the former approach since grid-based draping tends to amplify interpolation errors, especially in case of bigger difference in altitude between the adjacent lines, producing errors in the computed gradients orthogonal to the lines.

Subsequently, a microleveling correction was applied to the profile data to reduce the long-wavelength noise caused by the discrepancy between adjacent survey lines (Ferraccioli et al., 1998; Minty, 1991). The TMI data was then transformed into magnetic anomaly data by removing the mathematically approximated geomagnetic field—International Geomagnetic Reference Field (IGRF; Thébault et al., 2015). In the end, a reduction to the pole (RTP) transformation (Baranov, 1957) was applied by placing magnetic anomalies over their sources. The magnetic field direction in the survey area was assumed to have a declination of 2° and inclination of 80°. Finally, the resultant magnetic anomaly data were interpolated onto 30 m spaced grid (40 m for Survey 3b) by a minimum curvature algorithm.

Other techniques used in this paper have qualitative or semi-quantitative character, utilize total magnetic field derivatives for the interpretation and include tilt derivative (Miller & Singh, 1994), analytical signal (Nabighian et al., 2005; Roest et al., 1992) and Euler deconvolution (Reid et al., 1990; Thompson, 1982). The analytic signal is independent of the inclination of the magnetic field and of the source magnetization. Following the assumption that the isolated anomalies are caused by vertical contacts, the analytic signal can be used to estimate depth using a simple amplitude half-width rule (Roest et al., 1992). Euler deconvolution is an automated technique for depth estimation that is based on Euler's homogeneity relationship and does not require any a priori knowledge of the geology (Thompson, 1982). However, the depth resolution is limited by the grid spatial resolution. The data were analyzed using the standard Euler deconvolution for contacts and step-like structures (Reid et al., 1990) to aid interpretation of the gross structural trends. The Located Euler deconvolution, which locates confined peak-like structures in the data, was performed to examine cylinder-like structures that are assumed to represent the geometry of the studied deposits. In the case of Loki's Castle, we used the measured vertical gradient obtained by calculating the difference between the two datasets of low- and high-flight modes and dividing it by the difference in their nominal altitudes instead of using the calculated vertical derivative.

The magnetic tilt derivative enhances the magnetic fabric. Originally introduced by Miller and Singh (1994), it has the useful property of being positive over the source, and negative outside the source region, crossing through zero at, or near, the edge of a vertical-sided polygon. TDR aids in mapping subtle basement fabric through enhancing small-amplitude signals so weak magnetic bodies such as hydrothermal deposits are treated with the same weight as strongly magnetic bodies (Verduzco et al., 2004). The combination of these attributes provides a useful tool for data enhancement and further interpretation and mapping of geologic features.

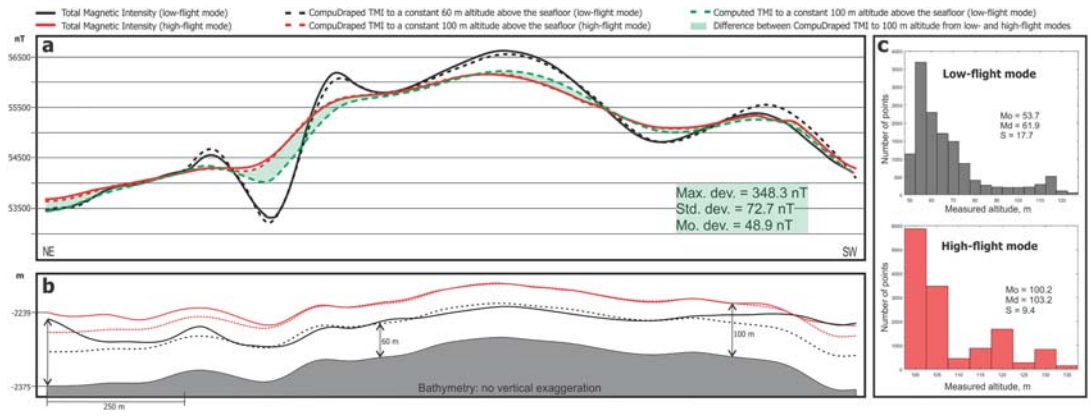

Figure 2. Comparison between the measured- and constructed-drape TMI profiles in the rough terrain of Loki's Castle: Line 5 in Figure 5. (a) Original TMI profiles are denoted by solid lines: low-flight mode is black, high-flight mode is red. Both modes were acquired with inconsistencies in altitude displayed in (b) and (c) panels. Dashed lines are obtained using a CompuDrape algorithm and correspond to the new constant altitudes above the seafloor: 60 and 100 m. (b) Bathymetric profile with original loose drapes for low- and high-flight mode surveys, in black and red solid lines respectively. Dashed lines mark fixed-drape profiles. (c) Original altitude distributions for low- and high-mode surveys for the displayed survey line with modal, median, and standard deviation values.

The 2-D magnetic forward modeling has been carried out using the GM-SYS Profile Modeling module integrated in *Oasis Montaj* software package. This type of analysis is used to calculate the magnetic response from a geological model and compare to the observed data. The method is based on calculation algorithm developed by Talwani and Heirtzler (1964) and refined according to Rasmussen and Pedersen (1979). The geologic model whose upper boundary is constrained by the observed topography was adjusted by a semi-automatic trial and error approach to ensure the best fit.

3.2. Rock Samples

All rock samples collected from the Loki's Castle hydrothermal venting site are non-in-situ grab-samples. A total of 25 samples were measured for their petrophysical properties and represented mudstone, hydrothermally altered basalt, and highly heterogeneous loose probable-chimney fragments from the mound flanks (Snook et al., 2018).

One sample from the Mohn's Treasure site is a drill-core that was first video recognized as a basalt (Figure 3d shows the drilling site): black hard rock that did not break or crumble in ROV-manipulator as immediately happened to sedimentary or hydrothermal rocks in the area (Ludvigsen et al., 2016). Upon closer examination, including petrophysical measurements at the Norwegian Geological Survey (NGU), this sample was recognized as a claystone. This fact changed our understanding of the lithology presented in the Mohn's Treasure area and largely contributed to the interpretation of hydrothermal deposits and their magnetic signatures.

All petrophysical measurements were performed at the NGU petrophysical laboratory using commercial and proprietary instruments. Rock density, volume and porosity were determined according to the methodology of EN 1936:2006 (CEN, 2006) using *Sartorius AX 4202* instrument. The rock-magnetic properties measurements included magnetic susceptibility (performed using *NGU* proprietary system) and magnetic remanence intensity (performed using a 3 × 3 component *Sensys FGM3D* fluxgate magnetometer system installed in a nullspace). The direction of the NRM could not be measured because the in-situ orientation of the samples was not known. The Königsberger ratio was calculated based on the average IGRF magnetic field intensity value for the area equal to 53,800 nT. Measurement uncertainties are presented in Table 1.

4. Results and Discussion

The surface geology at the Loki's Castle, Mohn's Treasure, and exploration site was video examined by the ROV mounted cameras. The observed geologic features can be grouped into five categories: (1) different

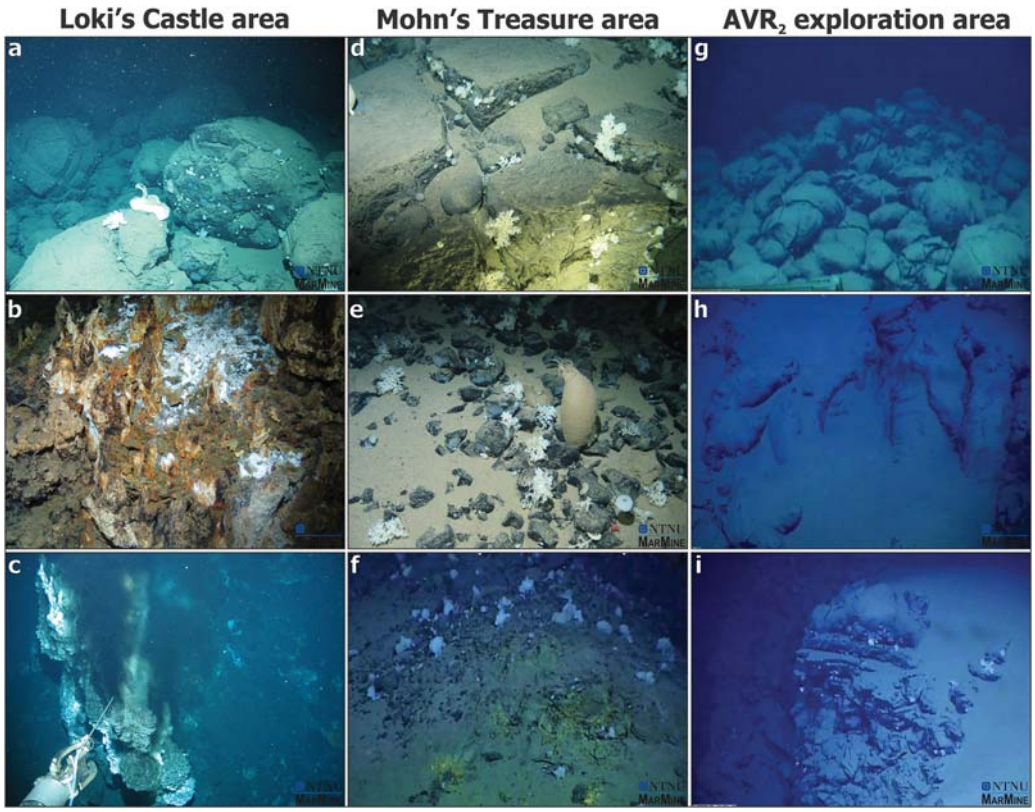

Figure 3. Photo observations from ROV-mounted photo and video cameras. AVR_1 Loki's Castle hydrothermal field: (a) Pillow basalt talus at the base of the border fault cliff near Loki's Castle. (b) Hydrothermal vent material commonly observed at the mound. (c) Black smoker at the eastern mound. Mohn's Treasure survey area: (d) Fractured lithified sediments outcrop. (e) Lithified sediment debris on top of loose sediments. (f) An outcrop of yellow hydrothermally altered material at the Mohn's Treasure deposit. AVR_2 exploration area: (g) Pillow lava mound. (h) Elongated lava flow tubes. (i) Lava flow beds exposed in a near-vertical cliff (ROV was at an altitude of more than 20 m above the valley floor giving a lower border estimate of the cliff height).

types of lava flows: low-relief sheet flows, lobate pillow flows, and interconnected lava tubes; (2) extensively fractured pillow-lava talus, truncated pillows, and basaltic breccia; (3) loose and partly lithified sediment cover; (4) lithified sediment; and (5) hydrothermal material including black and white smokers, broken chimney material, and sulfide deposits. Figure 3 shows typical photo-observations from each site.

Aside from geological expressions, all three study areas exhibit different biodiversity backgrounds. Since hydrothermal venting sites are also known as deep-sea "oases"—an abundant source of chemoautotrophic bacteria that attract underwater animals have developed to tolerate this extreme habitat and thrive (Fisher et al., 2013, and references therein), the presence of certain biospecies endemic to vent environments and their abundance become important direct characteristics of the present and or past hydrothermal activity. The video footage indicates that both Loki's Castle and Mohn's Treasure hydrothermal sites display notably greater abundance and diversity of species than the exploration AVR_2 site where no hydrothermal activity was reported. At the same time, Mohn's Treasure (a comprehensive study on biodiversity and community structure is reported in Paulsen, 2017) and Loki's Castle are distinctive from each other, which can indicate different stages of hydrothermal activity, in addition to the difference in host rock and overall setting.

Table 1
Petrophysical Properties of Loki's Castle Hydrothermal Field Grab Samples and Mohn's Treasure Area Drill Core

Description	IGSN	Volume (cm^3)	Density (g/cm^3)	Porosity (%)	Magnetic susceptibility (10^{-6} SI)	Magnetic remanence (mA/m)	Königsberger ratio
Measurement uncertainty		0.01 g			<1,000–6% >1,000–0.6%	<50–5% >50–1%	
Mohn's Treasure: Claystone	MT01	194.3	2.31	0.15	549	3	0.10
Loki's Castle: Mudstone	01	80.16	1.1	0.52	611	14	0.43
	02	130.31	1.05	0.52	630	6	0.18
Loki's Castle: Hydrothermally altered Basalt	03	74.32	2.84	0.02	1,194	2	0.03
	04	116.6	2.84	0.02	1,112	10	0.17
	05	104.65	2.86	0.02	1,126	7	0.12
Loki's Castle: Heterogeneous hydrothermal material	06	115.15	1.62	0.14	451	4	0.16
	07	112.22	1.58	0.16	538	5	0.17
	08	122.53	2.07	0.24	583	57	1.82
	09	115.6	1.84	0.21	559	102	3.39
	10	98.15	1.65	0.1	557	46	1.54
	11	101.09	1.95	0.22	543	88	3.01
	12	129.58	1.54	0.13	503	6	0.22
	13	191.7	2	0.14	518	60	2.15
	14	182.08	1.51	0.16	465	9	0.36
	15	119.85	1.49	0.21	460	5	0.20
	16	69.12	1.62	0.19	474	6	0.24
	17	93.29	2.08	0.1	497	106	3.96
	18	125.62	2.12	0.16	641	149	4.32
	19	137.57	2.22	0.1	624	159	4.74
	20	113.59	2.25	0.14	676	223	6.13
	21	141.03	1.67	0.19	527	12	0.42
	22	128.37	1.85	0.15	490	26	0.99
	23	140.57	1.9	0.11	447	66	2.74
	24	125.46	1.5	0.24	500	21	0.78
	25	117.35	1.42	0.27	513	23	0.83

Note. Volume gives the bulk volume of the measured sample material. All samples are assigned International GeoSample Numbers (IGSN) with a prefix IELIM00.

Loki's Castle active hydrothermal venting site. Detailed bathymetry and direct ROV observations reveal hummocky volcanic terrain composed of pillowed flows of varying ages, locally covered by sediments. Extensional tectonics influence is pronounced in the normally faulted terrain (Figure 4) that alternate with recent magmatic activity centers. Observed lithologies include fresh and fractured pillow-basalts and breccia (Figure 3a), patches of loose and partly lithified sediment, and diverse hydrothermal material (Figures 3b and 3c). Loki's Castle deposit consists of two mounds that are situated in the middle of the AVR on a flat-topped seamount, just west of the rift. Each mound is approximately 150 m in diameter, overlapping by roughly 30 m as their centers are approximately 120 m apart.

The detailed 1-m resolution bathymetry data provides a solid basis for the deposit detailed mapping. Bathymetry analysis shows that the mounds are situated on an en echelon normal faults structure complicated by connecting faults and a horse-tailing fault termination (Granier, 1985). They appear to be formed on relay structures—in between overlapping normal fault segments where multiple minor faults provide hard linkage to the major faults (Figure 4). The increased structural complexity associated with the increased number of faults and diversely oriented fractures enhances the vertical permeability, thus creates potential pathways for vertical migration of fluids. Hence, relay structures represent a very important control on fluid transport in the crust, for all types of fluids (Fossen & Rotevatn, 2016, and references therein) yielding important implications for hydrothermal systems—that is, creating favorable conditions for magma emplacement, and even more importantly, focusing of hydrothermal discharge. In the case of Loki's Castle, it is clear that the occurrence of the deposit can be attributed to fault relays and intersections as both mounds are formed on top of them with black smokers predominantly concentrated along the faults. Given that plumbing system is well established on a large scale—the heat source, deep faults and fractures facilitating vertical transport of melt and hydrothermal fluid, and long-lived nature of such systems (Johansen et al., 2019; Pedersen,

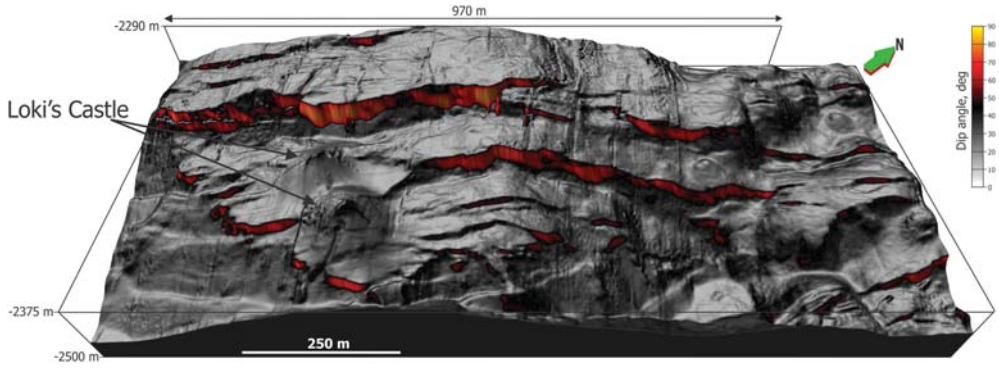

Figure 4. Loki's Castle hydrothermal venting field bathymetry in 3-D view. Color scheme corresponds to the change in dip angle. The sulfide deposit mounds are marked by the arrows.

Rapp, et al., 2010)—all these factors make a strong case for the formation of hydrothermal deposits in the studied area. We suggest that structural complexity associated with intensive faulting of diverse orientation, and transfer zones in particular, is the major factor in the localization of hydrothermal discharge on the seafloor and subsequent deposit formation.

Basalt-hosted hydrothermal sites are typically associated with a negative magnetic anomaly in normal polarity areas (Szitkar et al., 2014; Tivey et al., 1993; Tivey & Johnson, 2002; Zhu et al., 2010). The reduction in magnetic intensity observed over such sites can be caused by several reasons and often results from a combination of them: hydrothermal alteration of titanomagnetite to less magnetic minerals (Ade-Hall, 1964; Pariso & Johnson, 1991); and formation of thick nonmagnetic hydrothermal deposits above deep-seated magnetic layers (Szitkar et al., 2014); or the transient effect of thermal demagnetization of titanomagnetite in basalt as temperature of the circulating fluid in active sites—300+ °C—exceeds Curie temperature of titanomagnetite—120–200 °C (Kent & Gee, 1996).

Black smokers at Loki's Castle release 310–320 °C vent fluid that makes it a high-temperature vent field and the thermal demagnetization effect viable. A semi-quantitative XRD analysis of a basalt sample collected from the flank of the hydrothermal mound (a parent sample for samples no. 03–05 in Table 1) shows following composition: albite (52.06%: interior; 48.08%: outer rim) and augite (34.31%: interior, 28.61%: outer rim), chlorite (10.2%: interior, 18.16% outer rim), quartz (3.43%, 5.15%: outer rim; *B. Snook*, personal communication, 2017). A significant amount of alteration products such as chlorite and albite in the studied basalt sample suggests that it was subjected to hydrothermal alteration (Humphris & Thompson, 1978). Basalt samples previously collected in the vicinity of the Loki's Castle area were classified as typical tholeiitic basalt (Cruz et al., 2011). Magnetic properties of the same basalt sample split into three smaller samples (samples no. 03–05 in Table 1) coincide with the observation that chloritization and spilitization is associated with decreasing intensity of magnetization and Königsberger ratio (Opdyke & Hekinian, 1967). At the same time, the magnetic susceptibilities of the hydrothermal material and the mudstones, collected from the mounds, exhibit even lower values, on average twice as low as the altered basalt, and much lower than fresh mid-ocean ridge basalt (Ade-Hall, 1964). Each of these observations would indicate a magnetic low over Loki's Castle. However, the magnetic signature of this particular area is quite complex—we do not observe a confined magnetic anomaly directly above the mounds (Figure 5), even though the reduction to pole procedure was performed and the geological area was formed during the normal polarity Brunhes epoch (Heirtzler et al., 1968; Ogg, 2012). Instead, we observe a long-wavelength magnetic anomaly low skewed in the southeastern direction perpendicular to the major fault and a much steeper southeastern side of the anomaly. The emerged indentation in the TDR map coincides with the eastern mound of the Loki's Castle and could be explained by the presence of demagnetized sulfide mounds in the shallow part and potentially a hydrothermal fluid upflow zone shifted toward the eastern mound. Yet, the resolution and configuration of the magnetic survey requires close attention to the interpretation: the distance between the survey lines

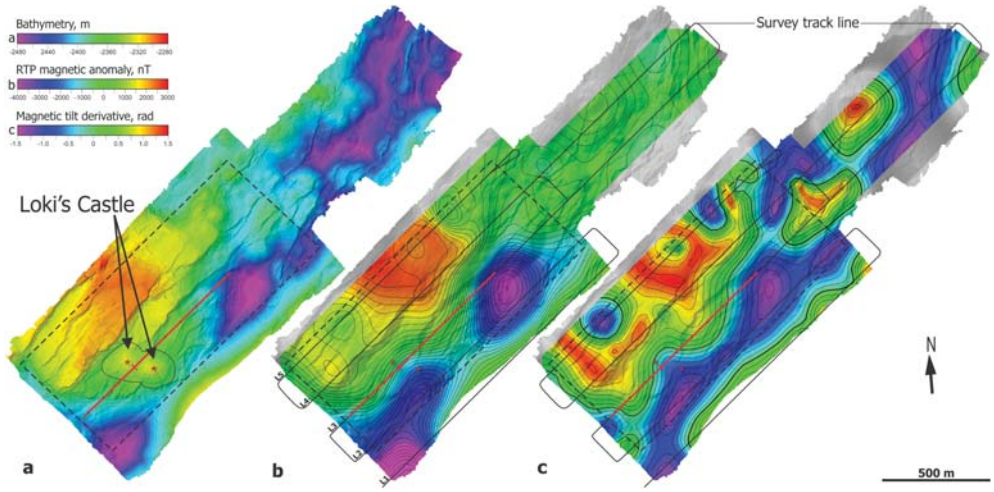

Figure 5. Loki's Castle survey area in color shaded-relief representation, all illuminated from northwest. Striped black line marks extent of the Figure 4. The bold solid red line marks the extent of the profile depicted in Figure 6. (a) Bathymetry resolved at 1-m scale. (b) Reduced-to-pole (RTP) total-field magnetic anomaly map generated from a low-flight mode dataset gridded at 30 m and draped over bathymetry grid. The spacing between isolines is 250 nT. Solid black line denotes survey track line with 150-m line spacing. (c) Magnetic Tilt Derivative (TDR) map with isolines at 0.2 and zero-crossing line in bold draped over bathymetry.

equal to 150 m is comparable with the mounds size; the survey track lines are aligned with the main faulting direction 044°. In fact, only one survey line runs over the deposit; however, it does not cross either mound but goes between them, while the two adjacent lines run over the very edges of the mounds parallel to the major faults defining the hosting structure (Figure 5). Such configuration of the survey does not allow a 3-D reconstruction of the deposit.

The profile crossing the deposit (L3 in Figures 5 and 6) indicates a negative magnetic anomaly that coincides with the Loki's Castle deposit. Magnetization low is present and detectable in the profiles collected at different altitudes of 60 and 100 m above the seafloor. The observed difference between the two profiles in this pseudo-measured gradient along the line 3 proposes that the anomaly derives from the shallow subseafloor source. Forward modeling was used to assess the hypothesis. While small variations in thickness of a layer with constant crustal magnetization value (Zhang et al., 2018, and references therein) were enough to explain the long-wavelength trends in the observed magnetic data, a short-wavelength anomaly over the deposit and the pseudo-measured vertical gradient required a reduced magnetization body to generate sufficient contrast in the data. Figure 6 shows the magnetic signal calculated from such model. The uniformly magnetized layer with a varying thickness represents recent extrusive basalts; a reduced magnetization body represents a narrow alteration pipe associated with hydrothermal upflow zone feeding the broader shallow mounds as in concept described by Tivey et al. (1993). Considering the small size of the mounds (~150 m each) and short distance between them (120 m between the mound peaks), an alteration pipe is shared by the mounds rather than they have two separate feeder zones. This conceptual model of the 137 data crossovers fits the data with the root-mean-square misfit of less than 100 nT after constant offset correction. Magnetic susceptibilities required to match the observed anomaly amplitudes, however, greatly exceed the range of susceptibility measurements indicating high remanent magnetization. The model is only able to identify the bulk contrasts in the subsurface and reveal the complexity in the magnetization structure, but it cannot uniquely resolve internal compositional and structural detail. Variations in both remanent and induced magnetization corresponding to the changes in lithology could explain the observed signal along with the variation in thickness. Closer line spacing and additional constraints are required to distinguish between different models and resolve the deposit in 3-D.

Mohn's Treasure extinct hydrothermal venting site. Figure 7 shows an off-axis area of the mid-ocean ridge, focused on the middle valley rift flank. The survey extends for 5,000 m along the rift valley wall fault and

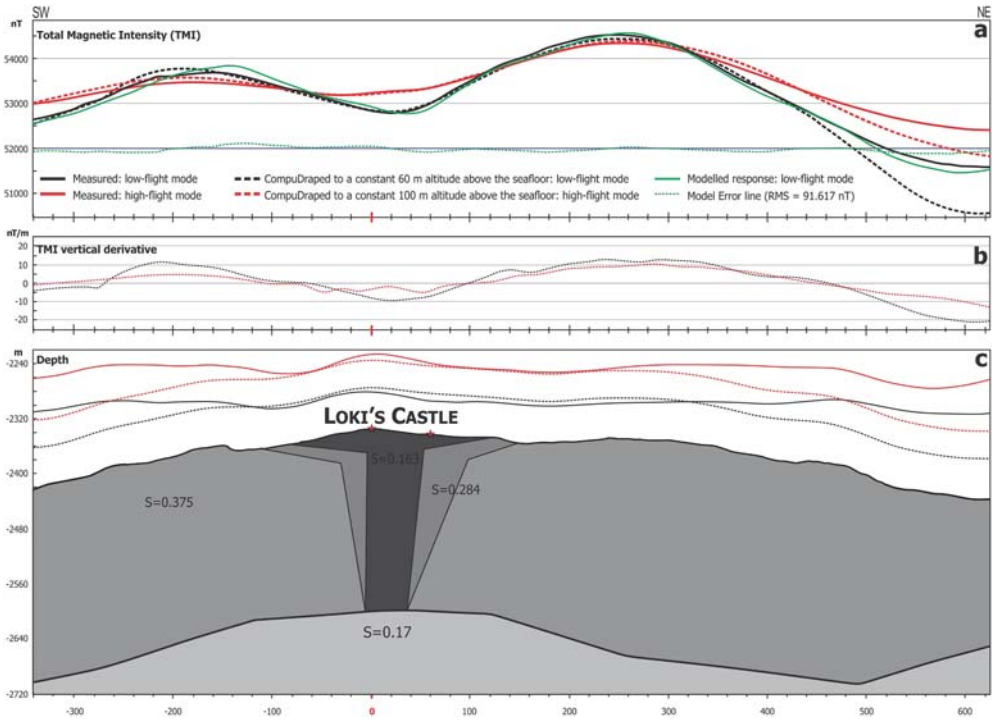

Figure 6. Profile across the Loki's Castle deposit, L3 (for location see Figure 5). The red stars denote projections of Loki's Castle mound peaks. (a) Original TMI profiles are denoted by solid lines: Low-flight mode is black; high-flight mode is red. Both modes were acquired with inconsistencies in altitude displayed in c panel. The dashed black and red lines are obtained using a CompuDrape algorithm and correspond to the new constant altitudes above the seafloor: 60 and 100 m. The solid green line indicates the synthetic magnetic response, the dashed green line denotes misfit between the observed and modeled data. (b) TMI vertical derivatives for drape-corrected TMI profiles: low-flight mode in black, high-flight mode in red. (c) Proposed concept of the subsurface structure below the Loki's Castle. Bathymetric profile with original loose drapes for low- and high-flight mode surveys, in black and red solid lines respectively. Dashed lines mark fixed-drape profiles: 60 and 100 m above the seafloor. Magnetic susceptibility values, S, are provided in SI units. Such high values were required by the model in order to match the observed anomaly amplitudes and indicate the presence of high remanent magnetization in the studied area, which we did not include in this model maintaining a simple approach focused on the geometry and susceptibility contrasts.

3,600 m across it, which almost fully covers the whole rift flank from the crest of a rift-forming fault to the bottom of the axial rift valley, including approximately 500 m west from the crest. Morphologically most of the studied area is a mass-wasting feature resulting from slope failure and landslides. An integrated analysis of the detailed bathymetry, seafloor video observations, and drilling shows that this area is predominantly composed of lithified, semi-lithified and unconsolidated sediments. No volcanic manifestations are observed on the seafloor in this area. Drilling results show that the hard rock observed within the area is a sedimentary rock (claystone), which is commonly exposed by the faults or present as debris sparsely distributed along the slope, and with a distinctive angular shape in contrast to the rounded pillow basalt fragments abundant at the AVRs (Figures 3d–3f, photo observations from the area; Figure 7e, drilling site location). A seismic-stratigraphy study approximately 10 km north of the site reports that the sediment layer thickness on the western flank of the rift valley varies between 150 to 800 m (Bruvoll et al., 2009). Near-seafloor magnetic exploration registers much lower peak-to-peak dynamic range of the reduced to the pole anomaly values of approximately 3,000 nT (survey area: 17.8 km^2), compared to the 7,000 nT observed over a much smaller area of Loki's Castle AVR survey (survey area: 1.15 km^2), and 12,000 nT over the southern AVR_2 (survey area: 28.6 km^2: 3a; 7.26 km^2: 3b). This could be explained by the presence of a thick layer of sediments separating basement rocks and the magnetic sensor in addition to possibly different

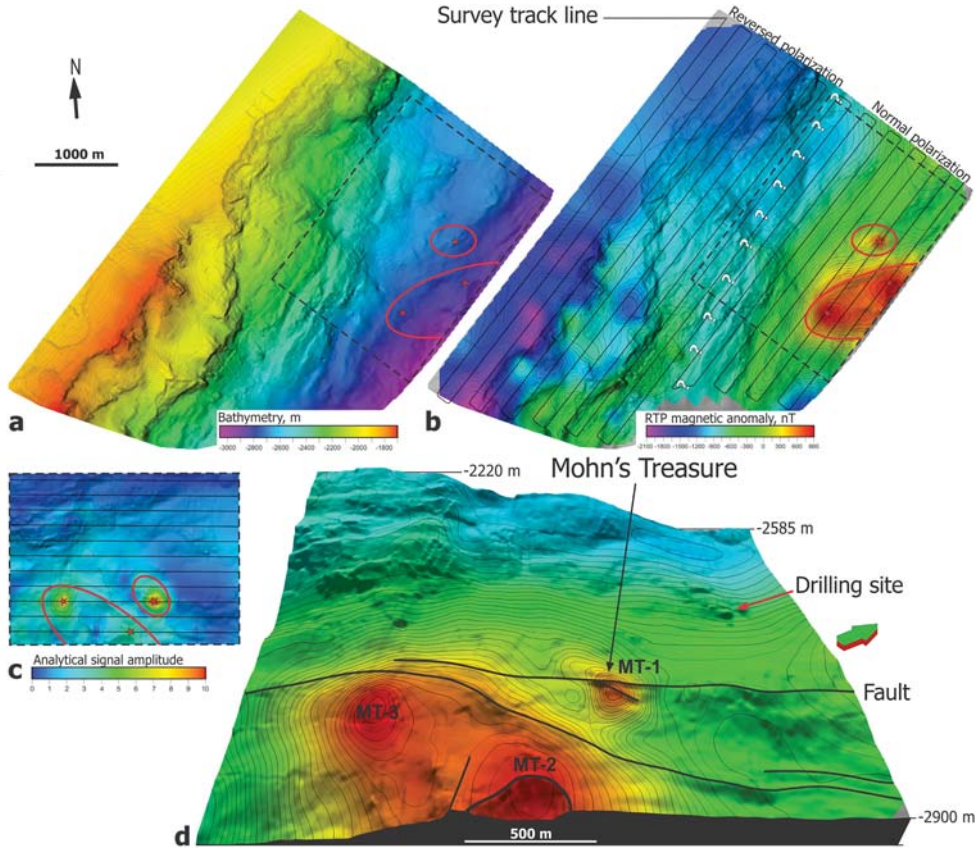

Figure 7. Mohn's Treasure survey area in color shaded-relief representation, all illuminated from northwest. All grids are draped over bathymetry grid. Solid black line denotes survey track line with 150 m line spacing. Striped black line marks the extent of panels c and d. (a) Bathymetry resolved at 4-m scale. (b) Draped reduced-to-pole (RTP) total-field magnetic anomaly map gridded at 30 m, isolines drawn every 150 nT. (c) Analytical signal amplitude map. (d) Three-dimensional representation of the (b) panel segment marked by the striped black line. Black arrow tip points at the location of the hydrothermal material exposure documented in Figure 3f and marks the previously reported hydrothermal deposit Mohn's Treasure. Red arrow tip marks the location of the drilling site where claystone core was retrieved. White question mark line denotes the supposed boundary between the normal polarity Brunhes and reverse-polarity Matuyama epochs. Green-red arrow points at the North.

magnetization of the basement rock. Following the assumption that the subsurface structure of the studied rift flank segment is similar to the northern segment of the ridge imaged by reflection seismic (Bruvoll et al., 2009), an overall trend of magnetic intensity decreasing in the downslope direction as the thickness of mass waste material increases would be expected. Yet, magnetic data reveals the opposite tendency, suggesting that not only the volume of nonmagnetized material is influencing, but also the change in magnetization of the underlying crustal rocks. Available regional low-resolution aeromagnetic data (10-km line spacing and 300 m altitude survey; Olesen et al., 2010; Ogg, 2012) indicate that this area belongs to a transition zone between reverse Matuyama and normal Brunhes polarity epochs. We believe that the discussed survey covers this transition in high-resolution. Such a topic deserves a separate detailed discussion and tests. For the purposes of the current paper, we infer that the border between the normal and reverse polarity segments lies in parallel with the rift-forming fault presumably as denoted in Figure 7. Therefore, positive magnetic anomalies to the south and east of the assumed reversal border can be attributed to locally elevated magnetization, and vice versa for the upper part of the flank.

The shapes of the positive anomalies depicted in Figures 7b and 7d do not give enough evidence to support a dike or sill intrusion; that is, there is no significant strike extent or localized character to the anomalies. We observe that these observations of two strong positive anomalies correlate with the presence of previously collected sulfide material at the same location (Pedersen, Rapp, et al., 2010) and suggest that these sulfide deposits are creating a magnetic signal. This type of magnetic signature was observed in several locations around the world and is explained by the contrast between nonmagnetic sediments and the massive sulfide deposit usually containing highly magnetized magnetite, pyrrhotite (Gee et al., 2001; Körner, 1994; Pedersen, Rapp, et al., 2010; Tivey, 1994). The interpretation for the smaller anomaly is confirmed by video material and sampling of hydrothermal material composed of pyrite and heterogeneous fine-grained chimney material (Pedersen, Rapp, et al., 2010) and corresponds to the Mohn's Treasure extinct hydrothermal field (MT-1 in Figure 7), as no water column indications of venting are registered at the site. The combination of the total magnetic field intensity data and its derivatives help to delineate the Mohn's Treasure deposit as a causative body of approximately 200 m by 150 m. Euler deconvolution suggests that the depth to the source is around 15 m. This can be interpreted as the depth to the stockwork because the mound was largely weathered, by a combination of physical and chemical destruction of the magnetic minerals, and covered by a thin layer of sediments that leads to the increase of the distance to the source.

The bigger anomaly south-west of the Mohn's Treasure deposit (Figure 7) consists of two smaller-wavelength anomalies approximately 350- and 400-m-long with peaks separated by approximately 800 m. These anomalies are slightly stretched in the downslope direction indicating influence of the dipping slope. All three seem to be separated from each other by faults. While Mohn's Treasure is directly associated with the intersecting faults (Figure 7d), confirming the importance of structural control on the fluid flow by increasing permeability, impermeable faults may act as a seal preventing hydrothermal fluids from lateral migration (Knipe, 1992). The south-western anomalies have not been studied with the ROV during the cruise, and show no particular indications of past hydrothermal activity on the bathymetric data except for being associated with faults. However, the intensity contrast observed over these anomalies and the character of the magnetic signature of the Mohn's Treasure make a strong case for interpreting these anomalies as another fossil hydrothermal deposit. On a larger scale, major rift-forming faults are recognized as major fluid pathways. The most recent electromagnetic data from the Mohns Ridge (Johansen et al., 2019) demonstrates the deep extent of the fluid circulation through such faults and its intensity across the ridge.

Euler deconvolution estimates the depth of the sources to be around 100 m assuming a cylindrical geometry, and twice as much for the spherical shape of the causative body. Since very little is known about the preservation of hydrothermal deposits after the venting activity has ceased and the deposits have been transported away from the ridge axis by seafloor spreading, the subsurface geometry is likely to be far more complex and should not be approximated by simple structures. Overall, close proximity of the anomalies, and their occurrence along one fault suggest that they belong to one plumbing system and share a fluid convection cell. Differences in the shape and intensity of the anomalies, and thus in the resulting depth estimations, their extent and relative position, could be a result of a different age of formation, and possibly reactivation of the hydrothermal activity. The southernmost anomaly MT-2 is adjacent to a deep landslide scarp. Such an extensive avalanche has resulted in a 75 m-deep fault scarp and should lead to the exposure of hydrothermal deposits, yet it is less pronounced in the magnetic intensity data. The analytical signal representation highlights the anomaly MT-3, whereas MT-2 is not resolved against the background. Due to the nature of the analytical signal, such effect can be explained by nonverticality of the source edges and the overall complexity of the shape of this body, also expressed by the scarp. Structural rotation has likely changed the direction of magnetization, which is not accounted for by analytic signal independent of the direction of magnetization. Another factor is the thinning of the magnetic source volume by an avalanche and its redistribution downslope. This relatively deep-seated collapse, with the magnetic anomaly centered on it, strongly supports the interpretation of the anomaly as a fossil hydrothermal deposit, and suggests a high proportion of hydrothermally altered material beneath it that eventually led to a collapse of the hydrothermally altered edifice.

Other anomalies observed in the upper part of the flank, presumably representing reversely-magnetized crust, need more careful analysis for further interpretation and are not discussed within this paper.

Exploration of AVR_2 and the implications for hydrothermal venting. For the third study area, we use high-resolution bathymetry and magnetic data along the axial volcanic ridge (AVR_2) (Figure 8) to investigate

its detailed morphology and the variation of the magnetic field intensity in order to address the following questions: Are there significant anomalies that can be associated with hydrothermal activity? What are the magnetic signatures of the distinctive volcanic features observed in the bathymetry? Are there tectonic features associated with the anomalies? What are the implications of these observations for the hydrothermal venting?

Video footage and detailed bathymetry captures the northern half of the AVR_2 displaying classic features of the neo-volcanic zone associated with the slow spreading. Essentially, the topography is entirely controlled by volcanic processes, and is mostly composed of relatively fresh pillow lava flows with a thin sediment cover (Figures 3g–3i). From video survey observations, and based on the assumption that sediment cover degree is indicative of the lava flow age (Mitchell et al., 1998), the ridge appears to become younger toward the central part of it, as sediment cover thins out. There is a strong correlation between the topographic and magnetic profiles, even after the loose drape geometry was corrected to a constant terrain offset. The magnetic intensity, in this context, could be an indicator of the extrusive lavas thickness and volume of the magnetized material, where the peaks indicate the most recent lava deposition (Schouten et al., 1999; Zhang et al., 2018). The observed along-strike variations in magnetic intensity at the AVRs are consistent with the seismic refraction data from the Mohns Ridge acquired further south, showing an unusually thin, 2–5 km, yet highly variable oceanic crust (Johansen et al., 2019; Klingelhöfer et al., 2000). The dynamic range of the total magnetic field within this area is around 11,000 nT highlighting the volcanic nature of the area (Figure 8b).

Sulfide material discoveries on both sides of the AVR_2 (Figure 1)—western rift flank and the rift valley floor on the east (Pedersen, Rapp, et al., 2010)—indicate the presence of a working plumbing system, that must have been active in the past. The cruise data, however, show no sign of a currently active hydrothermal venting—no water column anomaly was found in the survey area, and no visual evidence was found in the ROV footage. The abundance of fissures and recent lava flows suggests abundant dike intrusions and eruptions, which implies the presence of a magmatic heat source nearby which would drive hydrothermal fluid circulation. On the other hand, eruption events can cause a temporal or even permanent clogging of the hydrothermal vents, as well as cover mature deposits preventing their identification. Moreover, fresh volcanics that have not lost their reactive components are prone to faster clogging (Wolery & Sleep, 1976). Another explanation for the lack of hydrothermal venting at this AVR segment could be the lack of deep high-angle fault populations with diverse orientation, preferably intersecting faults. While downflow of the seawater is attributed to the porous flow mode, venting is mainly associated with the crack zones. Planar faults and fissures are not sufficient to sustain hydrothermal venting at neo-volcanic zones (Sleep & Wolery, 1978), though more likely to form deposits at the sediment-hosted environments where sediment-blanketing aids the process. Also, the cooler crust under the slow-spreading ridges requires an excessive depth of water penetration to harvest the heat. Comprehensive analysis of the area does not provide substantial data to attribute any of the observed magnetic anomalies to considerable hydrothermal deposits of more than 250 m across, given the survey configuration parameters.

However, each anomaly is associated with a distinct volcanic feature, for example, stand-alone volcanic cones or hummocks and their clusters, prominent linear fissure-controlled volcanoes following expected tectonic alignment, but also oblique, or even normal to the AVR edifices. The TDR of the total magnetic field data (Figure 8c) is very instrumental in constraining these features and identifying them in spite of the smaller amplitudes or shorter-wavelength. The deviations of volcanic lineaments and faults in the studied segment (31°NE) from the expected axial trend (39°NE) manifest the obliquity of the rifting, which is common in slow-spreading nontransform offsets and is explained by the oblique shear stress. Curved and sigmoidal faults also suggest the rotation of stresses between the offset spreading segments (Tyler et al., 2007). The stresses surrounding discontinuities and the rotation in the volcanic crust can create more complex cross-cutting fault populations that will grow in both horizontal and vertical direction forming soft-link relay structures, or evolving into hard-link relay structures at the later stages, promoting hydrothermal circulation.

Fissure-fed linear volcanic features are consistent with elongated magnetic highs across the survey, the intensity grows as it gets thicker toward the central part. Short-wavelength circular anomalies correspond to single volcanoes or small agglomerations of several cones, while longer anomalies spreading out from the central volcanic ridge have a smaller intensity and likely represent gravitational features, flows that

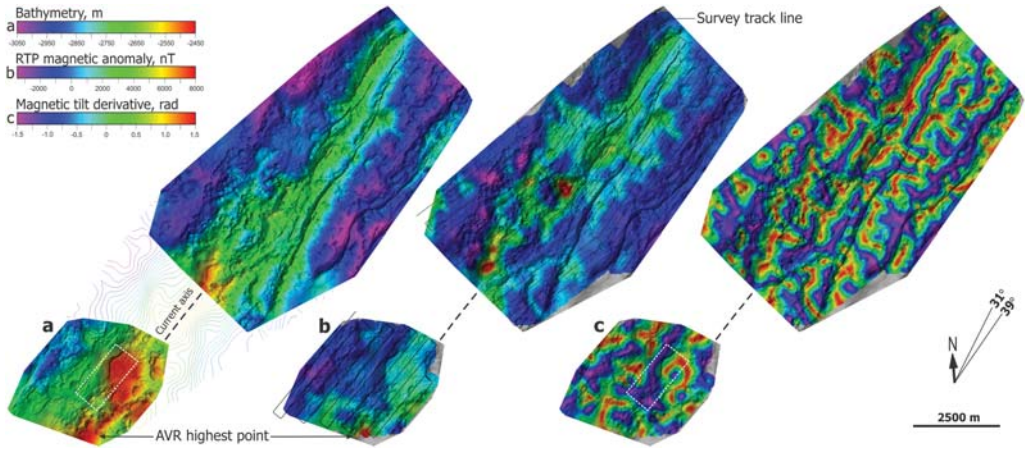

Figure 8. Exploration AVR survey area in color shaded-relief representation, all illuminated from northeast. Black line denotes survey track line with 250-m line spacing. All grids are draped onto the bathymetry grid. (a) Bathymetry resolved at 1-m scale. (b) Draped reduced-to-pole (RTP) total-field magnetic anomaly map gridded at 30 m for Survey 3a and 40 m for Survey 3b, isolines drawn at every 150 nT. (c) Magnetic Tilt Derivative (TDR) map. The white striped line box indicates the extent of the data presented in Figure 9.

extend further from its steep-flanked source under gravity. Such flow was observed with the ROV tracing it to its steep-flanked source. Nontransform offsets can explain bigger volcanic features elongated normal to the AVR axis that connects abundant axial ridges with the new one.

A distinctive magnetic signature is observed over a flat-topped volcano identified in the Survey 3b. A ring-shaped feature as outlined in TDR map (Figure 9) with 1,000 nT contrast in intensity between its central part or caldera and a rim perfectly contouring the seamount. This seamount has typical dimensions of a flat-topped volcano (Clague et al., 2000): approximately 1.2 km wide and 200 m high with a central caldera drained inside by roughly 5 m. The detailed bathymetry shows traces of overflowing lava on its steep southwestern slope, with several fissures dissecting it in the NE direction subparallel to the AVR trend, and a small-offset fault (Figure 9). The formation of such a seamount requires the presence of a near-surface magma chamber feeding it through the development of ring-fractures (Simkin, 1973). The TDR signature potentially captures the presence of such circumferential feeders, and a fractured caldera above hot magma chamber in the center. The zero-values define the source edges as they are assumed to be vertical (Figure 9).

A presence of a flat-topped volcano suggests a presence of a shallow magma chamber, known to serve as a primary heat source for many active hydrothermal venting systems found along the mid-ocean ridges. The maintenance of a long-lived eruption is essential to form lava ponds and sustain magma supply creating repeated lava overflows that eventually reach the balance between the outward and upward growth forming a flat-topped seamount (Clague et al., 2000). This also indicates the presence of a sustained magma supply, implying a later adolescent stage of development of the AVR according to Parson et al. (1993). Yet, a small number of such volcanic features and lack of faulting, suggests that the AVR has not yet finalized its volcanic construction stage and has not entered the tectonic stage. The identified magnetic signature of a flat-topped volcano informs our interpretation of the Loki's Castle hydrothermal field. The latter can be recognized as a flat-topped volcano that has been intensively faulted, suggesting that AVR_1 has been subjected to tectonic destruction and is at later development phase than AVR_2 (Parson et al., 1993. Morphological examination of the two AVRs and hydrothermal manifestations, or lack of thereof, suggest that later tectonic destruction phases of AVR development are more likely to sustain hydrothermal venting at the magma-starved ultraslow-spreading ridges than early phases of volcanic construction through increased population and complexity of the faults that weaken the crust and focus hydrothermal flow onto the seafloor.

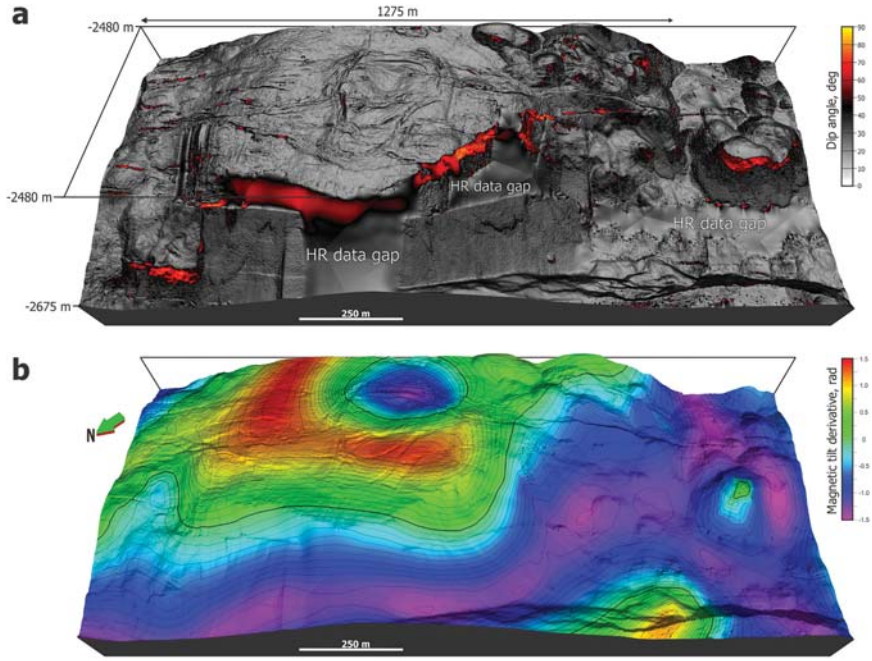

Figure 9. A flat-topped volcano in a 3-D view. (a) Color scheme corresponds to the change in the dip angle. This representation highlights volcanic nature of the topography: flat-topped volcano and its crater, overflowing lava lines, fissures and faults well-resolved at 1 m. High-resolution data gaps are interpolated using minimum curvature algorithm and marked by text. (b) Magnetic Tilt Derivative (TDR) draped onto the bathymetry grid with isolines at 0.1. The thick black line marks zero-crossing.

5. Conclusions

Near-seafloor magnetic data from the ultraslow-spreading Mohns Ridge is presented for the first time in this paper. Analysis of the high-resolution bathymetry and magnetic data enabled identification of hydrothermal deposits associated with both active and inactive hydrothermal venting sites, providing insights into magmatic and tectonic processes interplay along the axial volcanic ridges.

1. Loki's Castle, an active hydrothermal venting field, consists of two likely interconnected sulfide mounds located on top of a relay structure at the downthrown block of a significantly faulted flat-topped seamount. Rock magnetics and profile magnetic data suggest a negative magnetization contrast associated with the basalt-hosted Loki's Castle deposit. Forward 2-D modeling shows that a localized body having reduced magnetization fit the observed data as one of the concepts. Closer line spacing and stronger control on the altitude of the AUV is required to resolve the deposit in 3-D. Our current investigation can be used as guidelines for further data acquisition.
2. Mohn's Treasure, a fossil sediment-hosted hydrothermal deposit, is associated with a positive magnetic anomaly coincident with sulfide samples recovered from the site. The anomaly is centered at a fault crossing on the slope of a mass-wasting deposit of the western rift flank. It accounts for an approximately 200-m × 150-m causative body buried by sediments at approximately 15-m depth. The site has enhanced magnetization and produces a clear magnetic signature enabling identification of two new deposits.
3. Two strong positive magnetic anomalies near the Mohn's Treasure (MT-1) reveal new extinct hydrothermal venting sites, MT-2 and MT-3. They exhibit the same magnetic signature as the Mohn's Treasure and structural indications of hydrothermal alteration like a deep fault scarp exposed by the collapse.

4. The increasing prevalence of faulting and its complexity has positive implications for hydrothermal discharge and potentially controls the occurrence of active hydrothermal venting field in the northern AVR_1, currently undergoing a destructive tectonic stage.
5. In contrast, the southern AVR can be classified as adolescent AVR still going through volcanic construction phase. It is devoid of faulting, shows no indication of on-going hydrothermal activity, even though there are manifestations of the extinct hydrothermalism just outside of it.
6. Potentially, hydrothermal activity along slow-spreading centers follows the cyclicity of the AVR development and is likely to appear and sustain itself during tectonic destruction stages. Structural complexity driven by intensive faulting becomes a major controlling factor on the occurrence of hydrothermal venting within a neo-volcanic zone.

Acknowledgments
We thank NTNU Oceans for funding this research. The data used in the paper were collected by MARMINE/NTNU research cruise funded by the Research Council of Norway (Norges Forskningsråd, NFR) Project No. 247626/O30 and associated industrial partners. *Ocean Floor Geophysics* provided magnetometer that was used for magnetic data acquisition and pre-processed the magnetic data. *Geosoft Oasis Montaj* software was used in the preparation of this paper. We thank NGU for providing laboratory services in petrophysical measurements, and Marta Osinska in particular. We thank Maurice Tivey, Jeffrey Gee, and an anonymous reviewer for suggestions that helped to improve the original manuscript. The magnetic data that support the findings of this study are available from NTNU Open Research Data repository https://doi.org/10.18710/GXMK7K. Regional-scale bathymetric data are available from Norwegian Mapping Authority (https://kartkatalog.geonorge.no/metadata/kartverket/dybdedata-radata/2fe7b56c-334d-4660-ac50-6fcf973a0f70). High-resolution bathymetric data are managed by Norwegian Petroleum Directorate (NPD) and are available from the corresponding author upon reasonable request to NPD at postboks@npd.no. All samples used in the paper are assigned International GeoSample Numbers (IGSN).

References

Ade-Hall, J. M. (1964). The magnetic properties of some submarine oceanic lavas. *Geophysical Journal International*, *9*(1), 85–92.
Baker, E. T., Edmonds, H. N., Michael, P. J., Bach, W., Dick, H. J. B., Snow, J. E., et al. (2004). Hydrothermal venting in magma deserts: The ultraslow-spreading Gakkel and Southwest Indian Ridges. *Geochemistry, Geophysics, Geosystems*, *5*, Q08002. https://doi.org/10.1029/2004GC000712
Baranov, V. (1957). A new method for interpretation of aeromagnetic maps: Pseudo-gravimetric anomalies. *Geophysics*, *22*(2), 359–382.
Baumberger, T., Früh-Green, G. L., Thorseth, I. H., Lilley, M. D., Hamelin, C., Bernasconi, S. M., et al. (2016). Fluid composition of the sediment-influenced Loki's castle vent field at the ultra-slow spreading Arctic Mid-Ocean ridge. *Geochimica et Cosmochimica Acta*, *187*, 156–178.
Beaulieu, S. E., and K. Szafranski (2018), InterRidge Global Database of Active Submarine Hydrothermal Vent Fields, edited.
Bloomer, S., P. Kowalczyk, J. Williams, T. Wass, and K. Enmoto (2014), Compensation of magnetic data for autonomous underwater vehicle mapping surveys, paper presented at 2014 IEEE/OES Autonomous Underwater Vehicles (AUV).
Bruvoll, V., Breivik, A. J., Mjelde, R., & Pedersen, R. B. (2009). Burial of the Mohn-Knipovich seafloor spreading ridge by the Bear Island Fan: Time constraints on tectonic evolution from seismic stratigraphy. *Tectonics*, *28*, TC4001. https://doi.org/10.1029/2008TC002396
CEN (2006), EN 1936:2006 Natural stone test methods—Determination of real density and apparent density, and of total and open porosity, European Committee for Standardization, Brussels.
Clague, D. A., Moore, J. G., & Reynolds, J. R. (2000). Formation of submarine flat-topped volcanic cones in Hawai'i. *Bulletin of Volcanology*, *62*(3), 214–233.
Cordell, L. (1985), Techniques, applications and problems of analytical continuation of New Mexico aeromagnetic data between arbitrary surfaces of very high relief, paper presented at International meeting on potential fields in rugged topography, Institute of Geophysics, University of Lausanne Switzerland.
Crane, K., Doss, H., Vogt, P., & Sundvor, E. (1999). Morphology of the northeastern Mohns Ridge; results from SeaMARC II surveys in the Norwegian-Greenland Sea. *Exploration and Mining Geology*, *8*(3–4), 323–339.
Cruz, M. I., A. S. Dias, J. M. R. S. Relvas, C. Carvalho, R. Fonseca, R. B. Pedersen, and F. J. A. S. Barriga (2011), Geochemistry of the Artic Loki's Castle hydrothermal vent products, paper presented at Goldshmidt Conference, Prague, Czech Republic, 14-19 August 2011.
Dick, H. J. B., Lin, J., & Schouten, H. (2003). An ultraslow-spreading class of ocean ridge. *Nature*, *426*(6965), 405.
Edmonds, H. N., Michael, P. J., Baker, E. T., Connelly, D. P., Snow, J. E., Langmuir, C. H., et al. (2003). Discovery of abundant hydrothermal venting on the ultraslow-spreading Gakkel ridge in the Arctic Ocean. *Nature*, *421*(6920), 252.
Ferraccioli, F., Gambetta, M., & Bozzo, E. (1998). Microlevelling procedures applied to regional aeromagnetic data: An example from the Transantarctic Mountains (Antarctica). *Geophysical Prospecting*, *46*(2), 177–196.
Fisher, C., Rowden, A., Clark, M. R., & Desbruyères, D. (2013). Biology Associated with Sea-Floor Massive Sulphide Deposits. In E. Baker, & Y. Beaudoin (Eds.), Deep Sea Minerals: *Sea-Floor Massive Sulphides, A physical, biological, environmental, and technical review* (Vol. 1A, pp. 19–26). Noumea: Secretariat of the Pacific Community.
Fossen, H., & Rotevatn, A. (2016). Fault linkage and relay structures in extensional settings—A review. *Earth-Science Reviews*, *154*, 14–28.
Gee, J., Webb, S., Ridgway, J., Staudigel, H., & Zumberge, M. (2001). A deep-tow magnetic survey of Middle Valley, Juan de Fuca Ridge. *Geochemistry, Geophysics, Geosystems*, *2*(11). https://doi.org/10.1029/2001GC000170
Géli, L., Renard, V., & Rommevaux, C. (1994). Ocean crust formation processes at very slow spreading centers: A model for the Mohns Ridge, near 72 N, based on magnetic, gravity, and seismic data. *Journal of Geophysical Research*, *99*(B2), 2995–3013.
German, C. R., Baker, E. T., Mevel, C., & Tamaki, K. (1998). Hydrothermal activity along the southwest Indian Ridge. *Nature*, *395*(6701), 490.
Granier, T. (1985). Origin, damping, and pattern of development of faults in granite. *Tectonics*, *7*(4), 721–737.
Gripp, A. E., & Gordon, R. G. (2002). Young tracks of hotspots and current plate velocities. *Geophysical Journal International*, *150*(2), 321–361.
Heirtzler, J., Dickson, G., Herron, E., Pitman, W., & Le Pichon, X. (1968). Marine magnetic anomalies, geomagnetic field reversals, and motions of the ocean floor and continents. *Journal of Geophysical Research*, *73*(6), 2119–2136.
Honsho, C., Ura, T., & Kim, K. (2013). Deep-sea magnetic vector anomalies over the Hakurei hydrothermal field and the Bayonnaise knoll caldera, Izu-Ogasawara arc, Japan. *Journal of Geophysical Research: Solid Earth*, *118*, 5147–5164. https://doi.org/10.1002/jgrb.50382
Hopper, J. R., T. Funck, M. Stoker, U. Arting, G. Peron-Pinvidic, H. Doornenbal, and C. Gaina (2014), Tectonostratigraphic Atlas of the North-East Atlantic Region, Geological Survey of Denmark and Greenland.
Houghton, J. L., Shanks, W. C., & Seyfried, W. E. (2004). Massive sulfide deposition and trace element remobilization in the Middle Valley sediment-hosted hydrothermal system, northern Juan de Fuca Rdge Associate editor: E. M. Ripley. *Geochimica et Cosmochimica Acta*, *68*(13), 2863–2873.
Humphris, S. E., & Thompson, G. (1978). Hydrothermal alteration of oceanic basalts by seawater. *Geochimica et Cosmochimica Acta*, *42*(1), 107–125.
International Seismological Centre (2018), International Seismological Centre, On-line Bulletin, edited, Thatcham, United Kingdom.

Johansen, S. E., Panzner, M., Mittet, R., Amundsen, H. E. F., Lim, A., Vik, E., et al. (2019). Deep electrical imaging of the ultraslow-spreading Mohns Ridge. *Nature*, *567*(7748), 379–383.
Juliani, C., & Ellefmo, S. L. (2018). Probabilistic estimates of permissive areas for undiscovered seafloor massive sulfide deposits on an Arctic Mid-Ocean Ridge. *Ore Geology Reviews*, *95*, 917–930.
Kent, D. V., & Gee, J. (1996). Magnetic alteration of zero-age oceanic basalt. *Geology*, *24*(8), 703.
Klingelhöfer, F., Géli, L., Matias, L., Steinsland, N., & Mohr, J. (2000). Crustal structure of a super-slow spreading centre: A seismic refraction study of Mohns Ridge, 72° N. *Geophysical Journal International*, *141*(2), 509–526.
Knipe, R. J. (1992). Faulting processes and fault seal. In *Structural and tectonic modelling and its application to petroleum geology* (pp. 325–342). Amsterdam: Elsevier.
Körner, U. (1994). Rock magnetic properties of hydrothermally formed iron sulfides from Middle Valley, Juan de Fuca Ridge, paper presented at Proceedings of the Ocean Drilling Program. Scientific results, Ocean Drilling Program.
Ludvigsen, M., et al. (2016), MarMine cruise report—Arctic Mid-Ocean Ridge 15.08. 2016–05.09. 2016.
McCaig, A. M., Cliff, R. A., Escartin, J., Fallick, A. E., & MacLeod, C. J. (2007). Oceanic detachment faults focus very large volumes of black smoker fluids. *Geology*, *35*(10), 935–938.
Miller, H. G., & Singh, V. (1994). Potential field tilt a new concept for location of potential field sources. *Journal of Applied Geophysics*, *32*, 213–217.
Minty, B. R. S. (1991). Simple micro-levelling for aeromagnetic data. *Exploration Geophysics*, *22*(4), 591–592.
Mitchell, N. C., Allerton, S., & Escartín, J. (1998). Sedimentation on young ocean floor at the Mid-Atlantic Ridge, 29 N. *Marine Geology*, *148*(1–2), 1–8.
Mosar, J., Lewis, G., & Torsvik, T. (2002). North Atlantic sea-floor spreading rates: Implications for the Tertiary development of inversion structures of the Norwegian–Greenland Sea. *Journal of the Geological Society*, *159*(5), 503–515.
Nabighian, M. N., Grauch, V., Hansen, R., LaFehr, T., Li, Y., Peirce, J., et al. (2005). The historical development of the magnetic method in exploration. *Geophysics*, *70*(6), 33ND–61ND.
Norwegian Mapping Authority (2015), Sea shadow relief WMS.
Ogg, J. G. (2012). In F. M. Gradstein, J. G. Ogg, M. Schmitz, & G. Ogg (Eds.), *Geomagnetic polarity time scale, in The geologic time scale 2012*. Cambridge, UK: Elsevier, Cambridge University Press.
Olesen, O., J. Gellein, L. Gernigon, O. Kihle, J. Koziel, T. Lauritsen, et al. (2010), Magnetic anomaly map, Norway and adjacent areas. , Geological Survey of Norway.
Opdyke, N. D., & Hekinian, R. (1967). Magnetic properties of some igneous rocks from the Mid-Atlantic Ridge. *Journal of Geophysical Research*, *72*(8), 2257–2260.
Pariso, J. E., & Johnson, H. P. (1991). Alteration processes at Deep Sea Drilling Project/Ocean Drilling Program Hole 504B at the Costa Rica Rift: Implications for magnetization of oceanic crust. *Journal of Geophysical Research*, *96*(B7), 11,703–11,722.
Parson, L., Murton, B., Searle, R., Booth, D., Evans, J., Field, P., et al. (1993). En echelon axial volcanic ridges at the Reykjanes Ridge: A life cycle of volcanism and tectonics. *Earth and Planetary Science Letters*, *117*(1–2), 73–87.
Paterson, N. R., S. W. Reford, and K. C. H. Kwan (1990), Continuation of magnetic data between arbitrary surfaces: Advances and applications, paper presented at SEG Technical Program Expanded Abstracts 1990, Society of Exploration Geophysicists, 1990/01//.
Paulsen, E. (2017), Community structure and biodiversity of the benthic megafauna at the inactive hydrothermal site Mohn's Treasure, on the Mohns Ridge, Arctic Mid-Ocean Ridge (AMOR), Master thesis thesis, Norwegian University of Science and Technology, NTNU.
Pedersen, R. B., Rapp, H. T., Thorseth, I. H., Lilley, M. D., Barriga, F. J. A. S., Baumberger, T., et al. (2010). Discovery of a black smoker vent field and vent fauna at the Arctic Mid-Ocean Ridge. *Nature Communications*, *1*, 126.
Pedersen, R. B., Thorseth, I. H., Nygård, T. E., Lilley, M. D., & Kelley, D. S. (2010). Hydrothermal Activity at the Arctic Mid-Ocean Ridges. In P. A. Rona et al., (Eds.). *Diversity of Hydrothermal Systems on Slow Spreading Ocean Ridges*, *Geophysical Monograph Series* (Vol. 188, pp. 67–89). Washington, DC: AGU.
Pilkington, M., & Roest, W. (1992). Draping aeromagnetic data in areas of rugged topography. *Journal of Applied Geophysics*, *29*(2), 135–142.
Pilkington, M., & Thurston, J. B. (2001). Draping corrections for aeromagnetic data: Line-versus grid-based approaches. *Exploration Geophysics*, *32*(2), 95–101.
Rasmussen, R., & Pedersen, L. (1979). End corrections in potential field modeling. *Geophysical Prospecting*, *27*(4), 749–760.
Reid, A. B., Allsop, J. M., Granser, H., Millett, A. J. T., & Somerton, I. W. (1990). Magnetic interpretation in three dimensions using Euler deconvolution. *Geophysics*, *55*(1), 80–91.
Roest, W., Verhoef, J., & Pilkington, M. (1992). Magnetic interpretation using the 3D analytic signal. *Geophysics*, *57*(1), 116–125.
Schouten, H., Tivey, M. A., Fornari, D. J., & Cochran, J. R. (1999). Central anomaly magnetization high: Constraints on the volcanic construction and architecture of seismic layer 2A at a fast-spreading mid-ocean ridge, the EPR at 9 30′–50′ N. *Earth and Planetary Science Letters*, *169*(1–2), 37–50.
Simkin, T. (1973), Origin of some flat-topped volcanoes and guyots.
Sleep, N. H., & Wolery, T. J. (1978). Egress of hot water from midocean ridge hydrothermal systems: Some thermal constraints. *Journal of Geophysical Research*, *83*(B12), 5913–5922.
Snook, B., Drivenes, K., Rollinson, G., & Aasly, K. (2018). Characterisation of Mineralised Material from the Loki's Castle Hydrothermal Vent on the Mohns Ridge. *Minerals*, *8*(12), 576.
Szitkar, F., Dyment, J., Choi, Y., & Fouquet, Y. (2014). What causes low magnetization at basalt-hosted hydrothermal sites? Insights from inactive site Krasnov (MAR 16°38′N). *Geochemistry, Geophysics, Geosystems*, *15*, 1441–1451. https://doi.org/10.1002/2014GC005284
Talwani, M., & Eldholm, O. (1977). Evolution of the Norwegian-Greenland sea. *Geological Society of America Bulletin*, *88*(7), 969–999.
Talwani, M., & Heirtzler, J. R. (1964). Computation of magnetic anomalies caused by two-dimensional structures of arbitrary shape. In G. A. Parks (Ed.), *Computers in the Mineral Industries* (pp. 464–480). Stanford, Calif: Stanford Univ. Publ. of the Geol. Sci.
Thébault, E., Finlay, C. C., Beggan, C. D., Alken, P., Aubert, J., Barrois, O., et al. (2015). International geomagnetic reference field: The 12th generation. *Earth, Planets and Space*, *67*(1), 79.
Thompson, D. T. (1982). EULDPH: A new technique for making computer-assisted depth estimates from magnetic data. *Geophysics*, *47*(1), 31–37.
Tivey, M. A. (1994). High-resolution magnetic surveys over the Middle Valley mounds, Northern Juan de Fuca Ridge, Proc. ODP. *Scientific Results*, *139*, 29–35.
Tivey, M. A., & Johnson, H. P. (2002). Crustal magnetization reveals subsurface structure of Juan de Fuca Ridge hydrothermal vent fields. *Geology*, *30*(11), 979–982.

Tivey, M. A., Rona, P. A., & Schouten, H. (1993). Reduced crustal magnetization beneath the active sulfide mound, TAG hydrothermal field, Mid-Atlantic Ridge at 26 N. *Earth and Planetary Science Letters*, *115*(1–4), 101–115.

Tromsø Geophysical Observatory (2018), Geomagnetic Data, edited, University of Tromsø.

Tyler, S., Bull, J. M., Parson, L. M., & Tuckwell, G. W. (2007). Numerical modelling of non-transform discontinuity geometry: Implications for ridge structure, volcano-tectonic fabric development and hydrothermal activity at segment ends. *Earth and Planetary Science Letters*, *257*(1–2), 146–159.

Varentsov, I. M., Ryabushkin, P. K., Kazimirov, D. A., Koreneva, E. V., Gendler, T. S., Udintsev, G. B., et al. (1980). The metalliferous sediments of Iceland plateau, North-Atlantic—Geochemical features of formation. *Geokhimiya* (10), 1528–1541.

Verduzco, B., Fairhead, J. D., Green, C. M., & MacKenzie, C. (2004). New insights into magnetic derivatives for structural mapping. *The Leading Edge*, *23*, 116–119.

Vine, F. J., & Wilson, J. T. (1965). Magnetic anomalies over a young oceanic ridge off Vancouver Island. *Science*, *150*(3695), 485–489.

Vogt, P., Kovacs, L., Bernero, C., & Srivastava, S. (1982). Asymmetric geophysical signatures in the Greenland-Norwegian and southern Labrador seas and the Eurasia Basin. *Tectonophysics*, *89*(1–3), 95–160.

Vogt, P. R. (1986). Geophysical and geochemical signatures and plate tectonics. In B. G. Hurdle (Eds.). *The Nordic Seas* (pp. 413–664). New York: Springer.

Wolery, T. J., & Sleep, N. H. (1976). Hydrothermal circulation and geochemical flux at mid-ocean ridges. *The Journal of Geology*, *84*(3), 249–275.

Zhang, T., Gao, J., Xu, M., Shen, Z., & Wu, Z. (2018). Thickness of extrusive basalts dominating the magnetic structure along the ultraslow-spreading Mohns Ridge axis (71.8°–73.7° N). *Tectonophysics*, *742*, 1–14.

Zhu, J., Lin, J., Chen, Y. J., Tao, C., German, C. R., Yoerger, D. R., & Tivey, M. K. (2010). A reduced crustal magnetization zone near the first observed active hydrothermal vent field on the Southwest Indian Ridge. *Geophysical Research Letters*, *37*, L18303. https://doi.org/10.1029/2010GL043542

Zierenberg, R. A., Fouquet, Y., Miller, D. J., Bahr, J. M., Baker, P. A., Bjerkgård, T., et al. (1998). The deep structure of a sea-floor hydrothermal deposit. *Nature*, *392*(6675), 485.

Revisiting Austfonna, Svalbard, with potential field methods – a new characterization of the bed topography and its physical properties

M.-A. Dumais & M. Brönner

Research article published in The Cryosphere, 2020

My contribution to this article consisted in assembling the data from various sources, re-processing and compiling the magnetic data, producing the bed topography derived from the gravity data, producing the 2-D forward models, and writing the manuscript. Marco Brönner, in his role of supervisor, contributed to the data interpretation and improvement of the manuscript.

The Cryosphere, 14, 183–197, 2020
https://doi.org/10.5194/tc-14-183-2020

The Cryosphere Open Access EGU

Revisiting Austfonna, Svalbard, with potential field methods – a new characterization of the bed topography and its physical properties

Marie-Andrée Dumais[1,2] **and Marco Brönner**[1,2]

[1]Department of Geoscience and Petroleum, Norwegian University of Science and Technology, 7031 Trondheim, Norway
[2]Geological Survey of Norway, 7040 Trondheim, Norway

Correspondence: Marie-Andrée Dumais (marie-andree.dumais@ngu.no)

Received: 11 April 2019 – Discussion started: 30 April 2019
Revised: 9 August 2019 – Accepted: 14 November 2019 – Published: 22 January 2020

Abstract. With hundreds of metres of ice, the bedrock underlying Austfonna, the largest icecap on Svalbard, is hard to characterize in terms of topography and physical properties. Ground-penetrating radar (GPR) measurements supply ice thickness estimation, but the data quality is temperature dependent, leading to uncertainties. To remedy this, we include airborne gravity measurements. With a significant density contrast between ice and bedrock, subglacial bed topography is effectively derived from gravity modelling. While the ice thickness model relies primarily on the gravity data, integrating airborne magnetic data provides an extra insight into the basement distribution. This contributes to refining the range of density expected under the ice and improving the subice model. For this study, a prominent magmatic north–south-oriented intrusion and the presence of carbonates are assessed. The results reveal the complexity of the subsurface lithology, characterized by different basement affinities. With the geophysical parameters of the bedrock determined, a new bed topography is extracted and adjusted for the potential field interpretation, i.e. magnetic- and gravity-data analysis and modelling. When the results are compared to bed elevation maps previously produced by radio-echo sounding (RES) and GPR data, the discrepancies are pronounced where the RES and GPR data are scarce. Hence, areas with limited coverage are addressed with the potential field interpretation, increasing the accuracy of the overall bed topography. In addition, the methodology improves understanding of the geology; assigns physical properties to the basements; and reveals the presence of softer bed, carbonates and magmatic intrusions under Austfonna, which influence the basal-sliding rates and surges.

1 Introduction

During the last few decades, with satellite technology advancement and an increased need to understand climate change, the polar regions have become an important laboratory for studying ongoing environmental changes. In this context, icecaps, icefields and glaciers are of interest, as they are highly sensitive to climate variations (Vaughan et al., 2013; Dowdeswell et al., 1997). Glacial sliding and melting rates are often determined from Global Positioning System (GPS) measurements, satellite imagery and satellite altimetry (e.g. Przylibski et al., 2018; Bahr et al., 2015; Grinsted, 2013; Radić et al., 2013; Dunse et al., 2012; Gray et al., 2015; Moholdt et al., 2010b). The ice thickness and the ground topography at the glacier base, key factors in understanding the glacial-sliding and ice-melting mechanisms (Clarke, 2005), have proven challenging to derive. The glacier deformation mechanisms and sliding depend on the glacier roughness, the rheological properties of the bed, the distribution of the rheological properties of the ice and the hydrological system at the ice–bed interface (e.g. Gong et al., 2018; Gladstone et al., 2014; Olaizola et al., 2012; Clarke, 2005). Presence of sediments may also contribute to bed deformation, resulting in ploughing (basal sliding; e.g. Eyles et al., 2015; Iverson et al., 2007; Bamber et al., 2006; Boulton and Hindmarsh, 1987; Clarke, 1987). Thus, determining the glacier bed lithology is as critical as determining its topography to assess glacier responses to climate variations.

Ground-penetrating radar (GPR) is the preferred method to retrieve the glacial bed topography; however, scattering from englacial meltwater streams and dielectric absorption often hamper accurate imaging of the bed, especially for

temperate ice. For temperatures at pressure melting point, common in temperate glaciers, liquid water is present at the ice–bed interface. The correctness of the resulting topography depends on several glacier parameters, including density, porosity and the water content fraction, which determine the permittivity and, therefore, the radio wave velocity used to derive the thickness (Lapazaran et al., 2016). These parameters cannot be directly measured and are highly influenced by temporal and spatial variations of the water content fraction distribution through the glacier (Barrett et al., 2007; Navarro et al., 2009; Jania et al., 2005).

Using GPR and radio-echo sounding (RES) measurements from several campaigns, a bed topography has been derived for Austfonna on Svalbard (Fürst et al., 2018; Dunse et al., 2011). In this paper, we test the feasibility of retrieving the glacier thickness of Austfonna with airborne gravity data, as they are sensitive to the density contrast between the ice and the bedrock. Adding magnetic interpretation to the study contributes by indicating variations in the bedrock lithology and the density distribution, which must be considered to accurately derive ice thickness and bedrock topography. Combined gravity–magnetic interpretation is a powerful tool to define basement types and identify the presence of various geological structures, such as sedimentary basins under the ice in the bedrock. Gravity and magnetic methods have been used in the past for basement lithology studies in the Arctic (e.g. Gernigon et al., 2018; Døssing et al., 2016; Nasuti et al., 2015; Gernigon and Brönner, 2012; Olesen et al., 2010; Barrère et al., 2009) and for sea ice and glacier studies (e.g. An et al., 2017; Gourlet et al., 2015; Tinto et al., 2015; Zhao et al., 2015; Porter et al., 2014; Tinto and Bell, 2011; Studinger et al., 2008, 2006; Spector, 1966). In this study, we combine these methods with GPR data to obtain both an accurate glacial bed topography and also an understanding of the rheological changes of the basement. Magnetic and gravity modelling were used to assess the feasibility of retrieving topographical and geophysical properties in terms of ice thickness, bed softness, the presence of carbonates and till, and bed topography.

2 Austfonna and its underlying geology

With a geographic area of 8357 km^2, Austfonna, seen in Fig. 1, is the largest icecap on the Svalbard archipelago (Dallmann, 2015). It is located on Nordaustlandet, the second-largest island in Svalbard, northeast of Spitsbergen, and approximately 80 % of it is covered by ice. Austfonna has one main central dome with an ice thickness of up to 600 m (Dowdeswell et al., 1986) and feeds several drainage basins. Considered polythermal, consisting of a mixture of temperate and cold ice, it is relatively flat at its highest elevation and includes both land-terminating and tidewater glaciers. Studies suggest its basal temperature is near the pressure melting point (Dunse et al., 2011); thus Austfonna experiences

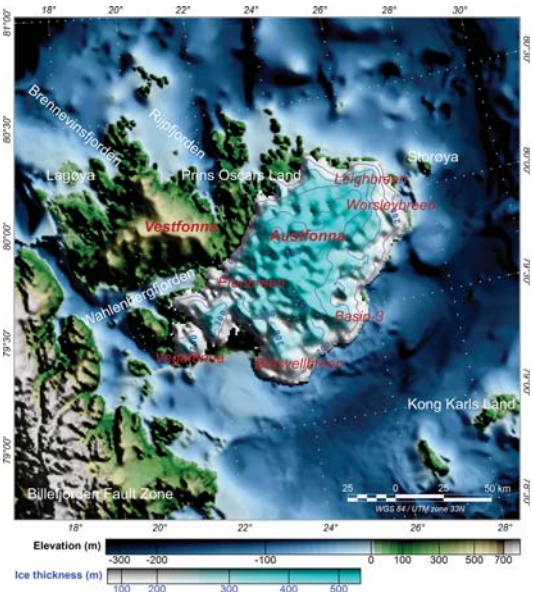

Figure 1. Surface topography map of Nordaustlandet, east of Spitsbergen, Svalbard, and the Austfonna icecap from Dunse et al. (2011). Approximately 80 % of Nordaustlandet is covered by ice, and the ice thickness is up to ca. 600 m. Polythermal and relatively flat at its highest elevation, Austfonna hosts both land-terminating and tidewater glaciers of which several have been observed to surge.

basal sliding and subglacial water might be present. Surging, or surge-type, glaciers have also been observed in the area (Schytt, 1969). Other studies link surging to the softness of the bedrock and tectonically active zones (e.g. Jiskoot et al., 2000). The bedrock topography (including cavities and obstacles), geothermal sources and the presence of sediments are also contributing factors to the glacier basal-sliding velocities (e.g. Boulton and Hindmarsh, 1987; Clarke, 1987).

During the last few decades, several campaigns have aimed to retrieve the underlying bedrock topography of Austfonna using RES (Moholdt et al., 2010a; Dowdeswell et al., 1986) and GPR (Dowdeswell et al., 2008; Dunse et al., 2011). Acquired profiles are shown in Fig. 2. McMillan et al. (2014) and Moholdt et al. (2010a, b) applied satellite altimeter data to estimate surface elevation changes and ice loss. They observed a significant increase in the dynamic activity and the outlet flow rate of the glaciers Vestfonna (Schäfer et al., 2012) and Austfonna (McMillan et al., 2014). Over 28 % of the area covered by Austfonna rests below sea level (Dowdeswell et al., 1986). Moreover, the lowest elevations of the bedrock are located at the tips of Basin 3 in the southeast and Leighbreen in the northeast, (Fig. 1), with bed elevation values of 150 and 130 m below sea level, respectively (Dunse et al., 2011; Dowdeswell et al., 2008).

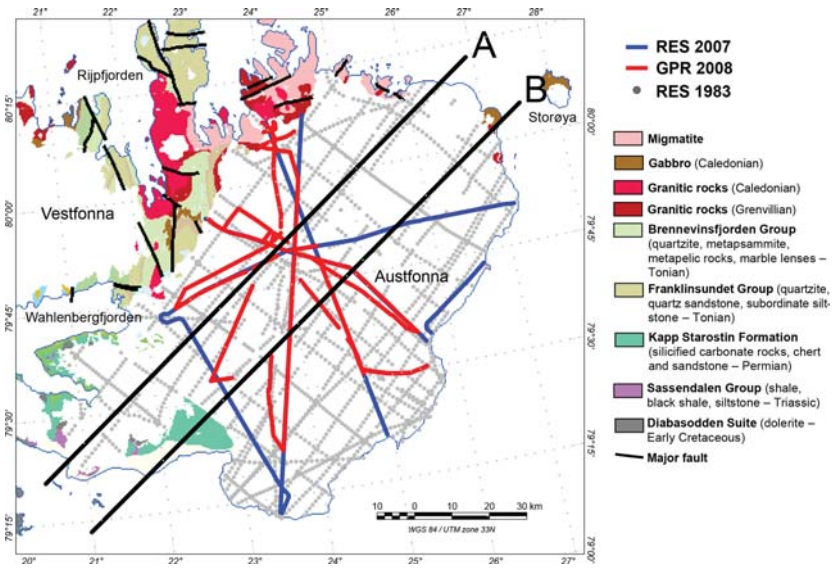

Figure 2. Geological map of Austfonna with GPR and RES campaign lines and gravity–magnetic profiles A and B (modified from Dallmann, 2015, and Dunse et al., 2011). The interpreted profiles, labelled A and B, have been chosen to cover a large area of Austfonna and to capture important geological trends.

The geology underneath the ice is barely understood, as very few outcrops are available to identify the main geological structures and basement affinity of Nordaustlandet (Fig. 2). However, based on the studied outcrops, the geology appears to be complex and the exposed rocks are dated to various geological epochs (Dallmann, 2015; Johansson et al., 2002). Basement outcrops at Wahlenbergfjorden identify different types of basements on each side of the fjord (Dallmann, 2015), which is assumed to represent a major geological north–south (N–S) division of the island. For the northern shore of the fjord and north of Nordaustlandet (including the totality of Vestfonna), the regional map of Lauritzen and Ohta (1984) and radiometric dating (Ohta, 1992) indicate a pre-Caledonian basement with Mesoproterozoic and Neoproterozoic rock exposures, mainly composed of metasedimentary rocks like marble, quartzite and mica schist. The rocks are significantly folded and faulted due to the Caledonian-deformation influence but not to the same degree as in the rest of Svalbard. Caledonian and Grenvillian Rijpfjorden granites are found on the northern tip of Nordaustlandet on Prins Oscars Land (Johansson et al., 2005, 2002). In the east, the bedrock comprises mainly Silurian diorites and gabbros as seen on Storøya (Johansson et al., 2005). On the southern shore of Wahlenbergfjorden, an abundance of Carboniferous to Permian limestones and dolomites with Early Cretaceous doleritic intrusions are exposed. Dallmann (2015) consequently concluded that the same geological demarcation observed at Wahlenbergfjorden continues under Austfonna. The southern basement of Austfonna is believed to be much younger than the one in the north and is composed of unmetamorphosed post-Caledonian rocks. The youngest rocks in Nordaustlandet are Jurassic–Cretaceous doleritic dikes, which intrude into the Tonian basement rocks (composed of dolomite, sandstone, quartzite and limestone) on the island of Lågøya, and the Meso- to Neoproterozoic basement composed of basal conglomerate, volcanic breccias and migmatites in the outlet of Brennevinsfjorden, northwest of Vestfonna (Overrein et al., 2015). South of Nordaustlandet, dolerite sills were emplaced during the Cretaceous in Kong Karls Land. Evidence of the locations of the sills can be found in seismic-reflection and magnetic data in the vicinity of Nordaustlandet (Polteau et al., 2016; Minakov et al., 2012; Grogan et al., 2000).

3 Magnetic and gravity data

The magnetic map is a compilation of two datasets compiled from campaign flights flown in 1989 and 1991 (Table 1). The data are sparse with line spacing of 4 to 8 km at a target ground clearance of 900 m. Having been originally processed by different entities with different processing algorithms, the datasets are reprocessed to a similar level. A control line, flown during both campaigns as an overlap, is used to level the two datasets to each other. This step ensures that the two datasets are levelled to the standard International Geomag-

netic Reference Field (IGRF) model (Thébault et al., 2015) and the compilation is smooth at the overlap.

The magnetic map (Fig. 3b) presents strong parallel anomalies crossing the centre of Nordaustlandet, oriented N–S. The magnetic intensity is correlated with the type and level of magnetization, which in turn is mainly related to the iron content, time of formation or metamorphic processes of the minerals found in the basement. Thus, the magnetization is a strong indicator of the mineralogy of the basement and its lithology. The strong anomaly observed across Austfonna also intersects the Caledonian Rijpfjorden granites, which have been identified on the geology map (Johansson et al., 2005). This anomaly is also parallel to the Billefjorden fault zone and to the Caledonian frontal thrust (Gernigon and Brönner, 2012; Barrère et al., 2009). The Caledonian is also associated with magmatic episodes. Northeast of Nordaustlandet, the sharp and low-frequency magnetic anomalies created by the known emplaced Cretaceous sills have a distinct and prominent signature.

The gravity data were acquired during a 1998–1999 campaign (Forsberg and Olesen, 2010; Forsberg et al., 2002). The flight routes were along a southwest–northeast (SW–NE) direction with a spacing of 18 km and at a ground clearance of 1 km (Table 1). The free-air anomaly map is presented in Fig. 3a. The gravity data produced 4000 m cell size grids with a standard deviation of ~ 2 mGal over a 6000 m half-wavelength resolution. Gravity lows are seen in the south and southwest of Nordaustlandet, with a higher signal on the ice-cap reflecting the ice coverage and its thickness. Gravity is sensitive to the density contrast between the various geological bodies and ice in this case. Low-gravity measurements reflect low densities, which are often linked to sediment accumulation or sedimentary basins.

The grid resolution provides an estimate of the smoothness level of the data and of the limitations to the modelling and data filtering. Given the magnetic grid resolution, features shallower than 2 km cannot be accurately resolved. Depth interpretations and body geometry are limited by the grid resolution. A single anomaly normally leads to several geometry and depth possibilities. In this paper, the most favourable possibility is chosen for its consistency with the GPR and RES investigations and for model simplicity. Therefore, depth estimates from the models in the present paper represent the deepest depth possibility and are limited by a 2 km resolution. The magnetic data also present several asymmetric anomalies which can be interpreted by dipping bodies. However, given the coarseness of the data, a simple model without dipping is preferred.

4 Bed topography revisited

Dunse et al. (2011) have presented a bedrock topography compilation with a 1 km spatial grid resolution from data acquired by RES and GPR, but the geospatial distribution of the measurements (Fig. 2) suggests lower resolution in areas with poor coverage. With these data, combined with the ice surface topography published by the Norwegian Polar Institute (NPI) in 1998 (Norwegian Polar Institute, 1998), an ice thickness is derived for Austfonna. This step allows for an estimate of the volume and mass of the icecap to derive the gravitational effect of the glacier. The density contrast and the topography of the bedrock–ice interface contribute to the sharpest and most prominent gravity effects. A valid approach to resolve the bedrock topography is to assume a simple basement geometry with a homogeneous density. Analogous to sedimentary-basin interpretation (Bott, 1960) and treating the glacier as an infinite slab, the free-air anomaly ($\mathrm{FA_c}$) along a profile is reconstructed as follows:

$$\mathrm{FA_c} = 2\pi G \rho_{\mathrm{ice}} h_{\mathrm{ice}} + 2\pi G \left(\rho_{\mathrm{bed}} - \rho_{\mathrm{ice}}\right) H_{\mathrm{ice}} + 2\pi G \rho_{\mathrm{bed}} h_{\mathrm{bed}}, \quad (1)$$

where G is the gravitational constant ($6.67 \times 10^{-11}\,\mathrm{N\,m^2\,kg^{-2}}$), ρ the density, h_{bed} the topography of the bed above sea level, and h_{ice} and H_{ice} the thickness of ice above sea level and below sea level, respectively. The full extent of the ice thickness is represented by $(h_{\mathrm{ice}} + H_{\mathrm{ice}})$. The free-air anomaly is referenced to the geoid. In the reconstruction of the free-air anomaly, the ice above sea level is regarded as an excess of mass, whereas the ice below sea level is considered a mass deficiency. The influence of the ice ($\rho_{\mathrm{ice}} = 910\,\mathrm{kg\,m^{-3}}$) depends on the surrounding media, which include air ($\rho_{\mathrm{air}} \approx 1\,\mathrm{kg\,m^{-3}}$, negligible) and the bed ($\rho_{\mathrm{bed}} = 2670\,\mathrm{kg\,m^{-3}}$) in this case. This reduction technique is valid under the condition that the thickness of the ice is smaller than the horizontal dimensions of the icecap by several magnitudes. As GPR and RES data were acquired solely onshore, only onshore gravity acquisition was considered in the model for comparison.

Assuming the difference between the free-air anomaly observed ($\mathrm{FA_o}$) and the free-air anomaly calculated is caused by erroneous bed topography measurements, the correction of the bed topography is as follows:

$$\partial h_{\mathrm{bed}} = \begin{cases} \frac{(\mathrm{FA_o} - \mathrm{FA_c})}{2\pi G(\rho_{\mathrm{bed}} - \rho_{\mathrm{ice}})} \\ \text{if the bed topography is below sea level} \\ \\ \frac{(\mathrm{FA_o} - \mathrm{FA_c})}{2\pi G(\rho_{\mathrm{bed}})} \\ \text{if the bed topography is above sea level.} \end{cases} \quad (2)$$

On average, this correction is 2 m for the analysis along the gravity profiles above Austfonna. With a standard deviation of 63 m, the difference in thickness varies between -190 and 290 m. The difference in thickness is applied to the initial bedrock topography derived from GPR and RES. Given the wide line spacing of the gravity profiles, both datasets are gridded with the same resolution (4000 m) for the analysis (Fig. 4). The highest summits of the bed topography remain at the same level. Small residual discrepancies are largely due to the approximation of an infinite slab and the accuracy of

Table 1. Survey acquisition parameters of the magnetic and gravity compilation.

Compilation	Magnetic	Gravity
Line spacing	4–8 km	18 km
Aircraft altitude (approx.)	900 m	1000 m
Grid resolution	2 km	4 km
Acquisition	1989–1991	1998–1999
Acquired by	Sevmorgeo	Norwegian Mapping Authority
	Amarok and TGS	Danish Geodata Agency
	University of Bergen	

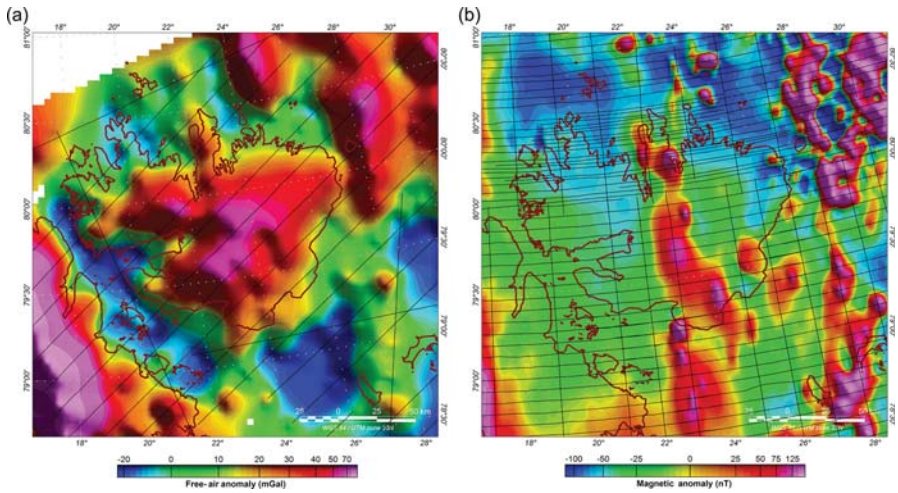

Figure 3. (a) Free-air gravity map and **(b)** a magnetic anomaly map of Nordaustlandet with the acquisition flight lines denoted by the thin black lines. The gravity data are sensitive to an excess or loss of mass. Low free-air gravity data are often linked to sedimentary basins. The magnetic data show important N–S-trending anomalies crossing Nordaustlandet and intersecting with the Caledonian Rijpfjorden granites.

the various datasets. It should be noted that both GPR–RES depth measurements and gravity ice thickness were calculated with the same ice surface topography dataset which acts as a control variable. It reduces the influence of the resolution and accuracy of the ice surface topography when comparing the two bed topography models. However, important discrepancies exist, for example, under Vegafonna on the southwest corner of Austfonna and under Leighbreen and Worsleybreen, northeast of Austfonna. These areas are discussed in detail in later sections when magnetic data are included in the interpretation. Less prominent misfits occur at the outer edge of the marine-terminating glaciers Basin 3 and Bråsvellbreen, where the ice surface topography and glacier geometry might undergo rapid and drastic variations, and where relatively faster ice surface velocities were observed in comparison to the thick, flat interior icecap (Gladstone et al., 2014; Moholdt et al., 2010a). As the ice surface topography and gravity data were acquired around the same time but independently of each other, the resolution and accuracy of the ice surface topography increase the misfit where the glacier geometry is most susceptible to drastic variations. Notably, the gravity profiles cross the glacier perpendicular to its flow and parallel to the shore with an uneven mass distribution; i.e. more mass is found on the northern side of the profile. This terrain effect is commonly corrected for in gravity processing for extreme topography relief (Lafehr, 1991) but requires accurate terrain topography acquired through methods such as laser scanning data acquisition or a high-resolution digital elevation model.

5 2-D forward models

Interpretation using 2-D forward modelling determines the interface between contrasting bodies of different magnetizations and densities. It provides depth and geometrical insights into lithological variations in the bedrock. The forward modelling (Fig. 5) is carried out along the actual airborne gravity lines to ensure the highest resolution of the gravity

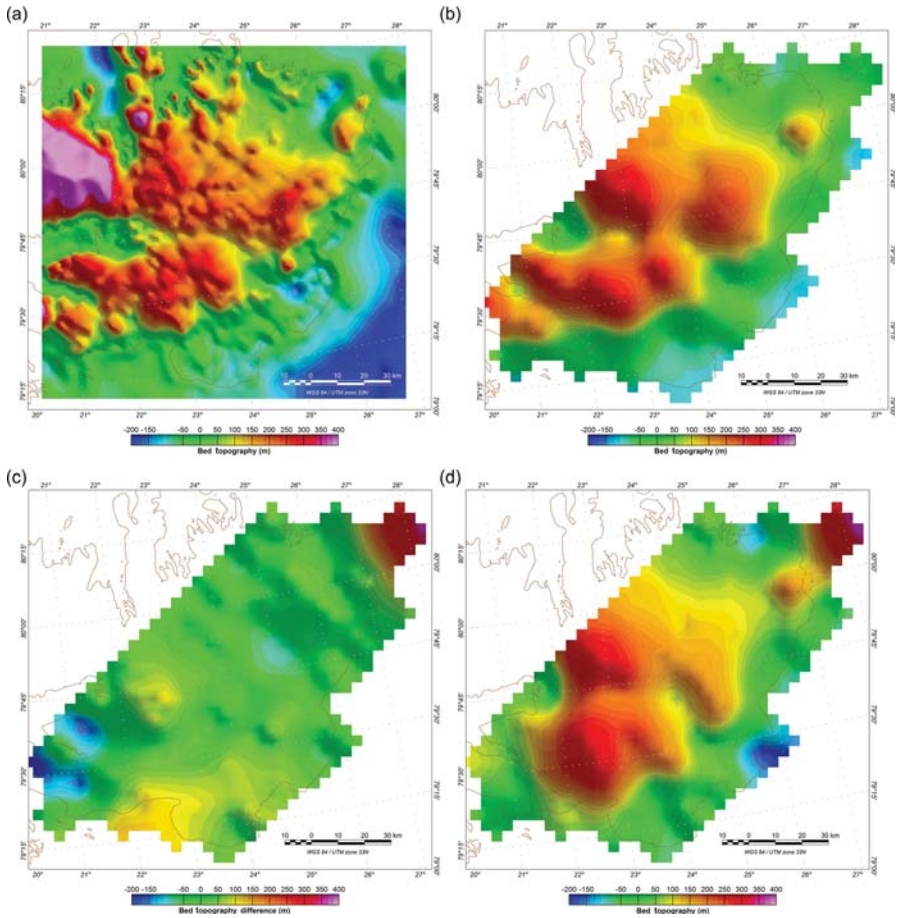

Figure 4. Bed topography derived from RES and GPR **(a)**, bed topography derived from RES and GPR gridded along gravity acquisition flight lines **(b)**, corrections applied to the bed topography **(c)** and bed topography corrected for gravity measurements gridded along gravity profiles **(d)**. Major discrepancies with deviations greater than 150 m occur under Vegafonna (southwest) and Leighbreen and Worsleybreen (northeast).

data. Two lines are modelled and referred to as profiles A and B (Fig. 2). The modelled profiles were chosen for their location and coverage. They contain several aspects of the geology under Austfonna (such as basements and intrusions), and they are located near or above RES and GPR measurements. Models are initially constrained by the bedrock topography derived by Dunse et al. (2011) and are independent of the free-air bed topography corrections. The measured data points from the GPR and RES are highlighted (purple circles, Fig. 5a).

Initial petrophysical parameters are assigned based on the comprehensive petrophysical database from mainland Norway (Olesen et al., 2010) provided by the Geological Survey of Norway (NGU) and on the described bedrock types (Dallmann, 2015). The basement is forward modelled according to gravity and magnetic signatures, using the software package GM-SYS (Geosoft, 2006). The mantle–crust boundary, i.e. the Mohorovičić discontinuity (Moho), was set at a depth of around 33 km following the interpretation of Ritzmann et al. (2007). In the northeast of Austfonna, the basement seems to have a very low magnetization (less than 0.001 SI), but a density higher than the surrounding media (2700 kg m^{-3}) is required to fit the observed field.

Along profile A (Fig. 5a), reducing the density in the southwest of Austfonna (where Vegafonna is located) was attempted but could not be fit to the observed free-air anomaly. Introducing layers of till with a density of 1600 kg m^{-3} did not significantly reduce the signal to account for the observed

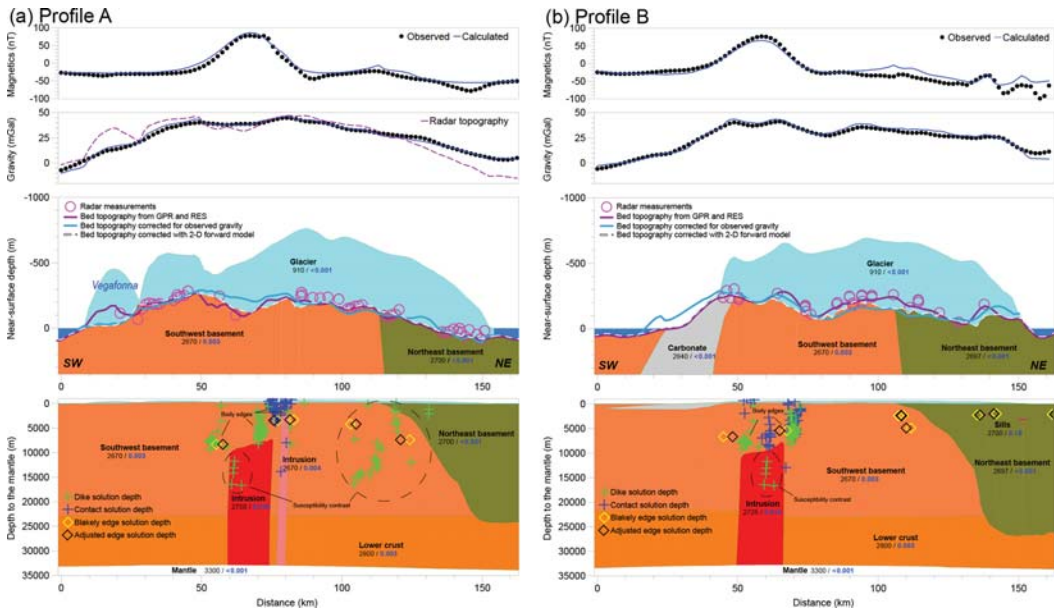

Figure 5. Observed and calculated magnetic and gravity profiles (top), the near-surface view of the basements (middle) and the depth to the mantle (bottom) for profile A **(a)** and profile B **(b)**, as defined in Fig. 2, with Werner deconvolution indicators of the intrusions and the basement interfaces. A gravity response (purple solid lines) is calculated for a homogeneous bedrock using GPR–RES bed topography. The misfit with the observed gravity measurements suggests the bedrock is heterogeneous and the bed topography from the radar needs refining. The gravity-corrected bed topography (blue lines in the near-surface view panel) is an improvement but fails to recognize the heterogeneity of the bed. The 2-D forward model (dashed white line) improves the accuracy of the bed topography by using a density more representative of the lithology. Each section representing a geological body is characterized with a density (kg m^{-3}; black values) and a susceptibility (SI units; blue values). Dike solution depths (green crosses), contact solution depths (blue crosses), Blakely edge solution depths (yellow diamonds) and adjusted-edge solution depths (black diamonds) are identified.

gravity data unless the till had a thickness of several hundreds of metres. Thus, the GPR–RES bed topography is adjusted in this area to be consistent with the gravity measurements. This discrepancy is more important under a region with scarce GPR and RES measurements (measurements are indicated with purple circles). A similar interpretation was made along profile B, where misfits between the two methods occur and only a few measurements exist. The GPR–RES data were not acquired in a grid pattern, and therefore the GPR–RES bed topography proposed in these discrepancy areas is the result of a gridding interpolation between profiles and data points. The bed topographies calculated from the free-air analysis and interpreted from magnetic and gravity modelling agree in general and suggest corrections to the GPR–RES topography in the same direction. However, misfits exist, since the free-air analysis presented in the previous section considers a homogenous basement, while the model interpretation indicates variable densities. The difference between the GPR–RES bed topography and the 2-D forward-model bed topography varies from −170 to 80 m with a standard deviation of 40 m. A smaller level of correction is required with the 2-D forward model than predicted from the gravity correction. The 2-D forward model accounts both for a certain degree of confidence in the GPR–RES data and for the bedrock density variation.

The centres of both profiles are characterized by a high magnetic anomaly requiring high susceptibility. This anomaly is a prominent and continuous N–S-oriented anomaly, which might at least be partly linked to exposed granites on Prins Oscars Land at the northern tip of Nordaustlandet. A relatively high density of 2725–2750 kg m^{-3} is assigned to this granitic intrusion. However, granites with comparable densities and susceptibilities are found on the mainland of Norway in Vest-Agder, Rogaland and Telemark (NGU petrophysics database available at http://geo.ngu.no/GeosciencePortal/, last access: 29 March 2019; 2016). Werner deconvolution (Phillips, 1997; Ku and Sharp, 1983; Werner, 1955), an automated depth-to-source estimation method, was applied to help quantify the depth and morphology of magnetic bodies under Austfonna (Fig. 5a and b). Using these empirical basement indicators that are sensitive to susceptibility variations, and approximating the geological

source to a simplified geometry of features such as contacts and dikes (Goussev and Peirce, 2010), the depth and edges of intrusions were estimated. Euler deconvolution (Thompson, 1982; Reid et al., 1990), with a structural index of 1 (for dike and sill models), was also used to compare the results. This method uses horizontal and vertical derivatives along with a predetermined structural index to estimate the source location. In our case, Euler deconvolution analyses provide similar depth values to those from Werner deconvolution analyses. Both Werner and Euler deconvolution analyses determined the existence of a dike at a depth of about 8 km with a width of almost 20 km. While Euler deconvolution results in a dike seated at 8 km, Werner deconvolution resolves the top of this intrusion to be tilted with a depth from 8 km in the southwest to 6 km in the northeast. A second dike was determined at a 2 km depth (or 1.5 km with Euler deconvolution) with a much narrower width of 2 km and was only seen on profile A, indicating a dike also shorter in length. The model suggests shallow magnetized bodies exist off the shore of Nordaustlandet with a depth of less than 2 km. These indications are used in the model to constrain the depth of the intrusions. Given the accuracy of the data, a certain degree of freedom is allocated to those indicators to fit the observed data with the geology expected.

The gridded tilt derivative of an anomaly, at a location x, y (Miller and Singh, 1994), characterizes the angle of the ratio between the amplitudes of the vertical derivative and the horizontal derivative. Thus, the zero contour indicates the border of a geological body where a density or susceptibility contrast with the surrounding media occurs. This indication from the magnetic tilt derivative (Fig. 6) was used to constrain the lateral extent of the intrusions. Blakely et al. (2016) have also developed a method to retrieve the edge of a body and its depth (Fig. 5) by using the reciprocal of the horizontal gradient at the zero contour of the tilt derivative grid (Fairhead et al., 2008; Salem et al., 2007). At high magnetic latitudes for a vertical dike geometry, the depth is estimated as equal to the half-width of the magnetic anomaly (Hinze et al., 2013). The lateral edge of the body is adjusted accordingly to the depth found with Blakely's method (2016). This reduces the size of the magnetic body (Fig. 5) to the minimum size required for this depth. Thus, a first magnetic body with a susceptibility 0.004 SI in a 0.003 SI surrounding, a density of 2670 kg m^{-3}, a width of 3 km and a depth of 2 km is modelled. The top of the second intrusion is deeper (10 km) and wider (15 km) with higher magnetic and density properties (0.016 SI and 2750 kg m^{-3}). For both profiles, the difference between the bed topography from the magnetic–gravity interpretation and the gravity estimation is caused by the large density intrusion located in the basement.

Along profile B, anomalies of smaller sizes are found on the eastern coastline of Austfonna. The nature of the magnetic signal and the results from Euler and Werner deconvolutions suggest the existence of shallow magmatic bodies such as sills. For simplification, they were modelled with a common magnetization value for sills of 0.15 SI susceptibility (Hunt et al., 1995). Another major difference between the two profiles modelled is the higher-density body (2840 kg m^{-3}) located west of the intrusions on profile B. The NPI geological map identifies a carbonate outcrop in this area of Austfonna. This carbonate body has a strong influence on the gravity signal, which is critical in the estimation of the bed topography (turquoise topography, Fig. 5b). Locally, the bed has a much higher density and should be considered when making bed topography corrections. The magnetic and gravity modelling provides an indication of this carbonate depth, orientation and thickness. Given the coarseness of the data and their limitations, the carbonate body is expected to be shallower and thinner.

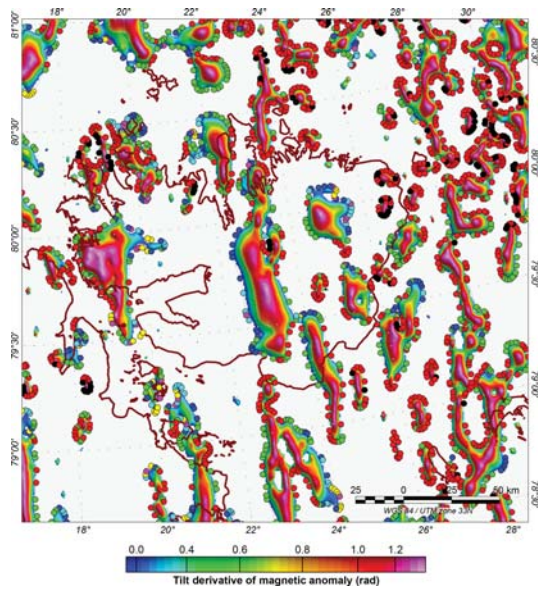

Figure 6. The tilt derivative of the magnetic anomaly superimposed by Blakely depth estimation is used to determine the location and depth of geological bodies and to constrain the model. Negative data are nulled. Sill bodies located in northeast Austfonna, both onshore and offshore, are generally shallower than the large and deep N–S-trending granitic intrusions crossing Austfonna.

6 Bed lithology revisited

The results from the 2-D modelling of profiles A and B are summarized in Fig. 7. According to the models, a prominent deep-seated, highly magnetic intrusion occurs underneath Austfonna crossing N–S, and the bedrock is divided into two types of basement with different geophysical properties.

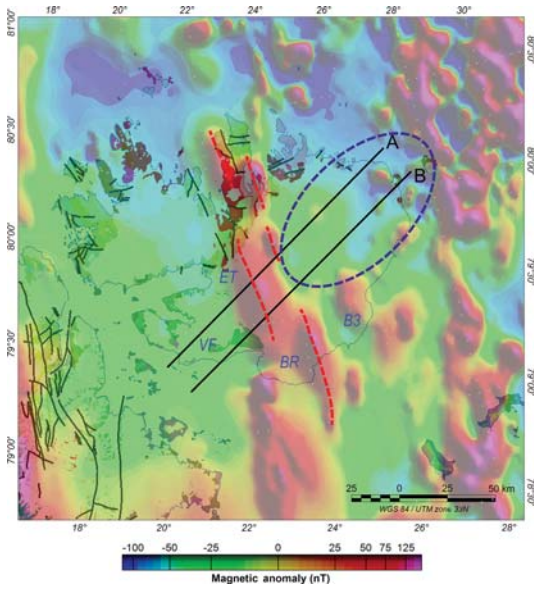

Figure 7. Profiles A and B, as defined in Fig. 2, against the magnetic anomaly and NPI geological map. Dashed red lines represent deep intrusion trends across Austfonna and the blue circle represents the change of basement seen on the lines modelled (B3: Basin 3; ET: Etonbreen; BR: Bråsvellbreen; VF: Vegafonna).

Given the densities and susceptibilities used and the presence of granites on the northern part of the island, the intrusion is likely to be granitic. It is probably of a different composition than the exposed rocks, since the modelled granitic densities indicate relatively high values but are within the expected values for granites (2500–2810 kg m^{-3}; Telford et al., 1990). Moreover, given the N–S-trending faults system across Svalbard, a similar process could explain the strong magnetic anomalies trending N–S and crossing Nordaustlandet. Major faults on Svalbard, trending N–S to north-northwest–south-southeast (NNW–SSE), have been reactivated and juxtaposed by strike-slip motion over several geological periods before, during and after the Caledonian orogeny (Dallmann, 2015). Granites were emplaced during the late stages of the Caledonian (late Silurian to Early Devonian) (Dallmann, 2015). One could argue the presence of N–S-striking sills in the near-offshore region could correspond to the magnetic signature seen under Austfonna. However, the frequency content of the magnetic signal (derived from high-frequency filters or vertical derivatives), the size of the structures revealed from tilt derivative signals and the depth estimates from Werner deconvolution suggest the existence of a rather wide (15 km), deep-seated (10 km) dike intrusion or dike complex onshore and shallow bodies offshore and on the coastline of Austfonna. In addition to the granite affinities suggested by the susceptibility and density interpreted in the 2-D forward models, the high magnetic anomalies correspond to the geological mapping of the observed granites (Fig. 7). Therefore, granite intrusions are proposed to exist in Nordaustlandet bedrock, such as the Caledonian Rijpfjorden granites seen on the central northern tip of Nordaustlandet (Johansson et al., 2005). These intrusions, trending N–S to NNW–SSE like the major faults found on Prins Oscars Land, suggest the faults are present and continue under Austfonna.

Along profile B, sill intrusions are modelled on the eastern coastline, where shallow sills have been previously interpreted and related to a tholeiitic phase (130–100 Ma) linked to the spreading of the Amerasia Basin in the Arctic Ocean and the uplift initiated by the mantle plume on the Yermak Plateau, northwest of Svalbard (Polteau et al., 2016; Minakov et al., 2012; Grogan et al., 2000).

Densities found under southwest Austfonna are also lower compared to the northeastern region. This is consistent with the terrain observations under the Etonbreen and Bråsvellbreen basins (Dunse et al., 2015, 2011), suggesting a more erodible bedrock in the southwestern area. It correlates with the late Paleozoic platform composed of limestones, dolomites, carbonate rocks and sedimentary rocks to the southwest of Austfonna compared to the metasedimentary rocks (marble, quartzite and mica schist) from the pre-Caledonian basement found to the northeast. Furthermore, the 2-D model suggests a smoother bed topography than the one suggested by GPR–RES measurements, which is consistent with a more erodible basement. While two types of bedrock are already expected from outcrop samples, the analysis of the two profiles suggests an oblique division (NE–SW) between the two basement types rather than a N–S division. The younger basement is more constrained to the northeast of Austfonna than previously thought. An oblique division of the basement is consistent with the major fault system found on Svalbard and the geological provinces division (often separated by faults), both trending N–S to NNW–SSE (Harland et al., 1974; Flood et al., 1969).

7 Methodology assessment

Additional magnetic and gravity data improve the bed accuracy and the spatial resolution by filling gaps in the GPR–RES data. Austfonna bed topography was assessed and recalculated using free-air anomaly measurements. The bed topography was enhanced and refined using the 2-D model interpretation, and its physical properties were extracted. Given the scarce sampling of the GPR–RES data under Vegafonna, the discrepancies might be due to gridding interpolation (Fig. 3), as previously discussed. Similarly, along profile B, the poorer fit of the bed topography derived from GPR and RES with the magnetic and gravity model is caused by the scarcer availability of GPR–RES data. Another source of error is the accumulation of water in the erodible basement,

causing an increase in uncertainty and underestimation of the ice thickness. The magnetic and gravity data provide consistent and regular coverage over the full area and are less sensitive to gridding interpolation. Gravity data processing requires the use of high-precision GPS measurements, which were estimated to have a 0.5 m vertical accuracy (Forsberg et al., 2002). In comparison, the distribution of GPR and RES measurements shows irregularities mainly due to the poor navigational guidance available at the time of acquisition (Dowdeswell et al., 1986; GlaThiDa Consortium, 2019). The navigational errors caused flight-line distortions and wider line spacings in certain areas. Positional errors were estimated as ±250 m (Dowdeswell et al., 1986). Therefore, the GPR–RES bed topography is more prone to gridding interpolation artefacts. GPR–RES measurements are susceptible to thickness errors in the presence of steep bed slopes, where the signal is reflected from a lateral wall instead of the bottom topography. While often corrected with a 2-D migration processing technique that corrects for the direction of profiling, transversal slopes are not corrected unless 3-D migration is used (Lapazaran et al., 2016; Moran et al., 2000). The water content in the glacier and the bedrock increases internal scattering and the dielectric absorption. It also affects the radio wave velocity, which contributes to the error in the time-to-thickness conversion (Brown et al., 2017; Lapazaran et al., 2016; Blindow et al., 2012; Matsuoka, 2011). Temporal and spatial variations of radio wave velocity account for uncertainties in ice thickness reconstruction (Jania et al., 2005; Navarro et al., 2014). The magnetic and gravity interpretation compensates indirectly for these errors, as it is less sensitive to water content in the bedrock and offers an additional control on the properties of the bedrock. The magnetic data show the bedrock heterogeneity, associated with susceptibility variations within the glacier bed, indicating different bedrock types and lithologies. These lithological changes suggest the presence of geological boundaries and provide constraints to assigning density changes. Thus, the magnetic data improve the final bed topography accuracy, as they provide constraints on the density distribution for the bed underlying the glacier. The effect of geology on gravity inversion for glacial bed topography was also noticed in other studies (An et al., 2019, 2017; Hodgson et al., 2019).

Using Austfonna bed topography and lithology derived from the 2-D forward model, the theoretical gravity response was modelled for ice loss by removing iteratively uniform and homogeneous layers of ice (Fig. 8). The model predicts that an ice thickness variation of 10 m causes an average variation in gravity of ∼ 0.5 mGal, which is resolved by state-of-the-art gravity measurements. Thus, the gravity anomaly is mainly driven by the bedrock topography and its physical properties, providing hard evidence of the interface between the ice and the rock. The cell size of the GPR–RES-gridded bed topography is 1000 m with extensive interpolation between the measurements. Flown in 1998–1999, the gravity data produced 4000 m cell size grids with a standard deviation of ∼ 2 mGal over a 6000 m half-wavelength resolution. Bed topography corrections with gravity data are more effective than GPR–RES gridding interpolation algorithms. The spatial resolution of airborne gravity measurements depends on the gravimeter together with the platform stability, line spacing, acquisition speed and distance to the source. A state-of-the-art fixed-wing airborne gravimeter, flown with the appropriate flight parameters, can produce 200 m cell size grids with a precision of ∼ 0.5 mGal over a 3000–4000 m half-wavelength resolution (e.g. An et al., 2019, 2017; Studinger et al., 2008). Therefore, using gravity modelling increases the confidence in and the accuracy of the bedrock topography under a glaciated area. Improvement of the spatial resolution of the final bed topography could also be achieved with the appropriate survey parameters and a denser line spacing for the gravity data.

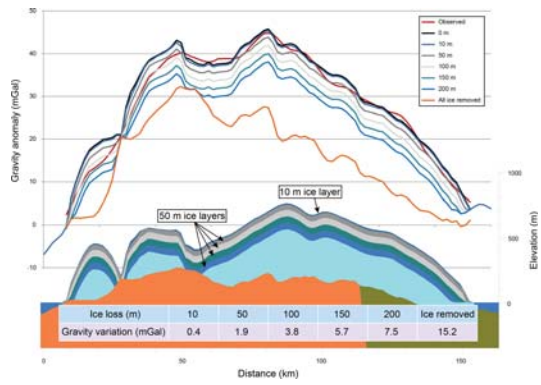

Figure 8. Predicted gravity signature variations with ice loss. The gravity response is calculated using, as the initial state, the 2-D forward model from profile A with the currently known ice thickness. Uniform layers of ice with thicknesses of 10, 50, 100, 150 and 200 m are removed from the model. The first 10 m layer of ice loss yields a gravity anomaly of approximately 0.5 mGal. Significant ice loss is detectable from long-term observations.

Till, commonly found at the base of the glacier, can account for the misfit between the observed and modelled gravity but could not be resolved given the resolution of the dataset. For a variation of 1 mGal, 50 m of till (1600 kg m^{-3}) needs to be emplaced in the model. Lower flight elevation and denser line spacing acquisition is required to model the till. For the accurate interpretation of till modelling, additional independent measurements are required, such as magnetic data which are sensitive to the susceptibility contrast with the surrounding bedrock.

Due to their chemical composition, calcium carbonate rocks erode subglacially and migrate in the glacier system along various transportation paths (Bukowska-Jania, 2007). Calcite dissolution and precipitation have an impact on the calcite saturation of the water film that lubricates the bed–

glacier interface, and they modify the bed morphology and roughness through melting and regelation processes (Ng and Hallet, 2002). The model from profile B suggests carbonate rocks underlie the glacier, and it maps the lateral extent of the body by an additional 7–8 km under the ice. While the thickness of the carbonate is small compared to the resolution of the data, the gravity measurements suggest an important excess of mass at that location but with no susceptibility variation from the surrounding media. Therefore, we must expect there to be a prominent volume of carbonate with an assumed density of 2840 kg m^{-3}.

Deep intrusions, possibly granites, and shallow sills were located and delineated from the 2-D forward model. Characterization of these intrusions provides information about the potential variation of the bed lithology in terms of thermal conductivity. Geothermal heat flux, resulting from the decay of radioactive isotopes present in the glacier bed, may raise the temperature of the basal ice and affect the ice sliding (Paterson and Clarke, 1978). Granites are prone to higher geothermal heat flux due to their mineral composition. On Austfonna, only one borehole has been drilled to reach the bedrock and provide heat flux information in the summit area, indicating a geothermal heat flux of ~ 40 mW m^{-2} (Ignatieva and Macheret, 1991; Zagorodnov et al., 1989). There are no other direct observations available to estimate this heat flux. However, our study suggests that this measurement may not be representative for the entire bed underlying Austfonna.

Located outside the 2-D modelled profiles, a high-intensity anomaly is apparent under Basin 3, subject to a high negative ice surface elevation change rate (Gladstone et al., 2014; Moholdt et al., 2010a). Due to the large variation of the ice surface topography in recent years (and decades), retrieving a valid ice topography for the gravity model has proven difficult. However, the results from profiles A and B with the Euler deconvolution, Werner deconvolution and Blakely depth methods indicate a basement that resembles the softer southwestern basement, largely intruded with shallow (less than 2 km) sills and deeper (8 km) granitic intrusions. Such physical properties are possible drivers for the high basal-sliding rate and surge mechanisms and can be linked to the high ice surface elevation changes seen on Basin 3. Further studies of the granitic intrusion and thermal modelling would be of great interest to link the geothermal flux under Basin 3 to ice changes currently observed.

The interpretation of the two profiles provides an insight into the basement and intrusion geology and a refined glacial bed topography, specifically where GPR and RES data are scarce and less reliable. These findings enhance the understanding of the regional geology of the area and demonstrate the potential to reconstruct the full bed lithology with the aid of high-resolution gravity and magnetic data. Granitic intrusions are known to be potential geothermal sources and can locally affect the heat flux profile of Austfonna. These intrusions can be linked to the basal sliding of Austfonna, and analyzing them can lead to a better understanding of the sliding mechanisms in the area.

8 Conclusions

Airborne magnetic and gravity data were used to study the Austfonna icefield basement on Svalbard. Considering a homogenous basement, the GPR–RES bed topography was corrected with gravity measurements. We demonstrated the importance of the geology for a gravity inversion to calculate the bed topography and presented a method that integrates magnetic, gravity, GPR and RES data. Several interpretation techniques (Euler deconvolution, Werner deconvolution, 2-D modelling) were used to create a model of the bedrock with assigned physical properties in terms of size, depth, susceptibility and density. These results suggest the bed topography derived from GPR–RES measurements can be corrected with gravity analysis, while knowledge of the basement lithology and/or magnetic interpretation further increases its reliability. Thus, the bed topography model derived from magnetic and gravity measurements contributes to a more accurate estimation of ice volume. One of the main challenges is that the data were acquired in different campaigns, in different years and with different acquisition patterns. On the other hand, this approach expands the coverage of the model. Given the difficulty of accessing the underlying lithology of Austfonna, increasing the magnetic and gravity coverage is an effective method to assess the physical properties of the basement.

Moreover, the geophysical interpretation provides insight into the geological and structural affinity of the basement under Austfonna. While the presence of two basement types on Nordaustlandet is well accepted, the new interpretation allows the boundary between the basements to be mapped. The physical properties of the basements provide indications of the basement types for softness and erodibility and provide information about the type of intrusions likely found under the icefield. Sills, granitic intrusions and carbonate rocks have been interpreted in the model and their evolution was set in a geotectonic time frame. Each of these geological bodies has a different impact on the basal thermal regime and the erodibility of the basement, consequently leading to heterogenous basal-ice-sliding rates.

The temperature of the ice at the base, which controls the basal thermal regime, is usually determined by ice thickness, ice advection, ice surface temperature, geothermal heat and frictional heat (related to softness and topography). Irregular basal topography leads to complex localized patterns of the thermal regime. The lithology identified with potentially higher radiogenic heat production can be correlated with areas of faster ice surface velocities or ice thickness variations. Here, with additional petrophysical properties from collected rock samples, thermal modelling is necessary and will help to improve understanding of the different geothermal domains and their effects on Austfonna basal thermal regimes.

In this paper, the resolution of the datasets limits the resolution of the geometry of the geological features modelled. Higher-resolution data from state-of-the-art instrumentation, i.e. gravimeters, GPS units, GPR, RES devices and magnetometers, would further refine the physical properties of the basement and allow for a full reconstruction of the bed lithology and topography.

Data availability. Bed elevation data are available from Dunse et al. (2011). Magnetic and revised bed topography data are available on the Geological Survey of Norway Geoscience Portal (http://geo.ngu.no/GeosciencePortal/search, last access: 21 November 2019; Geological Survey of Norway Geoscience Portal, 2016; contact person is Marie-Andrée Dumais). Gravity data are available upon request from the Norwegian Mapping Authority (contact person is Ove Omang) or on the Geological Survey of Norway Geoscience Portal.

Author contributions. MAD reprocessed the airborne magnetic dataset and produced the bed topography from the gravity data and the 2-D forward model. MB assisted in the data interpretation and commented on the paper.

Competing interests. The authors declare that they have no conflict of interest.

Acknowledgements. We would like to thank Thorben Dunse for providing the GPR–RES bed and related surface elevation maps and for his helpful discussions on the data. We thank Rene Forsberg and Ove Omang for providing the airborne gravity data. Chantel Nixon is also acknowledged for English proofreading of an earlier version of the paper. We thank Daniel Farinotti and the three anonymous reviewers for their valuable comments that improved the manuscript.

Review statement. This paper was edited by Daniel Farinotti and reviewed by three anonymous referees.

References

An, L., Rignot, E., Elieff, S., Morlighem, M., Millan, R., Mouginot, J., Holland, D. M., Holland, D., and Paden, J.: Bed elevation of Jakobshavn Isbrae, West Greenland, from high-resolution airborne gravity and other data, Geophys. Res. Lett., 44, 3728–3736, https://doi.org/10.1002/2017gl073245, 2017.

An, L., Rignot, E., Millan, R., Tinto, K., and Willis, J.: Bathymetry of Northwest Greenland Using "Ocean Melting Greenland" (OMG) High-Resolution Airborne Gravity and Other Data, Remote Sens., 11, 131, https://doi.org/10.3390/rs11020131, 2019.

Bahr, D. B., Pfeffer, W. T., and Kaser, G.: A review of volume-area scaling of glaciers, Rev. Geophys., 53, 95–140, https://doi.org/10.1002/2014RG000470, 2015.

Bamber, J. L., Ferraccioli, F., Joughin, I., Shepherd, T., Rippin, D. M., Siegert, M. J., and Vaughan, D. G.: East Antarctic ice stream tributary underlain by major sedimentary basin, Geology, 34, 33, https://doi.org/10.1130/g22160.1, 2006.

Barrère, C., Ebbing, J., and Gernigon, L.: Offshore prolongation of Caledonian structures and basement characterisation in the western Barents Sea from geophysical modelling, Tectonophysics, 470, 71–88, https://doi.org/10.1016/j.tecto.2008.07.012, 2009.

Barrett, B. E., Murray, T., and Clark, R.: Errors in radar CMP velocity estimates due to survey geometry, and their implication for ice water content estimation, J. Environ. Eng. Geophys., 12, 101–111, https://doi.org/10.2113/jeeg12.1.101 2007.

Blakely, R. J., Connard, G. G., and Curto, J. B.: Tilt Derivative Made Easy, Geosoft Technical Publications, 4, 1–4, 2016.

Blindow, N., Salat, C., and Casassa, G.: Airborne GPR sounding of deep temperate glaciers – Examples from the Northern Patagonian Icefield, 2012 14th International Conference on Ground Penetrating Radar (GPR), 664–669, 2012.

Bott, M. H. P.: The use of rapid digital computing methods for direct gravity interpretation of sedimentary basins, Geophys. J. Royal Astro. Soc., 3, 63–67, https://doi.org/10.1111/j.1365-246x.1960.tb00065.x, 1960.

Boulton, G. S. and Hindmarsh, R. C. A.: Sediment deformation beneath glaciers: rheology and geological consequences, J. Geophys. Res., 92, 9059-9082, https://doi.org/10.1029/JB092iB09p09059, 1987.

Brown, J., Harper, J., and Humphrey, N.: Liquid water content in ice estimated through a full-depth ground radar profile and borehole measurements in western Greenland, The Cryosphere, 11, 669–679, https://doi.org/10.5194/tc-11-669-2017, 2017.

Bukowska-Jania, E.: The role of glacier system in migration of calcium carbonate on Svalbard, Pol. Polar Res., 28, 137–155, 2007.

Clarke, G. K. C.: Subglacial till: A physical framework for its properties and processes, J. Geophys. Res., 92, 9023–9036, https://doi.org/10.1029/jb092ib09p09023 1987.

Clarke, G. K. C.: Subglacial Processes, Ann. Rev. Earth Planet. Sci., 33, 247–276, https://doi.org/10.1146/annurev.earth.33.092203.122621, 2005.

Dallmann, W. K.: Geoscience Atlas of Svalbard, Norsk polarinstitutt Rapportserie, 2015.

Døssing, A., Jaspen, P., Watts, A. B., Nielsen, T., Jokat, W., Thybo, H., and Dahl-Jensen, T.: Miocene uplift of the NE Greenland margin linked to plate tectonics: Seismic evidence from the Greenland Fracture Zone, NE Atlantic, Tectonics, 35, 1–26, https://doi.org/10.1002/2015tc004079, 2016.

Dowdeswell, J., Drewry, D., Cooper, A., Gorman, M., Liestøl, O., and Prheim, O.: Digital mapping of the Nordaustlandet ice caps from airborne geophysical investigations, Ann. Glaciol., 8, 51–58, https://doi.org/10.1017/s0260305500001130, 1986.

Dowdeswell, J. A., Hagen, J. O., Björnsson, H., Glazovsky, A. F., Harrison, W. D., Holmlund, P., Jania, J., Koerner, R. M., Lefauconnier, B., Ommanney, C. S. L., and Thomas, R. H.: The Mass Balance of Circum-Arctic Glaciers and Recent Climate Change, Quaternary Res., 48, 1–14, https://doi.org/10.1006/qres.1997.1900, 1997.

Dowdeswell, J. A., Benham, T. J., Strozzi, T., and Hagen, J. O.: Iceberg calving flux and mass balance of the Austfonna ice cap on Nordaustlandet, Svalbard, J. Geophys. Res., 113, F03022, https://doi.org/10.1029/2007JF000905, 2008.

Dunse, T., Greve, R., Schuler, T. V., and Hagen, J. O.: Permanent fast flow versus cyclic surge behavior: numerical simulations of the Austfonna ice cap, Svalbard, J. Glaciol., 57, 247–259, https://doi.org/10.3189/002214311796405979, 2011.

Dunse, T., Schuler, T. V., Hagen, J. O., and Reijmer, C. H.: Seasonal speed-up of two outlet glaciers of Austfonna, Svalbard, inferred from continuous GPS measurements, The Cryosphere, 6, 453–466, https://doi.org/10.5194/tc-6-453-2012, 2012.

Dunse, T., Schellenberger, T., Hagen, J. O., Kääb, A., Schuler, T. V., and Reijmer, C. H.: Glacier-surge mechanisms promoted by a hydro-thermodynamic feedback to summer melt, The Cryosphere, 9, 197–215, https://doi.org/10.5194/tc-9-197-2015, 2015.

Eyles, N., Boyce, J. I., and Putkinen, N.: Neoglacial (< 3000 years) till and flutes at Saskatchewan Glacier, Canadian Rocky Mountains, formed by subglacial deformation of a soft bed, Sedimentology, 62, 182–203, https://doi.org/10.1111/sed.12145, 2015.

Fairhead, J. D., Salem, A., Williams, S., and Samson, E.: Magnetic interpretation made easy: The Tilt-Depth-Dip- ΔK method, SEG Technical Program Expanded Abstracts 2008, 779–783, https://doi.org/10.1190/1.3063761, 2008.

Flood, B., Gee, D. G., Hjelle, A., Siggerud, T., and Winsnes, T. S.: The Geology of Nordaustlandet, northern and central parts, Norsk Polarinstitutt Skrifter, 146, 1969.

Forsberg, R. and Olesen, A. V.: Airborne Gravity Field Determination, in: Sciences of Geodesy – I: Advances and Future Directions, edited by: Xu, G., Springer Berlin Heidelberg, Berlin, Heidelberg, 83–104, 2010.

Forsberg, R., Olesen, A. V., Keller, K., and Møller, M.: Airborne gravity survey of sea areas around Greenland and Svalbard 1999–2001, Survey and processing report – KMS Technical Report, 18, 2002.

Fürst, J. J., Navarro, F., Gillet-Chaulet, F., Huss, M., Moholdt, G., Fettweis, X., Lang, C., Seehaus, T., Ai, S., Benham, T. J., Benn, D. I., Björnsson, H., Dowdeswell, J. A., Grabiec, M., Kohler, J., Lavrentiev, I., Lindbäck, K., Melvold, K., Pettersson, R., Rippin, D., Saintenoy, A., Sánchez-Gámez, Schuler, T. V., Sevestre, H., Vasilenko, E., and Braun, M. H.: The Ice-Free Topography of Svalbard, Geophys. Res. Lett., 45, 11760–711769, https://doi.org/10.1029/2018GL079734, 2018.

Geological Survey of Norway Geoscience Portal, available at: http://geo.ngu.no/GeosciencePortal/search (last access: November 2019), 2016.

Geosoft: GM-SYS profile modeling. Gravity and Magnetic Modeling Software, v. 4.10, Geosoft Incorporated, p. 116, 2006.

Gernigon, L. and Brönner, M.: Late Palaeozoic architecture and evolution of the southwestern Barents Sea: insights from a new generation of aeromagnetic data, Journal of the Geological Society, London, 169, 449–459, https://doi.org/10.1144/0016-76492011-131, 2012.

Gernigon, L., Brönner, M., Dumais, M.-A., Gradmann, S., Grønlie, A., Nasuti, A., and Roberts, D.: Basement inheritance and salt structures in the SE Barents Sea: Insights from new potential field data, J. Geodynam., 119, 82–106, https://doi.org/10.1016/j.jog.2018.03.008, 2018.

Gladstone, R., Schäfer, M., Zwinger, T., Gong, Y., Strozzi, T., Mottram, R., Boberg, F., and Moore, J. C.: Importance of basal processes in simulations of a surging Svalbard outlet glacier, The Cryosphere, 8, 1393–1405, https://doi.org/10.5194/tc-8-1393-2014, 2014.

GlaThiDa Consortium: Glacier Thickness Database 3.0.1, World Glacier Monitoring Service, Zurich, Switzerland, https://doi.org/10.5904/wgms-glathida-2019-03, 2019.

Gong, Y., Zwinger, T., Åström, J., Altena, B., Schellenberger, T., Gladstone, R., and Moore, J. C.: Simulating the roles of crevasse routing of surface water and basal friction on the surge evolution of Basin 3, Austfonna ice cap, The Cryosphere, 12, 1563–1577, https://doi.org/10.5194/tc-12-1563-2018, 2018.

Gourlet, P., Rignot, E., Rivera, A., and Casassa, G.: Ice thickness of the northern half of the Patagonia Icefields of South America from high-resolution airborne gravity surveys, Geophys. Res. Lett., 43, 241–249, https://doi.org/10.1002/2015GL066728, 2015.

Goussev, S. A. and Peirce, J. W.: Magnetic basement: gravity-guided magnetic source depth analysis and interpretation, Geophys. Prosp., 58, 321–334, https://doi.org/10.1111/j.1365-2478.2009.00817.x, 2010.

Gray, L., Burgess, D., Copland, L., Demuth, M. N., Dunse, T., Langley, K., and Schuler, T. V.: CryoSat-2 delivers monthly and inter-annual surface elevation change for Arctic ice caps, The Cryosphere, 9, 1895–1913, https://doi.org/10.5194/tc-9-1895-2015, 2015.

Grinsted, A.: An estimate of global glacier volume, The Cryosphere, 7, 141–151, https://doi.org/10.5194/tc-7-141-2013, 2013.

Grogan, P., Nyberg, K., Fotland, B., Myklebust, R., Dahlgren, S., and Riis, F.: Cretaceous Magmatism South and East of Svalbard: Evidence from Seismic Reflection and Magnetic Data, Polarforschung, 68, 25–34, 2000.

Harland, W. B., Cutbill, J. L., Friend, P. F., Gobbett, D. J., Holliday, D. W., Maton, P. I., Parker, J. R., and Wallis, R. H.: The Billefjorden fault zone, Spitsbergen: the long history of a major tectonic lineament, Norsk Polarinstitutt Skrifter, 161, 1974.

Hinze, W., Von Frese, R., and Saad, A.: Gravity and magnetic exploration: Principles, practices and applications, Cambridge University Press, 2013.

Hodgson, D. A., Jordan, T. A., De Rydt, J., Fretwell, P. T., Seddon, S. A., Becker, D., Hogan, K. A., Smith, A. M., and Vaughan, D. G.: Past and future dynamics of the Brunt Ice Shelf from seabed bathymetry and ice shelf geometry, The Cryosphere, 13, 545–556, https://doi.org/10.5194/tc-13-545-2019, 2019.

Hunt, C. P., Moskowitz, B. M., and Banerjee, S. K.: Rock physics and phase relations, A Handbook of Physical Constants: AGU Reference Shelf, Americain Geophysical Union Vol. 3, 189–204, 1995.

Ignatieva, I. Y. and Macheret, Y. Y.: Evolution of Nordaustlandet ice caps in Svalbard under climate warming, Glaciers-Ocean-Aonosphere Interactions, Proceedings of the International Symposium held at St Petersburg, September 1990, IAHS Publ. no. 208, 208, 301–312, 1991.

Iverson, N. R., Hooyer, T. S., Fischer, U. H., Cohen, D., Moore, P. L., Jackson, M., Lappegard, G., and Kohler, J.: Soft-bed experiments beneath Engabreen, Norway:regelation infiltration, basal slip and bed deformation, J. Glaciol., 53, 323–340, https://doi.org/10.3189/002214307783258431, 2007.

Jania, J., Macheret, Y. Y., Navarro, F. J., Glazovsky, A. F., Valisenko, E. V., Lapazaran, J. J., Glowacki, P., Migala, K., Balut,

A., and Piwowar, B. A.: Temporal changes in the radiophysical properties of a polythermal glacier in Spitsbergen, Ann. Glaciol., 42, 125–134, https://doi.org/10.3189/172756405781812754, 2005.

Jiskoot, H., Murray, T., and Boyle, P.: Controls on the distribution of surge-type glaciers in Svalbard, J. Glaciol., 46, 412–422, https://doi.org/10.3189/172756500781833115, 2000.

Johansson, Å., Larionov, A. N., Tebenkov, A. M., Ohta, Y., and Gee, D. G.: Caledonian granites of western and central Nordaustlandet, northeast Svalbard, GFF, 124, 135–148, https://doi.org/10.1080/11035890201243135, 2002.

Johansson, Å., Gee, D. G., Larionov, A. N., Ohta, Y., and Tebenkov, A. M.: Grenvillian and Caledonian evolution of eastern Svalbard – a tale of two orogenies, Terra Nova, 17, 317–325, https://doi.org/10.1111/j.1365-3121.2005.00616.x, 2005.

Ku, C. C. and Sharp, J. A.: Werner deconvolution for automated magnetic interpretation and its refinement using Marquart's inverse modeling, Geophysics, 48, 754–774, https://doi.org/10.1190/1.1441505 1983.

Lafehr, T. R.: Standardization in gravity reduction, Geophysics, 56, 1170–1178, 1991.

Lapazaran, J. J., Otero, J., Martín-Español, A., and Navarro, F. J.: On the errors involved in ice-thickness estimates I: groundpenetrating radar measurement errors, J. Glaciol., 62, 1008–1020, https://doi.org/10.1017/jog.2016.93, 2016.

Lauritzen, Ø. and Ohta, Y.: Geological map of Svalbard 1:500,000. Sheet 4G, Nordaustlandet, Nor. Polarinst. Skr. 154C, 1984.

Matsuoka, K.: Pitfalls in radar diagnosis of ice-sheet bed conditions: Lessons from englacial attenuation models, Geophys. Res. Lett., 38, L05505, https://doi.org/10.1029/2010gl046205, 2011.

McMillan, M., Shepherd, A., Gourmelen, N., Dehecq, A., Leeson, A., Ridout, A., Flament, T., Hogg, A., Gilbert, L., Benham, T. J., van den Broeke, M., Dowdeswell, J. A., Fettweis, X., Noël, B., and Strozzi, T.: Rapid dynamic activation of a marine-based Arctic ice cap, Geophys. Res. Lett., 41, 8902–8909, https://doi.org/10.1002/2014gl062255, 2014.

Miller, H. G. and Singh, V.: Potential field tilt - a new concept for the location of potential field sources, J. Appl. Geophys., 32, 213–217, https://doi.org/10.1016/0926-9851(94)90022-1, 1994.

Minakov, A., Mjelde, R., Faleide, J. I., Flueh, E. R., Dannowski, A., and Keers, H.: Mafic intrusions east of Svalbard imaged by active-source seismic tomography, Tectonophysics, 518–521, 106–118, https://doi.org/10.1016/j.tecto.2011.11.015, 2012.

Moholdt, G., Hagen, J. O., Eiken, T., and Schuler, T. V.: Geometric changes and mass balance of the Austfonna ice cap, Svalbard, The Cryosphere, 4, 21–34, https://doi.org/10.5194/tc-4-21-2010, 2010a.

Moholdt, G., Nuth, C., Hagen, J. O., and Kohler, J.: Recent elevation changes of Svalbard glaciers derived from ICESat laser altimetry, Remote Sens. Environ., 114, 2756–2767, https://doi.org/10.1016/j.rse.2010.06.008, 2010b.

Moran, M. L., Greenfield, R. J., Arcone, S. A., and Delaney, A. J.: Delineation of a complexly dipping temperate glacier bed using short-pulse radar arrays, J. Glaciol., 46, 274–286, https://doi.org/10.3189/172756500781832882, 2000.

Nasuti, A., Roberts, D., Dumais, M. A., Stampolidis, A., Ofstad, F., and Kurimo, M.: New high-resolution aeromagnetic and radiometric surveys in Finnmark and North Troms: linking anomaly patterns to geology and structure, Nor. J. Geol., 95, 217–243, https://doi.org/10.17850/njg95-3-10, 2015.

Navarro, F. J., Otero, J., Macheret, Y. Y., Valisenko, E. V., Lapazaran, J. J., Ahlstrøm, A. P., and Machío, F.: Radioglaciological studies on Hurd Peninsula glaciers, Livingston Island, Antarctica, Ann. Glaciol., 50, 17–24, https://doi.org/10.3189/172756409789097603, 2009.

Navarro, F. J., Martín-Español, A., Lapazaran, J. J., Grabiec, M., Otero, J., Vasilenko, E. V., and Puczko, D.: Ice Volume Estimates from Ground-Penetrating Radar Surveys, Wedel Jarlsberg Land Glaciers, Svalbard, Arct. Antarct. Alp. Res., 46, 394–406, https://doi.org/10.1657/1938-4246-46.2.394, 2014.

Ng, F. and Hallet, B.: Patterning mechanisms in subglacial carbonate dissolution and deposition, J. Glaciol., 48, 386–400, https://doi.org/10.3189/172756502781831214, 2002.

Norwegian Polar Institute: Kartdata Svalbard 1:250 000. Sheet 3, Norwegian Polar Institute, 1998.

Ohta, Y.: Recent understanding of the Svalbard basement in the light of new radiometric age determinations, Norsk Geologisk Tidsskrift, 72, 1–5, 1992.

Olaizola, M., van de Wal, R. S. W., Helsen, M. M., and de Boer, B.: An ice flow modeling perspective on bedrock adjustment patterns of the Greenland ice sheet, The Cryosphere, 6, 1263–1274, https://doi.org/10.5194/tc-6-1263-2012, 2012.

Olesen, O., Brönner, M., Ebbing, J., Gellein, J., Gernigon, L., Koziel, J., Lauritsen, T., Myklebust, R., Pascal, C., Sand, M., Solheim, D., and Usov, S.: New aeromagnetic and gravity compilations from Norway and adjacent areas: methods and applications, Geological Society, London, Petroleum Geology Conference series, 7, 559–586, https://doi.org/10.1144/0070559, 2010.

Overrein, Ø., Johansen, B. F., and Dallmann, W. K.: Nordauslandet's geology and landscape, Cruise Handbook for Svalbard, Norwegian Polar Institute, 2015.

Paterson, W. S. B. and Clarke, G. K. C.: Comparison of theoretical and observed temperature profiles in Devon Island ice cap, Canada, Geophys. J., 55, 615–632, https://doi.org/10.1111/j.1365-246X.1978.tb05931.x, 1978.

Phillips, J. D.: Potential-Field Geophysical Software for the PC, version 2.2, USGS open-File Report, 97, https://doi.org/10.3133/ofr97725 1997.

Polteau, S., Hendriks, B. W. H., Planke, S., Ganerød, M., Corfu, F., Faleide, J. I., Midtkandal, I., Svensen, H. S., and Myklebust, R.: The early cretaceous Barents Sea sill complex: distribution, 40Ar/39Ar geochronology, and implications for carbon gas formation, Palaeogeogr. Palaeoclimatol. Palaeoecol., 441, 83–95, https://doi.org/10.1016/j.palaeo.2015.07.007, 2016.

Porter, D. F., Tinto, K. J., Boghosian, A., Cochran, J. R., Bell, R. E., Manizade, S. S., and Sonntag, J. G.: Bathymetric control of tidewater glacier mass loss in northwest Greenland, Earth Planet. Sci. Lett., 401, 40–46, https://doi.org/10.1016/j.epsl.2014.05.058, 2014.

Przylibski, T. A., Ciężkowski, W., Głowacki, T., Grudzińska, K. K., Kasza, D., Zagożdżon, P. P., and Kasza, D.: Front of the Werenskiold Glacier (Svalbard) – changes in years 1957–2013, E3S Web of Conferences, 29, 00030, https://doi.org/10.1051/e3sconf/20182900030, 2018.

Radić, V., Bliss, A., Beedlow, A. C., Hock, R., Miles, E., and Cogley, J. G.: Regional and global projections of twenty-first century glacier mass changes in response to climate scenar-

ios from global climate models, Clim. Dynam., 42, 37–58, https://doi.org/10.1007/s00382-013-1719-7, 2013.

Reid, A. B., Allsop, J. M., Granser, H., Millett, A. J., and Somerton, I. W.: Magnetic interpretation in three dimensions using Euler deconvolution, Geophysics, 55, 80–91, https://doi.org/10.1190/1.1442774, 1990.

Ritzmann, O., Maercklin, N., Faleide, J. I., Bungum, H., Mooney, W. D., and Detweiler, S. T.: A three-dimensional geophysical model of the crust in the Barents Sea region: model construction and basement characterization, Geophys. J. Int., 170, 417–435, https://doi.org/10.1111/j.1365-246x.2007.03337.x 2007.

Salem, A., Williams, S., Fairhead, J. D., Ravat, D., and Smith, R.: Tilt-depth method: A simple depth estimation method using first order magnetic derivatives, The Leading Edge, 26, 1502–1505, https://doi.org/10.1190/1.2821934, 2007.

Schäfer, M., Zwinger, T., Christoffersen, P., Gillet-Chaulet, F., Laakso, K., Pettersson, R., Pohjola, V. A., Strozzi, T., and Moore, J. C.: Sensitivity of basal conditions in an inverse model: Vestfonna ice cap, Nordaustlandet/Svalbard, The Cryosphere, 6, 771–783, https://doi.org/10.5194/tc-6-771-2012, 2012.

Schytt, V.: Some comments on glacier surges in eastern Svalbard, Can. J. Earth Sci., 46, 867–873, https://doi.org/10.1139/e69-088, 1969.

Spector, A.: A gravity survey of the Melville Island ice caps, J. Glaciol., 6, 393–400, https://doi.org/10.3189/s002214300001950x, 1966.

Studinger, M., Bell, R., Fitzgerald, P., and Buck, W.: Crustal architecture of the Transantarctic Mountains between the Scott and Reedy Glacier region and South Pole from aerogeophysical data, Earth Planet. Sci. Lett., 250, 182–199, https://doi.org/10.1016/j.epsl.2006.07.035, 2006.

Studinger, M., Bell, R., and Frearson, N.: Comparison of AIRGrav and GT-1A airborne gravimeters for research applicationsComparison of airborne gravimeters, Geophysics, 73, I51–I61, https://doi.org/10.1190/1.2969664, 2008.

Telford, W. M., Geldart, L. P., and Sheriff, R. E.: Applied Geophysics, 2 ed., Cambridge University Press, Cambridge, 1990.

Thébault, E., Finlay, C. C., Beggan, C. D., Alken, P., Aubert, J., Barrois, O., Bertrand, F., Bondar, T., Boness, A., Brocco, L., Canet, E., Chambodut, A., Chulliat, A., Coïsson, P., Civet, F., Du, A., Fournier, A., Fratter, I., Gillet, N., Hamilton, B., Hamoudi, M., Hulot, G., Jager, T., Korte, M., Kuang, W., Lalanne, X., Langlais, B., Léger, J.-M., Lesur, V., Lowes, F. J., Macmillan, S., Mandea, M., Manoj, C., Maus, S., Olsen, N., Petrov, V., Ridley, V., Rother, M., Sabaka, T. J., Saturnino, D., Schachtschneider, R., Sirol, O., Tangborn, A., Thomson, A., Tøffner-Clausen, L., Vigneron, P., Wardinski, I., and Zvereva, T.: International Geomagnetic Reference Field: the 12th generation, Earth, Planet. Space, 67, 79, https://doi.org/10.1186/s40623-015-0228-9, 2015.

Thompson, D. T.: EULDPH: A new technique for making computer-assisted depth estimates from magnetic data, Geophysics, 47, 31–37, https://doi.org/10.1190/1.1441278, 1982.

Tinto, K. J. and Bell, R. E.: Progressive unpinning of Thwaites Glacier from newly identified offshore ridge: Constraints from aerogravity, Geophys. Res. Lett., 38, L20503, https://doi.org/10.1029/2011gl049026, 2011.

Tinto, K. J., Bell, R. E., Cochran, J. R., and Münchow, A.: Bathymetry in Petermann fjord from Operation IceBridge aerogravity, Earth Planet. Sci. Lett., 422, 58–66, https://doi.org/10.1016/j.epsl.2015.04.009, 2015.

Vaughan, D. G., Comiso, J. C., Allison, I., Carrasco, J., Kaser, G., Kwok, R., Mote, P., Murray, T., Paul, F., Ren, J., Rignot, E., Solomina, O., Steffen, K., and Zhang, T.: Observations: Cryosphere, in: Climate Change 2013: The Physical Science Basis. Contribution of Working Group I to the Fifth Assessment Report of the Intergovernmental Panel on Climate Change, edited by: Stocker, T. F., Qin, D., Plattner, G.-K., Tignor, M., Allen, S. K., Boschung, J., Nauels, A., Xia, Y., Bex, V., and Midgley, P. M., Cambridge University Press, Cambridge, United Kingdom and New York, NY, USA, 317–382, 2013.

Werner, S.: Interpretation of magnetic anomalies as sheet-like bodies, Sveriges Geologiska Undersökning, Series C, Årsbok, 43, 1955.

Zagorodnov, V. A., Sin'kevich, S. A., and Arkhipov, S. M.: Ice core express-analysis for structure and thermal regime studies of Austfonna, Mater. Glyatsiol. Issled./Data Glaciol. Stud., 66, 149–158, 1989.

Zhao, L., Forsberg, R., Wu, M., Olesen, A. V., Zhang, K., and Cao, J.: A Flight Test of the Strapdown Airborne Gravimeter SGA-WZ in Greenland, Sensors (Basel), 15, 13258–13269, https://doi.org/10.3390/s150613258, 2015.

4. Work Synthesis

Airborne magnetic data acquisition is a fast and economic way to gain knowledge on regional geological settings in remote frontier areas like in the Arctic. The data also bridge the gap between onshore and offshore allowing a joint interpretation from the oceanic domain in the Fram Strait to onshore Svalbard and Greenland providing a comprehensive overview of the conjugate margins development and the complex opening of the Fram Strait and seafloor spreading history along in the Knipovich Ridge. Combined with modern world gravity compilations, potential field interpretation facilitates the study of the regional tectonic of the basement both in the deep ocean and underneath the extensive ice caps in the Arctic.

The first article presents the interpretation of the aeromagnetic survey KRAS-16, covering the Fram Strait. The magnetic data were compiled with existing data from the surrounding areas of Gakkel Ridge, Boreas Basin, Barents Sea and Svalbard [*Jokat et al.*, 2016; *Olesen et al.*, 2010; *Jokat et al.*, 2008], allowing a regional interpretation of the Fram Strait and the spreading evolution of the Knipovich Ridge. Numerous oceanic fracture zones and lineaments are identified in the gridded data. The high-frequency striped magnetic anomalies delineate the oceanic domain, characterized by magnetized basalt and magnetic isochrons correlated to the chronostratigraphic chart of Ogg [2012]. The new magnetic compilation for the Fram Strait and the western Barents Sea margin image for the first time continuously the eastern continent-ocean boundary (COB) clearly replacing its location up to 150 km to the west compared to previous interpretations.

Line data were modelled with *ModMag* [*Mendel et al.*, 2005] to map the seafloor spreading chron-anomalies for several profiles. The most representative profiles are presented in the manuscript. To compensate for the sediment thickness affecting the magnetic signature, Engen et al. [2006] sediment thickness estimation was used. This sediment thickness was chosen for its full coverage of the study area on both sides of the Knipovich Ridge. Engen et al. [2006] sediment thickness is mainly derived from gravity and bathymetry data. It is also calibrated for the age of the crust with magnetic isochron and for the base of the sediment layer and the Moho depth with seismic data. It provides a sufficient approximation of the location of the top of the basalt layer to filter out smaller magnetic anomalies in the model from *ModMag*. Unfortunately, no basalt samples were available for palaeomagnetism measurements from the oceanic crust surrounding the Knipovich Ridge. These measurements would have provided an age associated with the magnetic anomalies mapped. However, despite the 90-degree bend between Knipovich Ridge and Mohns Ridge, the seafloor spreading is continuous with similar seafloor spreading rates as seen on the aeromagnetic data. Mohns Ridge spreading anomalies are used to calibrate the Knipovich Ridge spreading evolution. Magnetic isochrons were picked on the line profiles. Where the striped magnetic anomaly pattern is disrupted by magnetic lineaments, the width and intensity

of the magnetic isochron is used for identification, i.e. magnetic isochron C6 is expected to have a similar width and intensity along the Knipovich Ridge regardless of displacement. The first unambiguous magnetic isochron is C6 (20 Ma). The opening of the Knipovich Ridge's northern section was always linked to a high asymmetry spreading. However, from the new magnetic data, a failed spreading system opening at C6 and a ridge jump at C5E is identified and with subsequent fairly symmetric spreading until today.

The results are visualized with *Gplate 2.2* [*Müller et al.*, 2018] allowing the plate-tectonic reconstruction of the Fram Strait. The seafloor spreading initiation at C6 (20 Ma) is seen all along the ridge. Around 18 Ma (C5E-C5C), the section between N77° and N78° is abandoned and migrates to the east where the seafloor spreading continues, forming today's Knipovich Ridge. Within this new section, the seafloor spreading becomes asymmetric with faster seafloor spreading rates towards the Boreas Basin. Between N75° and N76°, the striped anomalies disappear after C5 (10 Ma), implying a weakening of the magnetization due to a significant change in the mantle melt chemistry, thermal regime, seafloor spreading velocity or a combination of all three conditions.

For the reconstruction model, the Euler poles from previous studies [*Gernigon et al.*, 2019; *Matthews et al.*, 2016; *Gernigon et al.*, 2015] were used. New Euler poles have been estimated qualitatively for the reconstruction of the extinct spreading ridge (Table 4.1). In the 18 Ma window of Figure 3 in the research paper, the extinct ridge overlaps with the continental crust. The tectonic plates are considered rigid in the calculation done with *Gplate 2.2*. Further simulations are needed to test crustal deformation. This would be better achieved with few more seismic profiles on both sides of the ridge from the East Greenland Ridge and Boreas Basin to the Svalbard margin to provide reliable constraints. Due to the Eurekan orogeny, the crust might have been thicker than what is seen today. Further investigation is needed to assess this portion and estimate the crustal thickness before the seafloor spreading. With more constraints and information on crustal deformation and extent, a quantitative calculation of the Euler poles would provide a more reliable and accurate reconstruction.

Chron	Age (Ma)	Longitude (˚)	Latitude (˚)	Angle (˚)
C5Eno	18.2	-58.8127	-39.6409	-3.857
C6no	19.7	-40.1769	-31.8535	-2.7283

Table 4.1 Euler rotation poles qualitatively estimated for the reconstruction of the extinct spreading ridge.

The opening of the Fram Strait occurs obliquely to the Mohns Ridge and developed after the opening of the Norwegian-Greenland Sea and the Eurasian Basin already initiated in the Early Eocene [*Brozena et al.*, 2003]. This coincides with the opening of the Molloy Ridge

(20 Ma [*Engen et al.*, 2008; *Srivastava and Tapscott*, 1986]) and Kolbensey Ridge (C7-6 [*Schiffer et al.*, 2019; *Blischke et al.*, 2017]), and the Gakkel Ridge extending and penetrating in the Fram Strait (C8-5 [*Glebovsky et al.*, 2006; *Brozena et al.*, 2003]). This may indicate a common link of mid-Atlantic ridge segments allowing a synchronous initiation breakup at several locations of the North Atlantic-Arctic realm.

The second article considers the implications of this new location of the COB and the oceanic domain. A 3-D magnetic inversion is derived from the KRAS-16 aeromagnetic data, constrained with the seismic Moho [*Funck et al.*, 2017] and a sediment thickness [*Engen et al.*, 2006]. Using available gravity, seismic, controlled source electromagnetic (CSEM) and magneto-telluric (MT) data, 2-D forward models are used to investigate the thermal and crustal heterogeneities of the Fram Strait and Svalbard Margin. For the 2-D forward models, the sediment and crustal layers are constrained by the available seismic and CSEM/MT data. Several scenarios were tested, but only the most realistic scenarios are presented in the manuscript. The initial densities are extracted from the seismic and gravity modelling and modified, with justification, to fit the magnetic and gravity observed fields. The densities, susceptibilities and remanence are selected to be comparable from profile to profile. The geometries from the seismic profiles are modified when necessary to obtain realistic densities and susceptibilities. A valuable contribution is profile P6 intersecting profiles P2 and P3. The 2-D models reduce mismatch at the intersection point between two profiles as the best fit with the gravity and magnetic responses is chosen to solve the mismatch. Moreover, a Werner deconvolution and a Curie depth is calculated from the KRAS-16 aeromagnetic data, providing depth estimation of the top and bottom crustal basement.

The model interpretation illustrates the spatial variation of the densities, susceptibilities, remanence and thermal properties of the crust and mantle along the Knipovich Ridge and across the Svalbard Margin. Along the oceanic domain, the magnetization varies in polarity and intensity. While the 3-D magnetization model assumes a homogeneous crust without differentiation for layers 2A, 2B and 3, it provides information on the type and strength of magnetization found along the Knipovich Ridge. With the stronger magnetization and the more prominent occurrence of bathymetric highs and volcanoes in the rift valley at the northern latitudes of the Knipovich Ridge, the oceanic crust has different physical properties than at the southern part of the Knipovich Ridge. Therefore, the mantle processes, the volume and composition of the magma chamber below the ridge and the cooling processes are expected to vary from South to North. An amagmatic segment is proposed at the lower latitudes (74°N-76°N) to explain the low magnetization. With basalt and gabbro samples and a few more seismic or CSEM/MT lines, it would be possible to build a reliable 3-D magnetization model of the oceanic crust below the Knipovich Ridge. With information about the location of lineaments such as fracture zones derived from the bathymetry and the magnetic data and the depth and location of the earthquakes, the magnetization response

associated with the fluid circulation, magmatic and amagmatic accretion, and the presence of mounds (bathymetric highs) and volcanoes could be studied in detail.

The continental domain starts roughly along the Hornsund Fracture Zone and comprises a basement varying in terms of susceptibilities and densities formed by the Caledonian nappes. A magmatic intrusion is also associated with Billefjorden Fracture Zone [*Skilbrei*, 1992]. Dike and sill intrusions are interpreted on the Edgeøya platform, but the data resolution does not allow for the resolution of the top and bottom depth of the causal sources or to distinguish the type of intrusion. The susceptibility and remanence parameters were chosen to represent the lithology variation between the layers from gabbro to basalts. Magmatic intrusions were modelled to fit the magnetic signature. The magnetic parameters derived in the continental crust were compared to those found on the continental shelf of the Barents Sea and on Nordaustlandet.

The oceanic and continental domains are separated by a transition domain that extends over tens of kilometres. The Curie depth allows for estimation of the extent of the transition domain where it migrates from shallow (6 km below sea-level) to deep (25-20 km below sea-level). This transition is marked by a gradual thickening of the crust and variation in crustal magnetization and density as interpreted in the 2-D forward models. The transition domain also shares mantle densities identical or comparable to the continental domain. The transition domain is wider at latitude 76°N and slowly narrows until latitude 80°N where it reaches its minimal extent on the eastern margin. On the western margin, the transition domain comprises the East-Greenland Ridge and a large portion of the Boreas Basin.

The transition domain could be interpreted as a thick oceanic crust, but a striped magnetic pattern is not observed on the data. It could be formed by mantle exhumation; however, the Moho is well defined with the refraction waves which does not correlate with a heavily serpentinized mantle [*Christensen*, 1996; *Horen et al.*, 1996; *Christensen*, 1978; 1966]. Thus, the transition domain could represent an exhumed lower continental crust as observed in many hyperextended rift systems [*Clerc et al.*, 2015]. During the rifting before the seafloor spreading initiation at C6, the intruded continental lower crust could have gradually migrated and exhumed towards the proto-oceanic domain. A pre-existing thick and low-viscosity lower continental crust caused by the Eurekan orogeny could explain a lateral flow of the ductile lower crust. Given the seafloor spreading initiation at C6 (20 Ma), the Eurekan deformation occurred prior to the ridge spreading [*Piepjohn et al.*, 2016]. The Eurekan deformation could have thickened and softened the crust before a rapid collapse and rifting leading to a lateral escape of the lower continental material. This scenario is consistent with the crustal and mantle properties interpreted in the 2-D forward models.

At the southernmost edge of KRAS-16, the third article dives in hydrothermal activity on Mohns Ridge northernmost segment near the bend junction with Knipovich Ridge. Magnetic surveying was performed by an autonomous underwater vehicle (AUV) while rock sampling was conducted with remotely operated vehicles during the *MarMine* cruise [*Ludvigsen et al.*, 2016]. Analysis of the high-resolution bathymetry [*Norwegian Mapping Authority*, 2015] and magnetic data combined with the physical properties of the rock samples collected yields to the identification of hydrothermal mineral deposits.

Loki's Castle, a known active hydrothermal venting field, consists of two sulphide mounds located on top of a relay structure at the downthrown block of a significantly faulted flat-topped seamount. Rock magnetics and profile magnetic data suggest a reduced magnetization contrast associated with the basalt-hosted Loki's Castle deposit. A 2-D forward model across the mound illustrates that a localized body with reduced magnetization explains the observed data as a possible concept. The parameters used in the model are based on the few rock samples available from the mission and values from the literature. A single body could be modelled with a wider opening. A body with a variation of the susceptibility closer to the bedrock illustrate a more realistic intrusion. Ideally a profile should be acquired above each mound. In the case of two adjacent profiles crossing each mound, it would be advantageous to use a 2.5-D model and test various configuration of the deposit. One hypothesis is that two sulphide mounds are interconnected. The 2.5-D modelling approach could resolve this hypothesis. However, the resolution of the deposit in 3-D requires closer line spacing and stronger control on the altitude of the AUV.

Mohn's Treasure (MT-1), a fossil sediment-hosted hydrothermal deposit, is associated with a positive magnetic anomaly coincident with sulphide samples recovered from the site. The anomaly is centred at a fault crossing on the slope of a mass-wasting deposit of the western rift flank. The causative body is approximately 200-m x 150-m buried by sediments at approximately 15-m depth. The site has enhanced magnetization and produces a clear magnetic signature that leads to the identification of two new deposits (MT-2 and MT-3).

In the third area acquired with the AUV, AVR_2, the magnetic signature is not as revealing as Loki's Castle or Mohn's Treasure but provides insights of the rim of the seamount. With a typical flat-topped volcano shape and the analysis of the detailed bathymetry showing traces of overflowing lava on its southwestern slope, a formation of such a seamount suggests the presence of a near-surface magma chamber. The tilt derivative of the magnetic data is most useful to identify the shape of the seamount and corroborates with the hypothesis of hot magma chamber.

Migrating away from the oceanic domain and its thermal and crustal properties to Svalbard continental domain, the last article addresses the underlying topography and lithology of the

Austfonna icecap. Potential field data can identify morphology and depth of the bedrock topography underneath ice caps due to the natural petrophyscial contrast in density and magnetisation between ice and basement rocks. Airborne magnetic data were collected during two campaigns (1989 and 1991) and re-processed and compiled for the purpose of this study. Airborne gravity data were acquired in 1999 and 2000 [*Forsberg and Olesen*, 2010; *Forsberg et al.*, 2002] while the ice topography was published by NPI in 1998 [*Norwegian Polar Institute*, 1998]. Several GPR-RES campaigns have contributed to the ice thickness and bed topography evaluation [*Dunse et al.*, 2011; *Moholdt et al.*, 2010; *Dowdeswell et al.*, 2008; *Dowdeswell et al.*, 1986].

In a first step, gravity measurements were used to adjust the bed topography under the ice. The preferred method used an analogous approximation to the sedimentary-basin interpretation [*Bott*, 1960]. This method allows for the correction of the input bed topography from GPR-RES data with the gravity data. The greatest corrections from the gravity have been found under Vegafonna (southwest of Austfonna) and Leighbreen and Worsleybreen (northeast of Austfonna). These areas are also scarce of GPR-RES data suggesting this method can complement GPR-RES acquisition. However, the method yields to erroneous correction in some area especially near known source of carbonate deposit and where the basement is heterogeneous.

In a second step, the paper presents a model of the lithology and basement affinities of the bed. Tilt-derivative of the magnetic anomaly is used to determine the depth and edges of the body by using Werner deconvolution, Blakely edge solution depth method [*Blakely et al.*, 2016], and adding an extra adjustment to consider the depth of cylindrical shape bodies. Combined to a 2-D forward model, shallow (less than 2 km) sills and deeper (8 km) granitic intrusions are interpreted under Austfonna. The presence of a large carbonate body is also derived from the model. The study concludes on the importance of using magnetic data as gravity solely used can lead to erroneous gravimetric adjustment when the underlying bed is not homogeneous. The model provides an extra source of correction of the bed topography from GPR-RES data.

The method enhances and refines bed topography derived from GPR-RES which can be contaminated by scarce sampling, accumulated water in an erodible basement, gridding interpolation, signal loss or reflection from lateral walls and steep bed slopes and time-to-thickness conversion. With a heterogeneous bed, rough topography, the presence of granitic intrusions and carbonate, the basal thermal regime can be more complex than previously thought.

5. Concluding remarks

This study uses potential field methods to improve the tectono-geological and environmental knowledge of the Norwegian Polar Regions. Several datasets and techniques were used jointly to map the crustal lithology at the Knipovich Ridge, the western Barents Sea margin and more specifically Loki's Castle, Mohn's Treasure and Austfonna, from regional to prospect scale. Filtering techniques highlighted the crustal domains, oceanic fracture zones, seafloor spreading anomalies, magnetized intrusions, and faults related to lineaments in the basement. Werner deconvolutions, Euler deconvolutions and the tilt derivative provided edge detection and depth-to-source estimations. 2-D forward modelling was used to determine the basement lithology in terms of density and magnetization variation and provided insights on the mantle thermal structure, hydrothermal venting fluid circulation and basal glacier thermal regime. The results presented in this thesis contribute to improve the understanding of the Fram Strait development, the magmatism in the Norwegian Polar Regions, and their consequences on the crustal settings and thermal regime.

5.1. Main conclusions

Magnetic data were acquired, processed or re-processed both airborne and submarine near the seafloor. Combined with gravity, seismic and controlled source electromagnetic – magneto-telluric data, and geological maps, these datasets were analysed through this study and several major conclusions have been drawn. Four specific objectives were targeted for this study.

1. *Resolving the seafloor spreading history of the Knipovich Ridge and refining the location of the continent-ocean boundary with aeromagnetic data (KRAS-16)*

For the first time, a complete coverage of the Knipovich Ridge and the Svalbard Margin with aeromagnetic data allows for a full interpretation of the seafloor spreading history of the Knipovich Ridge. The results highlight the magmatic / amagmatic nature of the Knipovich Ridge and the complexity of the development of this region. Magnetic isochrons are identified and a plate reconstruction is carried out. Magnetic isochron C6 is identified with several geological discontinuities related to the shear-forces component along the Knipovich Ridge. Two main conclusions are drawn.

- The Knipovich Ridge spreading onset occurred at C6 (20 Ma), the first unambiguous magnetic isochron identified in the aeromagnetic data. The seafloor spreading pattern asymmetry is explained by an abandoned ridge in the Boreas Basin followed by a ridge jump where the current Knipovich Ridge is located. This opening occurred shortly after the Kolbeinsey Ridge opening and Gakkel Ridge prolongation and may

indicate a synchronous seafloor spreading initiation of several mid-Atlantic ridge segments.

- The continent-ocean boundary was remapped according to the delineation of magnetic isochron C6 delimiting the seafloor spreading onset of the Knipovich Ridge. It changes the seafloor spreading history and the understanding of the crustal domains in the region, indicating the presence of a significant event of the continental crust stretching.

2. *Describing and explaining the crustal structure and the tectonic setting of the Fram Strait with the revised location of the continent-ocean boundary.*

The results from the new interpretation of the seafloor spreading of the Fram Strait and the remapping of the continent-ocean boundary prompt to do an integrated geophysical study including the available bathymetry, seismic, controlled source electromagnetic – magneto-telluric profiles and gravity data. Several interpretation techniques, such as Werner deconvolution, Curie point depth estimation, 3-D magnetic inversion modelling and 2-D magnetic and gravity forward modelling, indicates crustal heterogeneities in the Fram Strait and along the Svalbard Margin. Three points are concluded on this aspect.

- The delineation of several lineaments and the bend configuration of the Knipovich Ridge is associated with a variation in the magnetization and settings along the Knipovich Ridge. Along with magmatic and amagmatic accretion, it possibly controls the seafloor spreading settings and fluid circulation influences its composition and magnetization.

- The continent-ocean boundary derived from the aeromagnetic data correlates with the density and magnetization variation in the crustal domains and the density variation in the mantle. A wide transition zone is delineated between the Knipovich Ridge and the Svalbard Margin. From the densities and magnetizations interpreted, this domain can be modelled as an exhumed mantle or an exhumed intruded lower crust. The oblique spreading constrained by the Mohns Ridge and the East Greenland Ridge may have favoured a crustal stretching along the eastern continental margin.

- The analysis of the bathymetric data along the rift valley with the magnetization derived from the 3-D inversion model suggests a correlation between the bathymetric highs and volcanoes in the rift valley and a stronger magnetization beneath the ridge, supporting the model of multiple mantle magma cells along the ridge with possibly chemical composition variation.

3. *Recognizing the geophysical signature of hydrothermal activity at Loki's Castle, Mohn's Treasure and AVR$_2$ to develop a methodology enabling the identification of associated mineral deposits.*

Numerous studies have highlighted the mineral potential of ultraslow spreading ridges and the impact of their hydrothermal activity on the ocean chemistry balance. Magnetic data were acquired with an autonomous underwater vehicle to characterise the rift valley sub-surface. The results of this investigation concluded on the potential for magnetic data to target mineral deposits.

- Hydrothermal venting fields were interpreted at the bend between Knipovich and Mohns ridges. Loki's Castle active hydrothermal vent is associated with a negative magnetization, while Mohn's Treasure fossil sediment-hosted hydrothermal deposit is associated with a positive magnetization and suggests evidence of the presence of two new deposits. The magnetic data from AVR$_2$ identify the shape of the seamount supporting the hypothesis of a hot magma chamber beneath the seamount.

4. *Identifying the subglacial topography, ice thickness and regional geology of Austfonna on Nordaustlandet to evaluate a potential interaction of the overlying ice shield with the underlying geology and bedrock lithology.*

Ground penetrating radar is the preferred geophysical investigation tool for glacier ice thickness. However, the data interpretation can have important uncertainties caused by the water saturation of the bedrock underlying the glacier or the presence of englacial meltwater streams, common in temperate glacier. Gravity interpretation has been added to partially resolve this issue. This study proposes to use 2-D forward modelling with existing airborne gravity and aeromagnetic data to resolve the ice thickness and map the geology under the glacier. Two conclusions arise from this study.

- Gravity and magnetic interpretation enhanced the knowledge of the subsurface under Austfonna icecap. The bed topography derived from ground penetrating radar and radio-echo sounding measurements is improved with gravity analysis, but knowledge of the basement lithology, magnetic interpretation or both further increases its reliability. With accurate topography measurements at the surface of the glacier, an accurate ice thickness can be derived with ground penetrating radar and 2-D forward modelling.

- 2-D forward modelling also provides insight into the geological and structural affinity of the subglacial bed. It also indicates the basement types in terms of softness, erodibility, and presence of intrusions. Sills, granitic intrusions, and carbonate rocks are interpreted with their evolution time frame. Each of these

geological bodies has a different impact on the basal thermal regime and the erodibility of the basement, consequently leading to heterogenous basal-ice-sliding rates.

Through the four specific objectives of the study, potential field data have proven a useful tool to understand the regional tectonic and understand the complex settings of the Norwegian Polar Regions. The methodologies developed also lead to a better understanding of the hydrothermal venting activity at the mid-Atlantic ridge and the basal thermal regime on Svalbard and provide new tools to study the polar environmental systems.

5.2. Perspectives and further work

The work presented was based on the interpretation of aeromagnetic and gravity data available in the Norwegian Arctic. New aeromagnetic data (KRAS-16) were acquired in the Fram Strait to study the Knipovich Ridge. However, the modelling accuracies and uncertainties depend on the accuracy and resolution of the data available. Given the current state of the aeromagnetic data acquired since 1970 in the Norwegian Arctic, aeras without IGRF correction, such as Nordaustlandet, can be partially revisited to level adequately the dataset to the surrounding data. The location of several oceanic fracture zones and lineaments orthogonal to the Knipovich Ridge could be refined by adding flown lines perpendicular to those lineaments. However, this may not be an optimal solution economically. Areas covered by KRAS-16 with low magnetization or imprecise boundaries, such as the extent of the abandoned ridge, could be revisited with infill-lines between the current acquisition lines. With a water depth of 2,000-3,000 m and a shallow source layer, infill-lines with a line spacing of 2-2.5 km would increase the resolution of the models. Similarly, Nordaustlandet could be revisited with acquisition at lower altitude and denser line spacing to refine the geological model under the glacier. With a glacier thickness of less than 800 m and an altitude of 120 m above ground level, a line spacing of 1,000 m for both airborne gravity and aeromagnetic would improve the modelling resolution.

Collecting deep-tow magnetic profiles would provide shorter wavelengths allowing to resolve and interpret shallower source of the sub-surface. It would enhance the mapping of magnetic isochron C2A and lineaments. Other faint magnetic isochrons could be interpreted as well. However, the seafloor of the rift valley is 3-3.5 km below the sea level with a vertical drop of about 1,000 m. With deep tow magnetometry, usually acquired at constant height, the magnetometer would be in some instances further than 1,000 m from the seafloor, causing artefacts in the data from the variation in distance between the sensor and the source as described in the third manuscript. However, with careful processing, deep-tow magnetic profiles could be acquired with an on-board gravimeter along existing seismic profiles to improve the overall 2-D forward modelling interpretation.

The identification of the magnetic isochrons and seafloor spreading rates calculation relied on the international geological time scale. While the interpretation is potentially accurate for large-scale studies, as the technology of AUV and underwater investigations improves it would be valuable to collect basalt samples for palaeomagnetism measurements and to study at local scale the effects of the seafloor spreading.

The modelling of the Knipovich Ridge proved the complexity of the seafloor spreading and its heterogeneity. The magnetic isochron C1 presents variable intensity along the rift valley. This variation in intensity correlates with the presence of bathymetric highs and volcanoes. It yields to the hypothesis of significant changes in the mantle melt chemistry, thermal regime or seafloor spreading velocities. This can be studied further by combining existing data from seismicity and geochemistry studies.

Gravity data have generally lower resolution than aeromagnetic data due to their sampling rate and filtering requirements. Thus, they are more sensitive to deeper than shallower sources. Slower acquisition speed, lower acquisition height above the source or both would improve the gravity data resolution. Specially designed submarine or marine gravity acquisition across the ridge would improve the gravity modelling of the crust and mantle. The 2-D modelling of the Knipovich Ridge presented in this study identifies area with anomalous magnetization and strong asymmetry. Improving the gravity resolution would improve the density model of the upper mantle, giving more insights in the magmatic accretion and the spreading history.

Combining the refined mantle density model, the Curie depth estimation, sediment load, thermal interpretation from the magneto-telluric data, seismic interpretation, magnetic isochrons and location of the crustal domains, a thermal model of the mantle along the ridge could be proposed.

The bed topography and geology underneath Austfonna was derived from 2-D forward modelling. The same exercise can be extended to Vestfonna, a smaller icecap on Nordaustlandet. With accurate laser or radar altimetry acquired simultaneously to gravity and magnetic data, a 3-D model could be derived, improving the current GPR subglacial bed topography.

With the geology delineated and the bed topography revised, a thermal regime can be developed under Austfonna. Thermal conductivity is available for few rock samples collected on Nordaustlandet. Collecting additional rock samples at specific locations with the revised geological map derived from the geophysical interpretation would allow to establish a realistic subglacial thermal regime and compare it with models produced from surface ice velocity and surface temperature.

6. References

Airy, G. B. (1855), III. On the computation of the effect of the attraction of mountain-masses, as disturbing the apparent astronomical latitude of stations in geodetic surveys, Philosophical Transactions of the Royal Society of London, 145, 101-104.

Alken, P., E. Thébault, C. D. Beggan, H. Amit, J. Aubert, J. Baerenzung, T. N. Bondar, W. J. Brown, S. Califf, A. Chambodut, A. Chulliat, G. A. Cox, C. C. Finlay, A. Fournier, N. Gillet, A. Grayver, M. D. Hammer, M. Holschneider, L. Huder, G. Hulot, T. Jager, C. Kloss, M. Korte, W. Kuang, A. Kuvshinov, B. Langlais, J. M. Léger, V. Lesur, P. W. Livermore, F. J. Lowes, S. Macmillan, W. Magnes, M. Mandea, S. Marsal, J. Matzka, M. C. Metman, T. Minami, A. Morschhauser, J. E. Mound, M. Nair, S. Nakano, N. Olsen, F. J. Pavón-Carrasco, V. G. Petrov, G. Ropp, M. Rother, T. J. Sabaka, S. Sanchez, D. Saturnino, N. R. Schnepf, X. Shen, C. Stolle, A. Tangborn, L. Tøffner-Clausen, H. Toh, J. M. Torta, J. Varner, F. Vervelidou, P. Vigneron, I. Wardinski, J. Wicht, A. Woods, Y. Yang, Z. Zeren, and B. Zhou (2021), International Geomagnetic Reference Field: the thirteenth generation, Earth, Planets and Space, 73(1), 49.

Andersen, O. B., P. Knudsen, and P. A. M. Berry (2009), The DNSC08GRA global marine gravity field from double retracked satellite altimetry, Journal of Geodesy, 84(3), 191-199.

Baker, E. T., and C. R. German (2004), On the global distribution of hydrothermal vent fields, Washington DC American Geophysical Union Geophysical Monograph Series, 148, 245.

Beaulieu, S., and K. Szafranski (2018), InterRidge global database of active submarine hydrothermal vent fields, Version 3.4, World Wide Web Electronic Publication. Available at: http://vents-data. interridge. org.

Bickel, S. H. (1979), Small Signal Compensation of Magnetic Fields Resulting from Aircraft Maneuvers, IEEE Transactions on Aerospace and Electronic Systems, AES-15(4), 518-525.

Blaich, O. A., J. I. Faleide, F. Tsikalas, R. Lilletveit, D. Chiossi, P. Brockbank, and P. Cobbold (2010), Structural architecture and nature of the continent-ocean transitional domain at the Camamu and Almada Basins (NE Brazil) within a conjugate margin setting, Geological Society, London, Petroleum Geology Conference series, 7(1), 867-883.

Blakely, R. (1995), Potential Theory in Gravity and Magnetic Applications. Cambridge University, Cambridge, edited.

Blakely, R. J., G. G. Connard, and J. B. Curto (2016), Tilt Derivative Made Easy, Geosoft Technical Publications, 4.

Blischke, A., C. Gaina, J. R. Hopper, G. Péron-Pinvidic, B. Brandsdóttir, P. Guarnieri, Ö. Erlendsson, and K. Gunnarsson (2017), The Jan Mayen microcontinent: an update of its architecture, structural development and role during the transition from the Ægir Ridge to

the mid-oceanic Kolbeinsey Ridge, Geological Society, London, Special Publications, 447(1), 299-337.

Boillot, G., and N. Froitzheim (2001), Non-volcanic rifted margins, continental break-up and the onset of sea-floor spreading: some outstanding questions, Geological Society, London, Special Publications, 187(1), 9.

Bott, M. H. P. (1960), The use of rapid digital computing methods for direct gravity interpretation of sedimentary basins, Geophysical Journal of the Royal Astronomical Society, 3, 63-67.

Bouligand, C., J. M. G. Glen, and R. J. Blakely (2009), Mapping Curie temperature depth in the western United States with a fractal model for crustal magnetization, Journal of Geophysical Research: Solid Earth, 114(B11).

Bown, J. W., and R. S. White (1994), Variation with spreading rate of oceanic crustal thickness and geochemistry, Earth and Planetary Science Letters, 121(3), 435-449.

Breivik, A., R. Mjelde, P. Grogan, H. Shimamura, Y. Murai, and Y. Nishimura (2003), Crustal structure and transform margin development south of Svalbard based on ocean bottom seismometer data, Tectonophysics, 369, 37-70.

Breivik, A., R. Mjelde, P. Grogan, H. Shimamura, Y. Murai, and Y. Nishimura (2005), Caledonide development offshore–onshore Svalbard based on ocean bottom seismometer, conventional seismic, and potential field data, Tectonophysics, 401, 79-117.

Breivik, A. J., and R. Mjelde (2001a), Obs-98 survey: Final report oceanic profiles, Report, Univ. of Bergen, Alleġt. 41, N-5007 Bergen.

Breivik, A. J., and R. Mjelde (2001b), Obs-98 survey: Final report western continental profiles, Report, Univ. of Bergen, Alleġt. 41, N-5007 Bergen.

Brozena, J. M., V. A. Childers, L. A. Lawver, L. M. Gahagan, R. Forsberg, J. I. Faleide, and O. Eldholm (2003), New aerogeophysical study of the Eurasia Basin and Lomonosov Ridge: implications for basin development.(Author Abstract), Geology, 31(9), 825.

Bruvoll, V., A. J. Breivik, R. Mjelde, and R. B. Pedersen (2009), Burial of the Mohn-Knipovich seafloor spreading ridge by the Bear Island Fan: Time constraints on tectonic evolution from seismic stratigraphy, Tectonics, 28(4), n/a-n/a.

Cann, J. R., D. K. Blackman, D. K. Smith, E. McAllister, B. Janssen, S. Mello, E. Avgerinos, A. R. Pascoe, and J. Escartin (1997), Corrugated slip surfaces formed at ridge–transform intersections on the Mid-Atlantic Ridge, Nature, 385(6614), 329-332.

Cannat, M., C. Rommevaux-Jestin, D. Sauter, C. Deplus, and V. Mendel (1999), Formation of the axial relief at the very slow spreading Southwest Indian Ridge (49° to 69°E), Journal of Geophysical Research: Solid Earth, 104(B10), 22825-22843.

Cannat, M., D. Sauter, A. Bezos, C. Meyzen, E. Humler, and M. Le Rigoleur (2008), Spreading rate, spreading obliquity, and melt supply at the ultraslow spreading Southwest Indian Ridge, Geochemistry, Geophysics, Geosystems, 9(4).

Cannat, M., D. Sauter, V. r. Mendel, E. Ruellan, K. Okino, J. Escartin, V. Combier, and M. Baala (2006), Modes of seafloor generation at a melt-poor ultraslow-spreading ridge, Geology, 34(7), 605-608.

Christensen, N. I. (1966), Elasticity of ultrabasic rocks, Journal of Geophysical Research (1896-1977), 71(24), 5921-5931.

Christensen, N. I. (1978), Ophiolites, seismic velocities and oceanic crustal structure, Tectonophysics, 47(1), 131-157.

Christensen, N. I. (1996), Poisson's ratio and crustal seismology, Journal of Geophysical Research: Solid Earth, 101(B2), 3139-3156.

Clerc, C., L. Jolivet, and J.-C. Ringenbach (2015), Ductile extensional shear zones in the lower crust of a passive margin, Earth and Planetary Science Letters, 431, 1-7.

Cochran, J. R., G. J. Kurras, M. H. Edwards, and B. J. Coakley (2003), The Gakkel Ridge: Bathymetry, gravity anomalies, and crustal accretion at extremely slow spreading rates, Journal of Geophysical Research: Solid Earth, 108(B2).

Conley, M. M., and R. A. Dunn (2011), Seismic shear wave structure of the uppermost mantle beneath the Mohns Ridge, Geochemistry, Geophysics, Geosystems, 12(10).

Coogan, L. A., and M. J. O'Hara (2015), MORB differentiation: In situ crystallization in replenished-tapped magma chambers, Geochimica et Cosmochimica Acta, 158, 147-161.

Coyle, M., R. Dumont, P. Keating, F. Kiss, and W. Miles (2014), Geological Survey of Canada aeromagnetic surveys: Design, quality assurance, and data dissemination.

Czuba, W., O. Ritzmann, Y. Nishimura, M. Grad, R. Mjelde, A. Guterch, and W. Jokat (2005), Crustal structure of northern Spitsbergen along the deep seismic transect between the Molloy Deep and Nordaustlandet, Geophysical Journal International, 161(2), 347-364.

Czuba, W., M. Grad, A. Guterch, M. Majdański, M. Malinowski, R. Mjelde, M. Moskalik, P. Środa, M. Wilde-Piorko, and Y. Nishimura (2008), Seismic crustal structure along the deep transect Horsted'05, Svalbard, Polish Polar Research, 29(3), 279-290.

Dallmann, W. K. (2015), Geoscience Atlas of Svalbard, Norsk polarinstitutt Rapportserie.

Dauteuil, O., and J.-P. Brun (1993), Oblique rifting in a slow-spreading ridge, Nature, 361(6408), 145-148.

de Jong, K., M. Goode, X. Liu, and M. Stone (2014), Precise GNSS positioning in Arctic regions, paper presented at OTC Arctic Technology Conference, OnePetro.

Dentith, M., and S. T. Mudge (2014), Geophysics for the mineral exploration geoscientist, Cambridge University Press.

Dick, H. J. B., J. Lin, and H. Schouten (2003), An ultraslow-spreading class of ocean ridge, Nature, 426(6965), 405-412.

Dickinson, W. R. (2003), Plate Tectonics, in Encyclopedia of Physical Science and Technology (Third Edition), edited by R. A. Meyers, pp. 475-489, Academic Press, New York.

Dowdeswell, J., D. Drewry, A. Cooper, M. Gorman, O. Liestøl, and O. Prheim (1986), Digital mapping of the Nordaustlandet ice caps from airborne geophysical investigations, Ann. Glaciol., 8, 51-58.

Dowdeswell, J. A., T. J. Benham, T. Strozzi, and J. O. Hagen (2008), Iceberg calving flux and mass balance of the Austfonna ice cap on Nordaustlandet, Svalbard, Journal of geophysical research, 113(F03022).

Dumais, M. A., F. Ofstad, and J. Gellein (2020), Processing and Compilation of Gravity Data, in Coop Phase 3 Crustal Onshore-Offshore Project, NGU Report 2019.036, edited, pp. 41-62.

Dunse, T., R. Greve, T. V. Schuler, and J. O. Hagen (2011), Permanent fast flow versus cyclic surge behavior: numerical simulations of the Austfonna ice cap, Svalbard, Journal of Glaciology, 57(202), 247-259.

Edmond, J. M., C. Measures, R. E. McDuff, L. H. Chan, R. Collier, B. Grant, L. I. Gordon, and J. B. Corliss (1979), Ridge crest hydrothermal activity and the balances of the major and minor elements in the ocean: The Galapagos data, Earth and Planetary Science Letters, 46(1), 1-18.

Engen, Ø., J. I. Faleide, and T. K. Dyreng (2008), Opening of the Fram Strait gateway: A review of plate tectonic constraints, Tectonophysics, 450, 51-69.

Engen, Ø., L. N. Frazer, P. Wessel, and J. I. Faleide (2006), Prediction of sediment thickness in the Norwegian-Greenland Sea from gravity inversion, Journal of geophysical research, 111, B11403.

Fairhead, J. D., A. Salem, S. Williams, and E. Samson (2008), Magnetic interpretation made easy: The Tilt-Depth-Dip- ΔK method, SEG Technical Program Expanded Abstracts 2008, 779-783.

Faleide, J. I., F. Tsikalas, A. Breivik, R. Mjelde, O. Ritzmann, Ø. Engen, J. Wilson, and O. Eldholm (2008), Structure and evolution of the continental margin off Norway and Barents Sea, Episodes, 31(1), 82-91.

Ferraccioli, F., M. Gambetta, and E. Bozzo (1998), Microlevelling procedures applied to regional aeromagnetic data: an example from the Transantarctic Mountains (Antarctica), Geophysical Prospecting, 46(2), 177-196.

Forsberg, R., and A. V. Olesen (2010), Airborne Gravity Field Determination, in Sciences of Geodesy - I: Advances and Future Directions, edited by G. Xu, pp. 83-104, Springer Berlin Heidelberg, Berlin, Heidelberg.

Forsberg, R., A. V. Olesen, K. Keller, and M. Møller (2002), Airborne gravity survey of sea areas around Greenland and Svalbard 1999-2001, Survey and processing report – KMS Technical Report, 18.

Francheteau, J., and R. D. Ballard (1983), The East Pacific Rise near 21°N, 13°N and 20°S: inferences for along-strike variability of axial processes of the Mid-Ocean Ridge, Earth and Planetary Science Letters, 64(1), 93-116.

Funck, T., W. H. Geissler, G. S. Kimbell, S. Gradmann, Ö. Erlendsson, K. McDermott, and U. K. Petersen (2017), Moho and basement depth in the NE Atlantic Ocean based on seismic refraction data and receiver functions, Geological Society, London, Special Publications, 447(1), 207-231.

Gao, C., H. J. B. Dick, Y. Liu, and H. Zhou (2016), Melt extraction and mantle source at a Southwest Indian Ridge Dragon Bone amagmatic segment on the Marion Rise, Lithos, 246-247, 48-60.

Genevey, A., Y. Gallet, J. Rosen, and M. Le Goff (2009), Evidence for rapid geomagnetic field intensity variations in Western Europe over the past 800 years from new French archeointensity data, Earth and Planetary Science Letters, 284(1), 132-143.

Geometrics, i. (2004), G-822A and G-823A & B Cesium Magnetometer 27597-OM Rev. B, Operation Manual.

Geosoft (2006), GM-SYS profile modeling. Gravity and Magnetic Modeling Software, v. 4.10, Geosoft Incorporated, p.116.

Geosoft (2010), Geophysics Levelling System - Processing and Enhancing Geophysical Data Extension for Oasis montaj v7.1 - Tutorial and User Guide, Geosoft Incorporated, 70pp.

Geosoft (2014), Geosoft Oasis Montaj extension - GM-SYS 3D Modelling, Feature Sheet, Geosoft Inc.

German, C. R., and L. M. Parson (1998), Distributions of hydrothermal activity along the Mid-Atlantic Ridge: interplay of magmatic and tectonic controls, Earth and Planetary Science Letters, 160(3), 327-341.

Gernigon, L., A. Blischke, A. Nasuti, and M. Sand (2015), Conjugate volcanic rifted margins, seafloor spreading, and microcontinent: Insights from new high-resolution aeromagnetic surveys in the Norway Basin, Tectonics, 34(5), 907-933.

Gernigon, L., D. Franke, L. Geoffroy, C. Schiffer, G. R. Foulger, and M. Stoker (2019), Crustal fragmentation, magmatism, and the diachronous opening of the Norwegian-Greenland Sea, Earth-Science Reviews.

Glebovsky, V. Y., V. D. Kaminsky, A. N. Minakov, S. A. Merkur'ev, V. A. Childers, and J. M. Brozena (2006), Formation of the Eurasia Basin in the Arctic Ocean as inferred from geohistorical analysis of the anomalous magnetic field, Geotectonics, 40(4), 263-281.

Glicken, M. (1962), Eotvos corrections for a moving gravity meter, Geophysics, 27(4), 531-533.

Goussev, S. A., and J. W. Peirce (2010), Magnetic basement: gravity-guided magnetic source depth analysis and interpretation, Geophysical Prospecting, 58, 321-334.

Grad, M., and J. Majorowicz (2020), Geophysical properties of the crust and upper mantle of the ocean-continent transition in Svalbard area, Polish Polar Research, 1-22.

Gripp, A. E., and R. G. Gordon (2002), Young tracks of hotspots and current plate velocities, Geophysical Journal International, 150(2), 321-361.

Grogan, P., K. Nyberg, B. Fotland, R. Myklebust, S. Dahlgren, and F. Riis (2000), Cretaceous Magmatism South and East of Svalbard: Evidence from Seismic Reflection and Magnetic Data, Polarforschung, 68, 25-34.

Hager, B. H. (1984), Subducted slabs and the geoid: Constraints on mantle rheology and flow, Journal of Geophysical Research: Solid Earth, 89(B7), 6003-6015.

Hartman, R. R., D. J. Teskey, and J. L. Friedberg (1971), A system for rapid digital aeromagnetic interpretation, Geophysics, 36(5), 891-918.

Haymon, R. M. (1996), The response of ridge-crest hydrothermal systems to segmented, episodic magma supply, Geological Society, London, Special Publications, 118(1), 157.

Hermann, T., and W. Jokat (2013), Crustal structures of the Boreas Basin and the Knipovich Ridge, North Atlantic, Geophysical Journal International, 193, 1399-1414.

Hess, H. H. (1962), History of ocean basins, Petrologic studies, 4, 599-620.

Hopper, J. R., T. Funck, M. Stoker, U. Arting, G. Peron-Pinvidic, H. Doornenbal, and C. Gaina (2014), Tectonostratigraphic Atlas of the North-East Atlantic Region, Geological Survey of Denmark and Greenland.

Horen, H., M. Zamora, and G. Dubuisson (1996), Seismic waves velocities and anisotropy in serpentinized peridotites from xigaze ophiolite: Abundance of serpentine in slow spreading ridge, Geophysical Research Letters, 23(1), 9-12.

Hrvoic, I., G. M. Hollyer, and P. Eng (2005), Brief review of quantum magnetometers, GEM Systems Technical Papers.

Hulot, G., C. C. Finlay, C. G. Constable, N. Olsen, and M. Mandea (2010), The Magnetic Field of Planet Earth, Space Science Reviews, 152(1), 159-222.

Jackson, H. R., I. Reid, and R. K. H. Falconer (1982), Crustal structure near the Arctic Mid-Ocean Ridge, Journal of Geophysical Research: Solid Earth, 87(B3), 1773-1783.

Jain, S. (1976), An automatic method of direct interpretation of magnetic profiles, Geophysics, 41(3), 531-541.

Johansen, S. E., M. Panzner, R. Mittet, H. E. F. Amundsen, A. Lim, E. Vik, M. Landrø, and B. Arntsen (2019), Deep electrical imaging of the ultraslow-spreading Mohns Ridge, Nature, 567(7748), 379-383.

Johansson, Å., A. N. Larionov, A. M. Tebenkov, Y. Ohta, and D. G. Gee (2002), Caledonian granites of western and central Nordaustlandet, northeast Svalbard, GFF, 124(3), 135-148.

Johansson, Å., D. G. Gee, A. N. Larionov, Y. Ohta, and A. M. Tebenkov (2005), Grenvillian and Caledonian evolution of eastern Svalbard – a tale of two orogenies, Terra Nova, 17, 317-325.

Jokat, W., and M. C. Schmidt-Aursch (2007), Geophysical characteristics of the ultraslow spreading Gakkel Ridge, Arctic Ocean, Geophysical Journal International, 168(3), 983-998.

Jokat, W., W. Geissler, and M. Voss (2008), Basement structure of the north-western Yermak Plateau, Geophysical Research Letters, 35(5).

Jokat, W., P. Lehmann, D. Damaske, and J. Bradley Nelson (2016), Magnetic signature of North-East Greenland, the Morris Jesup Rise, the Yermak Plateau, the central Fram Strait: Constraints for the rift/drift history between Greenland and Svalbard since the Eocene, Tectonophysics, 691, 98-109.

Jokat, W., O. Ritzmann, M. C. Schmidt-Aursch, S. Drachev, S. Gauger, and J. Snow (2003), Geophysical evidence for reduced melt production on the Arctic ultraslow Gakkel mid-ocean ridge, Nature, 423(6943), 962-965.

Karson, J. A. (2017), The Iceland Plate Boundary Zone: Propagating Rifts, Migrating Transforms, and Rift-Parallel Strike-Slip Faults, Geochemistry, Geophysics, Geosystems, 18(11), 4043-4054.

Karson, J. A., E. M. Klein, S. D. Hurst, C. E. Lee, P. A. Rivizzigno, D. Curewitz, A. R. Morris, D. J. Miller, R. G. Varga, G. L. Christeson, B. Cushman, J. M. O'Neill, J. G. Brophy, K. M. Gillis, M. A. Stewart, and A. L. Sutton (2002), Structure of uppermost fast-spread oceanic crust exposed at the Hess Deep Rift: Implications for subaxial processes at the East Pacific Rise, Geochemistry, Geophysics, Geosystems, 3(1).

Kellogg, O. D. (1953), Foundations of potential theory, Courier Corporation.

Kilty, K. T. (1983), Werner deconvolution of profile potential field data, Geophysics, 48(2), 234-237.

Klitzke, P., J. I. Faleide, M. Scheck-Wenderoth, and J. Sippel (2015), A lithosphere-scale structural model of the Barents Sea and Kara Sea region, Solid Earth, 6(1), 153-172.

Ku, C. C., and J. A. Sharp (1983), Werner deconvolution for automated magnetic interpretation and its refinement using Marquart's inverse modeling, Geophysics, 48(6), 754-774.

LaCoste, L. J. B. (1934), A New Type Long Period Vertical Seismograph, Physics, 5(7), 178-180.

LaFehr, T. R. (1980), Gravity method, Geophysics, 45(11), 1634-1639.

LaFemina, P. C. (2015), Chapter 3 - Plate Tectonics and Volcanism, in The Encyclopedia of Volcanoes (Second Edition), edited by H. Sigurdsson, pp. 65-92, Academic Press, Amsterdam.

Lauritzen, Ø., and Y. Ohta (1984), Geological map of Svalbard 1:500,000. Sheet 4G, Nordaustlandet, Nor. Polarinst. Skr. 154C.

Leliak, P. (1961), Identification and Evaluation of Magnetic-Field Sources of Magnetic Airborne Detector Equipped Aircraft, IRE Transactions on Aerospace and Navigational Electronics, ANE-8(3), 95-105.

Lerch, F. J., S. M. Klosko, R. E. Laubscher, and C. A. Wagner (1979), Gravity model improvement using Geos 3 (GEM 9 and 10), Journal of Geophysical Research: Solid Earth, 84(B8), 3897-3916.

Li, X., and H. J. Götze (2001), Ellipsoid, geoid, gravity, geodesy, and geophysics, Geophysics, 66(6), 1660-1668.

Lim, A. (2020), Subsurface structure and hydrothermal fluid circulation at the Mohns mid-ocean ridge: a multi-geophysical investigation, Doctoral Thesis, 147 pp, Norwegian University of Science and Technology.

Ljones, F., A. Kuwano, R. Mjelde, A. Breivik, H. Shimamura, Y. Murai, and Y. Nishimura (2004), Crustal transect from the North Atlantic Knipovich Ridge to the Svalbard Margin west of Hornsund, Tectonophysics, 378, 17-41.

Lowes, F. J. (2000), An estimate of the errors of the IGRF/DGRF fields 1945–2000, Earth, Planets and Space, 52(12), 1207-1211.

Ludvigsen, M., K. Aasly, S. L. Ellefmo, A. Hilário, E. Ramirez-Llodra, F. X. Søreide, I. Falcon-Suarez, C. J. Juliani, A. Kieswetter, and A. Lim (2016), MarMine cruise report-Arctic Mid-Ocean Ridge 15.08. 2016-05.09. 2016.

Luhmann, J. G., and S. C. Solomon (2014), Chapter 22 - Space Weather, in Encyclopedia of the Solar System (Third Edition), edited by T. Spohn, D. Breuer and T. V. Johnson, pp. 479-492, Elsevier, Boston.

Lundin, E. R., and A. G. Doré (2011), Hyperextension, serpentinization, and weakening: A new paradigm for rifted margin compressional deformation, Geology, 39(4), 347-350.

Macdonald, K. C. (1982), Mid-ocean ridges: Fine scale tectonic, volcanic and hydrothermal processes within the plate boundary zone, Annual Review of Earth and Planetary Sciences, 10(1), 155-190.

Marello, L., J. Ebbing, and L. Gernigon (2013), Basement inhomogeneities and crustal setting in the Barents Sea from a combined 3D gravity and magnetic model, Geophysical Journal International, 193(2), 557-584.

Marsh, J. G., C. J. Koblinsky, H. J. Zwally, A. C. Brenner, and B. D. Beckley (1992), A global mean sea surface based upon GEOS 3 and Seasat altimeter data, Journal of Geophysical Research: Solid Earth, 97(B4), 4915-4921.

Mather, B., and R. Delhaye (2019), PyCurious: A Python module for computing the Curie depth from the magnetic anomaly, Journal of Open Source Software, 4(39), 1544.

Matthews, K. J., K. T. Maloney, S. Zahirovic, S. E. Williams, M. Seton, and R. D. Müller (2016), Global plate boundary evolution and kinematics since the late Paleozoic, Global and Planetary Change, 146, 226-250.

Maus, S., D. Gordon, and D. Fairhead (1997), Curie-temperature depth estimation using a self-similar magnetization model, Geophysical Journal International, 129(1), 163-168.

Maus, S., F. Yin, H. Lühr, C. Manoj, M. Rother, J. Rauberg, I. Michaelis, C. Stolle, and R. D. Müller (2008), Resolution of direction of oceanic magnetic lineations by the sixth-generation lithospheric magnetic field model from CHAMP satellite magnetic measurements, Geochemistry, Geophysics, Geosystems, 9(7).

Meinesz, F. V. (1931), Une nouvelle methode pour la reduction isostatique regionale de l'intensite de la pesanteur, Bulletin géodésique, 29(1), 33-51.

Mendel, V., M. Munschy, and D. Sauter (2005), MODMAG, a MATLAB program to model marine magnetic anomalies, Computers & Geosciences, 31(5), 589-597.

Michael, P. J., C. H. Langmuir, H. J. B. Dick, J. E. Snow, S. L. Goldstein, D. W. Graham, K. Lehnert, G. Kurras, W. Jokat, R. Mühe, and H. N. Edmonds (2003), Magmatic and amagmatic seafloor generation at the ultraslow-spreading Gakkel ridge, Arctic Ocean, Nature, 423(6943), 956-961.

Milbert, D. G., and W. T. Dewhurst (1992), The Yellowstone-Hebgen Lake Geoid obtained through the integrated geodesy approach, Journal of Geophysical Research: Solid Earth, 97(B1), 545-557.

Miller, H. G., and V. Singh (1994), Potential field tilt - a new concept for the location of potential field sources, Journal of Applied Geophysics, 32, 213-217.

Minakov, A., R. Mjelde, J. I. Faleide, E. R. Flueh, A. Dannowski, and H. Keers (2012), Mafic intrusions east of Svalbard imaged by active-source seismic tomography, Tectonophysics, 518-521, 106-118.

Minshull, T. A., M. R. Muller, and R. S. White (2006), Crustal structure of the Southwest Indian Ridge at 66°E: seismic constraints, Geophysical Journal International, 166(1), 135-147.

Minty, B. R. S. (1991), Simple Micro-Levelling for Aeromagnetic Data, Exploration Geophysics, 22(4), 591-592.

Mjelde, R., S. Kodaira, H. Shimamura, T. Kanazawa, H. Shiobara, E. W. Berg, and O. Riise (1997), Crustal structure of the central part of the Vøring Basin, mid-Norway margin, from ocean bottom seismographs, Tectonophysics, 277(4), 235-257.

Moholdt, G., J. O. Hagen, T. Eiken, and T. V. Schuler (2010), Geometric changes and mass balance of the Austfonna ice cap, Svalbard, The Cryosphere, 4, 21-34.

Momoh, E., M. Cannat, L. Watremez, S. Leroy, and S. C. Singh (2017), Quasi-3-D Seismic Reflection Imaging and Wide-Angle Velocity Structure of Nearly Amagmatic Oceanic Lithosphere at the Ultraslow-Spreading Southwest Indian Ridge, Journal of Geophysical Research: Solid Earth, 122(12), 9511-9533.

Moritz, H. (1980), Geodetic reference system 1980, Bulletin géodésique, 54(3), 395-405.

Morozov, A. N., N. V. Vaganova, E. V. Ivanova, Y. V. Konechnaya, I. V. Fedorenko, and Y. A. Mikhaylova (2016), New data about small-magnitude earthquakes of the ultraslow-spreading Gakkel Ridge, Arctic Ocean, Journal of Geodynamics, 93, 31-41.

Mosar, J., G. Lewis, and T. Torsvik (2002), North Atlantic sea-floor spreading rates: implications for the Tertiary development of inversion structures of the Norwegian–Greenland Sea, Journal of the Geological Society, 159(5), 503.

Muller, M. R., T. A. Minshull, and R. S. White (1999), Segmentation and melt supply at the Southwest Indian Ridge, Geology, 27(10), 867-870.

Müller, R. D., J. Cannon, X. Qin, R. J. Watson, M. Gurnis, S. Williams, T. Pfaffelmoser, M. Seton, S. H. J. Russell, and S. Zahirovic (2018), GPlates: Building a Virtual Earth Through Deep Time, Geochemistry, Geophysics, Geosystems, 19(7), 2243-2261.

Murray, A. S., and R. M. Tracey (2001), Best practice in gravity surveying, Geoscience Australia, 3(5).

Nabighian, M. N., V. J. S. Grauch, R. O. Hansen, T. R. LaFehr, Y. Li, J. W. Peirce, J. D. Phillips, and M. E. Ruder (2005), The historical development of the magnetic method in exploration, Geophysics, 70(6), 33ND-61ND.

Nagata, T., Y. Arai, and K. Momose (1963), Secular Variation of the Geomagnetic Total Force during the Last 5000 Years, Journal of Geophysical Research (1896-1977), 68(18), 5277-5281.

Neuendorf, K. K. (2005), Glossary of geology, Springer Science & Business Media.

Norwegian Mapping Authority (2015), Sea shadow relief WMS, edited.

Norwegian Polar Institute (1998), Kartdata Svalbard 1:250 000. Sheet 3, Norwegian Polar Institute.

Ogg, J. G. (2012), Geomagnetic Polarity Time Scale, 85-113.

Oldenburg, D. W. (1974), The inversion and interpretation of gravity anomalies, Geophysics, 39(4), 526-536.

Olesen, O., M. Brönner, J. Ebbing, J. Gellein, L. Gernigon, J. Koziel, T. Lauritsen, R. Myklebust, C. Pascal, M. Sand, D. Solheim, and S. Usov (2010), New aeromagnetic and gravity compilations from Norway and adjacent areas: methods and applications, Geological Society, London, Petroleum Geology Conference series, 7(1), 559-586.

Parker, R. L., and S. P. Huestis (1974), The inversion of magnetic anomalies in the presence of topography, Journal of Geophysical Research (1896-1977), 79(11), 1587-1593.

Paterson, W. S. B., and G. K. C. Clarke (1978), Comparison of theoretical and observed temperature profiles in Devon Island ice cap, Canada, Geophysical Journal, 55(3), 615-632.

Pedersen, R. B., H. T. Rapp, I. H. Thorseth, M. D. Lilley, F. J. Barriga, T. Baumberger, K. Flesland, R. Fonseca, G. L. Fruh-Green, and S. L. Jorgensen (2010), Discovery of a black smoker vent field and vent fauna at the Arctic Mid-Ocean Ridge, Nature Communications, 1, 126.

Perfit, M. (1999), Earth's oceanic crust, CP Marshall & RW Fairbridge (eds.): Encyclopedia of Geochemistry. Berlin–New York, Springer Verlag, 179, 182.

Phillips, J. D. (1997), Potential-Field Geophysical Software for the PC, version 2.2, USGS open-File Report, 97.

Phillips, J. L., S. J. Bame, A. Barnes, B. L. Barraclough, W. C. Feldman, B. E. Goldstein, J. T. Gosling, G. W. Hoogeveen, D. J. McComas, M. Neugebauer, and S. T. Suess (1995), Ulysses solar wind plasma observations from pole to pole, Geophysical Research Letters, 22(23), 3301-3304.

Piepjohn, K., W. von Gosen, and F. Tessensohn (2016), The Eurekan deformation in the Arctic: an outline, Journal of the Geological Society, 173(6), 1007-1024.

Polteau, S., B. W. H. Hendriks, S. Planke, M. Ganerød, F. Corfu, J. I. Faleide, I. Midtkandal, H. S. Svensen, and R. Myklebust (2016), The early cretaceous Barents Sea sill complex: distribution, 40Ar/39Ar geochronology, and implications for carbon gas formation, Palaeogeography, Palaeoclimatology, Palaeoecology, 441, 83-95.

Pratt, J. H., and J. Challis (1855), I. On the attraction of the Himalaya Mountains, and of the elevated regions beyond them, upon the plumb-line in India, Philosophical Transactions of the Royal Society of London, 145, 53-100.

Pratt, J. H., and G. G. Stokes (1859), XXIX. On the deflection of the plumb-line in India, caused by the attraction of the Himmalaya mountains and of the elevated regions beyond; and its modification by the compensating effect of a deficiency of matter below the mountain mass, Philosophical Transactions of the Royal Society of London, 149, 745-778.

Rastogi, R. G., and V. L. Patel (1975), Effect of interplanetary magnetic field on ionosphere over the magnetic equator, Proceedings of the Indian Academy of Sciences - Section A, 82(4), 121-141.

Reeves, C. (2005), Aeromagnetic surveys: principles, practice and interpretation, Geosoft.

Reford, M. S., and J. S. Sumner (1964), Aeromagnetics, Geophysics, 29(4), 482-516.

Reid, A. B., J. Ebbing, and S. J. Webb (2014), Avoidable Euler Errors – the use and abuse of Euler deconvolution applied to potential fields, Geophysical Prospecting, 62(5), 1162-1168.

Reid, A. B., J. M. Allsop, H. Granser, A. J. Millett, and I. W. Somerton (1990), Magnetic interpretation in three dimensions using Euler deconvolution, Geophysics, 55(1), 80-91.

Reid, I., and H. R. Jackson (1981), Oceanic spreading rate and crustal thickness, Marine Geophysical Researches, 5(2), 165-172.

Reid, T., T. Walter, J. Blanch, and P. Enge (2016), GNSS Integrity in the Arctic, NAVIGATION, Journal of the Institute of Navigation, 63(4), 467-490.

Reynolds, J. M. (2011), An introduction to applied and environmental geophysics, John Wiley & Sons.

Ritzmann, O., and W. Jokat (2003), Crustal structure of northwestern Svalbard and the adjacent Yermak Plateau: evidence for Oligocene detachment tectonics and non-volcanic breakup, Geophysical Journal International, 152(1), 139-159.

Ritzmann, O., W. Jokat, R. Mjelde, and H. Shimamura (2002), Crustal structure between the Knipovich Ridge and the Van Mijenfjorden (Svalbard), Marine Geophysical Researches, 23(5-6), 379-401.

Ritzmann, O., W. Jokat, W. Czuba, A. Guterch, R. Mjelde, and Y. Nishimura (2004), A deep seismic transect from Hovgård Ridge to northwestern Svalbard across the continental-ocean transition: A sheared margin study, Geophysical Journal International, 157, 683-702.

Roots, W. D., J. J. Veevers, and D. F. Clowes (1979), Lithospheric model with thick oceanic crust at the continental boundary: A mechanism for shallow spreading ridges in young oceans, Earth and Planetary Science Letters, 43(3), 417-433.

Russell, C. T., J. G. Luhmann, and R. J. Strangeway (2016), Space Physics: An Introduction, Cambridge University Press.

Salem, A., S. Williams, J. D. Fairhead, D. Ravat, and R. Smith (2007), Tilt-depth method: A simple depth estimation method using first order magnetic derivatives, The Leading Edge, 26, 1502-1505.

Salem, A., S. Williams, E. Samson, D. Fairhead, D. Ravat, and R. J. Blakely (2010), Sedimentary basins reconnaissance using the magnetic Tilt-Depth method, Exploration Geophysics, 41(3), 198-209.

Sandwell, D. T., R. D. Müller, W. H. F. Smith, E. Garcia, and R. Francis (2014), New global marine gravity model from CryoSat-2 and Jason-1 reveals buried tectonic structure, Science, 346(6205), 65.

Sauter, D., V. Mendel, C. Rommevaux-Jestin, L. M. Parson, H. Fujimoto, C. Mével, M. Cannat, and K. Tamaki (2004), Focused magmatism versus amagmatic spreading along the ultra-slow spreading Southwest Indian Ridge: Evidence from TOBI side scan sonar imagery, Geochemistry, Geophysics, Geosystems, 5(10).

Sauter, D., M. Cannat, S. Rouméjon, M. Andreani, D. Birot, A. Bronner, D. Brunelli, J. Carlut, A. Delacour, V. Guyader, C. J. MacLeod, G. Manatschal, V. Mendel, B. Ménez, V. Pasini, E. Ruellan, and R. Searle (2013), Continuous exhumation of mantle-derived rocks at the Southwest Indian Ridge for 11 million years, Nature Geoscience, 6(4), 314-320.

Schiffer, C., A. Peace, J. Phethean, L. Gernigon, K. McCaffrey, K. D. Petersen, and G. Foulger (2019), The Jan Mayen microplate complex and the Wilson cycle, Geological Society, London, Special Publications, 470(1), 393.

Schlindwein, V., C. Müller, and W. Jokat (2005), Seismoacoustic evidence for volcanic activity on the ultraslow-spreading Gakkel Ridge, Arctic Ocean, Geophysical Research Letters, 32(18).

Schmid, F., and V. Schlindwein (2016), Microearthquake activity, lithospheric structure, and deformation modes at an amagmatic ultraslow spreading Southwest Indian Ridge segment, Geochemistry, Geophysics, Geosystems, 17(7), 2905-2921.

Schmidt-Aursch, M. C., and W. Jokat (2016), 3D gravity modelling reveals off-axis crustal thickness variations along the western Gakkel Ridge (Arctic Ocean), Tectonophysics, 691, 85-97.

Schytt, V. (1969), Some comments on glacier surges in eastern Svalbard, Canadian Journal of Earth Sciences, 46, 867-873.

Scott, R. A. (2000), Mesozoic-Cenozoic evolution of East Greenland: implications of a reinterpreted continent-ocean boundary location, Polarforschung, 68, 83-91.

Searle, R. (2013), Mid-ocean ridges, Cambridge University Press.

Seton, M., J. M. Whittaker, P. Wessel, R. D. Müller, C. DeMets, S. Merkouriev, S. Cande, C. Gaina, G. Eagles, R. Granot, J. Stock, N. Wright, and S. E. Williams (2014), Community infrastructure and repository for marine magnetic identifications, Geochemistry, Geophysics, Geosystems, 15(4), 1629-1641.

Seyler, M., M. Cannat, and C. Mével (2003), Evidence for major-element heterogeneity in the mantle source of abyssal peridotites from the Southwest Indian Ridge (52° to 68°E), Geochemistry, Geophysics, Geosystems, 4(2).

Sheriff, R. E. (2002), Encyclopedic dictionary of applied geophysics, Society of exploration geophysicists.

Simpson, R. W., R. C. Jachens, and R. J. Blakely (1983), AIRYROOT; a Fortran program for calculating the gravitational attraction of an Airy isostatic root out to 166.7 km, Report 83-883.

Simpson, R. W., R. C. Jachens, R. J. Blakely, and R. W. Saltus (1986), A new isostatic residual gravity map of the conterminous United States with a discussion on the significance of isostatic residual anomalies, Journal of Geophysical Research: Solid Earth, 91(B8), 8348-8372.

Skeels, D. C. (1947), Ambiguity in gravity interpretation, Geophysics, 12(1), 43-56.

Skilbrei, J. R. (1992), Preliminary interpretation of aeromagnetic data from Spitsbergen, Svalbard Archipelago (76°–79°N): Implications for structure of the basement, Marine Geology, 106(1), 53-68.

Smith, D. K., J. R. Cann, and J. Escartín (2006), Widespread active detachment faulting and core complex formation near 13° N on the Mid-Atlantic Ridge, Nature, 442(7101), 440-443.

Spector, A., and F. S. Grant (1970), Statistical models for interpreting aeromagnetic data, Geophysics, 35(2), 293-302.

Srivastava, S. P., and C. R. Tapscott (1986), Plate kinematics of the North Atlantic, in The Western North Atlantic Region, edited by P. R. Vogt and B. E. Tucholke, Geological Society of America.

Srivastava, S. P., and W. R. Roest (1999), Extent of oceanic crust in the Labrador Sea, Marine and Petroleum Geology, 16(1), 65-84.

Swaszek, P. F., R. J. Hartnett, K. C. Seals, J. D. Siciliano, and R. Swaszek (2018), Limits on GNSS Performance at High Latitudes, paper presented at Proceedings of the 2018 International Technical Meeting of The Institute of Navigation.

Talwani, M., and O. Eldholm (1977), Evolution of the Norwegian-Greenland Sea, Geological Society of America Bulletin, 88, 969-999.

Talwani, M., J. L. Worzel, and M. Landisman (1959), Rapid gravity computations for two-dimensional bodies with application to the Mendocino submarine fracture zone, Journal of Geophysical Research (1896-1977), 64(1), 49-59.

Telford, W. M., L. P. Geldart, and R. E. Sheriff (1990), Applied Geophysics, Cambridge University Press, Cambridge.

Thébault, E., C. C. Finlay, C. D. Beggan, P. Alken, J. Aubert, O. Barrois, F. Bertrand, T. Bondar, A. Boness, L. Brocco, E. Canet, A. Chambodut, A. Chulliat, P. Coïsson, F. Civet, A. Du, A. Fournier, I. Fratter, N. Gillet, B. Hamilton, M. Hamoudi, G. Hulot, T. Jager, M. Korte, W. Kuang, X. Lalanne, B. Langlais, J.-M. Léger, V. Lesur, F. J. Lowes, S. Macmillan, M. Mandea, C. Manoj, S. Maus, N. Olsen, V. Petrov, V. Ridley, M. Rother, T. J. Sabaka, D. Saturnino, R. Schachtschneider, O. Sirol, A. Tangborn, A. Thomson, L. Tøffner-Clausen, P. Vigneron, I. Wardinski, and T. Zvereva (2015), International Geomagnetic Reference Field: the 12th generation, Earth, Planets and Space, 67(1).

Thompson, D. T. (1982), EULDPH: A new technique for making computer-assisted depth estimates from magnetic data, Geophysics, 47, 31-37.

Trocine, R. P., and J. H. Trefry (1988), Distribution and chemistry of suspended particles from an active hydrothermal vent site on the Mid-Atlantic Ridge at 26°N, Earth and Planetary Science Letters, 88(1), 1-15.

Trulsvik, M., R. Myklebust, S. Polteau, and S. Planke (2011), Geophysical atlas of the East Greenland Basin: Integrated seismic, gravity and magnetic interpretation, Volcanic Basin Petroleum Research AS, TGS-NOPEC Geophysical Company

Tucholke, B. E., and J. Lin (1994), A geological model for the structure of ridge segments in slow spreading ocean crust, Journal of Geophysical Research: Solid Earth, 99(B6), 11937-11958.

Tucholke, B. E., J. Lin, and M. C. Kleinrock (1998), Megamullions and mullion structure defining oceanic metamorphic core complexes on the Mid-Atlantic Ridge, Journal of Geophysical Research: Solid Earth, 103(B5), 9857-9866.

Urlaub, M., M. C. Schmidt-Aursch, W. Jokat, and N. Kaul (2009), Gravity crustal models and heat flow measurements for the Eurasia Basin, Arctic Ocean, Marine Geophysical Researches, 30(4), 277-292.

van Andel, T. H., and C. O. Bowin (1968), Mid-Atlantic Ridge between 22° and 23° north latitude and the tectonics of mid-ocean rises, Journal of Geophysical Research (1896-1977), 73(4), 1279-1298.

Vine, F. J., and D. H. Matthews (1963), Magnetic Anomalies Over Oceanic Ridges, Nature, 199(4897), 947-949.

Vogt, P. R. (1986), Geophysical and Geochemical Signatures and Plate Tectonics, in The Nordic Seas, edited by B. G. Hurdle, pp. 413-664, Springer New York, New York, NY.

Vogt, P. R., L. C. Kovacs, C. Bernero, and S. P. Srivastava (1982), Asymmetric geophysical signatures in the Greenland-Norwegian and Southern Labrador Seas and the Eurasia Basin, Tectonophysics, 89(1), 95-160.

Wang, P., and S. Liu (2019), Geological Database for Plate Tectonic Reconstruction: A Conceptual Model, Acta Geologica Sinica (English Edition), 1.

Wegener, A. (1915), The Origin of Continents and Oceans.

Werner, S. (1953), Interpretation of magnetic anomalies of sheet-like bodies: Sveriges Geologiska Undersökning, Series C, Arsbok, 43.

Wessel, P., and R. D. Müller (2007), Plate tectonics, Treatise on Geophysics, 6, 49-98.

White, R. S., T. A. Minshull, M. J. Bickle, and C. J. Robinson (2001), Melt Generation at Very Slow-Spreading Oceanic Ridges: Constraints from Geochemical and Geophysical Data, Journal of Petrology, 42(6), 1171-1196.

Whitham, K., and E. R. Niblett (1961), The diurnal problem in aeromagnetic surveying in Canada, Geophysics, 26(2), 211-228.

Whitmarsh, R. B., and P. R. Miles (1995), Models of the development of the West Iberia rifted continental margin at 40°30'N deduced from surface and deep-tow magnetic anomalies, Journal of Geophysical Research: Solid Earth, 100(B3), 3789-3806.

WHOI (1989), Drilling the oceanic lower crust and mantle: a global strategy for exploring the deep oceanic crust and mantle in the 1990's., Woods Hole Oceanographic Institution.

Zhang, T., J. Gao, M. Chen, C. Yang, Z. Shen, Z. Zhou, Z. Wu, and Y. Sun (2015), Mantle melting factors and amagmatic crustal accretion of the Gakkel ridge, Arctic Ocean, Acta Oceanologica Sinica, 34(6), 42-48.

Zhizhin, M., J. Battaglia, J. Dubois, and A. Gvishiani (1997), Syntactic recognition of magnetic anomalies along the Mid-Atlantic Ridge, Comptes Rendus de l'Académie des Sciences - Series IIA - Earth and Planetary Science, 325(12), 983-990.

Zhou, H., and H. J. B. Dick (2013), Thin crust as evidence for depleted mantle supporting the Marion Rise, Nature, 494(7436), 195-200.

A

Annexe A – KRAS-16 interpretation

KRAS-16: processing and interpretation, Chapter 1, 2, 3 & 4

M.-A. Dumais, O. Olesen, L. Gernigon, A. Lim, S. Johansen & M. Brönner

NGU report 2020.030

These chapters describe the processing and the interpretation of the magnetic data acquired in the Fram Strait.

1 Introduction

The Knipovich Ridge Aeromagnetic Survey 2016 (KRAS-16) is an initiative to map the ultraslow spreading ridge in the Fram Strait and the surrounding area with airborne magnetic measurement.

Aeromagnetic surveys are essential for detailed mapping of continent-ocean boundaries (COB), magnetic spreading anomalies, faults, fracture systems, lava flows and magmatic intrusions. The KRAS-16 survey represents the missing piece in the Norwegian-Greenland Sea puzzle and enables us to produce a complete map the complex system of abandoned (or extinct) spreading ridges and fracture zones in this area. A geodynamic interpretation of the new aeromagnetic compilation will facilitate a first order dating of the opening of the Fram Strait and the transition from a transform fault to a spreading ridge. The characteristic striped pattern of magnetic spreading anomalies is an imprint of the Earth's magnetic field reversals and therefore act as a timeline record of opening of the Arctic Ocean.

The magnetic signature of the spreading ridge also reveals the geological framework of the Fram Strait development and gives insights of the tectonic settings of the Northeast-Greenland and Svalbard-Barents Sea margins. Furthermore, aeromagnetic interpretation allows us to model the continent-ocean transition, estimate the depth-to-basement and to characterize the basement types.

2 Survey Characteristics and Acquisition

The Knipovich Ridge spreading history and the development of the Fram Strait are the main goals of the present study (Figure 1). Classified as an ultraslow-oblique spreading system (with spreading rates of less than 20 mm/year), the Knipovich Ridge comprises the Arctic Mid-Ocean Ridge system delimited by the Mohn's Ridge (~73°50' N) and Molloy Fracture Zone (~78°30' N) between Greenland and NE Atlantic oceanic realms. The Knipovich Ridge trends from NW in the south to N in the north with a 130 km-wide escarpment and largely covered with thick piles of sedimentary rocks along the Svalbard margin (Engen et al., 2006). Its tectonic structure differs from other oceanic ridges as it presents ultra-slow spreading features in an oblique system (Talwani & Eldholm, 1977; Vogt et al., 1982). The Fram Strait developed after a Late Cretaceous-Eocene rifting event between the Barents Sea and the Northeast Greenland. It forms a complex system of conjugate shear margins characterized by distinct crustal, structural and magmatic properties (Faleide et al., 2008; Ritzmann & Jokat, 2003; Srivastava & Roest, 1999). During the Paleocene-Eocene, the oblique system underwent a brief period of compression leading to the Eurekan-Spitsbergen fold and thrust belts (Piepjohn et al., 2016). The importance of this study is to delineate the continent-ocean boundary, determine the crustal domains and map the spreading of the ridge. The settings and timing of the Fram Strait opening contribute to the geological framework of the Greenland and Svalbard-Barents Sea margins.

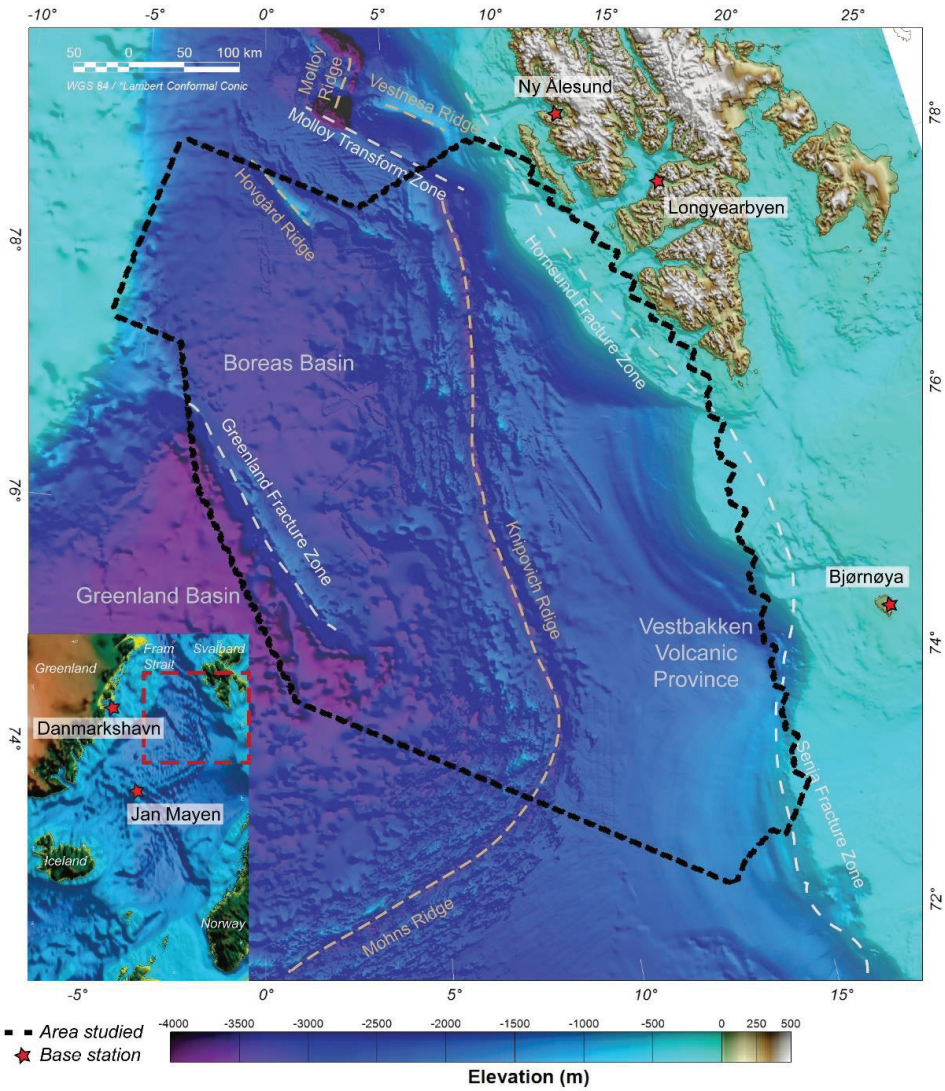

Figure 1. Survey area with magnetic stations available (Bjørnøya, Danmarkshavn, Jan Mayen, Longyearbyen and Ny Ålesund)

2.1 Survey Area and Survey Parameters

The survey area is 254,000 km^2, with a total of 56,906 line-km flown, 5.5 km line spacing and oriented 120-300° – perpendicular to the spreading anomalies. The acquisition took place during the two summers of 2016 and 2018 due to technical difficulties to fly the area.

Survey specifications	
Survey area	254,000 km^2
Survey size	56,906 line-km
Line direction	120-300°
Tie-line direction	30-210°
Line spacing	5.5 km
Tie-line spacing	20 km
Acquisition – phase 1	August 30th to October 6th, 2016
Acquisition – phase 2	May 26th to September 9th, 2018

2.2 Instrumentation and Technical Specifications

A concise description of the instruments on-board of the aircraft is found in the operation report provided by Novatem (Novatem, 2018).

Diurnal variation of the magnetic field was monitored before and during the flights. The magnetic base stations used were Ny Ålesund, Longyearbyen, Bjørnøya and Jan Mayen, operated by the Tromsø Geophysical Observatory (http://flux.phys.uit.no) and Danmarkshavn, operated by the Technical University of Denmark (http://www.space.dtu.dk). They constitute the closest magnetic observations available near the survey area (Figure 1).

2.3 Survey Operations

Survey operations were carried out by Novatem. A description is found in the operation report in (Novatem, 2018). Summary of the operations are found in the weekly reports produced by NGU (Appendix A in Dumais et al., 2020).

Figure 2. The aircraft over the Svalbard margin (curtesy of Novatem, Inc)

3 Data Processing

Processing of the data were carried out at NGU using the raw compensated data from Novatem with their proprietary methods as described in the acquisition report (Novatem, 2018).

3.1 Line Correction and De-spiking

The compensation filter is usually effective to remove noise generated by the aircraft and the engines. Small residual noise (0-3 nT) occurring from radio-communication or any external electro-

magnetic source can be manually adjusted (Figure 3). L1061-1 is the only line that required manual adjustment.

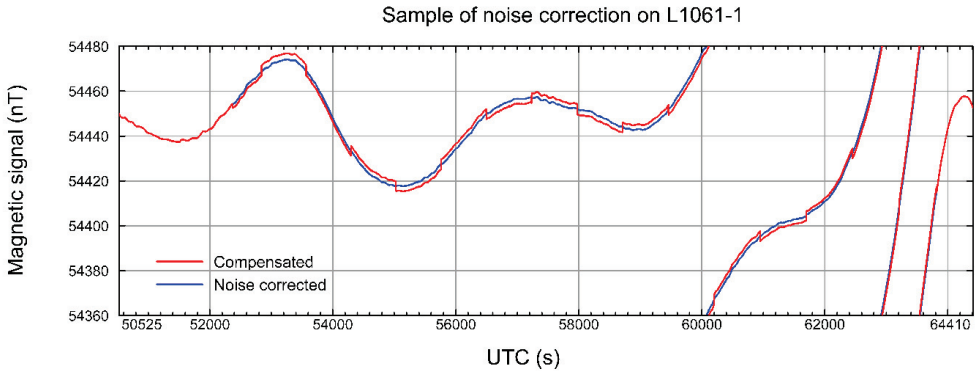

Figure 3. Sample data from L1061-1. Manual adjustment was carried on the data to remove external noise of 3 nT amplitude

3.2 IGRF

Long temporal variations of the inclination, declination, and field intensity, called secular variations, are important to consider for this survey which was flown over a long period during two non-consecutive summers. Therefore, the magnetic anomaly signal is calculated by subtracting the 12th International Geomagnetic Reference Field (IGRF-12) model, which is reliable to estimate secular variations.

3.3 Diurnals Correction

Located at high latitude, the survey area is particularly sensitive to diurnal noise. Frequent polar magnetospheric substorms cause large disturbances of the Earth's magnetic field and propagate diurnal noise over a large area with significant temporal and spatial variations. Substorms are transient processes causing disturbances of 300-800 nT of the horizontal field component over 0.5-3 hr. The aeromagnetic data acquired for KRAS-16 were acquired during low to moderate solar cycle activity optimizing the data quality.

3.3.1 Base Stations Monitoring

The diurnal noise was carefully assessed during the acquisition and processing steps. Five magnetic base stations from the Tromsø Geophysical Observatory (TGO) and the Technical University of Denmark (DTU) were closely monitored to provide a global overview of the magnetic activity in real time and were used for the data post-processing. This ensures high confidence and reliability of the final dataset products, representing the true geophysical nature of the Knipovich Ridge and its surroundings.

As an example, on September 1st, 2016, a flight was flown late during the day (Figure 4a). All base stations showed a very quiet magnetic activity until 20:00 (UTC) when the onset of polar magnetospheric substorms occurred. Figure 4a indicates how the time of the onset varied from one station to the other. It is also noticed that the amplitude of the horizontal deviation varies depending on the location of the base station. Figure 4b shows the profile as acquired and compared to a re-flight. The response is significantly different with ~300 nT difference in some areas. The

profile was first corrected with the base station of Jan Mayen and then compared to a correction with the base station of Longyearbyen. The line was flown from NW to SE, from the Greenland margin towards Svalbard. Near Svalbard, Longyearbyen diurnal corrections are more effective to correct the profile. Further west, Jan Mayen is more suitable to correct the profile. No base station is particularly efficient in the centre of the profile. Hence, the diurnal correction was carried with caution.

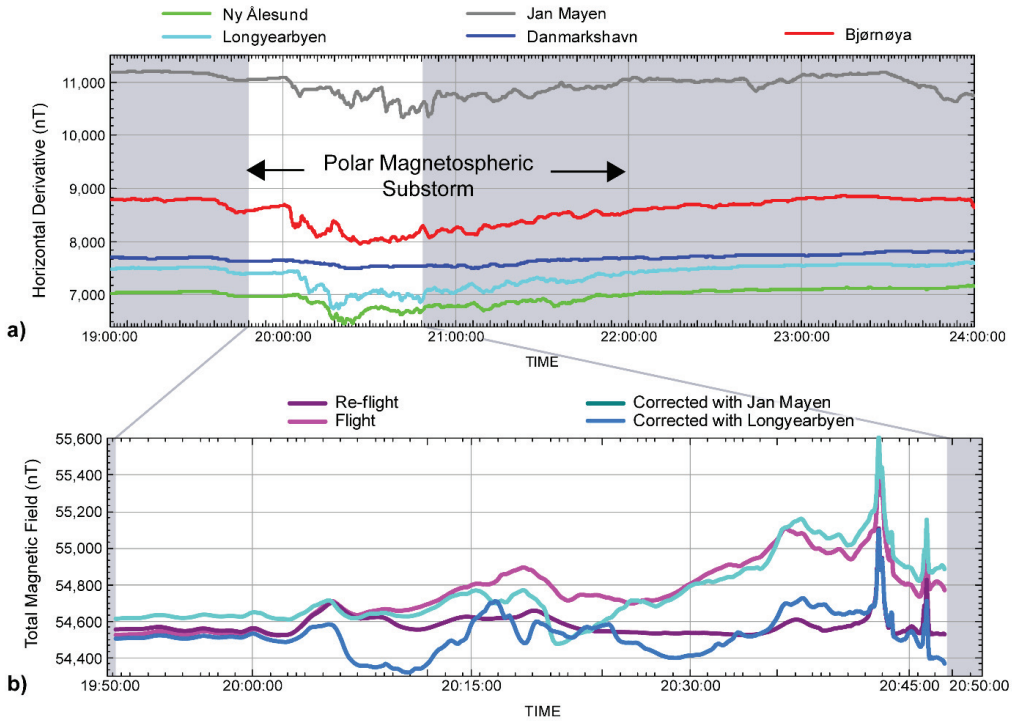

Figure 4. a) Magnetic recordings at five observatories during acquisition of the L1081 profile flown on September 1st, 2016 in a polar magnetospheric substorm b) profiles corrected with different base stations and compared to a re-flight.

3.3.2 Base Station Corrections

The data from the base station were collected at 1Hz and interpolated to the data sampling (10 Hz). For each base station, the average over the duration of the survey acquisition phase was removed to allow the correction of the long trend noise along the lines.

3.3.3 USGS Planar Interpolation

The USGS GX software package (Phillips, 2007) was used to correct for the diurnal noise. The module allows up to 5 stations to be used simultaneously and calculate a weighted average based on the inverse distance of the base station to the location of the measurements.

No base station correction was applied to profile L1008.0 as there was a weak correlation between the base station data and the flight data.

3.4 Levelling

The levelling was performed using the Geosoft Statistical Level module for the tie lines (Geosoft, 2010). For each tie line, this function calculates an average difference between the tie line values and the cross-over of the survey lines. Then it applied this average difference to shift each individual tie-line.

The second phase of the levelling was made using Geosoft Spline Level module (Geosoft, 2010). In this step, the tie lines are assumed to be properly levelled. Only the survey lines are corrected to match the levelled tie lines at each intersection. Several intersections corrections were manually adjusted or removed to allow a smooth and realistic levelling. A smooth Akima spline interpolation was applied to the correction to improve the levelling.

3.5 Micro-levelling

In order to remove the faint linear trend along the lines, one micro-levelling pass was applied to the dataset. The noise was first extracted from the gridded data using a decorrugation cut-off wavelength of 11,000 m for 5,500 m line spacing. Afterwards, a Naudy filter of 1,000 fiducials was applied to the profiled data. The final dataset is presented in Figure 5.

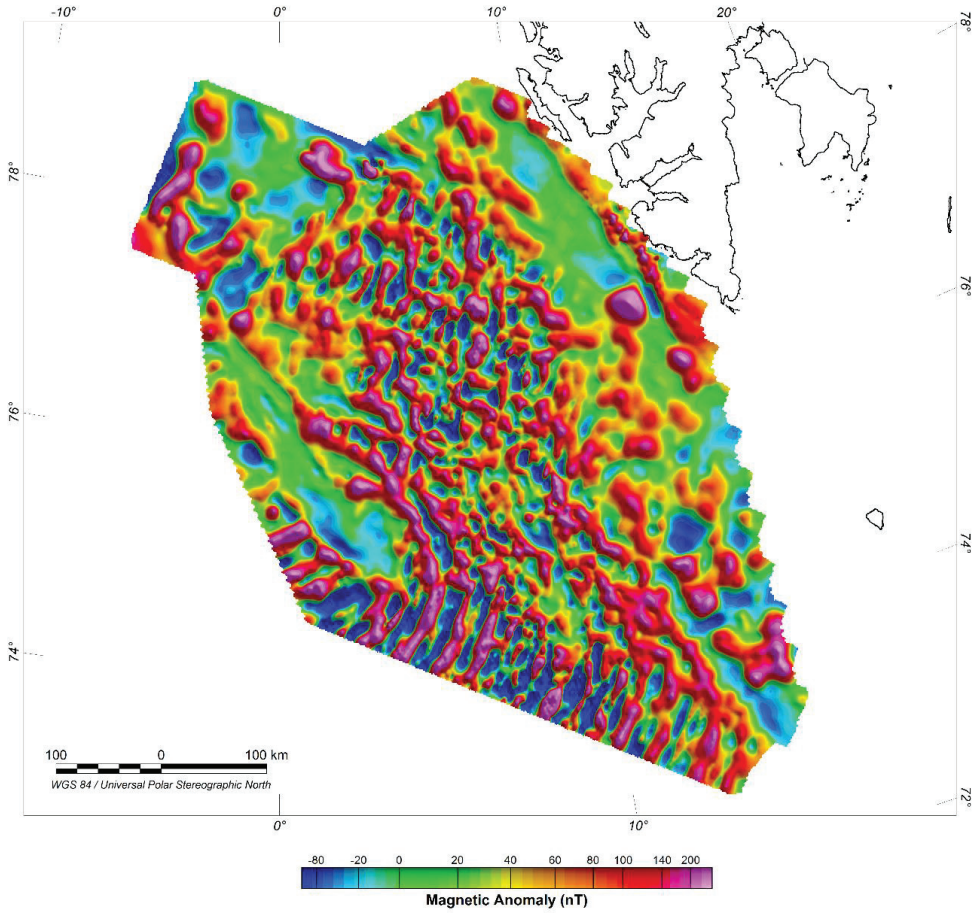

Figure 5. Processed magnetic data including base-station correction, levelling, and micro-levelling

4 Data Compilation

The KRAS-16 aeromagnetic dataset was gridded and merged with the available data in the surrounding areas. The surrounding areas are a compilation previously made for the EPOS-N project consisting of the publicly available datasets from the Arctic Circum Magnetic Map (Gaina et al., 2011). The data were upward continued to 1 km and the grid cell size is 2000 m.

The KRAS-16 aeromagnetic data generally fit with the surrounding data except in the Boreas Basin on the northwest corner of KRAS-16. Proprietary TGS data (Trulsvik et al., 2011) show significant differences in that area due to higher resolution and prove a better fit with the KRAS-16 aeromagnetic data.

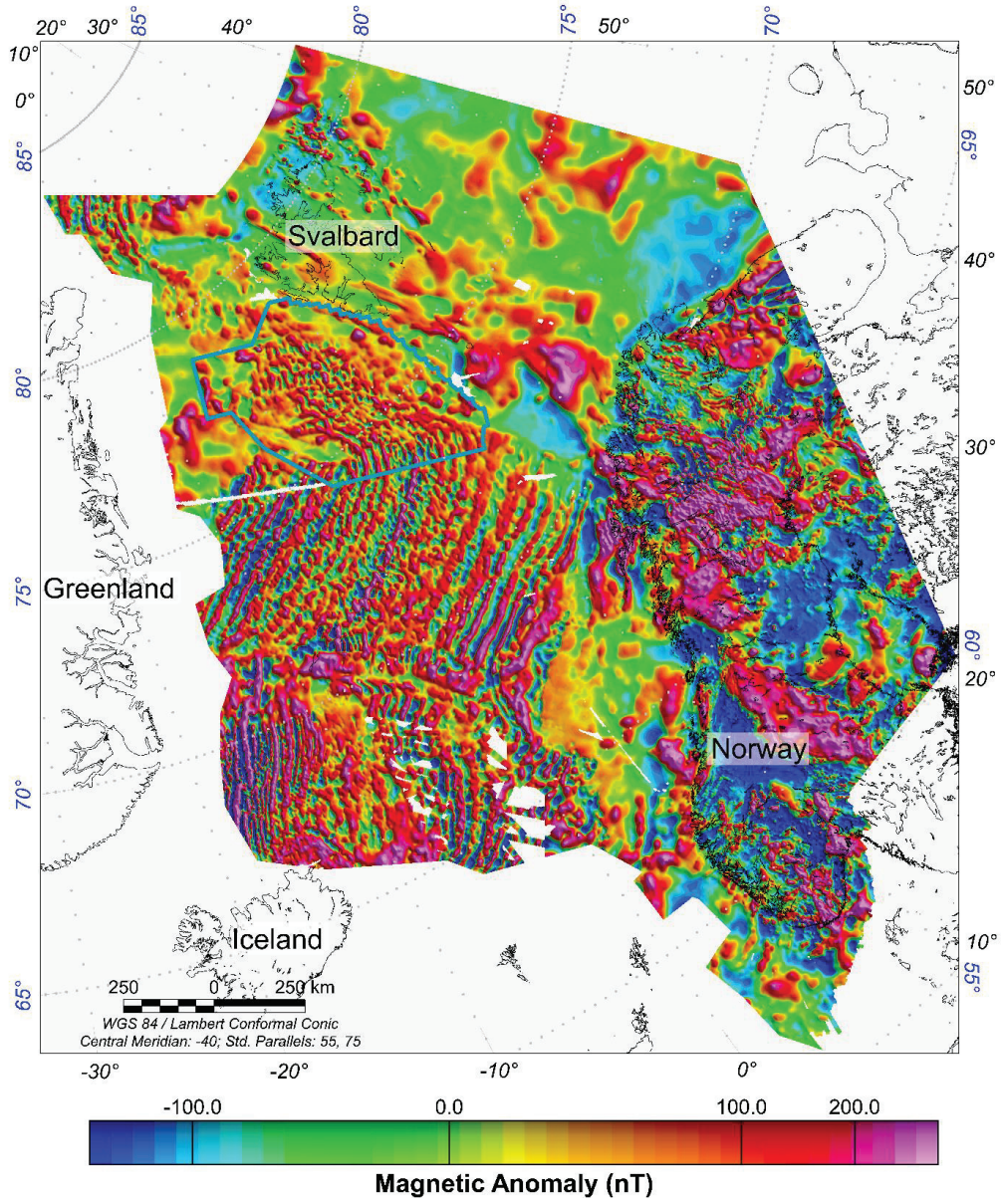

Figure 6. Magnetic anomaly compilation including the new KRAS-16 dataset

References (chapters 1-4)

Dumais, M. A., Olesen, O., Gernigon, L., Brönner, M., Lim, A., & Johansen, S. E. (2020). KRAS-16: processing and interpretation. NGU-rapport 2020.030.
Engen, Ø., Frazer, L. N., Wessel, P., & Faleide, J. I. (2006). Prediction of sediment thickness in the Norwegian-Greenland Sea from gravity inversion. Journal of geophysical research, 111, B11403.
Faleide, J. I., Tsikalas, F., Breivik, A., Mjelde, R., Ritzmann, O., Engen, Ø., et al. (2008). Structure and evolution of the continental margin off Norway and Barents Sea. Episodes, 31(1), 82-91.
Gaina, C., Werner, S. C., Saltus, R., & Maus, S. (2011). Chapter 3 Circum-Arctic mapping project: new magnetic and gravity anomaly maps of the Arctic. Geological Society, London, Memoirs, 35(1), 39. https://doi.org/10.1144/m35.3
Geosoft (2010). Geophysics Levelling System - Processing and Enhancing Geophysical Data Extension for Oasis montaj v7.1 - Tutorial and User Guide. Geosoft Incorporated, 70pp.
Novatem (2018). Knipovich Ridge airborne survey 2016 (KRAS-16) - Technical Report, 32pp pp.
Phillips, J. D. (2007). Geosoft eXecutables (GX's) developed by the U.S. Geological Survey, version 2.0, with notes on GX development from Fortran code. U.S. Geological Survey Open-File Report 2007-1355, 111 p.
Piepjohn, K., von Gosen, W., & Tessensohn, F. (2016). The Eurekan deformation in the Arctic: an outline. Journal of the Geological Society, 173(6), 1007-1024. https://doi.org/10.1144/jgs2016-081
Ritzmann, O., & Jokat, W. (2003). Crustal structure of northwestern Svalbard and the adjacent Yermak Plateau: evidence for Oligocene detachment tectonics and non-volcanic breakup. Geophysical Journal International, 152(1), 139-159. https://doi.org/10.1046/j.1365-246X.2003.01836.x
Srivastava, S. P., & Roest, W. R. (1999). Extent of oceanic crust in the Labrador Sea. Marine and Petroleum Geology, 16(1), 65-84. https://doi.org/10.1016/S0264-8172(98)00041-5
Talwani, M., & Eldholm, O. (1977). Evolution of the Norwegian-Greenland Sea. Geological Society of America Bulletin, 88, 969-999.
Trulsvik, M., Myklebust, R., Polteau, S., & Planke, S. (2011). Geophysical atlas of the East Greenland Basin: Integrated seismic, gravity and magnetic interpretation. Volcanic Basin Petroleum Research AS, TGS-NOPEC Geophysical Company
Vogt, P. R., Kovacs, L. C., Bernero, C., & Srivastava, S. P. (1982). Asymmetric geophysical signatures in the Greenland-Norwegian and Southern Labrador Seas and the Eurasia Basin. Tectonophysics, 89(1), 95-160. https://doi.org/https://doi.org/10.1016/0040-1951(82)90036-1

Annexe B – Austfonna magnetic data processing

The Svalbard area has been covered with aeromagnetic data from 1988 to 1991. For the study of Austfonna, the data were re-processed and merged to ensure a consistent magnetic signature between the surveys. It was decided to be re-processed because of the large discrepancies in the long-wavelength content between the original individual survey grids and the final merged grid.

B.1. Survey area and acquisition parameters

The survey area is 69,750 km², lines were spaced between 1 and 8 km, and flown E-W – perpendicular to the Hornsund and Billefjorden Fault Zones (Figure B.1). The acquisition was performed by different entities Sevmorgeo and Amarok / TGS (Table B.1).

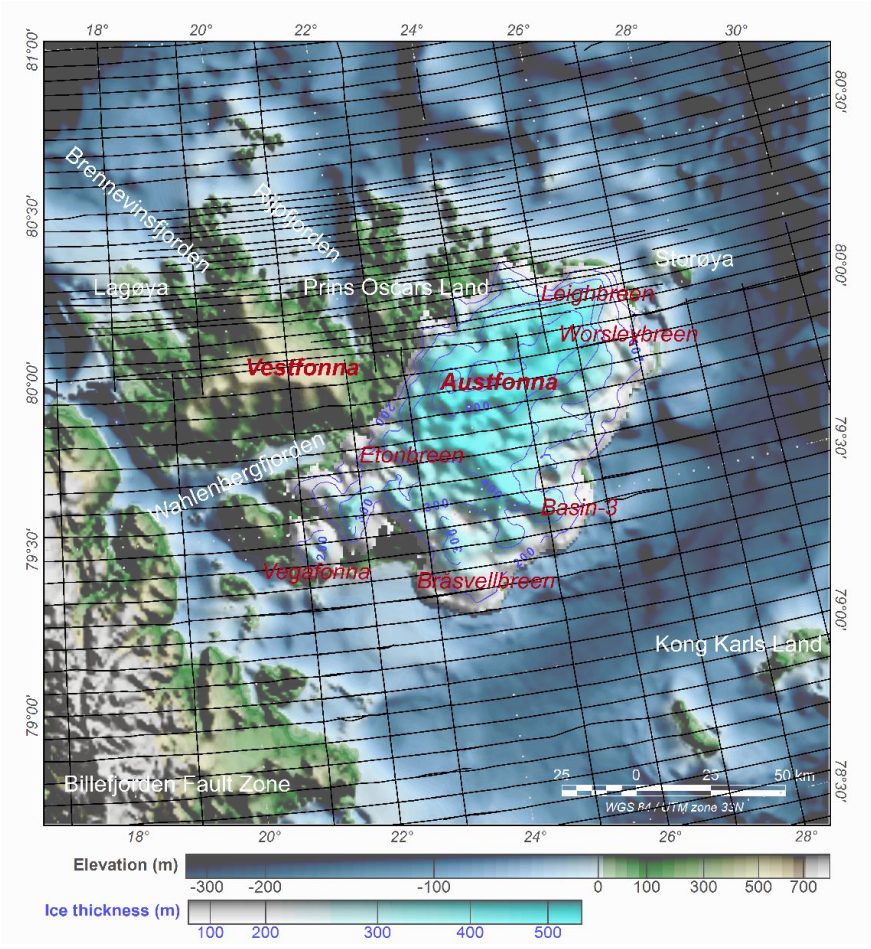

Figure B.1 Magnetic survey lines flown above Nordaustlandet

Survey parameters		
	North – above 80˚	**South – below 80˚**
Line direction	E-W	E-W
Tie-line direction	N-S	N-S
Line spacing	1 to 8 km	8 km
Tie-line spacing	20, 40 km	20, 40 km
Aircraft altitude	-	900 m
Acquisition	1989	1991
Acquired by	Sevmorgeo	Amarok / TGS

Table B.1 Survey parameters for the lines acquired above Nordaustlandet

B.2. Reprocessing

Reprocessing of the data was carried at NGU using the available data with Geosoft Oasis Montaj [*Geosoft*, 2010].

Line correction

Very few information was available on the Sevmorgeo dataset flown in 1979. X and Y coordinates were known, but no raw magnetic data, altitude, date, or time were recorded in the database. L1 from the 1989 survey and L8000 from the 1991 survey have a short overlap that was used for the initial correction. An average difference of 69 nT was found and applied before the levelling (Figure B.2). We assumed the difference was caused from a different field core model applied to the data flown in 1991. Therefore, a constant shift was applied to the data.

IGRF

No IGRF or any field core model corrections were available for the survey acquired in 1989. The date and IGRF corrected channels were available for the survey flown in 1991.

Levelling

The levelling was performed using the Geosoft Statistical Level module for the tie-lines [*Geosoft*, 2010]. This function calculates an average difference between the tie line values and the cross-over of the survey lines. Then it applied this average difference to shift each individual tie-line.

The second phase of the levelling was made using Geosoft Full Level module [*Geosoft*, 2010]. In this step, the tie lines are assumed to be properly levelled. The survey lines are corrected to match the levelled tie lines at each intersection. Several intersections corrections were manually adjusted or removed to allow a smooth and realistic levelling.

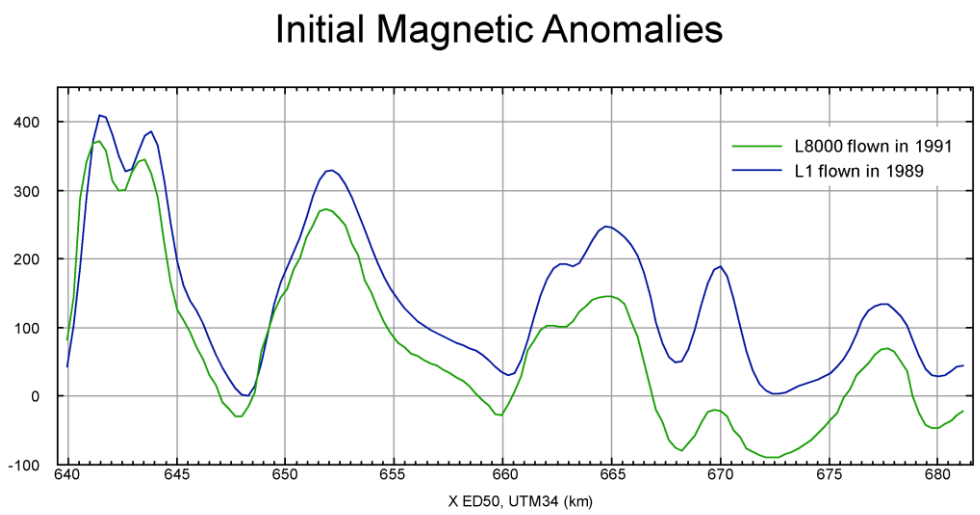

Figure B.2 Magnetic anomalies for L1 and L8000 flown in 1989 and 1991, respectively, as available in the databases.

Micro-levelling

Three micro-levelling passes were subsequently applied to the dataset. These passes were required to remove the trends left by the various line spacing. The noise was first extracted from the gridded data using a decorrugation cut-off wavelength of four times the line spacing and modified if necessary. A Naudy filter was also applied to the profiled data (Table B.2).

Micro-levelling parameters			
Passes	**Line Spacing (m)**	**Decorrugation cut-off wavelength (km)**	**Naudy filter (fiducials)**
1	8,000	32	16,000
2	4,000	16	8,000
3	1,000	4	2,000

Table B.2 Parameters used for the three micro-levelling passes

B.3. Final dataset

The final dataset shows a smooth transition between the data acquired in 1989 and 1991 instead of a rapid decay in the magnetic anomaly north of 80°. The accuracy of this dataset could be improved significantly with additional line-acquisition overlapping the two surveys to remedy with the level difference.

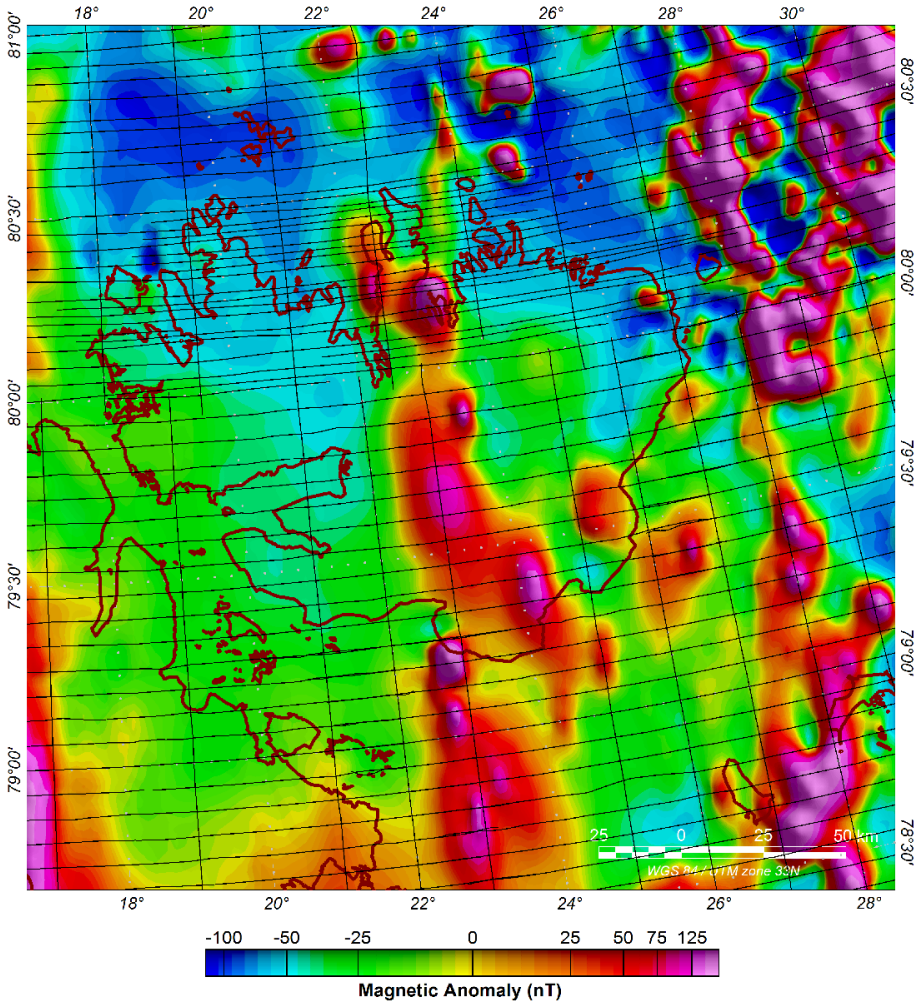

Figure B.3 Final re-processed magnetic anomaly

Annexe C – 2-D modelled profiles

2-D modelled profiles 1 to 7 from the second manuscript (Crustal and Thermal Heterogeneities across the Fram Strait and the Svalbard Margin) are presented in higher resolution in this annexe.

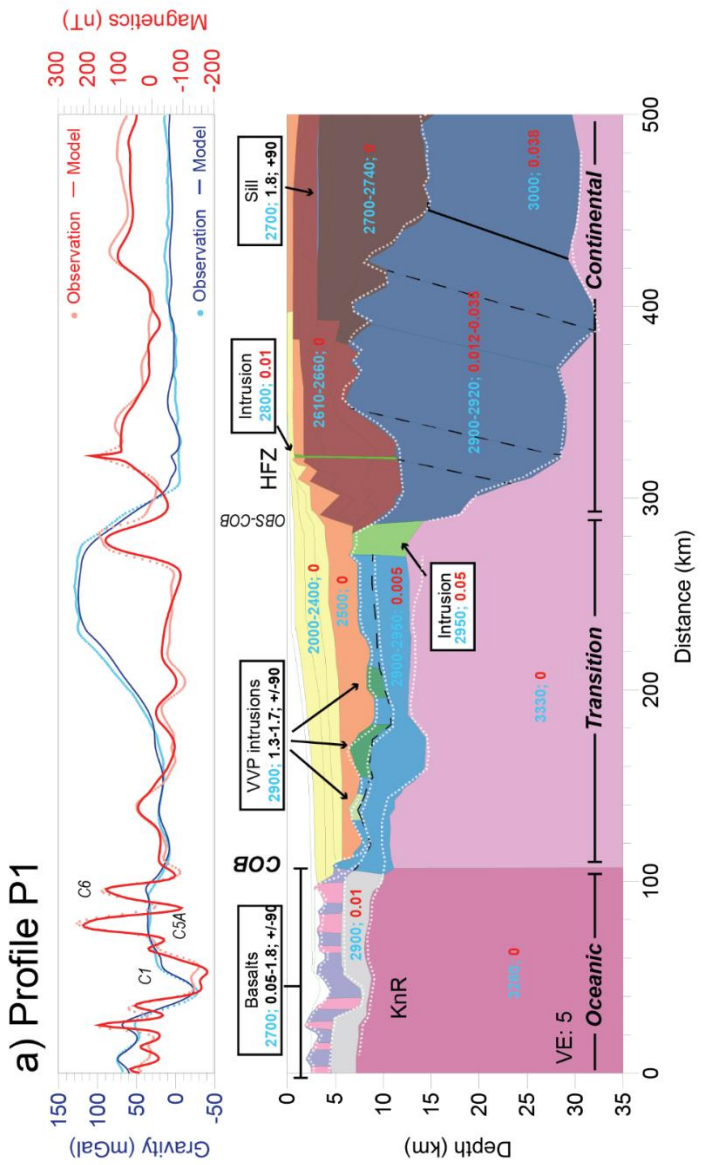

Figure 0.1 Profile 1 interpreted in the second manuscript with the modelled and observed data for gravity and densities (kg m^{-3}, blue), and for the magnetic, susceptibility (SI, red) and magnetization (A m^{-1}; inclination °) are shown. The bathymetric horizon is derived from [Olesen et al., 2010] and shows good correlation with the seismic horizons [Breivik et al., 2005; 2003; Breivik and Mjelde, 2001b; a] (white dashed lines). The magnetic isochrons resolved are identified on the profiles. (KnR: Knipovich Ridge, HFZ: Hornsund Fault Zone, VE: Vertical Exaggeration, OBS-COB: COB from seismic interpretation [Breivik et al., 2003])

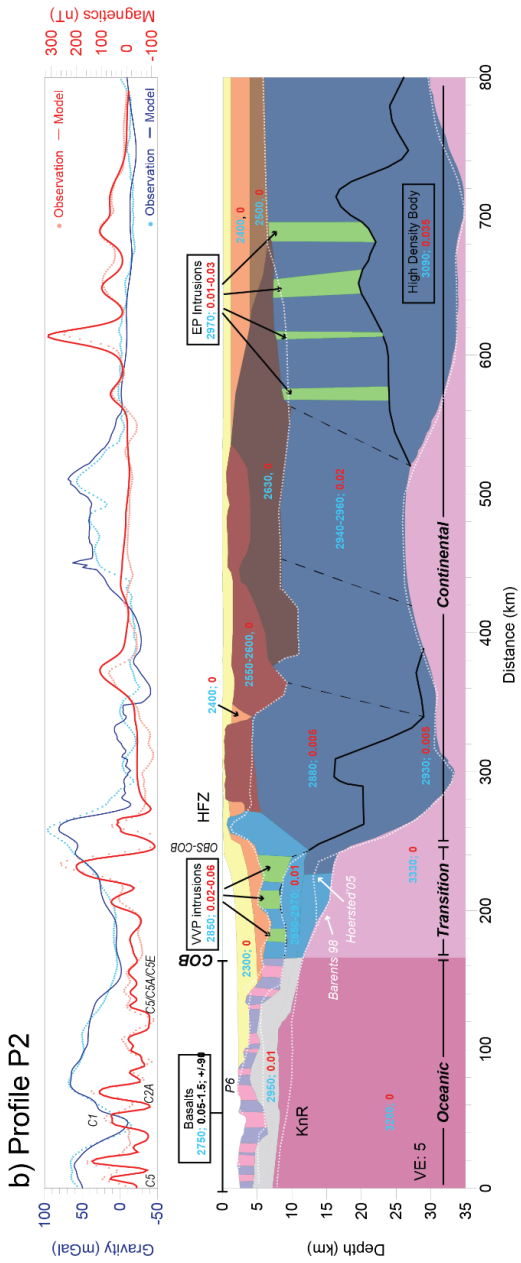

Figure 0.2 Profile 2 interpreted in the second manuscript with the modelled and observed data for gravity and densities (kg m^{-3}, blue), and for the magnetic, susceptibility (SI, red) and magnetization (A m^{-1}; inclination °) are shown. The bathymetric horizon is derived from [Olesen et al., 2010] and shows good correlation with the seismic horizons [Grad and Majorowicz, 2020; Czuba et al., 2008; Breivik et al., 2005; Ljones et al., 2004; Breivik and Mjelde, 2001b; a] (white dashed lines). The magnetic isochrons resolved are identified on the profiles. (EP: Edgeøya Platform, KnR: Knipovich Ridge, HFZ: Hornsund

Fault Zone, P6: Profile 6, VE: Vertical Exaggeration, OBS-COB: COB from seismic interpretation [Ljones et al., 2004; Breivik et al., 2003])

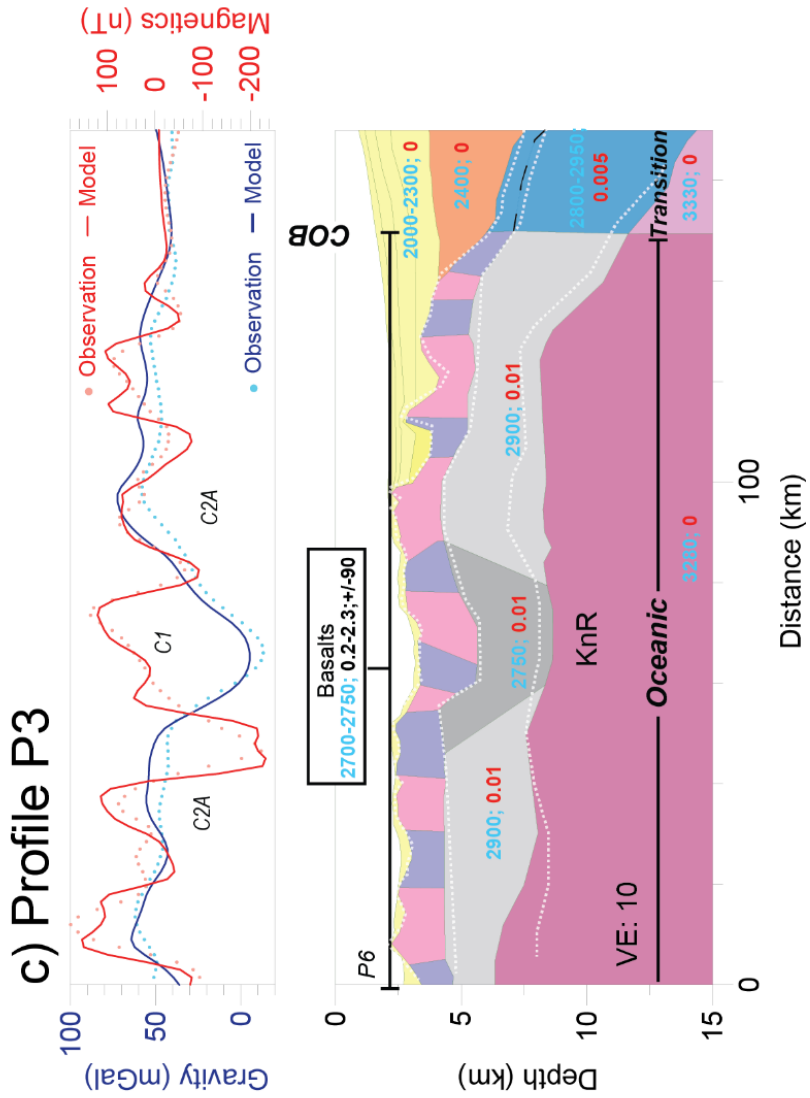

Figure 0.3 Profile 3 interpreted in the second manuscript with the modelled and observed data for gravity and densities (kg m^{-3}, blue), and for the magnetic, susceptibility (SI, red) and magnetization (A m^{-1}; inclination °) are shown. The bathymetric horizon is derived from [Olesen et al., 2010] and shows good correlation with the seismic horizons [Ritzmann et al., 2002; Breivik and Mjelde, 2001b; a] (white dashed lines). The magnetic isochrons resolved are identified on the profiles. (KnR: Knipovich Ridge, P6: Profile P6, VE: Vertical Exaggeration)

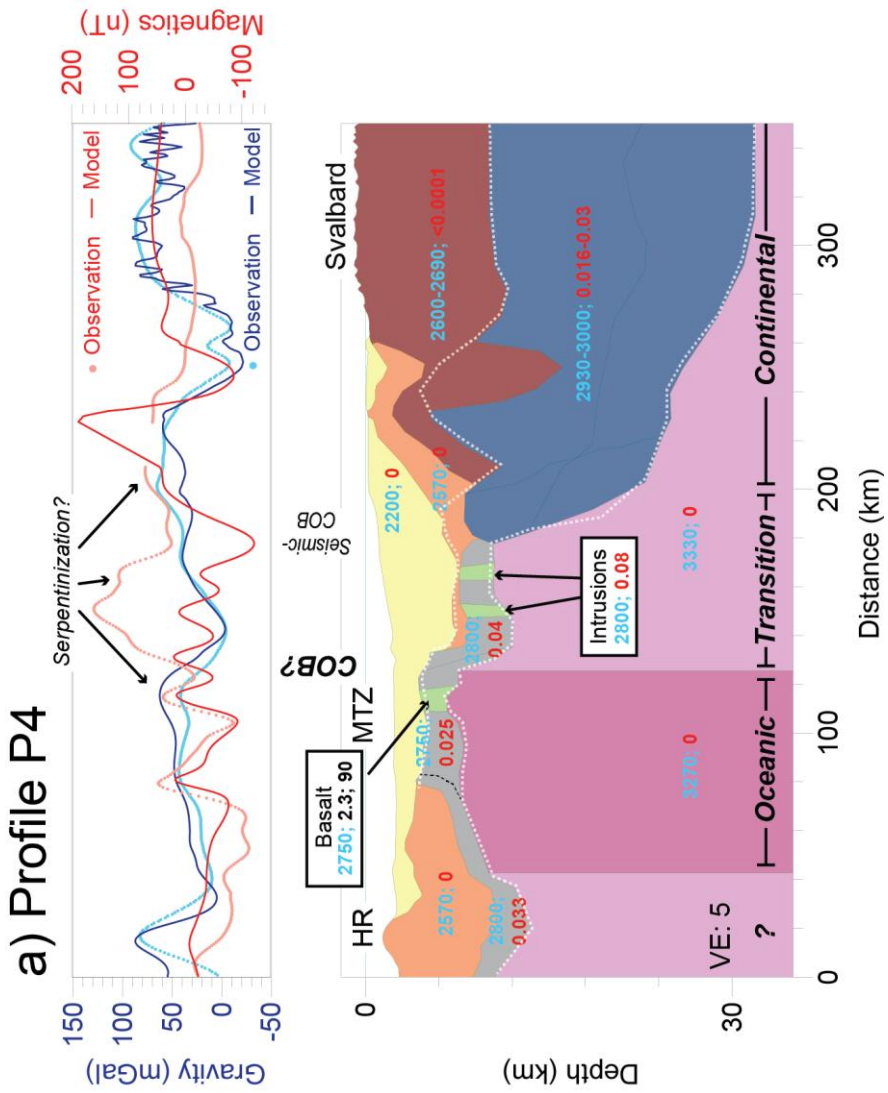

Figure 0.4 Profile 4 interpreted in the second manuscript with the modelled and observed data for gravity and densities (kg m^{-3}, blue), and for the magnetic, susceptibility (SI, red) and magnetization (A m^{-1}; inclination °) are shown. The bathymetric horizon is derived from Olesen et al. [2010] and shows good correlation with the seismic horizons [Ritzmann et al., 2004] (white dashed lines). The magnetic isochrons resolved are identified on the profiles. (HR: Hovgaard Ridge, MTZ: Molloy Transform Zone, VE: Vertical Exaggeration)

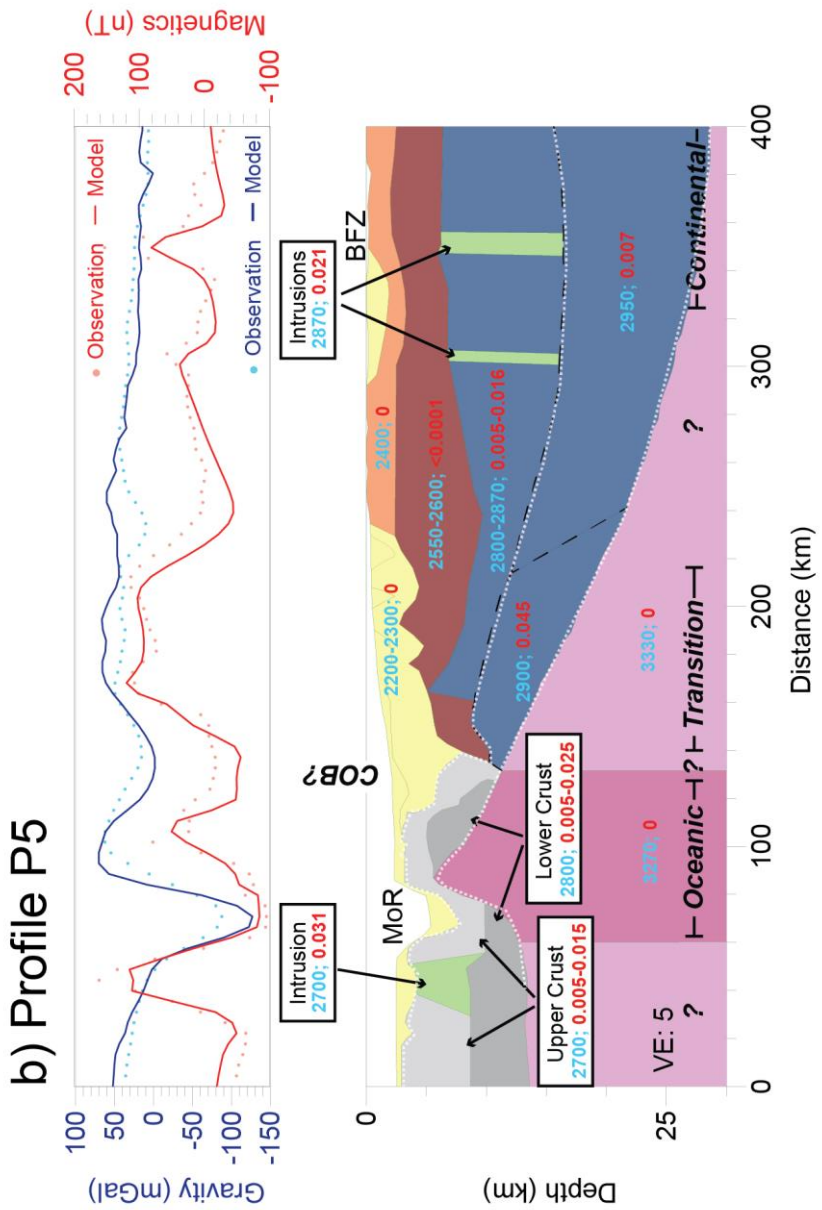

Figure 0.5 Profile 5 interpreted in the second manuscript with the modelled and observed data for gravity and densities (kg m^{-3}, blue), and for the magnetic, susceptibility (SI, red) and magnetization (A m^{-1}; inclination °) are shown. The bathymetric horizon is derived from Olesen et al. [2010] and shows good correlation with the seismic horizons [Czuba et al., 2005] (white dashed lines). The magnetic isochrons resolved are identified on the profiles. (MoR: Molloy Ridge, BFZ: Billefjorden Fault Zone, VE: Vertical Exaggeration)

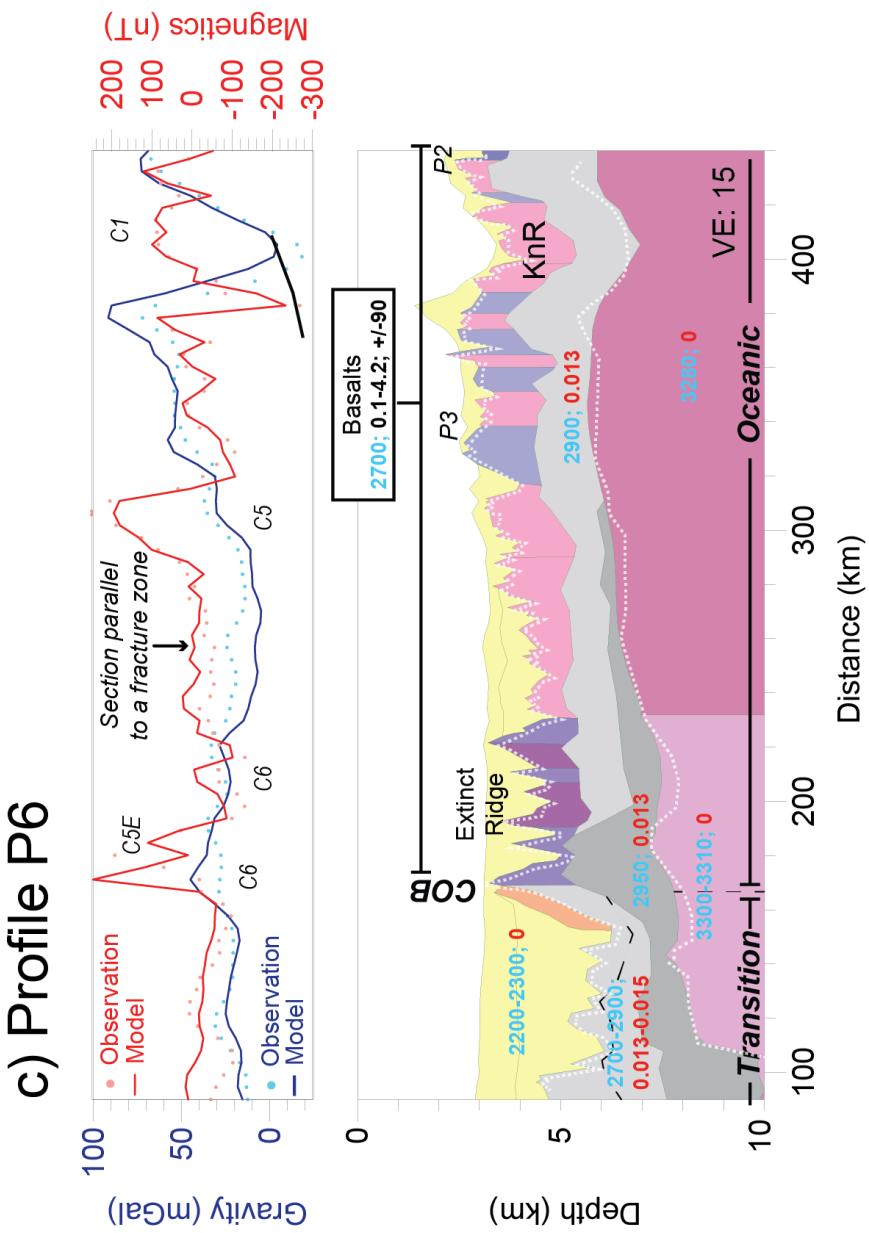

Figure 0.6 Profile 6 interpreted in the second manuscript with the modelled and observed data for gravity and densities (kg m^{-3}, blue), and for the magnetic, susceptibility (SI, red) and magnetization (A m^{-1}; inclination °) are shown. The bathymetric horizon is derived from Olesen et al. [2010] and shows good correlation with the seismic horizons [Hermann and Jokat, 2013] (white dashed lines). The magnetic isochrons resolved are identified on the profiles. (KnR: Knipovich Ridge, P2: Profile P2, P3: Profile P3, VE: Vertical Exaggeration)

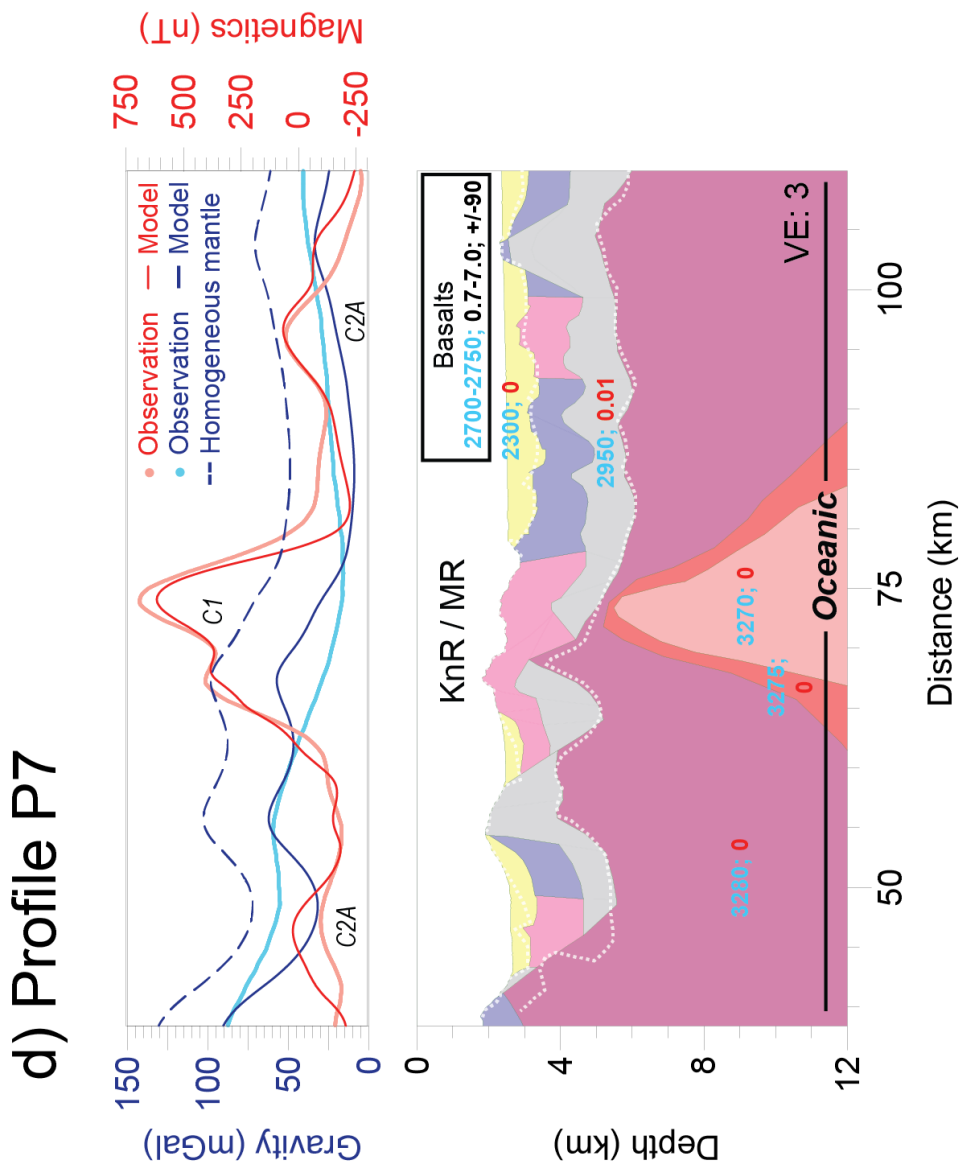

Figure 0.7 Profile 7 interpreted in the second manuscript with the modelled and observed data for gravity and densities (kg m^{-3}, blue), and for the magnetic, susceptibility (SI, red) and magnetization (A m^{-1}; inclination °) are shown. The bathymetric horizon is derived from Olesen et al. [2010] and shows good correlation with the CSEM/MT horizons [Lim, 2020; Johansen et al., 2019] (white dashed lines). The magnetic isochrons resolved are identified on the profiles. (KnR: Knipovich Ridge, MR: Mohn's Ridge, VE: Vertical Exaggeration)